Laser cooling and optical trapping of Ytterbium

Stefan L. Kemp

A thesis submitted in partial fulfilment
of the requirements for the degree of
Doctor of Philosophy

Department of Physics
Durham University

May 29, 2017

Laser cooling and optical trapping of Ytterbium

Stefan L. Kemp

Abstract

This thesis presents the development of an experimental apparatus designed to investigate the ultracold collisional properties for mixtures of Cs and Yb, with a long-term view to the creation of ultracold CsYb molecules via indirect cooling methods. The unpaired electron spin that is inherent to molecules of this form gives rise to a magnetic dipole moment in addition to a ground state electric dipole moment. This enables extra control over molecular interactions and should enable the experimental simulation of spin lattice models.

We focus on the implementation of a system designed to controllably laser cool and optically trap Yb. The first step in this system is the production of a magneto-optical trap (MOT) on the triplet $^1S_0 \rightarrow {}^3P_1$ transition of Yb. With careful control over the cooling beam detunings and power, gravitational-assisted Doppler cooling allows samples of Yb to be prepared at 22 μK. This regime of enhanced Doppler cooling is investigated and proves to be a crucial step to ensuring good transfer of cold Yb to optical traps.

The construction and characterisation of single and crossed beam optical dipole traps for Yb are discussed. The single beam optical trap has been used to verify a model for the optical trapping of Yb in its ground state. This trap has also been utilised as a tool for the measurement of the light shift on the $^1S_0 \rightarrow {}^3P_1$ transition at a wavelength of 1070 nm. In the main experimental sequence, Yb atoms are loaded from the magneto-optical trap into the crossed optical dipole trap, allowing evaporative cooling ramps to quantum degeneracy to be performed. This highly-reproducible system typically forms Bose-Einstein condensates with 2×10^5 ^{174}Yb atoms.

This thesis additionally reports on the progress made towards measurements of the interspecies scattering length for ^{133}Cs and Yb isotopes. We present two approaches that are being developed in tandem: rethermalisation in a conservative trap, and two-photon photoassociation. Progress towards rethermalisation measurements has focussed on developing systems for the efficient transfer of Cs to an optical trap. For photoassociative measurements, a laser system has been developed and tested by producing one-photon photoassociation spectra of Cs_2.

Declaration

I confirm that no part of the material offered has previously been submitted by myself for a degree in this or any other university. Where material has been generated through joint work, the work of others has been indicated.

Stefan L. Kemp
Durham, May 29, 2017

All the data from this thesis are available at **doi:10.15128/r2gx41mh85n**.

Dedicated to Mum and Dad,
for everything

Acknowledgements

It has taken five years to get to this point. Five of the most exciting, eventful, as well as difficult, years of my life. During this time a great number of people have contributed both technically and emotionally to this thesis, without whom it would not exist. I thank you all from the bottom of my heart. I apologise to anyone I fail to name here — I need to keep this brief, you already have enough to be reading in the following pages — your contribution is not forgotten.

First and foremost I must thank my supervisor, Simon Cornish, for convincing me as a naïve masters student that this would be a good idea. Without his support and guidance, both in the lab and after leaving Durham, I would never have completed writing this thesis. His guidance and dedication to the CsYb project have taught me so much, providing skills that I will keep with me during my future endeavours. Here, I would also like to acknowledge the funding of my PhD studentship from the UK Engineering and Physical Sciences Research Council and the MicroKelvin Molecules in a Quantum Array (MMQA) programme.

Special thanks must also be reserved for Steve Hopkins, a permanent part of team CsYb during my time in Durham. Some of his ideas may have been a little out there, but whether you need advice on physics, plumbing, electronics, or an excuse for a curry outing, Steve is your man. I'll always remember our late nights hunting for an Yb BEC, never giving up despite unfavourable circumstances. Steve has been a truly invaluable part of this project and I'm sure he will be missed across the wider atmol group. I hope you enjoy your well-earned retirement.

I've also had the privilege to work with every member of team CsYb to date. I could not have asked for a better person to show me the ropes than Kirsteen Butler. I have many fond memories of "dancing" to Kirsteen's infamous lab playlist, interpreting her unique form of sign-language, and Friday chocolate (which turned into Monday, Tuesday, Wednesday and Thursday chocolate astonishingly quickly). I must thank her for making my first few years in the lab such an entertaining experience, although I promise to never let her forget the incident of the lab stool. Ruben Freytag had the unenviable task

of moving half of the experiment up to Durham from Imperial, but brought with it welcome additions to the lab playlist. Without his experience of the Yb laser systems our first MOT would have been a long way further down the road. Lastly, I must thank Alex Guttridge for his immense support in my final few months in the lab and beyond. With his dedication and enthusiasm I know that this experiment will go on to much greater things.

I must also thank the other members of Team Cornish that have made this experience all the more enjoyable: Michael Köppinger for all of the corridor conversations, beer, and renditions of Hey Jude; Manfred Yu for his continued support both in the lab and in our time already spent out in the "real world", and Phil Gregory for coming back despite his time spent testing the Zeeman slower as a summer student. Further thanks go to Anna Marchant, Ana Rakonjac, and Peter Molony for countless useful discussions over the years.

Steve Lishman's team in the mechanical workshop have provided invaluable support since the inception of this project — I dare say we've contributed to more of his team's man-hours than many other projects combined. In particular I must thank Malcolm, Kevin, the Andrews, and Steve himself for allowing me to use their machinery myself when time was critical, and for putting up with the sheer number of designs we submitted. I also apologise to Kevin for the number of near-heart attacks suffered during the winding of the Zeeman slower.

On a personal note, I have to thank Mum and Dad for their love and endless support in everything I do. Without their encouragement I would not be in the position that I am in today. Three-hundred miles of separation didn't stop them from supporting me in their own way each and every day. I hope they know that I am forever grateful for everything they have done and sacrificed to support Chelsea and me over the years. This thesis is their thesis.

Lastly, I must thank the incredible Lucy Gardner. I'm sure the boundless fun we have each and every day contributed to the delay in crossing the finish line, but without you I would never have got there at all. Eternally patient, you have been my rock throughout times of panic and stress, whether by proofreading the entirety of this ridiculously large document several times, distracting me with your unique range of noises, or simply delivering sushi to the lab at weekends. I know you recently realised your dream of winning a medal, but trust me, you have deserved one for a long time. You never fail to put a smile on my face and I can't wait for all of our adventures to come.

Contents

List of Figures

List of Tables

Chapter 1

Introduction

In recent years the field of ultracold molecular gases has gained significant interest and momentum, producing many exciting directions for fundamental research, technology and precision measurement [1]. This interest stems from the production of ultracold ensembles of atoms that has revolutionised atomic and optical physics. This revolution was born from the first implementation of laser cooling and trapping in the 1980s, a technique that is now commonplace in atomic physics labs worldwide and for which the 1997 Nobel Prize for Physics was awarded [2–4]. The experimental realisation of a new phase of matter, the Bose-Einstein condensate (BEC), shortly followed. Using the technique of evaporative cooling, BECs of ^{87}Rb [5] and ^{23}Na [6] were produced, milestones for which the 2001 Nobel Prize was awarded. Since the original realisation of the BEC, the list of condensed elements has been ever-growing. Originally the domain of alkali elements [7–11], alkaline-earth, lanthanide, and other elements have since been condensed. These include ^{40}Ca [12], Sr [13–15], Yb [16–18], ^{168}Er [19], and the highly-magnetic ^{52}Cr [20] and ^{164}Dy [21].

Whilst a highly interesting phenomena in its own right, the phase transition to BEC has given rise to many research areas and applications. These include – but are not limited to – the study of vortices in superfluid gases and vortex lattices [22–25], the realisation of the atom laser [26–28], the production of bright matter-wave solitons [29–32], the observation of condensate collapse [33], and Anderson localisation [34]. Many of the alkaline-earth and

lanthanide elements possess no magnetic dipole moment in their ground state, as such the conventional method of accessing the phase transition by evaporatively cooling in a magnetic trap is redundant. Instead groups resorted to all-optical production of BECs by utilising the optical dipole force [35], in which intense laser fields are used to confine atoms. A natural extension to this technique was to load ultracold atoms into optical lattices, in which the interference of counter-propagating laser beams form periodic intensity patterns [36]. This tool has blurred the boundary between ultracold atomic physics and condensed matter physics, such as the simulation the band structure of solid-state systems [37] and the observation of the superfluid-Mott insulator transition [38].

There has also been considerable interest in mixtures of two quantum degenerate (or near quantum degenerate) species, opening the door to many experiments that are not possible with a single element. An area of considerable theoretical and experimental interest is that of phase separation between the two constituent species [15, 39–42]. Furthermore, combining the two species with an optical lattice potential offers a wide range of novel quantum phases to be accessed [43–45]. However, a significant reason for this interest is the possibility to associate heteronuclear dimers from two sources of ultracold atoms, offering a route to use well-established ultracold atom techniques in the production and trapping of ultracold molecules [1, 46].

1.1 Ultracold polar molecules

The extent of the research interest in ultracold polar molecules is justified by their vast number of applications [1]. Molecules, with their complex internal structure, offer great potential for precision measurement of fundamental constants. These include the measurement of the electron electric dipole moment, predicted by many different fundamental particle theories [47, 48]; a test of whether fundamental constants are changing with time, by comparison to astronomical observations [49, 50]; precision tests of the electron-to-proton mass ratio [51]; and measurements of parity-violating effects [52]. Not limited to measurements of fundamental properties, molecules may also be used as precision sensors [53]. Ultracold atoms also offer a testing ground for cold

chemistry and few-body physics [54, 55]. Further applications of interest include single photon sources [56] and quantum computation [57]. A significant reason for the production of ultracold polar molecules is in the application of quantum simulation of condensed matter systems [58]. The internal structure of heteronuclear dimers gives rise to long-range anisotropic dipole-dipole interactions, as opposed to the isotropic contact interactions present in atomic ultracold atomic ensembles [59]. Molecules in an optical lattice coupled by these long-range interactions offer an opportunity to explore effects such as high-temperature superconductivity, the fractional quantum Hall effect, and exotic forms of magnetism [36]. Despite this wave of interest centred on the association of ultracold molecules from ensembles of ultracold atoms, only five groups have succeeded in producing ultracold dimers in their ground state by association of ultracold atoms: KRb, JILA [60]; RbCs, Innsbruck and Durham [61, 62]; NaRb, Hong Kong [63]; and NaK, MIT [64].

One of the main motivations for the creation of ultracold molecules is the extra degrees of freedom offered by the rich vibrational and rotational structure. However, it is such structure that is often a hindrance in their production; typically these extra levels offer a multitude of decay channels which must often be worked around in order to produce molecules in their absolute ground state. Unfortunately this means, for the most part, that the simple and elegant technique of laser cooling, utilised as the start point for the vast majority of cold atoms experiments, is not easily applicable for the production of cold molecules. However, in some select systems, favourable Franck-Condon factors allow complex repumping schemes to "close" a cooling transition and allow for the production of magneto-optical traps of cold molecules. This is an area of considerable interest, and much progress has been made in recent years and looks like being a very promising area of research [65–68]. This method of laser cooling of molecules is only accessible to a few systems, and is generally not a practical scheme for many molecules of interest. Owing to these unfavourable circumstances, many methods of producing ultracold molecules have been put forward over recent years. Generally these methods fall into one of two categories – the direct or indirect cooling of molecules.

Direct cooling of molecules

The direct cooling of molecules involves taking a molecular source produced at high temperatures and subsequently cooling them. Several stages and methods are typically combined in an attempt to achieve this. Often the molecular source utilises buffer gas cooling in an attempt to make a bright beam of cold molecules. This usually involves a chamber containing a target material that is laser ablated to produced the desired molecules, which are then cooled by a buffer gas of Helium flowing through the source in order to create a cold beam [69, 70]. Despite these sources producing relatively cold molecules, they still need to be decelerated and a multitude of methods exist for this purpose. One of the most common methods is the use of rapidly switching electric fields to produce a Stark decelerator [71–75]. Alternatively, those molecules with magnetic dipole moments can be decelerated magnetically [76, 77]. The use of these decelerators is often limited by the length required to bring the molecules to a standstill. A novel solution to this problem is the use of a centrifuge decelerator as demonstrated by the Rempe group [78]. From this stage further trapping and cooling is performed, with magnetic or microwave traps often considered. There is also considerable theoretical interest in the sympathetic cooling of molecules with cold atoms [79–81].

There exist a number of advantages to the direct cooling of molecules, with the obvious being that the desired molecule is abundantly available by the use of a bright molecular source. Furthermore, no frequency stabilised laser light is required for the majority of these techniques, meaning that during the early stages of an experiment the choice of molecule to study may be changed. However, for the reasons mentioned above, the cooling of the molecules is generally a difficult task, and often leads to low phase-space density ensembles that are not suitable for studying the properties of ultracold molecular gases.

Indirect cooling of molecules

Where the direct approach to cooling molecules fails in producing high phase-space density ensembles, the indirect cooling of molecules often succeeds. In

this approach ultracold ensembles or mixtures of atoms are produced using the standard tools of laser cooling, magnetic trapping, and optical trapping that are typically available to the cold atom physicist. By creating atom clouds of low temperature and with high phase-space density, they may then be associated to form ultracold molecules with a minimal loss in phase-space density. Typically photoassociation [82] or magneto-association [83] are the techniques used to associate cold atoms into cold molecules.

Photoassociation excites colliding free atoms into a molecular bound state by the absorption of a resonant photon. This process requires favourable Franck-Condon factors to ensure good transfer to a bound state of the ground electronic state of the molecule. In some systems fortuitous circumstances can lead to efficient decay straight to the ro-vibrational ground state. This is the case for Cs_2, in which an unusual double-well potential in the electronically excited state leads to a favourable Franck-Condon factor [84]. This was also the case for LiCs, in which only a single photoassociation excitation was required for efficient decay to the ground state [85]. However, in many systems this is not the case, with further work required to reach the ground state. For example, in the photoassociation of $^{41}K^{87}Rb$ molecules, the process of Stimulated Raman Adiabatic Passage (STIRAP) was used to coherently transfer molecules from a high-lying vibrational state within the ground electronic state of the molecule, to the ro-vibrational ground state [86, 87]. Using STIRAP as a means to associate free atoms into molecular bound states in the electronic ground state is also possible, as has been demonstrated with Sr_2 in the work of Stellmer *et al*, albeit not to the absolute rovibrational ground state as yet [88]. In this work a Sr BEC is prepared in the Mott insulator phase with two atoms on each site of an optical lattice, from which STIRAP is used with a 30% efficiency in associating the localised atom pairs into molecules. This work is particularly of use for systems where magneto-association is difficult or even impossible.

Magneto-association utilises the phenomena of Feshbach resonances to coherently produce atoms in a single bound state of the molecule. Since their discovery, Feshbach resonances have been found and used in a variety of homonuclear and heteronuclear molecules [55]. STIRAP is often used to coherently transfer molecules in these weakly bound Feshbach states to the ab-

solute ro-vibrational ground state of the molecule. Indirect cooling methods have been used to produce a large number of homonuclear and heteronuclear molecules: $^{6}Li_2$ [89, 90], $^{23}Na_2$ [91], $^{40}K_2$ [92], $^{85,87}Rb_2$ [93, 94], $^{133}Cs_2$ [95], $^{40}K^{87}Rb$ [60], $^{23}Na^{40}K$ [96], $^{23}Na^{6}Li$ [97], $^{87}Rb^{133}Cs$ [61, 62], $^{23}Na^{133}Cs$ [98], and $^{23}Na^{87}Rb$ [63]. Work is ongoing with mixtures of Li-Cs [99], Yb-Rb [100], Yb-Li [101, 102], K-Cs [103], Rb-Sr [104], and Yb-Cs [105]. To the author's knowledge, these lists are up to date at the time of writing.

1.2 Why CsYb?

To date the only controllable ultracold molecules produced in their rovibrational ground state have been bialkali dimers. Molecules of this form have "paired up" valence electrons, as such any magnetic dipole moment is minimal and due to nuclear spin alone. Whereas heteronuclear dimers consisting of an alkali atom and an alkaline-earth type atom with two valence electrons exhibit $^{2}\Sigma$ symmetry, with an unpaired electron spin giving the molecule a magnetic dipole moment in addition to an electric dipole moment. This gives an extra handle on controlling the molecule and, when loaded into an optical lattice, gives the possibility of simulating lattice-spin models [58].

The primary long term aim of this experiment is to obtain near-unity filling of an optical lattice with Cs and Yb atoms, followed by in-lattice association to molecular states. The elements of Yb and Cs have been specifically chosen for a number of reasons. Firstly, both elements have independently been studied in numerous ultracold atom experiments, and the techniques for individually cooling the species to quantum degeneracy are well-established. The use of Yb allows for the study of seven different isotopic combinations of CsYb. By using one of the heaviest alkali elements in Cs, this allows for the tuning of the reduced mass of the system over quite a large range. Cs is also predicted to be favourable for a novel form of Feshbach resonance [106]; since the reduced mass of the system can be used to tune the background interspecies scattering length, this makes CsYb a favourable candidate for magneto-association of this form.

1.3 Thesis outline

In this thesis we look towards the indirect cooling and association of Yb and Cs with the aim of creating ultracold CsYb molecules. The route to producing these molecules, whether using photo- or magneto-association, is unclear. However, whichever method is used, it is necessary to understand the molecular potential in order to determine where the bound states of the molecule are likely to lie. Whilst the shape of the potential is well-known, exact details can only be found by measurement. The measurement of the background scattering length provides a knowledge of the last bound state supported. Together with the long-range shape of the potential, this enables the prediction of the positions of potential Feshbach resonances. The apparatus used in this thesis is described in detail elsewhere [107, 108], here we give an overview of the apparatus, describing any changes or additions to the system in detail. The apparatus in its current form is designed as a "proof of principal" for establishing a route to ultracold CsYb molecules. It is likely that the apparatus will need to be modified or overhauled before any experiments using ultracold molecules can be performed; this is owing to the lack of optical access for an optical lattice in the apparatus' present state.

The remaining chapters in this thesis address the following:

- Chapter 2 outlines the existing experimental setup, including detailed discussion on the implementation of additional features to the experiments and any extensive modifications that have been made. This includes a redesign of the atomic oven and an overhaul of the Yb laser systems. A number of experimental techniques and diagnostics used within the experiment are also described.

- Chapter 3 provides a detailed description of the atomic beam fluorescence spectroscopy techniques used to stabilise the frequency of the Yb laser systems. This includes the design of the "beam machine" and fluorescence detectors. We also discuss a technique for the separation of the fluorescence spectra for bosonic and fermionic isotopes of Yb.

- Chapter 4 fully characterises an Yb magneto-optical trap (MOT) on the $^1S_0 \rightarrow {}^3P_1$ transition, including an investigation of the enhanced

Doppler cooling in a narrowband MOT at low laser intensities. We also describe a technique for calibrating the absolute detuning of the MOT beams. The design, production, and performance of our dual-species Zeeman slower is reported, including an analysis of real-world problems affecting Zeeman slower design and techniques with which to overcome them.

- Chapter 5 outlines the incorporation of a number of optical trap designs into the experiment, describing the effective loading of the traps directly from a narrowband Yb MOT. We report on the first realisation of a BEC of ^{174}Yb with this apparatus.

- Chapter 6 reports on the progress made towards a measurement of the interspecies scattering length for a system of Yb and Cs. We describe the implementation of a two-photon photoassociation spectroscopy system and efforts to produce rethermalisation measurements of the elastic scattering cross section. Whilst a measurement of the scattering length is not yet within our grasp, these methods have further refined the experimental routines required to reach this goal.

- Chapter 7 draws conclusions and summarises the experiments performed in the previous chapters. We look ahead to the future and offer short-term and long-term outlooks for the experiment.

The relevant background theory is outlined at appropriate points within the thesis, although only a brief treatment of the various topics is given. For a more thorough treatment of any topic the reader is directed to references for more detailed review articles.

1.4 Publications

The following publications have resulted from the work presented within this thesis:

- **Production and characterization of a dual species magneto-optical trap of cesium and ytterbium**
  S. L. Kemp, K. L. Butler, R. Freytag, S. A. Hopkins, E. A. Hinds, M. R. Tarbutt, and S. L. Cornish
  Rev. Sci. Instrum. ***87*** *023105 (2016)*

- **A versatile dual-species Zeeman slower for caesium and ytterbium**
  S. A. Hopkins, K. L. Butler, A. Guttridge, R. Freytag, S. L. Kemp, E. A. Hinds, M. R. Tarbutt, and S. L. Cornish
  Rev. Sci. Instrum. ***87*** *043109 (2016)*

- **Direct loading of a large Yb MOT on the $^1S_0 \rightarrow {}^3P_1$ transition**
  A. Guttridge, S. A. Hopkins, S. L. Kemp. D. Boddy, R. Freytag, M. P. A. Jones, E. A. Hinds, M. R. Tarbutt, and S. L. Cornish
  J. Phys. B: At. Mol. Opt Phys. ***49*** *145006 (2016)*

Chapter 2

Experimental apparatus

The experimental apparatus is described in this chapter. Due to the inherent development process involved in building a cold atom experiment, some of the details presented here are reported elsewhere [107]. In addition to reviewing the experiment to date, a discussion of changes and additions to the experimental apparatus is given.

2.1 Experimental overview

Whilst an ultracold atom experiment typically utilises only a few simple concepts such as laser cooling, dipole trapping, and magnetic fields, the apparatus required can be quite complex. The experiment is split between two optical tables. The first table, referred to as the "main table", houses the vacuum system, magnetic field coils including the Zeeman slower, and the optical trapping system. The second table, referred to as the "laser table", is where the majority of laser light is derived for the experiment. All laser frequency stabilisation is performed on this table and light is fibre coupled to the main table for the purposes of laser cooling, Zeeman slowing, optical pumping, and imaging. The exception to this rule is the laser used to derive the 399 nm Zeeman slower light for Yb. For this operation, laser power is at a premium, as such the laser is situated on a breadboard above the vacuum system. Light for 399 nm spectroscopy and laser frequency stabilisation is fibre coupled to the laser table.

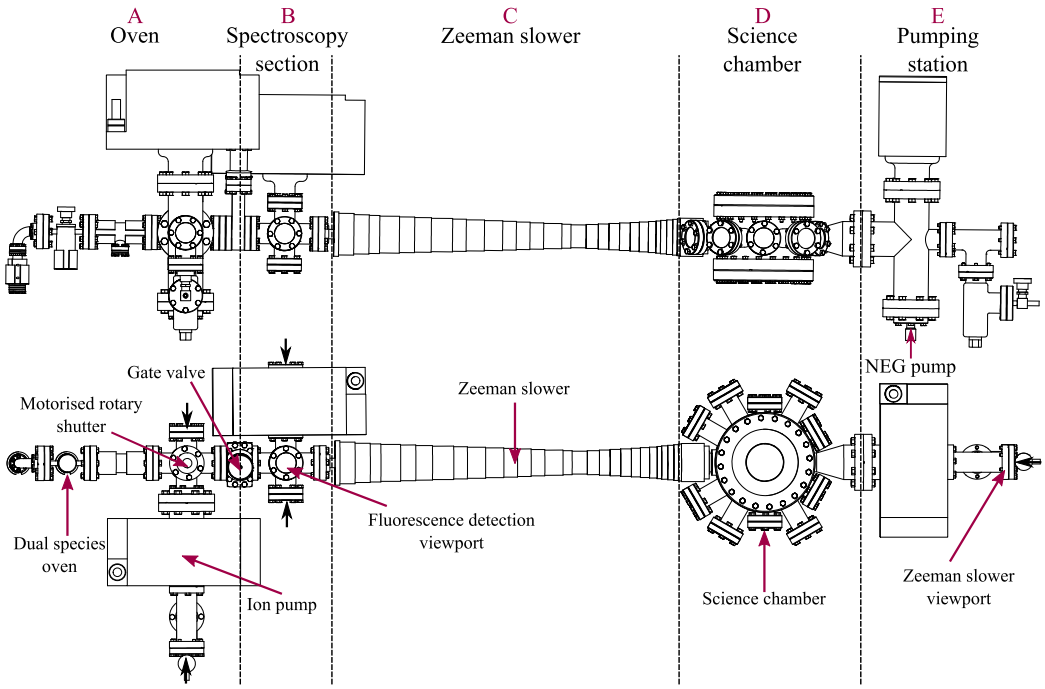

Figure 2.1: Side and top schematic drawings of the updated vacuum system. The dotted lines and corresponding labels split the apparatus into the constituent sections described in the text: A, the updated dual species oven; B, the spectroscopy cross; C, the Zeeman slower; D, the science chamber; and, E, the pumping station that maintains UHV pressures in the science chamber.

The primary aims of this apparatus are to prepare Yb and Cs atoms in a dual species MOT, to transfer them to an optical trap for further cooling, and to investigate the interspecies scattering properties of the two elements. These investigations are designed to find a route towards the production of ultracold CsYb molecules using the techniques of magnetoassociation or photoassociation. The aims set out above define a series of critical design specifications for the apparatus: good optical axis for the MOT, optical pumping, absorption imaging, fluorescence detection, optical trapping, and photoassociation laser beams; the ability to generate large magnetic bias fields in order to access interspecies Feshbach resonances; a ultra-high vacuum (UHV) vacuum environment to minimise trap loss from background collisions; and the possibility to incorporate an optical lattice in order to stabilise CsYb molecules against exchange interactions of the form $2\mathrm{CsYb} \rightarrow \mathrm{Cs}_2 + \mathrm{Yb}_2$ [109].

These specifications are met by using a fully dual species apparatus, a

schematic of which can be seen in figure 2.1. The atomic source is a dual species oven, a design that has been improved since it was first reported in reference [107]. A dual species Zeeman slower (described in detail in section 4.2) is used to load the Yb and Cs into a dual species MOT in a single stainless steel science chamber. This chamber is maintained at UHV pressures and features a total of twelve anti-reflection coated viewports, two of which are mounted in re-entrant flanges. These flanges allow magnetic field coils to be located close to the trapped atoms, enabling large bias fields to be generated with minimal compromise on optical access to the chamber. A further two vacuum ports on the chamber are reserved for Zeeman slowing and vacuum pumping. Throughout the apparatus, a total of three ion pumps and two non-evaporable getter (NEG) pumps are used to maintain low pressures.

Sequential loading of the two species into the MOTs is provided by the dual species Zeeman slower by decelerating the overlapped thermal beams of Cs and Yb originating from the dual species oven. Loading an Yb MOT on the $^1S_0 \rightarrow {}^3P_1$ transition is experimentally challenging due to its narrow linewidth, a consequence of which is a low MOT capture velocity, and so careful design of the Zeeman slower is crucial. However, this has the advantage of a correspondingly low Doppler temperature (see table 2.1 for a summary of experimentally important properties of Cs and Yb and the optical transitions used in this experiment). Another advantage of loading an Yb MOT directly on the 556 nm transition is that it negates the need for a collection MOT operating on the 399 nm $^1S_0 \rightarrow {}^1P_1$ transition, preserving optical access for future experiments. It also avoids the problem of optical pumping into metastable ^3D states, which limits the lifetime and number of atoms in a 399 nm MOT [110, 111].

The following sections describe the design and performance of these features of the apparatus, as well as improvements, changes, and additions made to the laser and diagnostic systems since the publication of [107].

Table 2.1: A table summarizing the key properties of Cs and Yb and the associated transitions used in this apparatus

	Cs	Yb	
Number of stable isotopes	1	7	
Vapour pressure, P_V ($T = 300$ K) [112, 113] (torr)	7×10^{-7}	3×10^{-21}	
Temperature at which $P_V = 10^{-3}$ torr (°C)	109	408	
Transition	$6\,^2S_{1/2} \rightarrow 6\,^2P_{3/2}$	$6s^2\,^1S_0 \rightarrow 6s\,6p\,^1P_1$	$6s^2\,^1S_0 \rightarrow\ 6s\,6p\,^3P_1$
Wavelength, λ (nm)	852.3	398.9	555.8
Linewidth, $\Gamma_0/2\pi$ (MHz)	5.234	28.0	0.182
Doppler Temperature, T_D (μK)	126	673	4.4
Saturation intensity, I_{sat} (mW cm^{-2})	1.10	63.1	0.139
Maximum acceleration, a_{max} (m s^{-2})	5.79×10^4	5.06×10^5	2.36×10^3

2.2 Vacuum system

2.2.1 Dual species oven

The vapour pressures for Cs and Yb at room temperature are summarised in table 2.1. There exist numerous methods of loading a MOT, and with its large background vapour pressure, a Cs MOT can be loaded from a vapour cell alone. However, this high background pressure [112] is not conducive to the production of ultracold or quantum degenerate gases. For this reason Cs should be loaded from either a second collection MOT [114–116] or from a Zeeman slower. Table 2.1 shows the low room temperature vapour pressure of Yb, which is insufficient to produce a simple vapour pressure collection MOT. Thus Yb needs an effusive oven to create a high-flux, collimated atomic beam, which is then decelerated so that a MOT may capture the atoms. The use of a Zeeman slower is the most common choice with which to load an Yb MOT, although a selection of other loading techniques have also been demonstrated [117, 118]. We have opted to use a dual species oven and Zeeman slower as the more elegant solution; one which saves optical access to the science chamber.

The oven currently used in this apparatus is shown schematically in figure 2.2. The previous incarnation of the oven [107] incorporated Cs dispensers mounted inside a heated chamber. However, a vacuum leak in the Yb part of the oven prompted a redesign of the system, which is based on the design described in references [119, 120]. The Yb and Cs sources are located in separate chambers of the oven, which are heated to different temperatures: the Yb source is heated to 485 °C, whereas the Cs source is maintained at 80 °C. These different temperatures are chosen so that the vapour pressure of each element in the oven is $\sim 10^{-3}$ torr. Both of the sources hang below the beam line of the experiment (the axis defined by the Zeeman slower), with the Cs at the far end and the Yb closer to the oven exit. This ordering is necessary to maintain a temperature gradient across the oven to ensure the oven exit is the hottest part, this means that the temperature of the sources alone determine the flux of their respective atomic beams. The atomic beams travel through two semicircular channels (figure 2.2), which are separated by

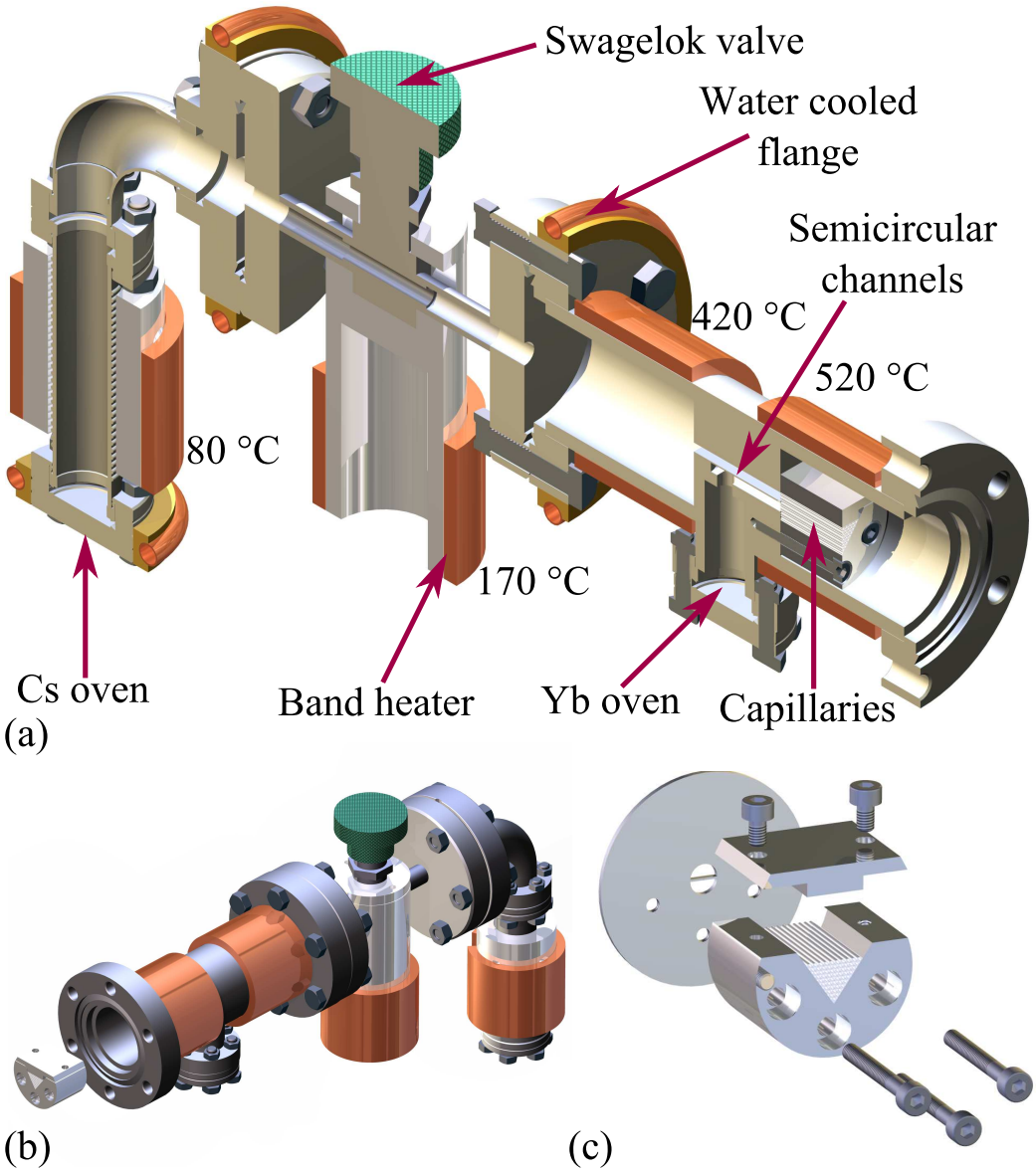

Figure 2.2: (a) A cutaway schematic of the dual species oven showing the paths of the two species through the oven. The nozzle heaters are shown as copper bands and the water cooling as copper tubes. The temperatures displayed are the nozzle heater set points, the Yb chamber is typically measured to be at 485 °C. (b) Rendering of the oven with the capillary clamp shown outside the oven for detail. (c) Exploded view of the capillary array and the wire-eroded semicircular channels that the array is clamped over within the oven.

a 0.4 mm dividing wall. The channels are made by the wire-erosion of a custom vacuum part, and may be seen in more detail in figure 2.2 (a) and (c).

The MOT capture region is located 1.5 m away from the oven, and as such the beam needs to be well collimated in order to prevent Cs and Yb coating the inner surface of the vacuum system in undesired locations. For collimation of the atomic beam we use an array of 55 capillary tubes, each tube of length 20 mm having an internal diameter of 0.58 mm. The tubes are clamped in a triangular recess which is bolted over the exit of the semicircular channels and can be seen in figure 2.2 (b) and (c). References [121, 122] provide further detailed analysis of the theory and practice of the production of collimated atom beams.

An ampoule containing 1 g of Cs is used to load the Cs part of the oven, replacing the dispensers used in reference [107]. This ampoule is placed in the bellows shown in figure 2.2 (a) and, once the oven has been evacuated and baked, is broken inside the bellows to release the Cs. Figure 2.2 (a) shows that this new version of the oven incorporates a valve (Swagelok, SS-4H-TW) between the Cs and Yb chambers of the oven, allowing the Cs oven to be sealed when it is not being used. This is an important feature as Cs has an appreciable flux even at room temperature; a small MOT of Cs can even be produced with the valve open and the Cs oven maintained at room temperature. This allows Cs to be studied and optimised independently of Yb. An additional purpose of the valve is to allow the Yb to be replenished without bring the Cs source up to air.

Four band heaters (Watlow, MB1J1JN2-X66) are used to maintain a temperature gradient across the oven body. The temperatures at which the band heaters are heated to are shown in figure 2.2 (a). This temperature gradient is required to prevent the Cs and Yb migrating from their respective reservoirs. It is important that the capillary tubes, which mark the exit of the oven, are the hottest point in the system. This ensures that the atoms, in particular Yb, do not stick to the internal capillary walls and block the system. To cool the oven and to ensure that the apparatus further down the beam line remains cool, a series of water cooled flanges are used. The locations of these flanges are shown in figure 2.2 (a).

The oven shown in figure 2.2 is connected to a six-way cross which is followed by an all metal DN40 CF gate valve (MDC Vacuum, E-6V-1500M-11). The purpose of the gate valve is to seal off the oven from the rest of the appara-

tus when the experiment is not running, and to allow the maintenance of the oven section without bringing the science chamber up to air. The six-way cross includes connections to an ion pump (Agilent, VacIon55), a NEG pump (SAES, Capacitorr C400-2-DSK), and a pair of viewports. The NEG pump has a large pumping rate for hydrogen within the vacuum system, whereas the ion pump removes any other unwanted atoms or molecules, such as any Cs that builds up over the course of running the experiment. The top vacuum port of the six-way cross is attached to a motorised feedthrough (MDC Vacuum, BRM- 275-03), which is used to rotate an atomic beam shutter. The shutter features two 5 mm channels orthogonal to one another, allowing the atomic beam flux to be probed when the shutter is open. Control software is used to remotely block the beams by rotating the shutter 45 °. To maintain the rest of the vacuum system at temperatures as close to that of the room as possible, an additional two water cooling jackets are attached to the six-way cross. All of these features and the connection to the oven may be seen in figure 2.3.

2.2.2 Spectroscopy chamber

The spectroscopy section (section B in figure 2.1) consists of a second six-way cross, allowing further probing of the atom beams, and a 40 $\mathrm{l\,s^{-1}}$ ion pump to be attached. A rendering of this section is shown in figure 2.3. The cross is separated from the oven section by a differential pumping tube and the aforementioned all-metal gate valve. The differential pumping tube has a 5 mm diameter and is 60 mm in length, leading to a conductance of 0.25 $\mathrm{l\,s^{-1}}$.

Simple absorption spectroscopy was performed on the Cs atomic beam through this six-way cross and at the rotary beam shutter (figure 2.3) in order to test the collimation of the atomic beam. These measurement points are 23.5 cm apart. A resonant probe beam, orthogonal to the atomic beam, with a $1/e^2$ diameter of 0.75 ± 0.06 mm was translated across the atomic beam, and the amount of absorption at each point was recorded. We find the width of the atomic beam to be 6.1 ± 0.5 mm at the rotary shutter and 6.5 ± 0.6 mm at the spectroscopy six-way cross, showing that the oven produces a well-

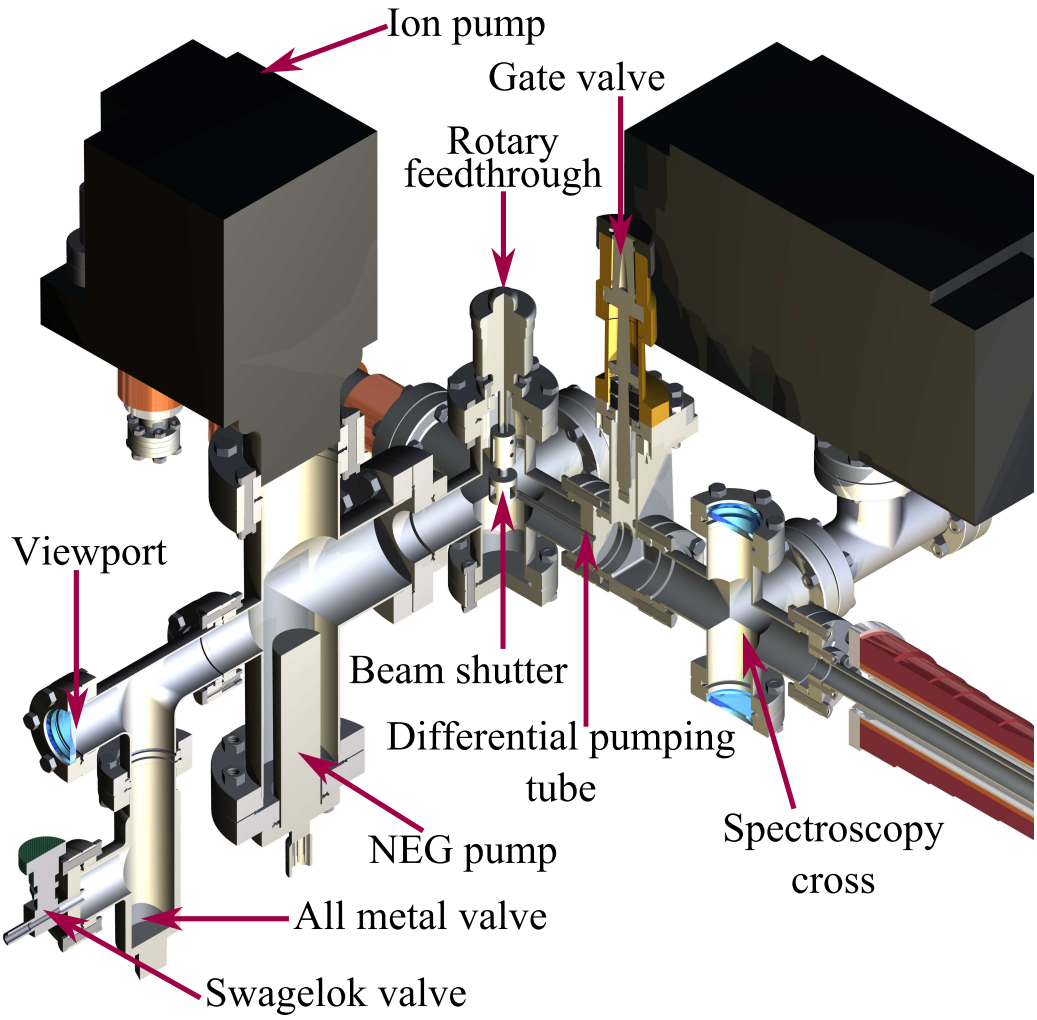

Figure 2.3: Schematic showing a cutaway of the six-way cross connected to the oven and all of the vacuum pumps, valves, and shutters that are attached to it. Optical access for probing the atomic beam is also shown.

collimated atomic beam. By probing the atomic beam at an angle of 6° from orthogonal, we observed a Doppler shift of 31 ± 1 MHz of the absorption peak. This corresponds to a mean atomic velocity of 260 ± 10 $\mathrm{m\,s^{-1}}$, which is as expected from the Maxwell-Boltzmann distribution for the Cs oven temperature (at the time of taking the data, the leftmost band heater in figure 2.2(a) was at 100 °C).

2.2.3 Zeeman slower vacuum

Section C in figure 2.1 shows the dual species Zeeman slower. A dual species design saves optical access to the science chamber with only one line of entry, and a single viewport reserved for the decelerating light. In terms of the vacuum system itself, the Zeeman slower is very simple consisting of a single 77 cm long DN16 tube. The tube connects the spectroscopy section to the science chamber via 3 ” flexible couplers (MDC, 075-X), which relieves any strain when the final connections are made. This section has a vacuum conductance of 0.64 $\mathrm{l\,s^{-1}}$ and gives a pressure ratio of approximately 10^4 between the oven and science chamber when combined with the differential pumping tube described above. In order to produce an Yb MOT on the ${}^1S_0 \rightarrow {}^3P_1$ transition, the atoms need to be entering the capture region at very small velocities, typically around 7 $\mathrm{m\,s^{-1}}$ for an Yb MOT on the ${}^1S_0 \rightarrow {}^3P_1$ transition. A consequence of this is that the point at which the Zeeman slower releases atoms needs to be as close as possible to the MOT, otherwise the atoms would fall too far under gravity or their transverse motion would reduce the MOT capture efficiency. Our Zeeman slower exit is located 7.5 cm away from the MOT, allowing the large magnetic field at the end of the Zeeman slower to drop to zero, ensuring any unwanted residual magnetic field in the MOT capture region is minimal. For more information on these considerations, see section 4.2

2.2.4 Science chamber

The heart of the vacuum system is a custom-made science chamber by VG Scienta, which is labelled as section D on figure 2.1. In this experiment

optical access to the science chamber is essential because a vast variety of beams must have entry and exit to the chamber: six MOT beams for each species, repump light for Cs, optical pumping light for Cs, imaging light for each species, a Zeeman slower beam for each species, an optical dipole trap, and photoassociation beams to name those currently in the setup. It is also possible that additional dipole traps and lattices will need to be included. For this reason, the science chamber features ten anti-reflection coated viewports around its circumference, and a further two vacuum ports set aside for the Zeeman slower and pumping station. The viewports and the beams passing through them can be seen in figure 2.4.

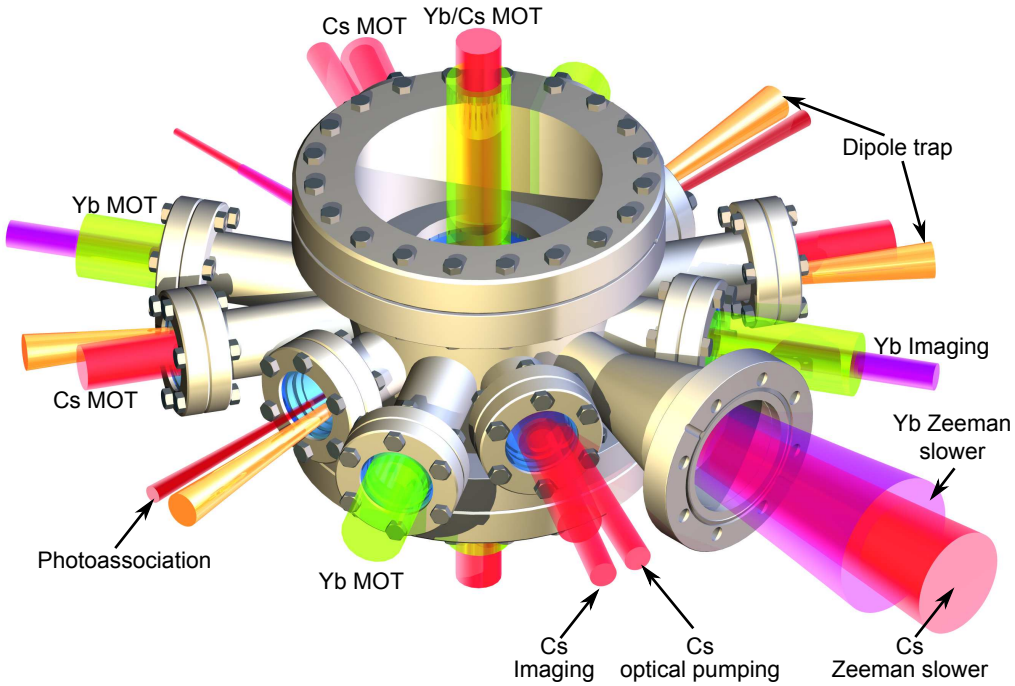

Figure 2.4: A rendering of the science chamber demonstrating the optical access available. The laser beams currently passing through the chamber are shown passing through their respective viewports; 399 nm light is shown in purple, 556 nm light in green, 852 nm light in red, 895 nm light in dark red (photoassociation beam), and 1070 nm light in orange. Note that the Zeeman slower viewport is not shown on the figure as it is located beyond the pumping station that attaches to the science chamber.

If interspecies Feshbach resonances are to be found for a Yb-Cs mixture, the widest resonances are likely to require large magnetic fields [106]. To apply magnetic fields up to ∼2000 G, we have incorporated re-entrant flanges on the topside and underside of the science chamber. These allow multiple

sets of coil pairs to be mounted as close to the atoms as possible. The science chamber is mounted between circular plates. These plates feature an array of tapped holes for a variety of mounting purposes, but also have grooves running around their circumference to incorporate vertical "shim" coils, allowing for finer control of the magnetic field in the chamber. For more information of the magnetic coils used in the experiment, see section 2.5. The re-entrant flanges also house a further two anti-reflection viewports, as can be seen in figure 2.4. These viewports are currently used for the "Up-Down" beams of the MOT for each species.

A further pumping station is connected to one of the vacuum flanges on the science chamber. This station consists of the same vacuum pumps as are on the oven, allowing UHV pressures to be maintained in the science chamber. The pumping station is shown in figure 2.1 as section E. On the far right of the schematic, a further viewport is shown. This viewport is the entry port of the two overlapped Zeeman slowing laser beams for Yb and Cs. The Zeeman slower itself is connected to the opposite vacuum flange on the science chamber.

2.3 Vacuum Assembly

The apparatus was split into three parts during construction, which were independently baked at 200 °C in order to increase outgassing, whilst being turbo-pumped. The three sections were the oven (parts A and B in figure 2.1), the Zeeman slower tube (part C), and the science chamber (parts D and E). Following baking the individual sections were moved to the main table and connected.

Prior to making the final connections, the Zeeman slower vacuum tube was inserted into the Zeeman slower former tube upon which the coils are mounted. We have used a series of aluminium mounts to bear the weight of the Zeeman slower coils and former tube, so as to relieve stress on the vacuum tube. The bellows at each end of the Zeeman slower vacuum tube were then attached to the science chamber and the oven respectively.

Heater tape was then used to bake the whole system whilst activating the ion

and NEG pumps in both the oven and science chamber sections. The Zeeman slower vacuum tube had been wrapped in heater tape before being inserted into the former tube, allowing this long section to be baked too. Following this procedure the science chamber reached UHV conditions ($< 10^{-9}$ torr). More details on the pumping and baking process may be found in [107].

2.4 Laser light and frequencies

For both Cs and Yb we require several different sources and frequencies of laser light, both resonant and off-resonant. These beams are used to trap, cool, decelerate, detect, and associate the atoms into molecules. Cooling and trapping is fairly routine for both species due to a favourable atomic level structure and accessible laser wavelengths. The structure of the low-lying levels of both species may be seen in figure 2.5.

Despite the favourable levels, the method for cooling each species in a MOT is different in character due to the differing numbers of valence electrons. Cs has a single valence electron, giving a ground state total angular momentum quantum number of $J = 1/2$. This couples to the nuclear spin of $I = 7/2$ to give two ground state hyperfine levels. The result of this is that light is required to repump atoms that have decayed into the dark $F = 3$ hyperfine ground state. Yb has two valance electrons, pairing up to give $J = 0$ in the ground state: there is no hyperfine splitting of the ground state and consequently there is no need for repumping light in a MOT. However, the two valence electrons give rise to singlet and triplet excited states. The singlet transition to the $^1P_1$ state has a wavelength of 399 nm and is used for Zeeman slowing, whereas the 556 nm transition to the triplet $^3P_1$ state is used as the MOT cooling transition. More information on the choice of transition for deceleration and cooling purposes can be found in later sections.

In addition to the MOTs and Zeeman slowing light, we also use lasers for optical trapping and photoassociation. The optical trap operates using off-resonant 1070 nm light. The photoassociation light operates at wavelengths red-detuned from the Cs D_1 dissociation threshold at 895 nm. The following sections describe in more detail the generation of all laser light used in the

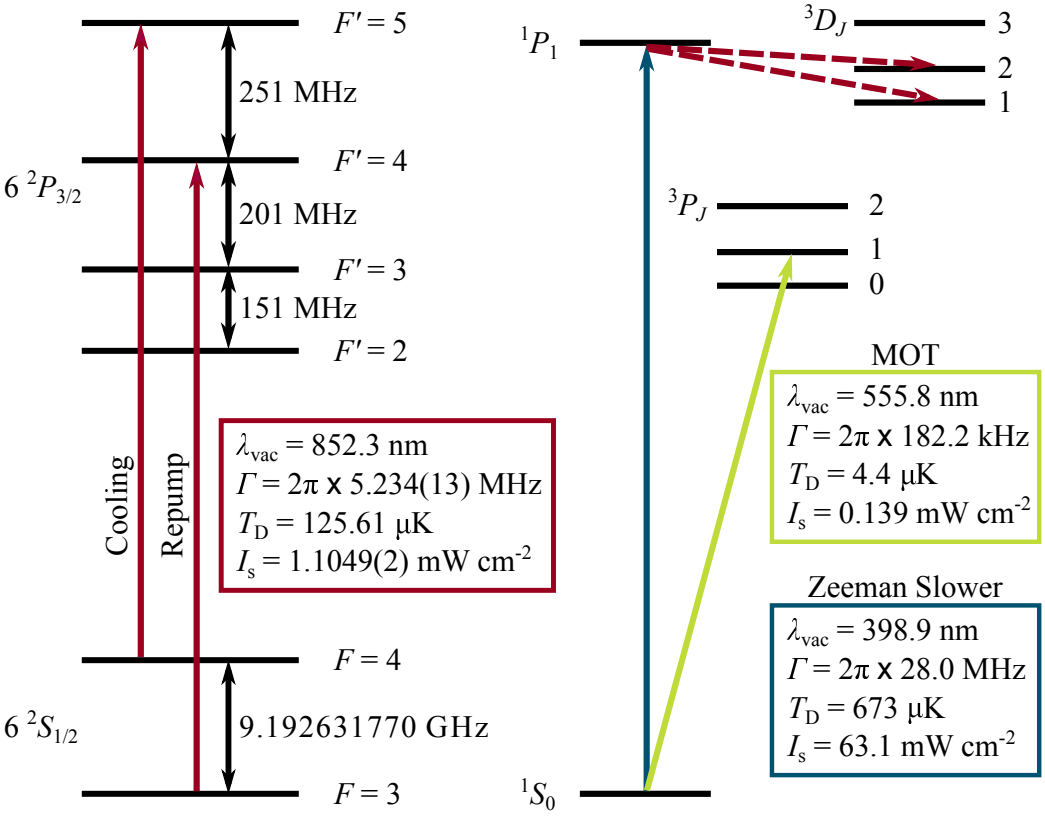

Figure 2.5: (a) A level diagram illustrating the D_2 lines in Cs. The cooling and probe light operates on the $F = 4 \rightarrow F' = 5$ transition, with repumping light on the $F = 3 \rightarrow F' = 4$ transition. These transitions are shown in red. (b) The lower level structure of Yb. The singlet transition from the single ground state to the $^1P_1$ state, as is used for Zeeman slowing, is shown in blue, and the decays from this state to the ^3D states are shown by the dashed red arrows. The triplet transition from the ground state to the $^3P_1$ state, as used for the MOT, is shown in green. Relevant parameters of each transition are shown in the coloured boxes [18, 123, 124].

experiment.

2.4.1 Yb: 399 nm

Over the course of the work presented in this thesis, the Yb laser systems have undergone a major overhaul. These changes have impacted the 399 nm system and, to a lesser extent, the 556 nm laser system. The previous master-slave configuration of two diodes lasers (Nichia, NDV4314) was initially developed by Imperial College London and was successful in achieving the first MOT of Yb in our lab [107]. In this system both laser housings were water

cooled to improve temperature stabilisation. Both lasers were situated on a breadboard above the main table, owing to the need for a high intensity Zeeman slower laser beam. The master was not only used to inject the slave laser, but a small amount of light was fibre coupled to the laser table for locking. The output of the slave laser ($\sim$ 60 mW) was spatially filtered and focussed down the vacuum system to form the Zeeman slower beam.

There were a number of issues with this system. The first problem was due to the large detuning required for Zeeman slowing of Yb. Our Zeeman slower is designed to operate at a detuning of around -600 MHz from resonance. We previously used a homebuilt transfer cavity lock to offset lock the 399 nm master laser. However, this system was often unreliable and did not leave any resonant light available for imaging: all the laser light was at the Zeeman slower detuning. Plans were made to introduce a third homebuilt 399 nm laser for the purposes of imaging, however the diode needed to be cooled below the dew point temperature, which drastically shortened the lifetime of the new laser. Instead of constructing an additional laser, an overhaul of the 399 nm frequency stabilisation scheme was performed. Rather than using a cavity to offset lock the master laser, we now lock to resonance using fluorescence spectroscopy. Further details of this technique may be found in chapter 3.

The right hand side of figure 2.6 shows the new locking and imaging layout for the 399 nm laser system. The light is still fibre-coupled from the Zeeman slower breadboard, but now a series of acousto-optical modulators (AOMs) are used to bridge the frequency gap from the Zeeman slower detuning to resonance. All of the light from the fibre is double-passed through a 200 MHz AOM (Gooch and Housego, M220-4A-GH11), before being split on a polarising beam splitter cube (PBS). The beam from each output port of the PBS is double-passed through a 100 MHz AOMs (Isomet 1206C-833) giving the total change of frequency of 600 MHz that is required. The first-order light from one of these AOMs is sent to the Yb "Beam Machine" for spectroscopy and locking, whilst the first-order light from the other AOM is fibre-coupled back to the main table. This light is used as a probe beam for absorption imaging. By setting the probe AOM frequency to that of the spectroscopy AOM we ensure the probe is resonant. The probe itself is launched and colli-

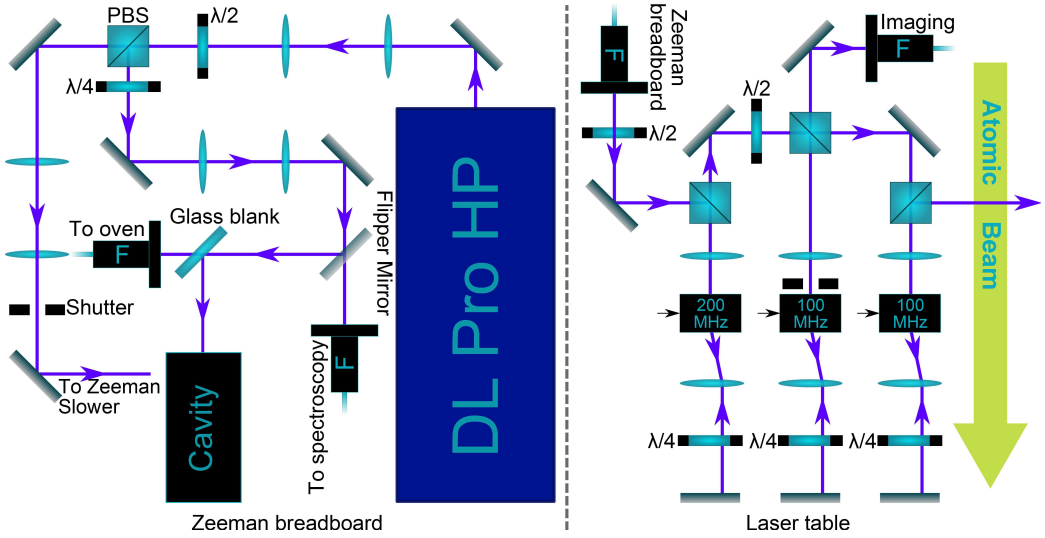

Figure 2.6: The left hand side of the figure shows the optical layout of the new 399 nm laser system. This part of the setup is on a breadboard mounted above the Zeeman slower viewport (right hand of figure 2.1). On this breadboard the majority of the laser output is sent to the Zeeman slower, whilst the remainder is coupled down a polarisation maintaining optical fibre. The fibre output is on the spectroscopy table, with the layout of the spectroscopy imaging optics shown on the right hand side of the figure.

mated using a fibre cage system. Typically we use around 25 μW in a beam with a $1/e^2$ diameter of 13.6 ± 0.2 mm for absorption imaging. The probe beam is combined with one of the 556 nm MOT beams on a dichroic mirror before entering the science chamber, as can been seen in figures 2.4 and 4.6.

Whilst this change to the spectroscopy setup gave enough light for absorption imaging, the mode structure of the laser system was very erratic: the master and slave laser were very sensitive to current and temperature alike. For this reason we made the decision to switch to a commercial high power diode laser (Toptica DL Pro HP). This laser outputs up to 100 mW of tunable, single-mode light, and replaced both lasers in the previous setup on the Zeeman slower breadboard. The new setup is shown in the left hand side of figure 2.6. The laser output aspect ratio is first corrected by a pair of cylindrical lenses, and then split using a combination of a half wave plate ($\lambda/2$) and a PBS. The majority of the laser output (up to 70 mW) is sent via a telescope to form the Zeeman slowing beam. This light passes through another telescope and a mechanical shutter, before a periscope takes the beam down through the Zeeman breadboard towards the vacuum system. En-route the beam

passes through several lenses to form a waist of (307 ± 8) μm at a distance of (1.93 ± 0.01) m beyond the Zeeman slower viewport (the focus is close to the capillaries in the dual species oven).

The smaller fraction of the laser output power is passed through a telescope and coupled into the same fibre used by the previous setup to send light to the laser table. A quarter wave plate ($\lambda/4$) is used to reduce the polarisation drift of the polarisation maintaining optical fibre [125]. We typically obtain an output power of 5 mW at the laser table for spectroscopy and imaging. A flipper mirror is included before this fibre for diagnostic purposes. In the case that the mirror is down, the light travels down the fibre to the laser table as normal. When the mirror is up, a glass blank splits off some light for coupling into another optical fibre, with the remaining light going into a cavity. This setup enables spectroscopy to be performed on the atomic beam emanating from the dual species oven.

2.4.2 Yb: 556 nm

With the changes made to the 399 nm laser system, the 556 nm system has been greatly simplified. Since the transfer cavity is no longer required, the 556 nm laser light is needed only for the MOT, with a small amount of power used to lock the laser to resonance. Figure 2.7 shows the layout of the 556 nm laser system. The second-harmonic generator of the laser (Menlo Systems Orange One) is mounted on the laser table and gives a typical output of ~ 250 mW. The output is immediately split by a PBS to give two pathways for the 556 nm light: one for the spectroscopy light and one for the MOT light.

The spectroscopy beam is passed through a 200 MHz AOM (Gooch and Housego, 46200-0.3-LTD) and a telescope is used to expand the beam size. The beam is then guided by a series of mirrors through the atomic beam of the Yb "Beam Machine". Prior to entering the beam machine, the beam size is expanded further by another telescope in order to increase the interaction volume of the laser light with the atomic beam. Laser locking is performed using a similar method to that of the 399 nm light, and is described fully along with the operation of the beam machine in chapter 3.

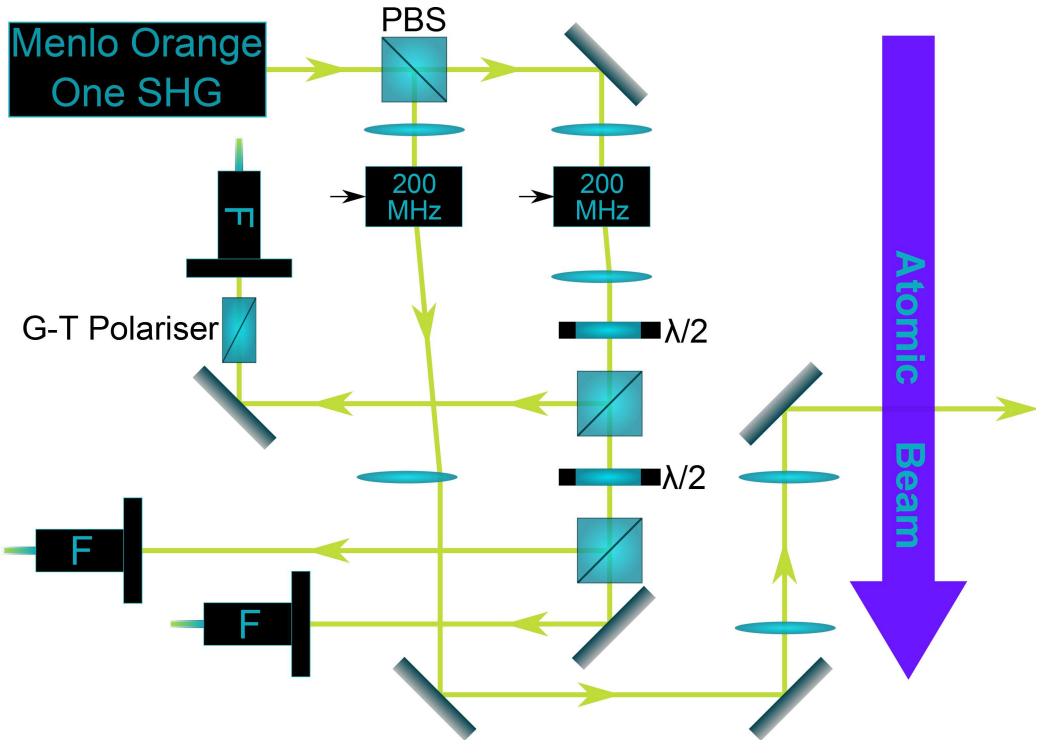

Figure 2.7: Optical layout of the 556 nm laser system. This setup is entirely located on the laser table. The laser output is split by a PBS into two branches: MOT and spectroscopy light. The MOT light is split and sent down three optical fibres to the main table. The spectroscopy light is sent through the atomic beam of the beam machine and the fluorescence is detected.

The MOT light also passes through a 200 MHz AOM and is then split into three beams by a combination of $\lambda/2$ waveplates and PBS cubes. Each beam is then coupled down a polarisation maintaining optical fibre and sent to the main table where cage systems collimate the beams for use in the Yb MOT. The MOT detuning is set by the difference between the two AOM frequencies.

One of the optical fibres is found to have a poorer extinction ratio compared to the other two, limiting the long-term reliability of the MOT load. To resolve this issue, we couple a very pure polarisation into the optical fibre by using a Glan-Taylor (G-T) polariser prior to the fibre input. The polariser is optimised by using a second G-T polariser at the output of the fibre, measuring the polarisation stability of the transmitted beam whilst the optical fibre is placed under thermal stress. By optimising the angle of the input G-T polariser, the power oscillations are minimised to within 5% of the mean

transmitted power, a variation consistent with the other MOT fibres.

2.4.3 Cs laser systems

The D_2 lines at 852 nm provide the closed transition required for laser cooling of Cs [2–4]. In our experiment, a series of three lasers provide all of the D_2 light needed for the deceleration, cooling, imaging, and optical pumping of Cs atoms. The cooling light is provided by a Toptica DL 100 Pro diode laser, the output of which is stabilised at a detuning of -395.4 MHz from the $F = 4 \rightarrow F' = 5$ cooling transition through the use of a double-passed AOM prior to the spectroscopy setup. The laser frequency stabilisation is achieved by resonant locking to the transition via modulation transfer spectroscopy [126, 127]. The rest of the output from this laser is used for an imaging probe and for seeding a tapered amplifier (Toptica BoosTA). The light from the BoosTA is used for the MOT cooling light and Zeeman slower cooling light. All of these beams operate at different detunings from the cooling transitions, which are controlled using a series of AOMs, as may be seen in figure 2.9.

In a Cs MOT there is a chance that an atom may be off-resonantly excited to the $F' = 4$ excited state, from which it may decay into the dark $F = 3$ ground state. To combat atom loss via this mechanism, repump light is used. The repump light is provided by a Toptica DL Pro diode laser, with an output detuning of 79.9 MHz from the $F = 3 \rightarrow F' = 4$ transition. Frequency modulation spectroscopy [128, 129] is used to resonantly stabilise the repump laser to this detuning, again via an AOM. The rest of the laser output is used for the repumping of atoms in the MOT and the Zeeman slower, and for the optical pumping of cold atoms. The optical pumping light is shifted via a double-passed AOM to be close to resonance with the $F = 3 \rightarrow F' = 3$ transition. All of the default detunings used in the experiment may be seen in table 2.2 and figure 2.8.

The optical setup is largely unchanged from that reported by [107]. However, there have been some minor changes and additions to the setup, including certain beams and frequencies being used for the first time. Figure 2.9 shows the complete optical setup, including the modifications that have been made from the previous setup. Many of the AOMs are backed up by mechanical

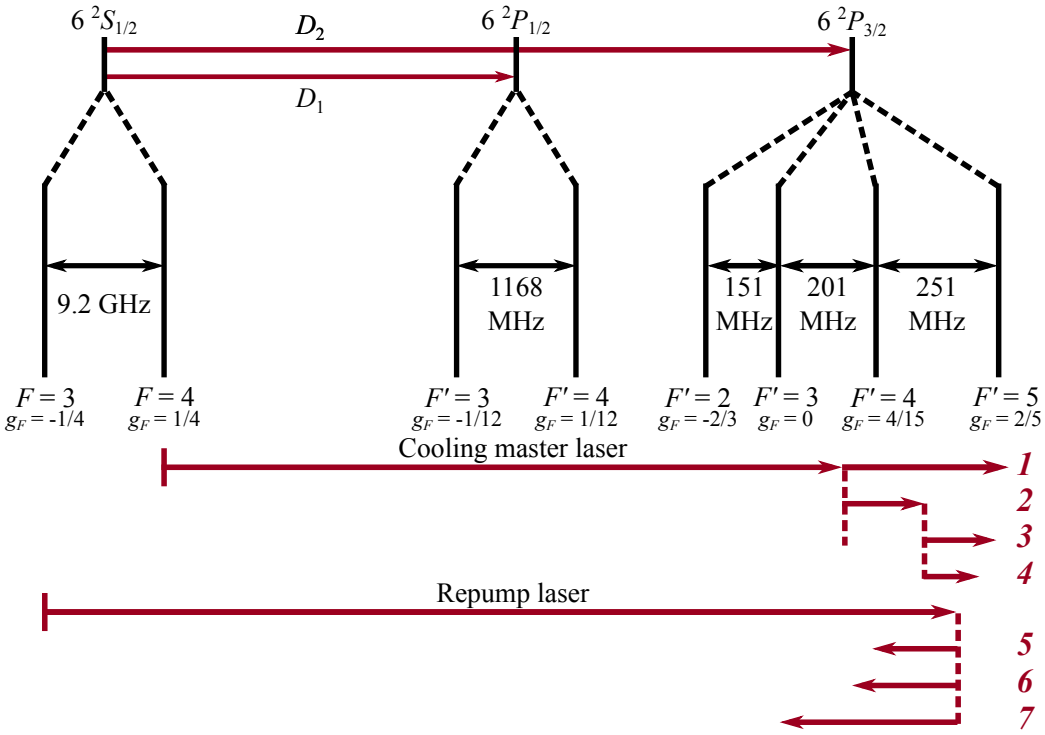

Figure 2.8: The upper section of the figure shows the energy levels making up the D_1 and D_2 lines of Cs. Shown are the hyperfine states associated with each line, with the labels denoting the value of F and g_F for both the ground and hyperfine states [123]. The lower section of the figure shows schematically the approximate frequencies of the various Cs lasers and beams used in the experiment. The smaller arrows denote the frequency shifts given by AOMs and the red numbers next to them denote the beams at the corresponding frequency: 1 is the cooling spectroscopy and imaging probe, 2 is the BoosTA seed, 3 is the MOT cooling light, 4 is the Zeeman slower cooling beam, 5 is the MOT repump light, 6 is the Zeeman slower repump light, and 7 is the optical pumping beam. The Cs photoassociation laser is tunable to frequencies red-detuned from the D_1 lines.

shutters: the probe, the MOT cooling, MOT repump, Zeeman slower cooling, and optical pumping. These shutters, along with the AOMs are now controlled by LabVIEW experimental control software, allowing both beam powers and detunings to be changed within experimental sequences.

The fibres in figure 2.9 designated for degenerate Raman sideband cooling (DRSC) are currently unused, but are kept in the setup ready for future use. For the time being, the DRSC polariser light (AOM 10) has been converted to an optical pumping beam, operating on the $F = 3 \rightarrow F' = 3$ transition. The purpose of this light is to pump cold Cs atoms into the $|F = 3, m_F = 3\rangle$

	Transition	Detuning (MHz)
Cooling master laser	$F = 4 \rightarrow F' = 5$	-385.4
Cooling spectroscopy	$F = 4 \rightarrow F' = 5$	0.0
Imaging probe	$F = 4 \rightarrow F' = 5$	1.2
BoosTA	$F = 4 \rightarrow F' = 5$	-132.0
Zeeman slower cooling	$F = 4 \rightarrow F' = 5$	-49.4
MOT Cooling	$F = 4 \rightarrow F' = 5$	-7.9
Repump spectroscopy	$F = 3 \rightarrow F' = 4$	0.0
Repump master laser	$F = 3 \rightarrow F' = 4$	79.9
Zeeman slower repump	$F = 3 \rightarrow F' = 4$	-32.4
MOT repump	$F = 3 \rightarrow F' = 4$	-5.3
Optical pumping	$F = 3 \rightarrow F' = 3$	-0.5

Table 2.2: A table showing the detunings of the Cs laser beams used in the experiment from the relevant transitions.

or $|3, -3\rangle$ stretched states of the lower hyperfine manifold. The zero-order light from two of the AOMs is also coupled into polarisation maintaining optical fibres. The zero-order light from the MOT AOM (AOM 6) is used for fluorescence measurements on the atomic beam emanating from the dual species oven; this beam is used when the lasers are scanning, giving a diagnostic on the Cs atomic beam flux. The zero-order light from the Zeeman slower repump AOM (AOM 8) is fibre coupled and sent to the photoassociation setup as a reference for the cavity. This particular AOM was used as there is no shutter backing up the AOM, meaning continuous operation is possible. The uses of these beams are described more thoroughly in later sections.

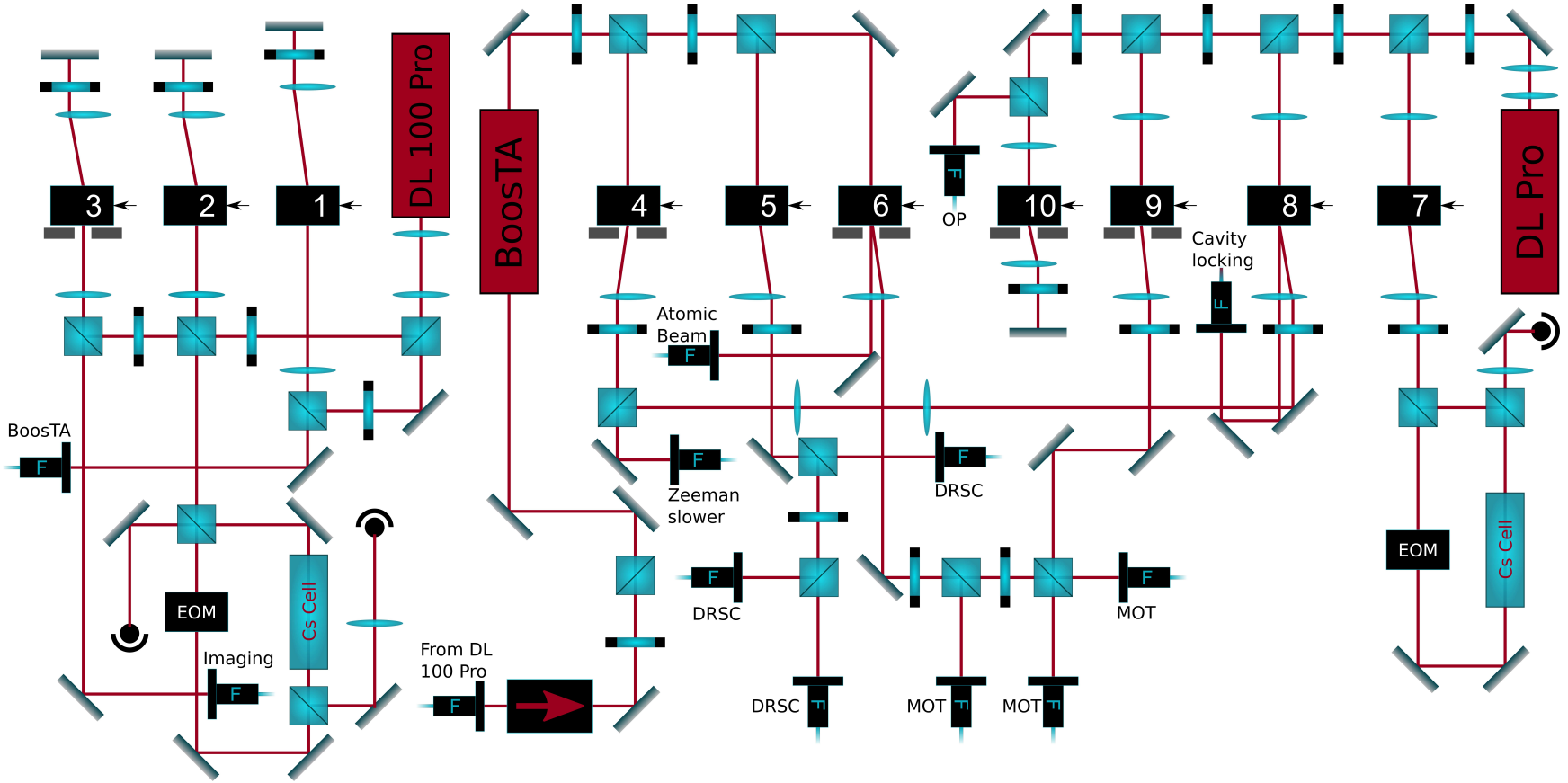

Figure 2.9: A schematic drawing of the Cs optical setup based on the figure in [107]. Changes have been made to show the derivation of the atomic beam probe, cavity locking light, and optical pumping light. Cooling light is produced close to the $F = 4 \rightarrow F' = 5$ transition by the Toptica DL 100 Pro and Toptica BoosTA on the left of the figure, whereas repump light near the $F = 3 \rightarrow F' = 4$ transition is produced by the Toptica DL Pro on the right of the figure. Note that with the implementation of the optical pumping light, the degenerate Raman sideband cooling (DRSC) fibres are currently unused.

2.5 Magnetic field generation

It is important to have a good control on the magnetic fields present in a cold atom experiment for a number of reasons, especially in the science chamber where precise measurements may be made. Since the MOT is a start point for almost all cold atom experiments it is important to be able to produce a magnetic field gradient with a zero crossing at the trap location. This will be discussed further in section 4.1.3. At the MOT stage it is also important to have any residual fields well under control. This is especially crucial for Yb MOTs on the 556 nm transition: the small linewidth of the transition means a small excited state Zeeman shift can drastically reduce MOT loading [130]. It is important to be able to achieve modest bias fields too. For example, three-body losses of Cs in a dipole trap can be controlled by using a broad zero crossing of the scattering length at 17 G, with the losses minimised at a magnetic field strength of 22 G [131]. It is also likely that any useful interspecies Feshbach resonances between Yb and Cs will be found at large bias fields [106, 132], and so this must be kept in mind when designing the magnetic fields for use in the experiment.

Considering these reasons, our experiment includes a number of different magnetic field coils for use in controlling the atoms in a number of ways. One major set of coils is the Zeeman slower, which is discussed in more detail in section 4.2. We also use "shim" coils for fine control over magnetic fields in the three Cartesian directions, and bias coils for larger magnetic field strengths in a defined direction. Finally, we make use of an anti-Helmholtz coil pair for the MOT and magnetic trapping.

The shim coils are usually used to null stray magnetic fields from other coils or the Earth's magnetic field. However, they are also used to produce a quantisation axis for optical pumping and absorption imaging. Three pairs of shim coils are incorporated in the experiment, aligned along the Zeeman slower axis (East-West direction), along the dipole trapping viewport axis (North-South direction), and along the re-entrant viewport axis (Up-Down direction). The Up-Down shims are wound using 1 mm diameter wire directly onto the science chamber mount, whereas the other shim coils are wound using the same wire onto Tufnol formers and mounted on posts around the

science chamber. Typically each coil consists of around 50 turns of wire, and the bias magnetic field strength that they produce are summarised in table 2.3.

Shim Coils	Magnetic field strength ($\mathrm{G\,A^{-1}}$)
East-West	1.89 ± 0.05
North-South	2.09 ± 0.03
Up-Down	2.81 ± 0.06

Table 2.3: A table showing the magnetic bias field strength produced per Ampere of current flowing through each shim coil pair. The values are the measured axial field strength at the centre of the coil pairs. Note that the field can not be measured at this position for the Up-Down coils as the science chamber obstructs the Hall probe used. Instead the value is inferred from fits to the axial magnetic field profile outside the science chamber.

For the larger bias fields and field gradients required in the experiment, we have designed a new coil array to be inserted into the re-entrant flanges, replacing the simple MOT coils used in [107]. The designed array features four coil pairs: two large bias coil pairs, a small bias coil pair, and a quadrupole coil pair used for generating field gradients. These coils are produced by winding wire of a square cross-section onto formers under tension, and secured using Araldite 2011. The wire itself has either a 4.3×4.3 mm or a 3.4×3.4 mm cross section, and has a 2.75 mm or a 2 mm diameter bore running along its length for water cooling purposes. Alternative options, such as an array of Bitter coils [133, 134], were also considered. However, the simple solution of wire coils was chosen for initial experiments in the setup described here.

The axial magnetic field strength for a pair of circular wire turns of radius, R, and separation, S, is given by the Biot-Savart law as

$$B_z = \frac{\mu_0 I R^2}{2\left(R^2 + (z + S/2))^2\right)^{3/2}} \pm \frac{\mu_0 I R^2}{2\left(R^2 + (z - S/2))^2\right)^{3/2}}, \qquad (2.1)$$

where I is the current flowing in the coils, and z is the axial position, with $z = 0$ being at the centre of the coil pair. The plus and minus represent that the coil current may flow with the same handedness in each coil (bias

configuration) or the opposite handedness (gradient configuration). It may be shown that the most uniform bias field for coils of radius, R, occurs when

$$S = R. \tag{2.2}$$

This is the Helmholtz condition for a coil pair, this condition also gives the largest possible gradient for a coil pair of a given R. Since only relatively small magnetic field gradients are required in this experiment, we have opted to position the three bias coils as close as possible to the atoms and as close to the Helmholtz condition as possible. The gradient coil is positioned in the remaining space, and as close as possible to the uniform gradient condition ($S = \sqrt{3}R$). The turns, diameter, separation and bias magnetic field or field gradient for each coil are presented in table 2.4. Figure 2.10 shows the simulated magnetic field profile for each of the coils in the array. The inset of the figure shows the coils in their respective positions inside one of the re-entrant flanges.

Coil	Turns	$2R$ (mm)	S (mm)	B_z ($\mathrm{G\,A^{-1}}$)	B'_z ($\mathrm{G\,cm^{-1}\,A^{-1}}$)
Fast	4	84	55	0.69	-
Large 1	16	105	65	2.33	-
Large 2	16	105	98	1.54	-
Quad	16	67	64	-	0.62

Table 2.4: A table showing the number of turns, separation, diameter, axial magnetic bias field per Ampere, and axial magnetic field gradient per Ampere of the individual coil pairs in the coil array. The magnetic properties of the coils are measured at the centre of the two coils and are inferred from fits to the measured magnetic field profiles. The separation is the distance between the centre of each coil, and the diameter is the average diameter of the turns making up the coil.

In the first instance, we have opted to incorporate just the fast bias coils and the quadrupole coils in the experimental setup. This is simply because we require more information on the interspecies scattering properties of a Yb-Cs mixture before a decision can be made on using the large field bias coils: it may be that the fields they produce still aren't large enough to access wide Feshbach resonances. These coils are currently housed inside a nylon mount, which clamps the coils into position. The position of these coils and the

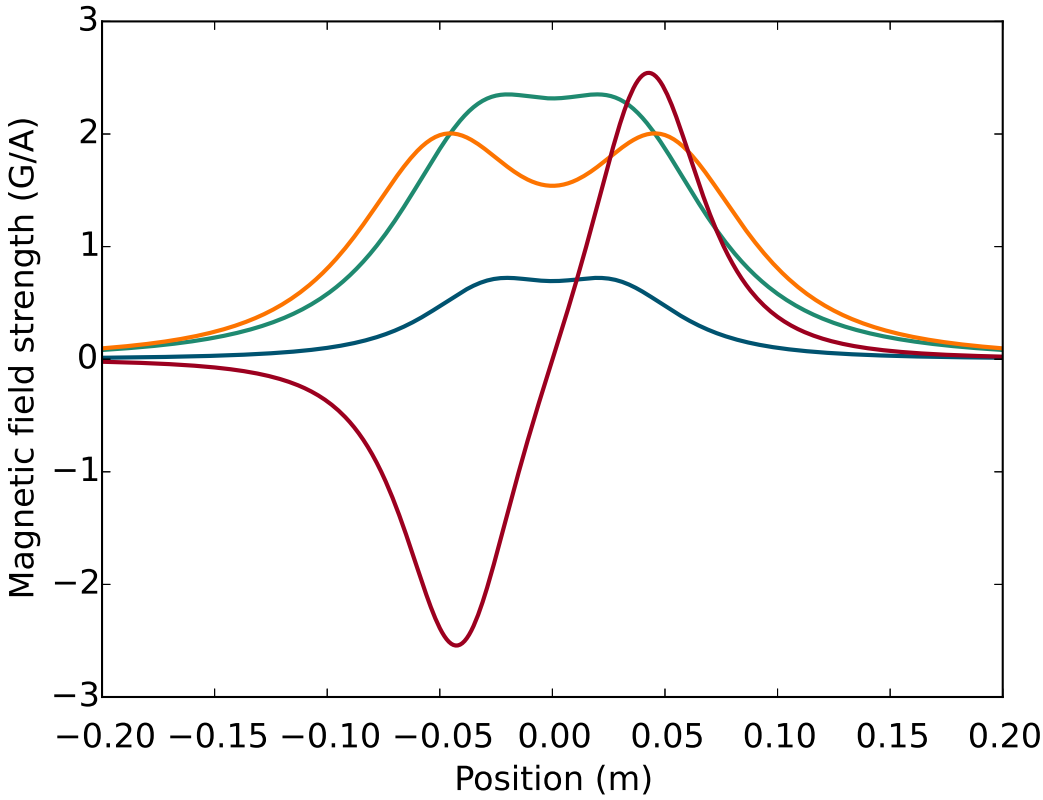

Figure 2.10: A plot showing the expected magnetic field profiles of the complete coil array. Shown are the profiles for the fast bias coil pair (blue curve), the quadrupole coil pair (red), and the two larger bias coil pairs (green and orange). The field strength is shown per Ampere flowing through the coil pair.

bottom half of the nylon mount can be seen relative to the science chamber in figure 2.11.

Figure 2.12 shows the measured axial magnetic field profile of the fast bias coil pair and the quadrupole coil pair. The magnetic field is measured using an axial Hall probe and a current of 30 A flowing in the coils. The coils are clamped in their nylon mounts and the mounts set to be at the separation of the re-entrant flanges. The solid lines on the plots show the expected field profile from a simulation of the coils running at this current. These show a good agreement with the measured profile, suggesting the coils are free of internal shorts.

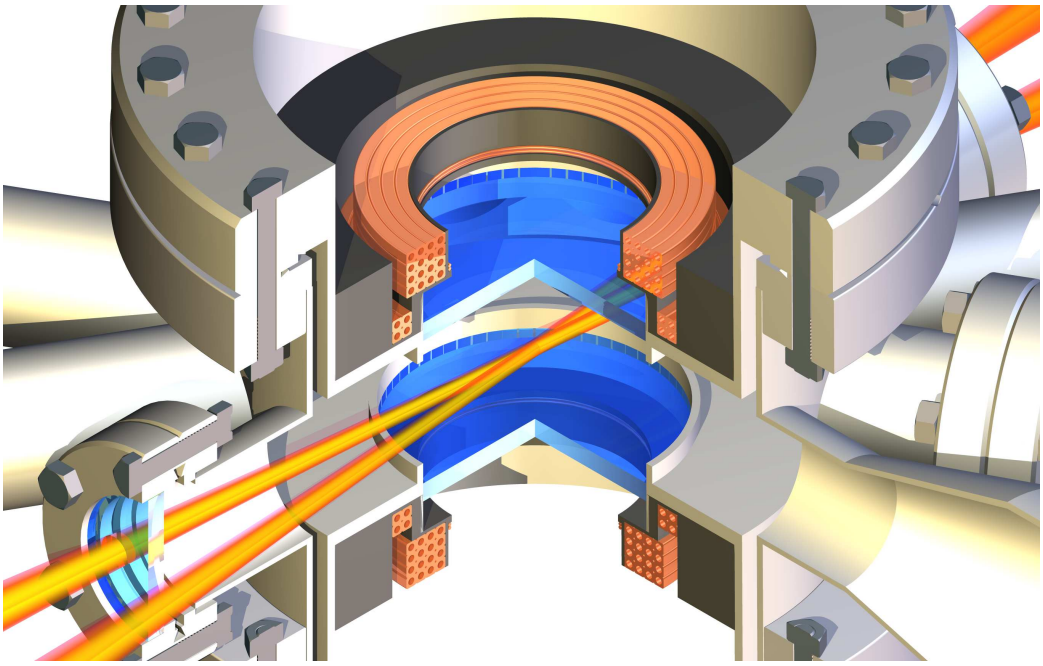

Figure 2.11: A rendering of the current coil arrays located within the re-entrant flanges of the science chamber. A representation of the dipole beams have been included as a reference to the centre of the chamber. The quadrupole field is provided by the larger coil pair, each with 16 turns, whereas the bias field is provided by the smaller coils, with only 4 turns in each coil. The coils are held within nylon mounts of which only the bottom halves are shown in this illustration.

2.6 Diagnostics

2.6.1 Fluorescence imaging

The technique of fluorescence imaging measures the light scattered by a cloud of atoms when they are illuminated by a resonant, or near-resonant, laser beam. A portion of the atom fluorescence is collected by a lens at a distance, L, from the atoms. The collected fluorescence is focussed onto a CCD camera to form an image of the atoms, or onto a photodiode to produce a photocurrent proportional to the power of the collected light. Typically an aperture of diameter, d, is placed in front of the lens to ensure the response of the detector is linear with atom number.

If the scattering rate of N atoms is NR, where R is the scattering rate of a single atom, then the power of the fluorescence radiated by the atoms is

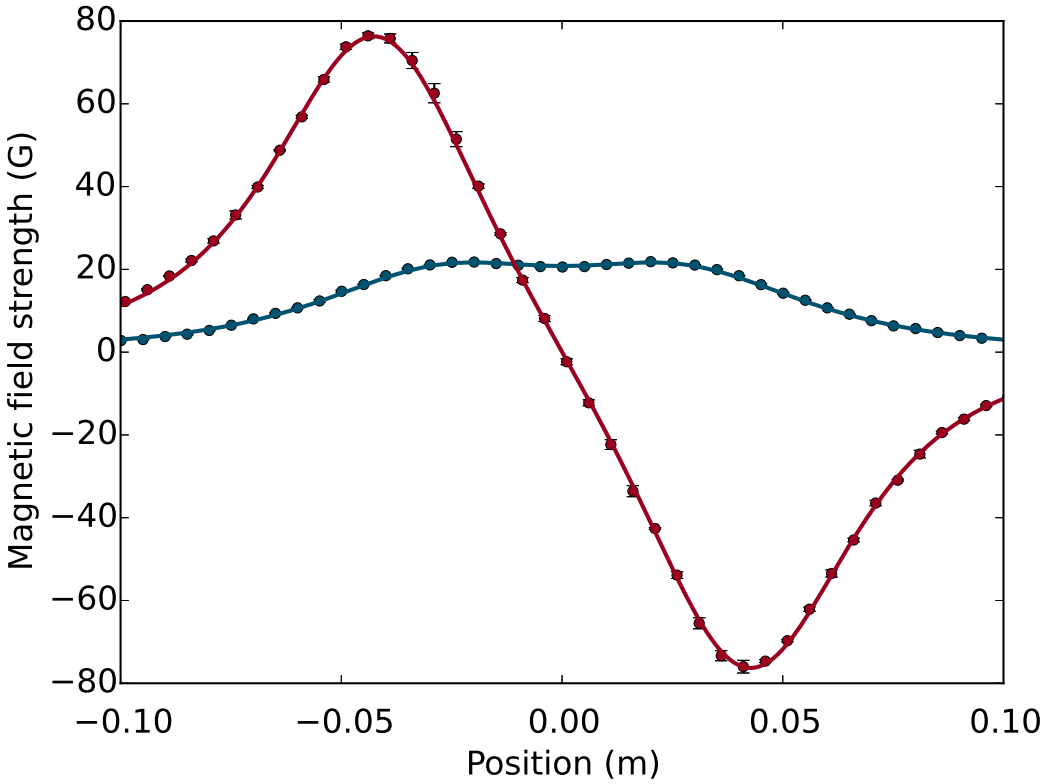

Figure 2.12: The measured axial magnetic field profile as a function of position of the bias coil (blue points) and quadrupole coils (red points). The fields are produced with 30 A flowing through the coil pair in a series configuration. The solid curves show the expected field of the coils based upon the Biot-Savart law.

given by

$$P_{\mathrm{Flu}} = NR\hbar\omega_{\mathrm{L}}, \tag{2.3}$$

where ω_{L} is the angular frequency of the laser light. The aperture in front of the lens subtends a solid angle, Ω. If the distance to the atoms is much larger than the diameter of the aperture then this solid angle may be approximated as

$$\Omega = \frac{\pi d^2}{4L^2}. \tag{2.4}$$

Assuming the light is scattered isotropically by the atoms, the power of the light detected is given as

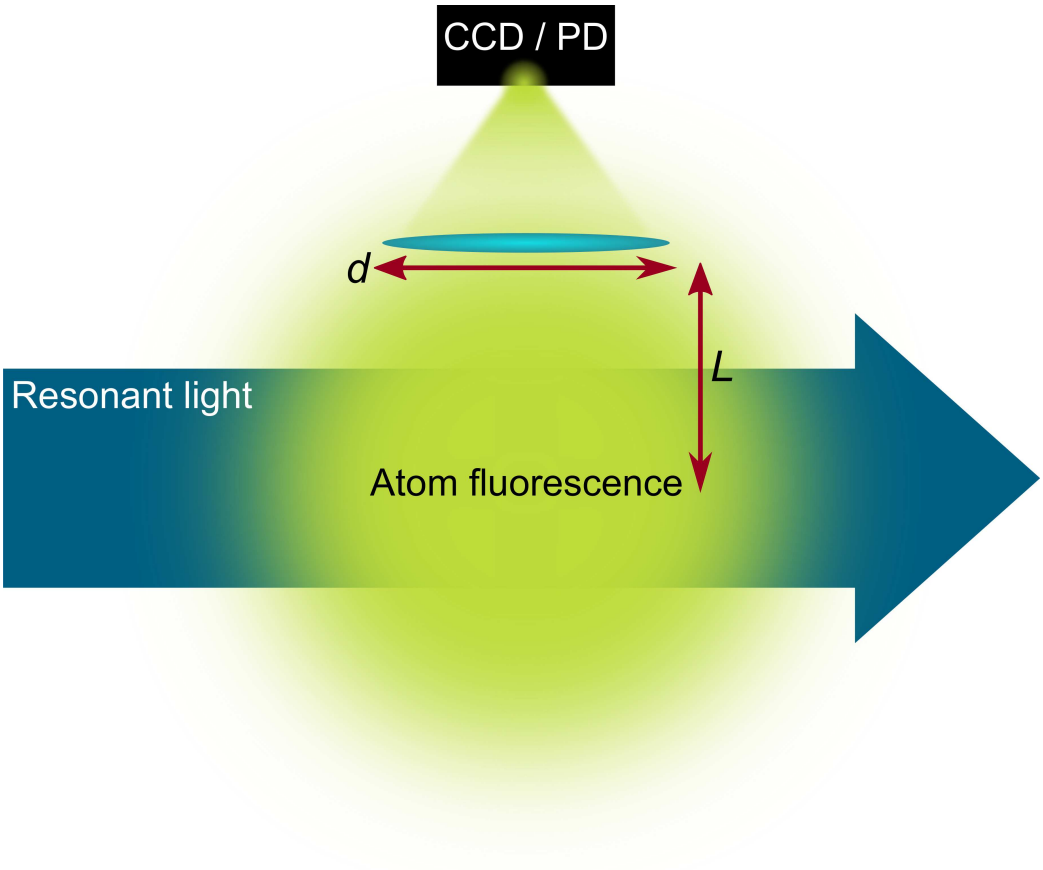

Figure 2.13: A schematic representation of a fluorescence imaging setup. Light scattered by the atoms is collected by a lens and focussed onto a CCD or photodiode for detection

$$P_{\mathrm{det}} = \frac{d^2}{16L^2} N R \hbar \omega_{\mathrm{L}}. \tag{2.5}$$

If the detector is a photodiode it will produce a photo-current proportional to the incident power, with the responsivity of the photodiode, $\eta(\lambda)$, being the constant of proportionality, where λ is the wavelength of the transition being driven. The photo-current is detected by measuring the voltage dropped, V, over a resistor of resistance, Z. Thus, the atom number is given as

$$N = \frac{V}{\eta(\lambda) Z} \frac{16L^2}{d^2} \frac{\lambda}{hcR}. \tag{2.6}$$

The responsivity of a photodiode at the 852 nm line in Cs is about 0.55 $\mathrm{A\,W^{-1}}$, and is around 0.41 $\mathrm{A\,W^{-1}}$ for the 556 nm line in Yb. How-

ever, the scattering rate is much lower in Yb owing to the narrow natural linewidth of the transition, and so a larger gain resistor is used when detecting 556 nm fluorescence.

The limiting factor in determining atom number using fluorescence detection is the scattering rate, R, of the atom. A rate for a two-level atom is presented in section 4.1. However, cold atomic clouds often can't be approximated as a two-level system. A more thorough analysis is presented in reference [135], but a thorough knowledge of beam intensities and detuning is still required for an accurate atom number.

Fluorescence imaging is used extensively in this experiment. Whilst not as accurate as absorption imaging in terms of measuring atom numbers, it nonetheless has many convenient properties. For example, fluorescence detection was used extensively in the optimisation of both MOTs. Atoms in a MOT are constantly fluorescing, and so fluorescence imaging may be used to monitor relative changes to the atom number in real-time, whereas optimisation using absorption imaging would require multiple runs under identical loading conditions. The fluorescence detection setup is also used to monitor MOT loading during experimental sequences, as well as atom losses from the MOT during photoassociation experiments. This method is also used to measure the percentage recapture into a MOT following the atoms being held in a conservative trap for some time. In later sections we will show how this technique is used to perform spectroscopy on the atoms in the MOT and in measuring the light shift in optical dipole traps.

2.6.2 Absorption imaging

Atom number

Absorption imaging typically gives a more accurate atom number than fluorescence imaging, and can also be used to measure the temperature and density of a cloud of atoms. These observables are all inferred from the number density of atoms, as measured by the absorption of a resonant probe. If we consider a laser beam of initial intensity $I_0(x, y)$ propagating along the z-direction, the transmitted probe intensity is given by

$$I\left(x,y\right)=I_{0}\left(x,y\right)\mathrm{e}^{-\mathrm{OD(x,y)}}, \tag{2.7}$$

where $\mathrm{OD\left(x,y\right)}$ is the spatial optical depth profile of the atomic sample. Alternatively this may be written as

$$I\left(x,y\right)=I_{0}\left(x,y\right)\mathrm{e}^{-n(x,y)\sigma_{\mathrm{tot}}}, \tag{2.8}$$

where $n\left(x,y\right)$ is the column density of the atomic cloud at position (x,y), and σ_{tot} is the absorption cross section of the transition, which is given by

$$\sigma_{\mathrm{tot}}=\frac{\sigma_{0}}{1+4\frac{\Delta^{2}}{\Gamma^{2}}+\frac{I_{0}}{I_{\mathrm{sat}}}}, \tag{2.9}$$

where Δ is the detuning of the probe laser from resonance, Γ is the natural linewidth of the transition, and I_{sat} is the saturation intensity of the transition. For a resonant probe beam and $I_{0}\ll I_{\mathrm{sat}}$, then the absorption cross section reduces to the resonant cross section, σ_{0} given by

$$\sigma_{0}=\frac{\Gamma\hbar\omega_{0}}{I_{\mathrm{sat}}}=\frac{3\lambda^{2}}{2\pi}, \tag{2.10}$$

where ω_{0} is the resonant angular frequency of the transition, and λ is the wavelength of the transition. The optical depth profile, or equivalently the number density profile, can be determined by a comparison of the probe intensity with and without the atomic cloud present:

$$\mathrm{OD}\left(x,y\right)=n\left(x,y\right)\sigma=\ln\left(\frac{I_{0}\left(x,y\right)}{I\left(x,y\right)}\right). \tag{2.11}$$

From this it is possible to calculate the number of atoms in the cloud, N, by integrating over the optical depth profile and using equations 2.7 and 2.8, so that

$$N=\int\int n\left(x,y\right)dxdy=\frac{1}{\sigma_{\mathrm{tot}}}\int\int\mathrm{OD}\left(x,y\right)dxdy. \tag{2.12}$$

Atoms in a harmonic trap

If the atomic cloud is in a harmonic trap, then the number density distribution of the atoms will be a Gaussian of the form

$$n\left(x,y,z\right)=n_{\max}\exp\left(-\frac{m}{2k_{\mathrm{B}}T}\left(\omega_x^2x^2+\omega_y^2y^2+\omega_z^2z^2\right)\right), \tag{2.13}$$

where $n_{\max}$ is the maximum number density (here located at $x=y=z=0$), m is the mass of the atom, T is the temperature of the ensemble, and $\omega_{x,y,z}$ are the harmonic trap frequencies in the x,y,z directions. It is then possible to define the widths of the clouds in each dimension, $\sigma_{x,y,x}$, as where the density falls to $\mathrm{e}^{-1/2}n_{\max}$, giving

$$\sigma_{x,y,z}^2=\frac{k_{\mathrm{B}}T}{m\omega_{x,y,z}^2}. \tag{2.14}$$

Additionally, equation 2.12 may be normalised to give the total number of trapped atoms

$$N=\frac{n_{\max}}{\omega_x\omega_y\omega_z}\left(\frac{2\pi k_{\mathrm{B}}T}{m}\right)^{3/2}. \tag{2.15}$$

If we once more consider a resonant weak probe beam travelling in the z-direction, then after passing through an atomic layer of thickness δz, where the ingoing intensity is I, the new intensity of the probe beam will be $I+\delta I$ where δI is given by

$$\begin{aligned}\delta I &= -nI\sigma_0\delta z \\ &= -\frac{3\lambda^2}{2\pi}In_{\max}\exp\left(-\frac{m}{2k_{\mathrm{B}}T}\left(\omega_x^2x^2+\omega_y^2y^2+\omega_z^2z^2\right)\right)\delta z. \end{aligned}\tag{2.16}$$

Then, in the limit $\delta I,\delta z\to 0$, and integrating over the extent of the cloud,

$$\begin{aligned} \ln\left(\frac{I_0(x,y)}{I(x,y)}\right) &= \mathrm{OD}(x,y) \\ &= \frac{3\lambda^2 n_{\max}}{\omega_z}\sqrt{\frac{k_\mathrm{B}T}{2\pi m}}\exp\left(-\frac{m}{2k_\mathrm{B}T}\left(\omega_x^2x^2+\omega_y^2y^2\right)\right). \end{aligned} \quad (2.17)$$

This gives the expected form of the optical depth profile. The maximum optical depth depends only on the number of atoms, the cloud temperature and the trapping frequency in the propagation direction of the probe:

$$\mathrm{OD}_{\max} = \frac{3\lambda^2 n_{\max}}{\omega_z}\sqrt{\frac{k_\mathrm{B}T}{2\pi m}}. \quad (2.18)$$

This implies that by measuring the peak optical depth of the cloud, and knowing either the trap frequencies or cloud sizes, the number of atoms in the trap may be calculated:

$$N = \frac{4\pi^2 k_\mathrm{B}T}{3\lambda^2 m\omega_x\omega_y}\mathrm{OD}_{\max} = \frac{4\pi^2}{3\lambda^2}\sigma_x\sigma_y\mathrm{OD}_{\max}. \quad (2.19)$$

Cloud temperature

It is clear from equation 2.19 that, provided the trap frequencies and cloud sizes are known, then the temperature may be extracted. However, this only holds if the cloud sizes are those representing the atoms in the trap. Typically the optical depth in a dipole trap is very high, therefore absorption imaging is often employed after releasing the atoms from a trap and allowing the cloud to freely expand during a time of flight, τ. In a given dimension, the root mean square speed of thermal atoms, v_{RMS}, will be

$$v_{\mathrm{RMS}} = \sqrt{\frac{k_\mathrm{B}T}{m}}. \quad (2.20)$$

It follows that the root mean square size of the atomic cloud will evolve under free expansion as

$$\sigma^2 = \sigma_0^2 + v_{\mathrm{RMS}}^2\tau^2 = \sigma_0^2 + \frac{k_\mathrm{B}T}{m}\tau^2, \quad (2.21)$$

where σ_0 is the root mean square cloud size at $\tau = 0$, the instantaneous size upon release from the trap. Using equation 2.21 it is possible to infer the temperature of thermal atoms by measuring the evolution of the cloud size with time of flight. By substitution of equation 2.14 it can be shown that atoms expanding out of a harmonic trap will have a size given by

$$\sigma = \sigma_0 \sqrt{1 + \omega^2 \tau^2}, \tag{2.22}$$

where ω is the trap frequency in the direction of the measured expansion, allowing the cloud size after the expansion to be directly related to size in the trap.

Figure 2.14 shows an example of using time of flight expansion of an atomic cloud to determine the cloud's temperature, in this example an Yb MOT. The MOT is released and the optical depth of the cloud is determined at several durations of expansion. The inset contains images showing the evolution of the cloud size. Note that as the duration of the expansion increases, the cloud size gets larger as expected. We also see that the atoms drop under gravity and that the maximum optical depth of the cloud reduces as the density of the cloud decreases. By plotting the square of the cloud width against the square of the expansion time, we are able to fit a straight line to the gradient where the gradient will be $k_{\mathrm{B}}T/m$, thus giving a measure of the temperature.

Optical setup

The setup in figure 2.15 demonstrates how the optical depth profile of the atoms may be measured experimentally. A resonant collimated probe beam passes through the science chamber and through the atomic cloud where photons are absorbed in accordance to equation 2.8, effectively producing a shadow of the atomic cloud. A series of two lenses of focal lengths f_1 and f_2 respectively are then used to form an image of this shadow on the CCD camera.

To determine the optical depth profile of the atom cloud a series of three images are taken on the CCD, giving three intensity profiles: I_{atoms}, the intensity profile recorded on the CCD of the probe light with the atomic

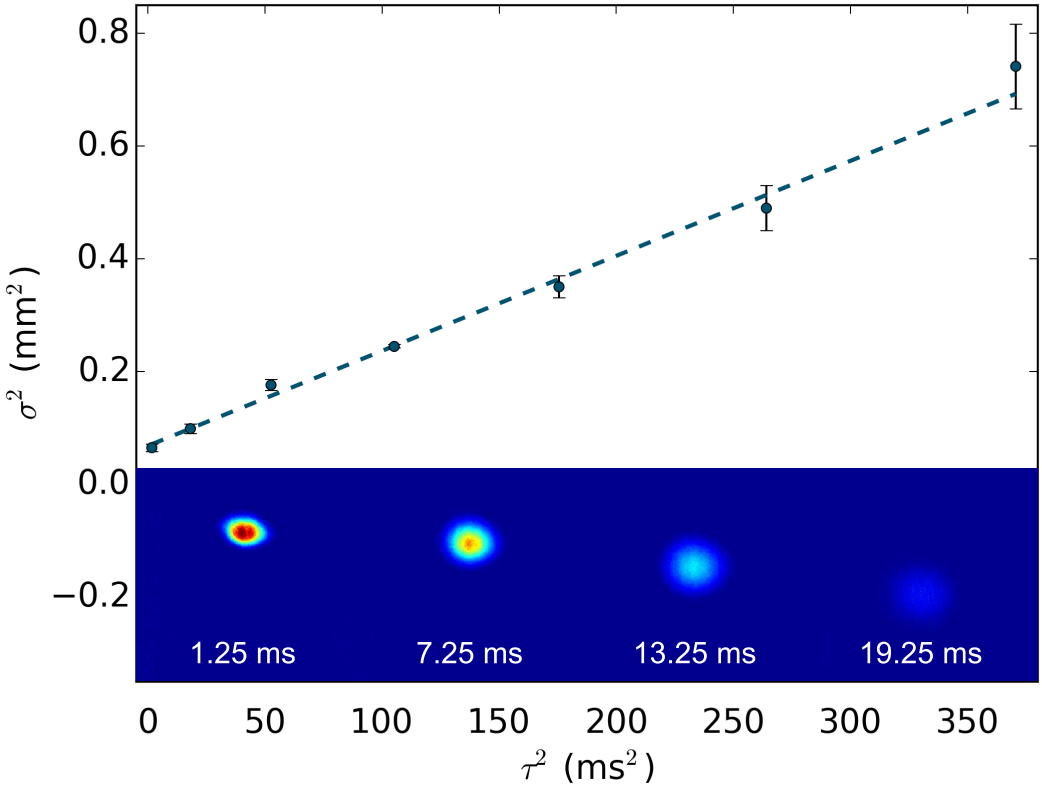

Figure 2.14: An example time of flight expansion curve demonstrating how a temperature may be extracted from the free expansion of an atomic cloud. The points show the square of the cloud size, σ, plotted against the square of the time of flight at which they are taken. The dashed curve shows a fit to equation 2.21 which gives a temperature of (36 ± 2) μK for this Yb MOT. The inset shows a selection of absorption images taken at different times which are used to derive the points in the main figure.

cloud present; I_{light}, the intensity profile of the probe light only; and I_{dark}, the intensity profile resulting from the same exposure without the probe beam being fired (non-resonant light only). The optical depth may then be calculated on a pixel-by-pixel basis using the operation

$$\text{OD} = \ln\left(\frac{I_{\text{light}} - I_{\text{dark}}}{I_{\text{atoms}} - I_{\text{dark}}}\right). \tag{2.23}$$

A two-dimensional Gaussian is fit to the processed image during analysis. From this fit the vertical and horizontal cloud sizes are extracted, as well as the vertical and horizontal cloud centres. If the cloud is released from a harmonic trap the temperature, density, and phase-space density are also calculated using the time of flight with which the images were taken.

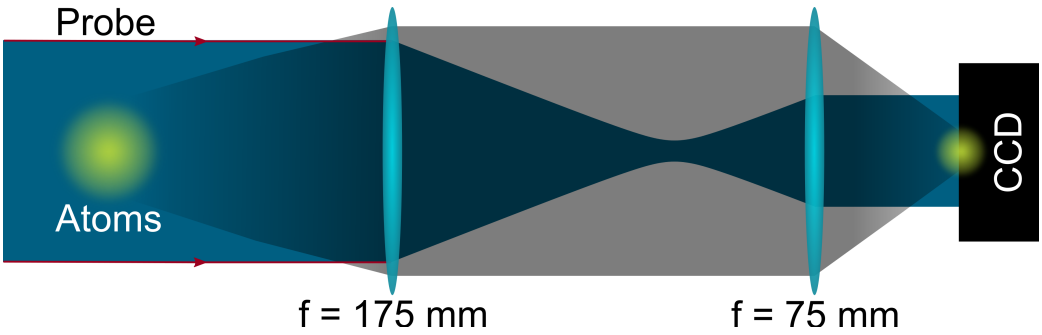

Figure 2.15: A simplified schematic of the optical setup for absorption imaging, using the Yb setup as an example. A resonant 399 nm probe beam illuminates the cloud of atoms, which absorbs some of the probe light. The pair of lenses act as a telescope for the probe beam, with a magnification determined by the ratio of the focal lengths of the lenses. The probe light is collected on a CCD camera and the result is an image of the shadow of the atom cloud.

If the system described above is engineered so that the separation between the atom cloud and the first lens is f_1, then the image will be focussed when the CCD camera is placed a distance f_2 from the second lens. In this perfect system the magnification, M, is given by

$$M = \frac{f_2}{f_1}. \tag{2.24}$$

Experimentally, the magnification of the imaging system is determined using the vertical position of the cloud under freefall. Figure 2.16 demonstrates this method for a cloud of Yb released from a MOT. The vertical position of the cloud centre on the CCD (measured in pixels) is recorded for a range of time of flights. The dashed curves shows a parabolic fit to the data of the form $z = a\tau^2 + b\tau + c$. To interpret this fit it must be compared to the displacement, s, of a body under freefall where

$$s = \frac{1}{2}g\tau^2 + u\tau + s_0, \tag{2.25}$$

where s_0 is the initial vertical position of the cloud, g is the acceleration due to gravity. The parameter u is the initial velocity of the cloud, which in the experiment outlined in figure 2.16 is found to be consistent with zero when fitting the above model to the data. A displacement of the atom cloud on

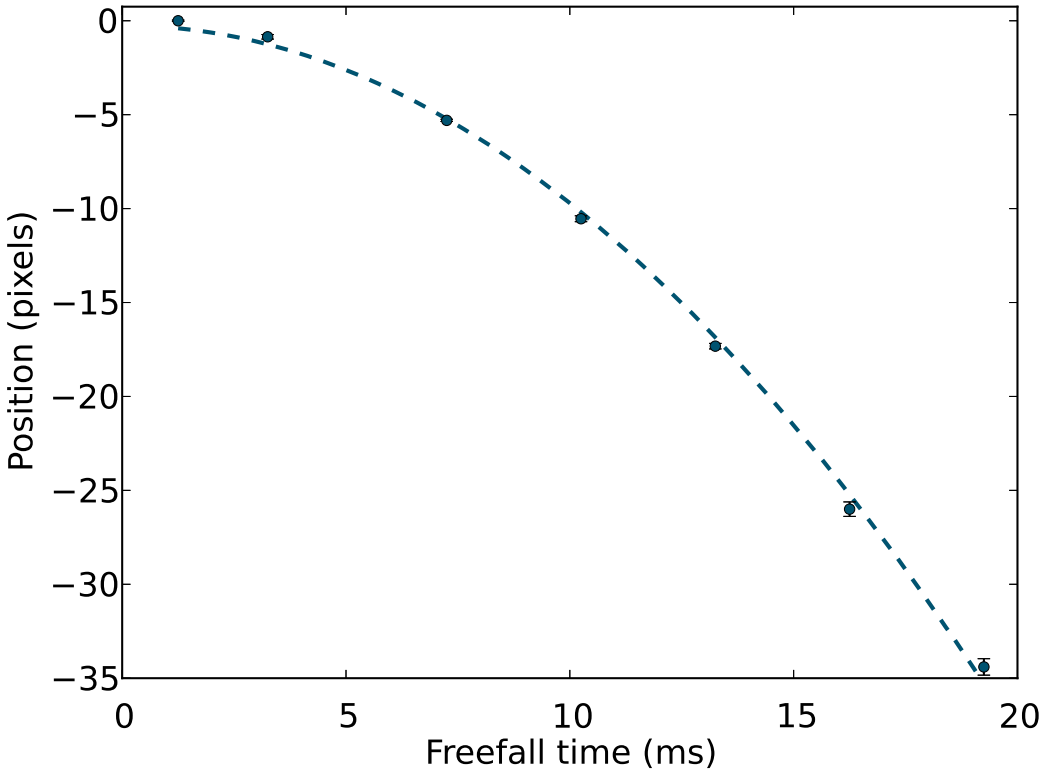

Figure 2.16: The evolution of an atomic cloud's vertical position in pixels (relative to its starting position) as it falls freely under gravity. In this example an Yb MOT is released and absorption images are fitted to a two-dimensional Gaussian to find the cloud's centre for different freefall durations. The dashed blue curve shows a parabola fit to the data in order to extract the magnification of the imaging system.

the CCD is related to the actual displacement by

$$s = \frac{bd_{\text{pixel}}}{M} z, \tag{2.26}$$

where bd_{pixel} is the effective pixel size, with d_{pixel} being the physical length of the edge of one of the camera's pixels and b being the pixel binning used in the imaging. In figure 2.16 2×2 binning is used with a pixel size of 10×10 μm. It is then simple to show that the magnification of the system can be extracted from the coefficient of the squared term in the parabolic fit:

$$M = \frac{2bd_{\text{pixel}}A}{g}. \tag{2.27}$$

Yb is ideally suited to calibrating an imaging system in this manner: unlike

Cs, Yb does not have a ground state magnetic moment and so the measurement is insensitive to gradients in magnetic field.

Absorption imaging of Cs

The optical set up for absorption imaging of both Cs and Yb can be seen in figure 4.6. For imaging of Cs we use a probe beam collimated to a waist of 11.5 mm using a fibre cage system. This beam is combined with one of the Cs MOT beams on a polarising beam splitter cube prior to passing through a $\lambda/4$ waveplate (the probe and MOT beams have opposite circular polarisations). The two beams are separated after the chamber using another waveplate and cube. Figure 4.6 shows that both the probe and MOT beams pass through the first imaging lens, an $f = 160$ mm achromatic doublet. The retroreflection mirror for the MOT beam is positioned to be a focal length away from this lens. The probe frequency is set using a double-passed AOM and is typically chosen to be resonant with the $F = 4 \rightarrow F' = 5$ transition, with an intensity at the atoms of around 0.1 I_{sat}. The low intensity is chosen to minimise saturation and hyperfine pumping effects.

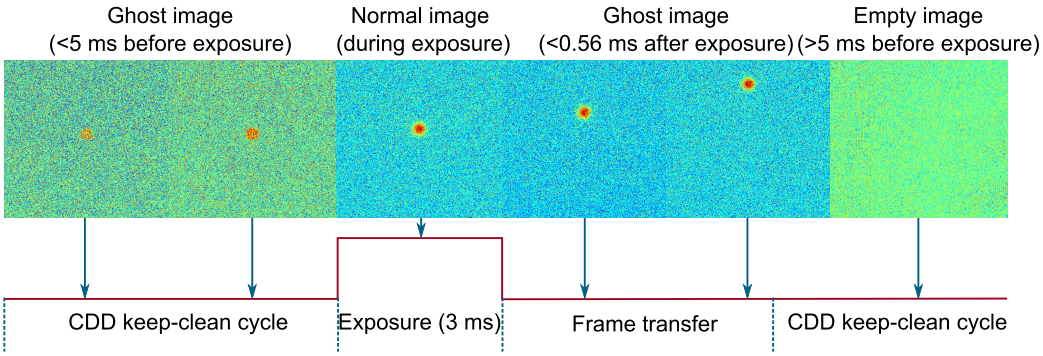

Figure 2.17: CCD image obtained when firing a 30 μs weak probe ($I \approx 0.1 I_{\mathrm{sat}}$) of 852 nm Cs imaging light at different points during the CCD timing cycle. If the probe is fired within 5 ms prior to the exposure, a ghost image of residual charge that is not removed during the "keep clean" function of the CCD may be seen. Firing the probe during the exposure results in a correctly positioned image. Finally, firing the probe within 0.56 ms after the exposure is complete causes exposure of pixels whilst the CCD frame is being transferred to a masked area for reading.

The camera used for Cs absorption imaging is an Andor iXon 885, which has a quantum efficiency of around 35 % at 852 nm. The overlapping of

the probe beam on a MOT beam does increase optical access to the rest of the chamber, however this setup makes imaging of a Cs MOT challenging: the intense MOT beam and MOT fluorescence can leak through the PBS and saturate the CCD prior to the probe exposure. The CCD does have a keep-clean function, carrying away charge accumulated when the camera is not being exposed. However, in the case of a MOT beam, the photons are impinging on the camera faster than the charge can be transported away. Figure 2.17 demonstrates this effect. Here a probe beam ($I \approx 0.1 I_{\text{sat}}$) is fired for 30 μs. The camera is exposed in bulb mode for 3 ms and the time at which the probe is fired is varied. It can be seen that firing the probe before the CCD exposure results in a 'ghost' image - an image in which we can still see the probe beam despite no probe light falling on the CCD. The longer the time between the probe firing and the camera exposure starting, the less charge there is remaining on the CCD. No ghost image is seen if the probe is fired 5 ms before the camera exposure. If the probe pulse is fired at any point during the camera exposure then a normal image is recorded. After the exposure period of the CCD, the frame is transferred to a masked area of the sensor. If the probe pulse is fired during this frame transfer, we observe a displaced image due to the transfer of pixel charge. This charge transfer is observed at a rate of 0.89 pixels μs^{-1} and is in agreement with the camera settings.

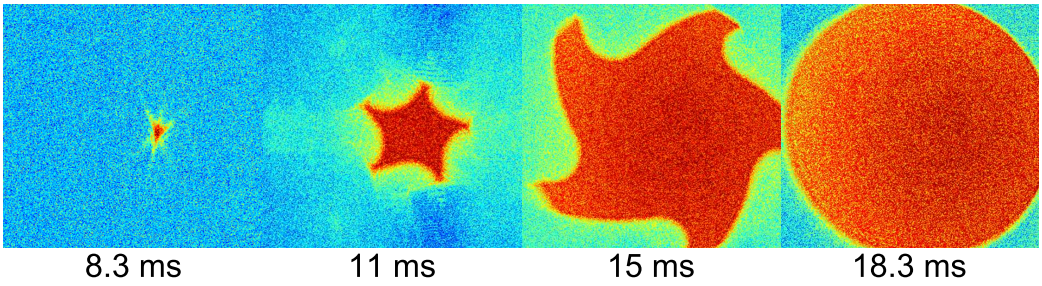

Figure 2.18: Images showing the timing of the opening of the Thorlabs SHB1 shutter. The time of each exposure is recorded relative to the trigger sent to the shutter.

The result of these camera tests is that the CCD needs to be blocked whilst the atoms are in the MOT, where the ghost imaging effect will be much more apparent due to the intense MOT beams. In addition, the fluorescence of the MOT itself would also be imaged onto the camera CCD. We use a large-

area mechanical shutter (Thorlabs SHB1) mounted to the camera, which is triggered so that the shutter is fully open at the start of the CCD exposure. Figure 2.18 shows the evolution of the shutter opening as a function of the time after which the trigger is sent. It takes 8.3 ms before the shutter starts to open, and is fully open after 18.3 ms. Because the MOT light must be turned off prior to the shutter starting to open, this limits our minimum time of flight for Cs absorption images to 10 ms.

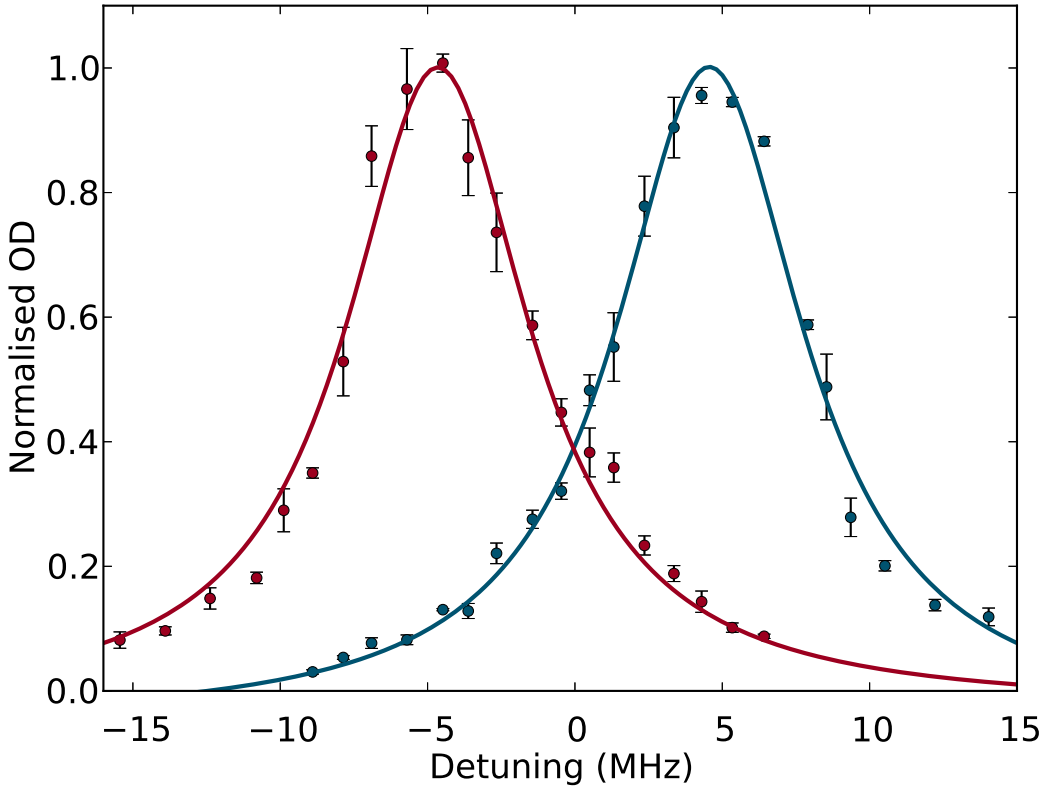

Figure 2.19: Normalised optical depth of a cloud of Cs atoms after 15 ms of optical molasses. The Cs is imaged using a 30 μs probe pulse that is preceded by a 100 μs pulse of repump light. The repump light remains on during the probe pulse. The red data shows the optical depth, as a function of probe detuning from the zero-field $F = 4 \rightarrow F' = 5$ transition, in the case where a magnetic bias field is applied such that σ^- transitions are driven. The blue data show the case in which the bias field is reversed and σ^+ transitions are driven. The curves are Lorentzian fits to the data sets, and the data are normalised to these curves for clarity.

In order to image Cs, the atoms need to be in a stretched state so that they continuously absorb probe light. To do this, a quantisation field of ± 3.7 G is applied along the direction of probe propagation, and the polarisation is

set to drive the corresponding $\sigma^{\pm}$ transitions to the stretched state. Since the probe acts on the $F = 4 \rightarrow F' = 5$ transition, repump light is needed throughout the probe pulse. In typical imaging sequences we apply 100 μs of repump light, which then remains on during the 30 μs probe pulse. Applying the quantisation field causes a Zeeman shift of the m_F sublevels and, as such, the maximum optical depth is observed when detuned from the zero-field $F = 4 \rightarrow F' = 5$ transition. If the quantisation field is reversed in direction and the polarisation remains the same, then the probe light drives σ transitions of the opposite handedness and, as such, the optimum detuning is of the opposite sign. By varying the frequency of the probe AOM and recording the peak optical depth for each orientation of the quantisation field we obtain figure 2.19. A Lorentzian can be fit to each data set in order to extract the optimum detuning for imaging in each configuration. In the configuration in which σ^- transitions are driven we find an optimum detuning of -(4.6 ± 0.1) MHz, and an optimum of (4.6 ± 0.1) MHz for the σ^+ transitions. The widths of the Lorentzian fits were (7.6 ± 0.7) MHz and (7.8 ± 0.4) MHz respectively. These values are in agreement with each other, but do not agree with the Cs linewidth of 5.23 MHz (5.49 MHz including the expected power broadening). This may be due to the quantisation field not being perfectly aligned to the probe propagation or possibly due to a small π transition driving component to the probe light. It is more likely that the line is simply broadened by the moderate magnetic field strength: the atoms are being pumped across to the stretched states, and so some light is still absorbed at detunings closer to 0 MHz.

Absorption imaging of Yb

Absorption imaging of Yb is somewhat simpler than the imaging of Cs. Firstly, there are two transitions accessible for imaging ground state atoms: imaging on the 399 nm $^1S_0 \rightarrow {}^1P_1$ transition or the narrow 556 nm $^1S_0 \rightarrow {}^3P_1$ transition is possible with our laser systems. Secondly, there is no need for repump light nor issues with hyperfine pumping. Finally, no quantisation magnetic field is required. We image using a CCD camera (Andor Luca) that has measured quantum efficiencies of 49 % and 18 % for the 556 nm and 399 nm transitions respectively, and a digitisation of 14 bit. Despite

the higher quantum efficiency for the 556 nm transition, we elect to use the 399 nm transition as the probe beam can be overlapped with the MOT beams using dichroic mirrors. Therefore, by using a camera-mounted interference filter in combination with the dichroic mirrors, we are able to block the Yb MOT light and fluorescence without the need for a large area shutter, allowing in situ imaging of the MOT and sub-ms times of flight.

The generation of the resonant probe light is discussed in section 2.4.1. This light is fibre-coupled to the main table and collimated using a fibre cage system to a waist of 6.8 mm. To achieve good signal to noise ratios, the incident probe needs to create a large electron count on the pixels without saturating them. For the purpose of the following example we will use 12000 counts. Given the quantum efficiency of the camera, it is clear that we will require $N = 6.7 \times 10^4$ photons to be incident on a single pixel to generate the required electron counts. For the purposes of imaging a MOT, a typical magnification of the imaging system is 0.5. The probe intensity required at the position of the atoms, I_{atoms}, for an exposure of time t is then

$$I_{\text{atoms}} = M I_{\text{camera}} = \frac{MNhc}{A_{\text{pixel}} t \lambda}, \tag{2.28}$$

where I_{camera} is the intensity at the camera and A_{pixel} is the physical area of the pixel. For the camera described above, an intensity of 2.6×10^{-2} I_{sat} to 2.6×10^{-3} I_{sat} is required at the atoms for typical pulse durations from 10 μs to 100 μs. The probe fibre has a maximum output of 50 μW, giving an intensity at the atoms of 1.1×10^{-3} I_{sat} and a corresponding pulse duration of around 40 μs.

2.7 Summary

In this chapter we have presented an overview of the experimental apparatus. In particular, we have highlighted the ongoing evolution of the apparatus into a system that can reliably produce clouds of ultracold ytterbium or caesium. The laser systems, including the implementation of a new 399 nm laser setup, have been outlined in detail along with the new magnetic field coil array.

Further detail on the performance of these upgrades on the path towards our goal of an array of ultracold CsYb molecules is given in later chapters.

Chapter 3

Ytterbium fluorescence spectroscopy

In this chapter we present our approach for the laser frequency stabilisation of both the 399 nm laser and the 556 nm laser. A multitude of spectroscopic techniques exist for stabilising laser frequencies to alkali metal D line transitions [126, 127, 129, 136–138], whereas the options for referencing a laser to the Yb transitions at 556 nm and 399 nm are limited. Our method involves fluorescence spectroscopy on a high-flux atomic beam that is produced in a "Beam Machine", a dedicated atomic oven under vacuum. In the following sections we discuss the limiting factors in obtaining spectra of Yb, the design of the Beam Machine, the fluorescence detector, and the method for stabilising the lasers, which is fundamentally the same for both lasers. We also present the fluorescence spectra obtained using these methods, including a technique to remove the bosonic lines from such spectra.

3.1 The "Beam Machine"

3.1.1 Spectroscopy of ytterbium

As we have seen in the previous chapter, Yb possesses two transitions that are often used for laser cooling; the 399 nm transition from the ground state to the singlet $^1P_1$ state, and the 556 nm transition from the ground state

to the triplet $^3P_1$ state. Typical laser cooling experiments with Yb require laser light resonant or near-resonant with each of these transitions, and so a robust method of referencing the laser frequency is required. We previously stabilised the 399 nm laser to a reference cavity, which is described in more detail in the previous chapter, but we have since found it much more reliable to stabilise both lasers to the atomic transitions themselves.

For our 852 nm Cs light, locking to atomic transitions is a trivial task: the vapour pressure of Cs (see table 2.1) at room temperature is sufficiently enough to use glass vapour cells and achieve excellent signal-to-noise ratios in many variations of spectroscopy on the D_2 lines. However, the vapour pressure of Yb at room temperature is only 3×10^{-21} torr [113]: it is impossible to detect Yb spectroscopy signals using room-temperature vapour cells. For sufficient absorption of a weak probe, the Yb vapour would have to be heated to at least 420 °C. However, at such extreme temperatures Yb reacts with conventional glass cells, making the cell opaque to the probe light. It is possible that a sapphire cell would negate this issue, but this would be at an unnecessary expense. A number of vapour cell designs exist for counteracting this problem, but tend to be bulky instruments [139–141].

A number of alternatives to vapour cell-based spectroscopy exist. For example, hollow-cathode lamps are an alternative source for absorption spectroscopy [142]. However, these sources significantly broaden the absorption features, often to more than 1 GHz wide, a characteristic that is not ideal for sub-MHz laser frequency stabilisation. The ideal situation would be to stabilise the laser to the reflected signal of a high-finesse passive optical cavity [143, 144]. This has the advantage of narrowing the laser linewidth, a feature that is a necessity for cold strontium experiments, where the triplet transition is even narrower than for Yb [145]. However, this is a solution with a high associated cost, and is often as bulky as the vapour cell designs mentioned above. Furthermore this solution offers precision that is simply not required for an Yb MOT. Finally, one may detect the fluorescence resulting from a resonant probe laser beam crossing a high-flux atomic beam. Some groups utilise this method with a photo-multiplier tube (PMT) used to detect the resulting fluorescence [117, 146, 147]. This is the basis for the method we have adopted, with the exception of using a high-gain photodi-

ode system instead of the costly PMT. The following sections describe the simple, robust and relatively inexpensive spectroscopy device, starting with the vacuum system and following with the fluorescence detection setup.

3.1.2 Design of the Beam Machine

The complete Beam Machine is shown schematically in figure 3.1 (b). It is comprised of a steel vacuum chamber, constructed mostly from standard DN40 CF vacuum components, and two fluorescence detection assemblies. The Beam Machine features an oven nearly identical to that on the vacuum system of the main experiment. This oven only contains a 5 g ingot of ytterbium, and is heated to a typical temperature of ∼470 °C using a single band heater (Watlow, MB1J1JN2-X73). As with the oven on the main experiment, an array of 55 capillary tubes each of internal diameter 0.58 mm and length 20 mm, are used to collimate the beam. The array of capillaries is clamped over a 5 mm diameter circular aperture. Further enhancing the collimation of the atomic beam is a differential pumping tube, used to connect the oven to the body of the beam machine.

The effusing atomic beam of ytterbium passes first through a "tee" used to connect a 55 $\mathrm{l\,s^{-1}}$ ion pump to the system, and then passes through two six-way crosses, each of which have four AR coated viewports on the arms of the cross that lie perpendicular to the atomic beam. Prior to each six-way cross is an aperture to provide further collimation of the atomic beam. These apertures are holes drilled into the solid copper gaskets used to form the vacuum seal at the first vacuum port of each six-way cross along the direction of propagation of the atomic beam. The positions of these apertures may be seen in figure 3.1 (b). The first aperture is 6 mm in diameter, with the second being 8 mm in diameter. The final element in the chain of vacuum components is a second tee, which is connected to an all-metal valve. Following the loading of the oven, the Beam Machine is baked out into a turbo pump connected to the system via this valve. Once the bake out is complete, the valve is closed and the ion pump activated. In using the beam machine we have found the 5 g ingot of Yb sufficient for ∼2 years of running. The initial model of the Beam Machine used nickel gaskets to

form the vacuum seals, however investigation of a vacuum leak on the oven of the main experiment showed signs of the Yb corroding the gaskets at high temperatures in the oven. This prompted the move to using copper gaskets in the redesigned dual species oven and Beam Machine.

The horizontally aligned viewports on the two six-way crosses allow a laser beam at a wavelength of either 399 nm or 556 nm to intersect the atomic beam at 90 °, resulting in the scattering of light by atoms in the atomic beam. These viewports are covered by light baffles featuring a 5 mm diameter aperture. The purpose of the baffles is primarily to reduce the amount of background light picked up by the detection systems, however they also serve to guide the laser beam onto a path that is perpendicular to the propagation of the atomic beam.

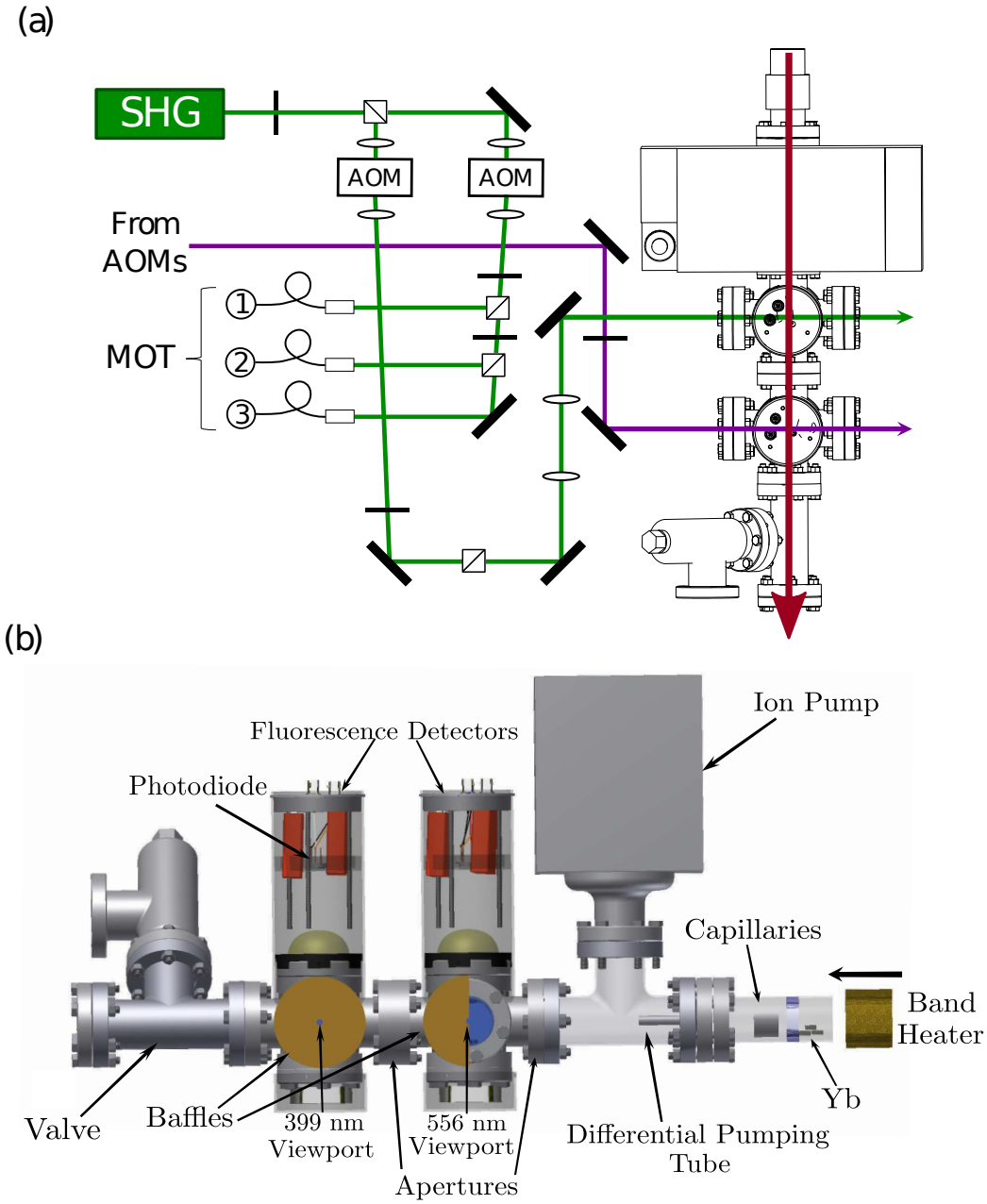

Figure 3.1: (a) A schematic figure showing the generation of the spectroscopy probes for both the 399 nm and 556 nm transitions. Weak probes cross the atomic beam generated by the beam machine (shown in red) at a 90° angle. The fluorescence is picked up by photodiodes mounted perpendicular to both the atomic beam and the probe light. (b) A schematic rendering of the atomic beam machine. The rightmost part of the figure shows the oven, over which a band heater is attached to produce an atomic beam. Collimation of the atomic beam is provided by a capillary array clamped over the exit of the oven chamber. Further collimation is provided by the use of a differential pumping tube and apertures. Two pairs of anti-reflection coated viewports provide optical access for the probe beams. These viewports are covered by sets of baffles to reduce background light reaching the detectors. Further viewports are mounted above and below the atomic beam on these crosses, which support the fluorescence detectors and retroreflection mirrors respectively.

3.1.3 Fluorescence detection

The vertically aligned viewports on the two six-way crosses are used to detect the fluorescence resulting from atomic beam scattering the probe laser photons. The upper viewports have 50 mm diameter aspheric lenses, each with a focal length of 32 mm, fitted immediately above the glass surface of the viewports. The purpose of these lenses is to focus fluorescence onto a photodiode mounted above them. The bottom viewports are likewise fitted with 50 mm diameter retroreflecting mirrors with focal lengths of 38 mm. The mirrors are designed to enhance the photodiode signal by focussing the downwards propagating fluorescence onto the photodiode, which would otherwise go uncollected. The increase in signal is larger than the factor of two that one might expect: fluorescence reflected off the vacuum system interior may be collected by the combination of the mirror and collection lens.

The critical component of our fluorescence spectroscopy setup is the detector itself. The photodiode is mounted on a circular printed circuit board (PCB), the circuit of which is shown in figure 3.2. This PCB features a custom amplifier of the photodiode signal, giving an excellent signal-to-noise ratio, despite the low levels of fluorescence. Figure 3.2 shows a transimpedance amplifier of very high gain placed near a standard large-area photodiode. The operational amplifier is a low input-noise device (Analog Devices, AD795), with input pins protected by a guard ring on the PCB, thus minimising the effects of small currents that may flow on the PCB substrate. A "tee-resistor network" [148], shown in figure 3.2, can be used to create a large transimpedance gain of up to 10^9 $\mathrm{V\,A^{-1}}$. We find that a gain of 10^8 $\mathrm{V\,A^{-1}}$ is more than sufficient for our purposes, whilst maintaining the bandwidth required to detect the frequency modulation used on the probe beam.

The PCB features three clearance holes through which nylon rods are used to adjust the height of the photodiode above the collection lens on the upper viewport. The nylon rods are mounted to the lid of a brass tube, which is designed to fit tightly over the upper viewports of the Beam Machine. The brass tube further reduces background light reaching the photodiode and forms a Faraday cage, protecting the entire circuit from unwanted RF pickup. The cores of BNC cables are used to transmit an amplified differential

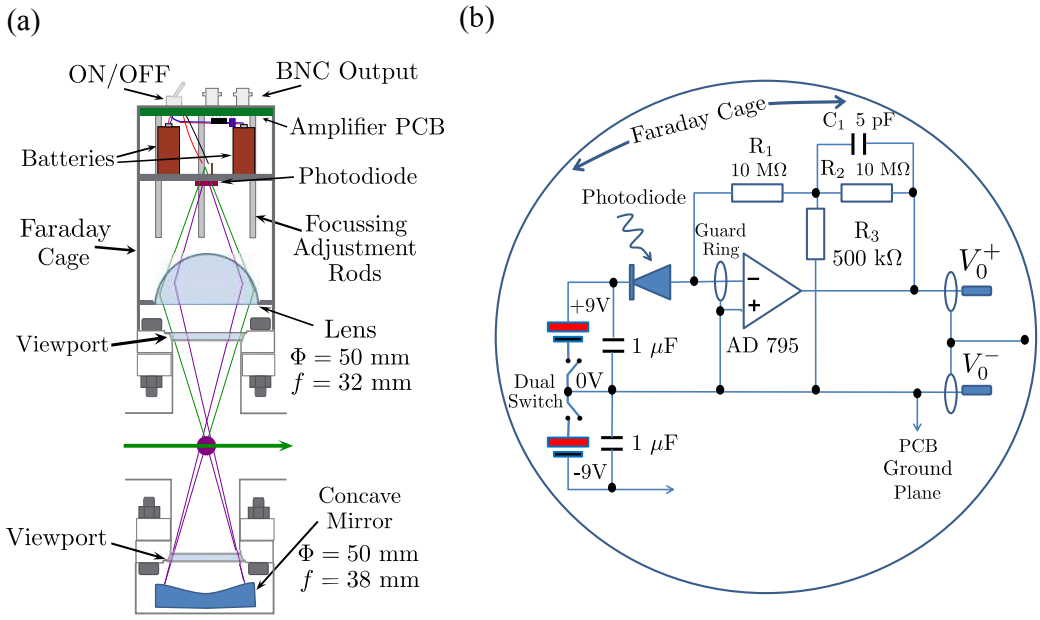

Figure 3.2: (a) A schematic drawing of the photodiode assembly used for fluorescence detection. The detector is entirely mounted within a brass cylinder, which forms a Faraday cage (depicted by the grey outer border). This mounts securely to the viewport immediately above the atomic beam. A lens with a numerical aperture of 0.6 is used to collect atomic fluorescence due to the incident probe beam (cross section shown in purple) and focus onto a battery-powered photodiode. The solid angle of the fluorescence collected by this lens is shown in green. Below the atomic beam a concave mirror is used to collect the downward propagating fluorescence and focus it back onto the photodiode (shown in purple). The printed circuit board (PCB) shown schematically in (b) is also housed within the Faraday cage on nylon studding. The PCB produces an amplified signal carried on differential outputs V_0^+ and V_0^-.

signal to a lock-in amplifier, with the cladding of the BNC cables used to extend the shielding from RF signals.

The large gain and excellent resulting signal-to-noise ratio has reduced the typical operating temperature of the oven to around 470 °C, which has the effects of improving the lifetime of the Yb source and reducing the transverse spread of the atomic beam. It should also be possible to miniaturise the design by the use of smaller vacuum components, however we have found that an ion pump is essential. Without the pump background pressure builds up and impedes molecular flow of the atomic beam [122]. We observe these effects as a gradual broadening of the spectral lines observed when scanning

the lasers over the transitions. Finally, one of the biggest advantages of this system is that it may be used for detecting both the 399 nm and the 556 nm transitions in Yb; the same atomic beam is used along with the same detector design to stabilise both lasers to resonance.

3.2 Fluorescence spectroscopy

Both the 399 nm laser for Zeeman slowing and imaging, and the 556 nm laser for the MOT light are stabilised to the fluorescence signals obtained using the Beam Machine. As described in sections 2.4.1 and 2.4.2, the first-order diffracted beam from an AOM is used to generate a probe beam for spectroscopy. In this section we will discuss the spectra observed and the performance of the Beam Machine, including a technique for subtracting the Bosonic spectra to reveal the spectra of the fermions.

3.2.1 399 nm spectroscopy

One of the principal reasons for our choice of Yb to pair with Cs in this experiment is the number of isotopes available: Yb has seven stable isotopes, five of which are bosonic isotopes. Having such freedom effectively gives the ability to tune the background interspecies scattering length of system, achieved by the scaling of the reduced mass of the two elements [132]. For this reason, we require our chosen form of spectroscopy to deliver the possibility of stabilising the laser systems for any of the seven isotopes. In the ground state the two valence electrons pair up, giving a spin of $S = 0$. The bosons have a nuclear spin of $I = 0$, and as such there is no ground state hyperfine splitting and only a single $F' = 1$ excited state. The non-zero nuclear spin of the fermionic isotopes couples to the orbital angular momentum of the excited state to give excited state hyperfine structure. Table 3.1 summarises the isotope shift and, where relevant, the hyperfine splitting for the 399 nm lines of Yb [149].

A typical fluorescence spectrum of the $^1S_0 \rightarrow {}^1P_1$ transition is shown in figure 3.3. The spectrum shows a scan of the probe frequency across the transition for all seven of the Yb isotopes, achieved by modulating the volt-

Isotope	Abundance [150]	Nuclear spin	Shift from ^{174}Yb (MHz) [149]
^{176}Yb	12.70%	0	-509.310(50)
^{173}Yb ($F' = 5/2$)	16.10%	5/2	-253.418(50)
^{174}Yb	31.80%	0	0
^{173}Yb ($F' = 3/2$)	16.10%	5/2	515.975(200)
^{172}Yb	21.90%	0	533.309(53)
^{173}Yb ($F' = 7/2$)	16.12%	0	587.986(56)
^{171}Yb ($F' = 3/2$)	14.30%	1/2	832.436(50)
^{171}Yb ($F' = 1/2$)	14.30%	1/2	1153.696(61)
^{170}Yb	3.05%	0	1192.393(66)
^{168}Yb	0.13%	0	1887.400(50)

Table 3.1: A table showing the natural abundance for the seven stable isotopes of ytterbium and their respective nuclear spins. Note the the abundance refers to the isotope alone, and does not reflect the transition strengths of the various hyperfine transitions in the fermionic isotopes. Also shown are the isotope and hyperfine splitting of the $^1P_1$ state relative to the most abundant element, ^{174}Yb.

age on the laser's piezoelectric transducer (PZT). The scan has been linearised by use of the cavity peaks of a Fabry-Pérot etalon. Following the linearisation process, we can see that the fluorescence peaks align with the expected isotope shifts, which are shown on the figure as dashed red lines. For all 399 nm spectra presented in this section, the probe beam has a modest power of 33 μW, and a $1/e^2$ diameter of 0.50 ± 0.01 mm. The main spectrum in the figure was produced with a temperature of 470 °C set on the oven band heater.

We can see that the use of the Beam Machine gives us excellent resolution of all of the transitions. By increasing the temperature to 520 °C, the increased atomic beam flux allows the resolution of the elusive ^{168}Yb with a signal-to-noise ratio greater than 100. The 399 nm transition does not lend itself to a study of the collimation of the atomic beam produced by the Beam Machine: the width of the fluorescence peaks is dominated by the large natural linewidth of the transition of 28 MHz. Even though this thesis reports on experiments using ^{174}Yb alone, the quality of the spectra obtained gives us confidence of being able to stabilise our laser system for the Zeeman slowing of any isotope of Yb using a combination of the fluorescence detection setup

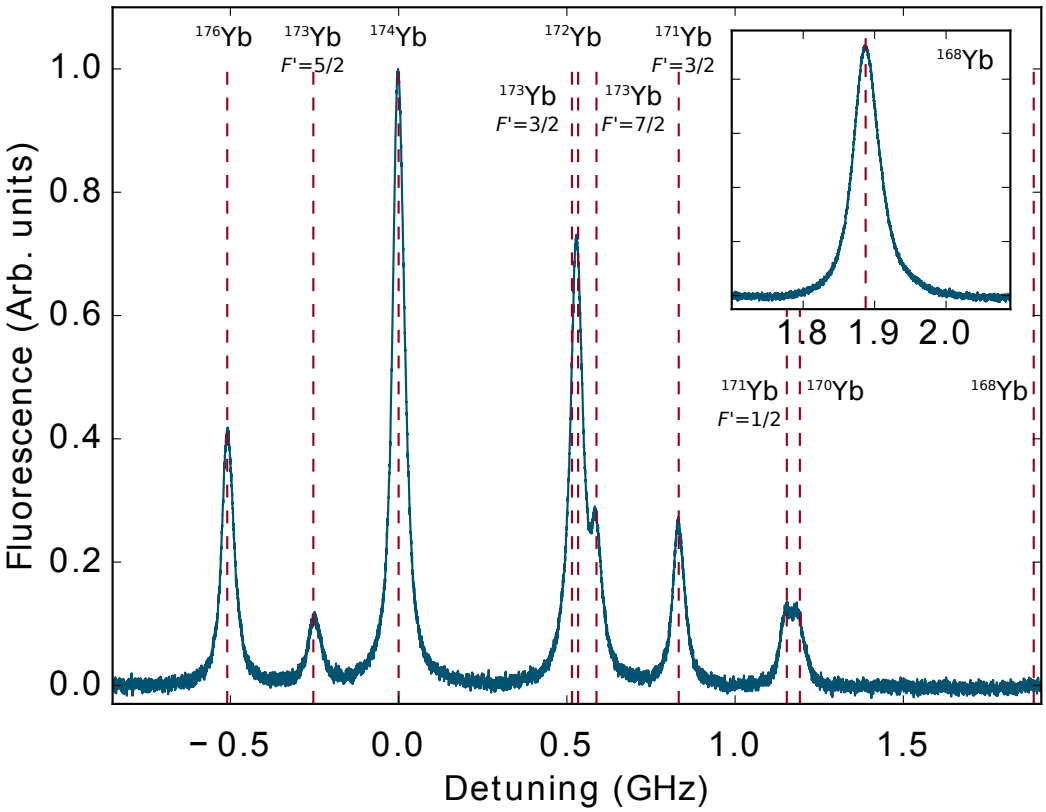

Figure 3.3: Fluorescence spectrum of the 399 nm transition for all Yb isotopes. The spectrum was taken using the beam machine and the fluorescence photodiode. The labels identify the fluorescence peaks for each Yb isotope and the corresponding excited hyperfine states for the fermionic isotopes. Note that the fluorescence peaks of many of the fermionic isotopes are obscurred by the fluorescence peaks of more abundant bosonic isotopes. Zero detuning has been chosen as the peak of the ^{174}Yb peak. The red dashed lines show the expected isotope shifts for this transition. The inset shows the ^{168}Yb fluorescence peak taken by running the beam machine at a higher temperature of 520 °C.

and the probe AOM. This is true even for ^{168}Yb, albeit the Beam Machine's supply of Yb will need to be replenished more frequently when running at a temperature of 520 °C. We can also see that, with the exception of the $F' = 5/2$ transition in ^{173}Yb and the $F' = 3/2$ transition in ^{171}Yb, the fluorescence peaks associated with the hyperfine transitions in the fermionic isotopes of Yb are obscured or partially obscured by the fluorescence peaks of transitions in the bosonic isotopes of Yb. A method for resolving the fermionic isotopes is discussed in section 3.2.3.

3.2.2 556 nm spectroscopy

The Yb transition at 556 nm is a sterner test of our spectroscopy system: the natural linewidth of the transition is only 182 kHz [141], owing to the fact that it is an electric dipole forbidden transition. This greatly reduces the scattering rate and the resulting fluorescence signal. Similarly to the 399 nm transition there is isotope and hyperfine shifts in the excited state, and these are summarised in table 3.2.

Isotope	Shift from ^{174}Yb (MHz) [151]
^{173}Yb ($F = 7/2$)	-2386.704(85)
^{171}Yb ($F = 1/2$)	-2132.063(85)
^{176}Yb	-954.832(60)
^{174}Yb	0
^{172}Yb	1000.020(85)
^{170}Yb	2286.345(85)
^{173}Yb ($F = 5/2$)	2311.411(85)
^{171}Yb ($F = 3/2$)	3804.608(100)
^{173}Yb ($F = 3/2$)	3807.278(134)
^{168}Yb	3655.128(100)

Table 3.2: A table setting out the isotope shifts for the $^1S_0 \rightarrow {}^3P_1$ transition. Where relevant the hyperfine splittings are included for the fermionic isotopes of ytterbium.

Fluorescence spectroscopy of the $^1S_0 \rightarrow {}^3P_1$ transition is carried out in much the same way as for the 399 nm transition. A probe of $1/e^2$ waist 1.97 ± 0.01 mm crosses the atomic beam at a crossing angle as close to 90° as possible, and the resulting fluorescence is picked up using one of the detectors described in section 3.1.3. We find that a power of around 460 μW ($\sim$50 I/I_{sat}) is sufficient to obtain good quality spectra.

Figure 3.4 shows a typical spectrum obtained when using the 556 nm laser. Once more, a temperature setting of 470 °C on the oven band heater is used to obtain this spectrum. Table 3.2 shows that the total isotope shift is much larger for the 556 nm transition than for the 399 nm transition. Given the limited scan range of the 556 nm laser using its PZT and the large isotope shift between the peaks, we are typically only able to scan over around three isotopes in a given scan. The spectrum shown in figure 3.4 shows the ^{176}Yb,

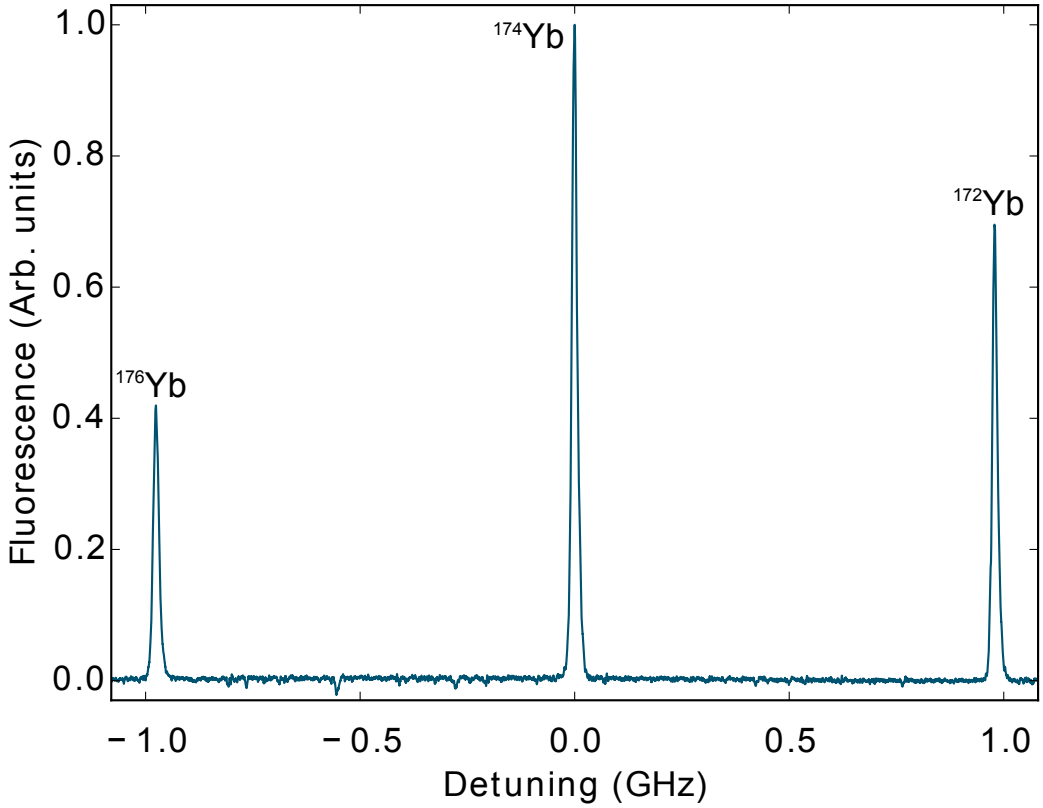

Figure 3.4: A typical fluorescence spectra of the $^1S_0 \rightarrow {}^3P_1$ transitions obtained by scanning the 556 nm laser across three isotopes of Yb. Zero detuning is choosen to be the transition frequency for ^{174}Yb. The two other isotopes visible in this scan are ^{176}Yb (leftmost peak) and ^{172}Yb (rightmost peak). Scanning over further peaks requires changing the temperature of the second harmonic generator of the laser output.

^{174}Yb, and ^{172}Yb fluorescence peaks from left to right. An excellent signal-to-noise ratio of greater than 300 is evident in these narrow features. Unlike the 399 nm transition, the dominant broadening feature here is Doppler broadening due to the transverse spreading of the atomic beam; even though the atomic beam is well-collimated using the capillary tubes and apertures in the Beam Machine design, this inhomogeneous broadening is still significant compared to the narrow natural linewidth of the transition. In addition to Doppler broadening we can expect around 1.3 MHz of power broadening due to the intensity of the probe beam. This all results in a FWHM of 15.2±0.2 MHz of the fluorescence peaks. Doppler-free fluorescence techniques are possible [145], however for the purposes of a MOT where we are likely to use high intensity beams at a large detuning we consider this width to be

sufficient. Using these results we estimate the HWHM effusion angle of the atomic beam to be 11 mrad at this operating temperature.

This spectroscopy technique again makes it possible to stabilise the laser to the fluorescence peak for any isotope. If the isotopes overlap then it is possible to lock to the combined peak and use the AOM frequency to control the detuning of the MOT light. This has been tested in conjunction with the 399 nm laser stabilisation, so far we have produced Yb MOTs for ^{176}Yb, ^{174}Yb, and ^{172}Yb. In the scope of this thesis we will study ^{174}Yb alone, however the Beam Machine should be a useful tool to switch the isotope being studied.

As an aside, the crossing angle of the probe and the atomic beam is crucial. Given the velocity of the atoms emerging from the Beam Machine oven, we would expect a Doppler shift in the signal of around 10 MHz per degree from orthogonal crossing. The sensitivity of this can be seen when producing a 556 nm MOT of Yb; small adjustments to the final mirror prior to the beam machine can cause the MOT to dramatically move across the capture region as the combination of the MOT forces and the pushing force from the Zeeman slower beam changes. We suspect this leads to a systematic offset to the MOT beam detuning, a suspicion which is investigated further in section 4.5.

3.2.3 Fermionic spectra

An important factor in determining the spectra obtained using the method outlined above is the polarisation of the probe beam; especially so for the fluorescence detected for the Bosonic isotopes of Yb. Figure 3.3 shows that all bar two of the fluorescence peaks due to the fermionic isotopes are overlapped with other bosonic fluorscence peaks. This led to confusing results in our initial spectra, where the relative height of the fluorescence peaks did not seem in line with the abundances of the Yb isotopes such as the red curve shown in figure 3.7. The reason for this was the orientation of the plane of polarisation of the linearly polarised probe relative to the collection axis of the detector. In this section we present the implementation of a method involving the subtraction of fluorescence signals to obtain spectra that only

contains the fermionic isotopes of Yb [152].

An atom is excited from a state $|F, m_F\rangle$ to $|F', m_{F'}\rangle$, where F is the total angular momentum quantum number and $m_F = -F, -F+1, ..., F$ is the associated magnetic quantum number of the sublevel. The atom may then decay spontaneously to a ground state according to the selection rules

$$\begin{aligned} \Delta F &= \pm 1, 0 \\ \Delta m_F &= \pm 1, 0. \end{aligned} \tag{3.1}$$

An exemption these rules to this is that $\Delta F = 0$ is forbidden if $F' = F = 0$.

A π-transition, a decay where $\Delta m_F = 0$, will have the same angular fluorescence distribution, $S_\pi(\theta, \phi)$, as for an oscillating classical dipole [123], where

$$S_\pi(\theta, \phi) = \frac{3}{8\pi} \sin^2(\theta), \tag{3.2}$$

where θ and ϕ are the polar and azimuthal angles respectively. Note that $\theta = 0$ corresponds the the plane of polarisation of the probe light. A $\sigma^\pm$ decay changes m_F by ± 1 and results in an angular fluorescence distribution, $S_\sigma(\theta, \phi)$, equivalent to that of a rotating classical dipole [123], where

$$S_\sigma(\theta, \phi) = \frac{3}{16\pi} \left(1 + \cos^2(\theta)\right). \tag{3.3}$$

To determine the average angular fluorescence distribution for a given $F' \to F$ transition of an Yb isotope, we require a weighted average of equations 3.2 and 3.3, where the weighting is by the relative probability of a π-transition or σ-transition respectively. This probability can be found by considering the dipole matrix element

$$\langle F', m'_F | e r_q | F, m_F \rangle. \tag{3.4}$$

The Wigner-Eckart theorem allows this matrix element to be factorised into the product of a Wigner 3 - j symbol and reduced matrix element [153],

$$\begin{aligned}\langle F', m'_F | e r_q | F, m_F \rangle &= \langle F' || e\mathbf{r} || F \rangle \, (-1)^{F-1+m'_F} \\ &\times \sqrt{2F'+1} \begin{pmatrix} F' & 1 & F \\ m'_F & q & -m_F \end{pmatrix}, \end{aligned} \tag{3.5}$$

where $q = m'_F - m_F$. Since Yb only has one hyperfine ground state, the probability of a transition from $|F', m'_F\rangle \rightarrow |F, m_F\rangle$ is then given by

$$P_{F',m'_F \rightarrow F,m_F} = (2F'+1) \begin{pmatrix} F' & 1 & F \\ m'_F & q & -m_F \end{pmatrix}^2. \tag{3.6}$$

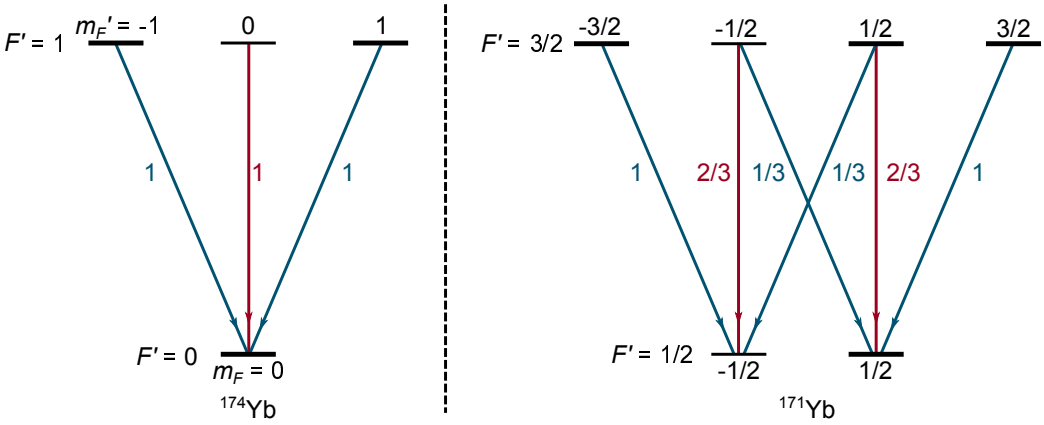

Figure 3.5: The probabilities of decay from excited state $|F', m'_F\rangle$ to $|F, m_F\rangle$ as determined by equation 3.6 for the ${}^1S_0 \rightarrow {}^1P_1$ transition. The diagram on the left shows the transition probabilities for ^{174}Yb, although all bosonic isotopes are represented by the same diagram. The diagram on the right shows the probabilities for the $F' = 3/2 \rightarrow F = 1/2$ transition in ^{171}Yb. π-transitions, leading to an angular fluorescence distribution of the form given by equation 3.2, are shown in red. σ-transitions are shown in blue and lead to a fluorescence distribution given by 3.3.

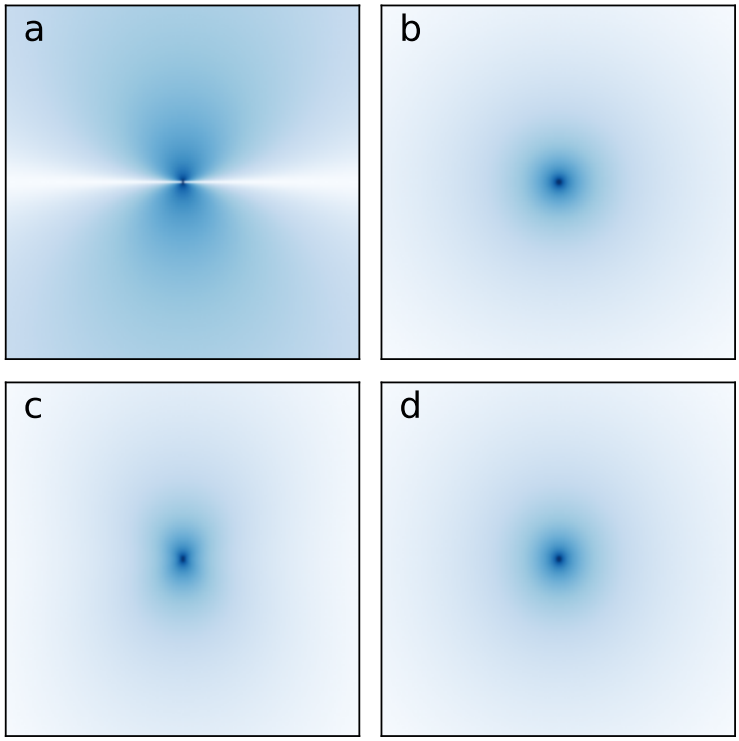

Figure 3.6: Angular fluorescence distributions for the 399 nm transition for different isotopes of Yb. The distributions are shown looking along the direction of propagation of the probe beam. In each distribution shown, the polarisation of the probe beam is along the horizontal direction. (a) The fluorescence distribution for all bosonic isotopes of Yb. (b) The distribution for ^{171}Yb $F = 1/2 \rightarrow F' = 1/2$, ^{173}Yb $F = 5/2 \rightarrow F' = 5/2$, and ^{173}Yb $F = 5/2 \rightarrow F' = 3/2$. (c) The distribution for ^{171}Yb $F = 1/2 \rightarrow F' = 3/2$. (d) The distribution for ^{173}Yb $F = 5/2 \rightarrow F' = 7/2$. The white parts of the distributions are regions with no fluorescence, and the blue regions show the strongest levels of fluorescence. Note that the figures include a $1/r^2$ decay of the fluorescence, where r is the distance from the dipole. The colour map is logarithmic for clarity.

Figure 3.5 shows the transition probabilities for the various magnetic sublevels of ^{174}Yb and the $F' = 3/2$ excited state of ^{171}Yb. These diagrams give insight into the average fluorescence distribution of the different transitions and isotopes of Yb. Since we are only considering a probe that drives π-transitions, only excitations with $\Delta m_F = 0$ can occur. In ^{174}Yb, and indeed in all bosonic isotopes of Yb, this means atoms can only be excited to $|F', m'_F = m_F\rangle$. As a result of this, only decay with $\Delta m_F = 0$ can occur, leading to an angular fluorescence distribution given purely by equation 3.2.

Figure 3.6 (a) shows the resulting fluorescence for bosonic isotopes when the probe polarisation is along the x-axis. The fluorescence distribution is anisotropic with the majority of the fluorescence perpendicular to the probe polarisation. In our system this translates into a maximum fluorescence when the probe polarisation is horizontal, and near extinction of the fluorescence when the polarisation of the probe is vertical.

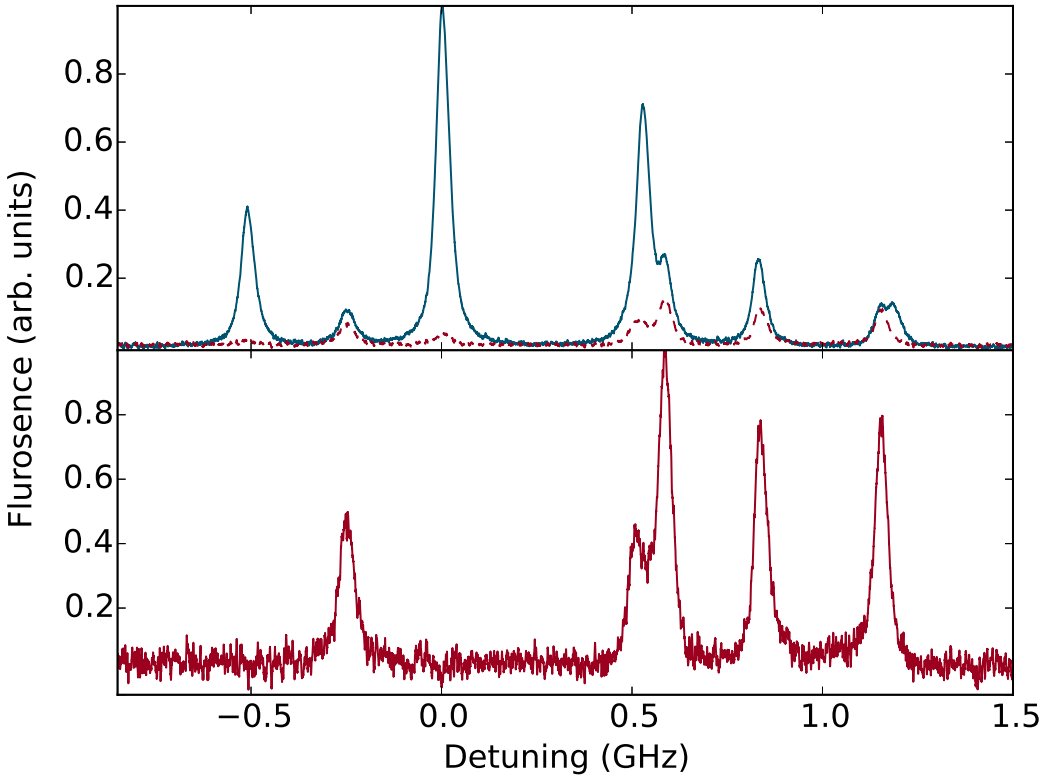

Figure 3.7: The blue curve in the upper figure shows the 399 nm fluorescence spectrum for Yb as presented in figure 3.3. The dashed red curve shows the same spectrum taken with the orthogonal probe polarisation giving near extinction of the fluorescence of the bosonic isotopes. By scaling the red dashed signal to match the bosonic peaks of the blue spectrum, we are able to subtract the two spectra to obtain a spectrum of the fermionic isotopes.

In the fermionic isotopes more transitions can occur, as can be seen in the right hand side of figure 3.5. In this example atoms still cannot be excited to the stretched $m'_F = \pm 3/2$ states of the upper hyperfine manifold due to the linear polarisation of the probe beam. However, atoms can now decay via σ or π-transitions to either ground state. A similar analysis holds for the other possible hyperfine transitions in the fermionic isotopes of Yb. To find the average angular distribution of fluorescence, we consider that the atom may

start in any of the lower hyperfine sublevels and is then excited to the state with $m'_F = m_F$. From here equations 3.2 and 3.3 are weighted by the probability of each form of decay to give the average distribution. The normalised angular distributions for different values of F' for the fermionic isotopes are shown figure 3.6 (b-d), again for horizontally polarised probe light. We can see that in each case the angular fluorescence distributions are isotropic, or nearly isotropic. The impact of this is that the fluorescence due to fermionic isotopes is reduced much less by rotation of the probe polarisation.

The top plot in figure 3.7 shows the spectrum obtained with our system using horizontally (blue curve) and vertically polarised probe light (red dashed curve). Due to the large solid angle of collection of the detector, we do not observe perfect extinction of the bosonic isotopes in the scan taken with vertically polarised light. However, by scaling this spectrum so that the height of the bosonic isotopes match those in the scan taken with horizontal probe polarisation, subtraction of the two scans then yields a spectrum featuring only the fermionic isotopes [152]. Particularly note that the $F' = 3/2$ transition of ^{173}Yb is resolvable, a transition usually obscured by the large fluorescence signal of the bosonic ^{172}Yb isotope.

3.3 Laser frequency stabilisation

3.3.1 399 nm laser frequency stabilisation

Frequency stabilisation of the 399 nm Toptica DL Pro HP laser is achieved using one of the peaks in the fluorescence signal shown in figure 3.3 as a reference. The laser current is modulated at a frequency of 3.7 kHz with an amplitude that gives ± 0.5 MHz excursions of the laser frequency. The resulting modulated fluorescence signal is demodulated using the laser's internal locking system to produce a dispersive error signal, which allows a 2-channel PID controller to lock to the fluorescence peak. It should be noted that whilst this is a resonant form of frequency stabilisation, a combination of AOMs shown in figure 2.6 is used to generate the probe light. This allows the Zeeman slowing beam to be red detuned from resonance by 587.5 MHz and deliver optimal loading of the 556 nm MOT. Figure 2.6 also shows the

laser is fibre coupled to the spectroscopy setup, allowing the majority of the laser output power to be used for Zeeman slowing. Owing to the laser's proximity to the mechanical shutter used during Cs absorption imaging, we use sorbathane sheets to isolate the laser mount from unwanted vibrations, which would otherwise cause erroneous measurements of atom number during absorption imaging.

3.3.2 556 nm laser frequency stabilisation

A similar scheme is used to stabilise the 556 nm laser that is used to derive light for the Yb MOT beams. Here we choose to dither the AOM that generates the spectroscopy probe at a frequency of 3 kHz so as to not add unwanted modulation to the MOT cooling light. The amplitude of the modulation signal gives frequency excursions of around ±2 MHz to the probe beam. The blue curve in figure 3.8 shows the modulated fluorescence signal produced during a small scan over the the ^{174}Yb peak.

The modulated fluorescence signal is fed into the differential input of a lock-in amplifier in order to demodulate the signal and produce a dispersive error signal shown in figure 3.9. This signal has a central slope of 1.2 V MHz^{-1}, and is used to provide negative feedback to the laser's PZT and stabilise the probe light to resonance. The red curve in figure 3.8 shows the modulated fluorescence signal when the laser is locked to resonance. The root mean square noise in this signal suggests short term fluctuations of the laser frequency are less than 1 MHz. We have found this suitable for the purposes of loading and cooling a MOT, as discussed in section 4. If we were to require further stabilisation it may be possible to use Lamb dip spectroscopy, a sub-Doppler technique using retroreflected probe beams [145, 154].

Given that the linewidth of the $^1S_0 \rightarrow {}^3P_1$ transition in Yb is only 182 kHz, the behaviour of atoms in the MOT can be extremely sensitive to the detuning of the MOT beams, particularly at low intensities as described later in section 4.4.2. As such, any systematic offsets in the detuning of the MOT beams can have a critical impact on the performance of the experiment. One drawback of this stabilisation system is the potential for a large systematic offset in the detuning as a result of the atomic beam. An atom travelling in

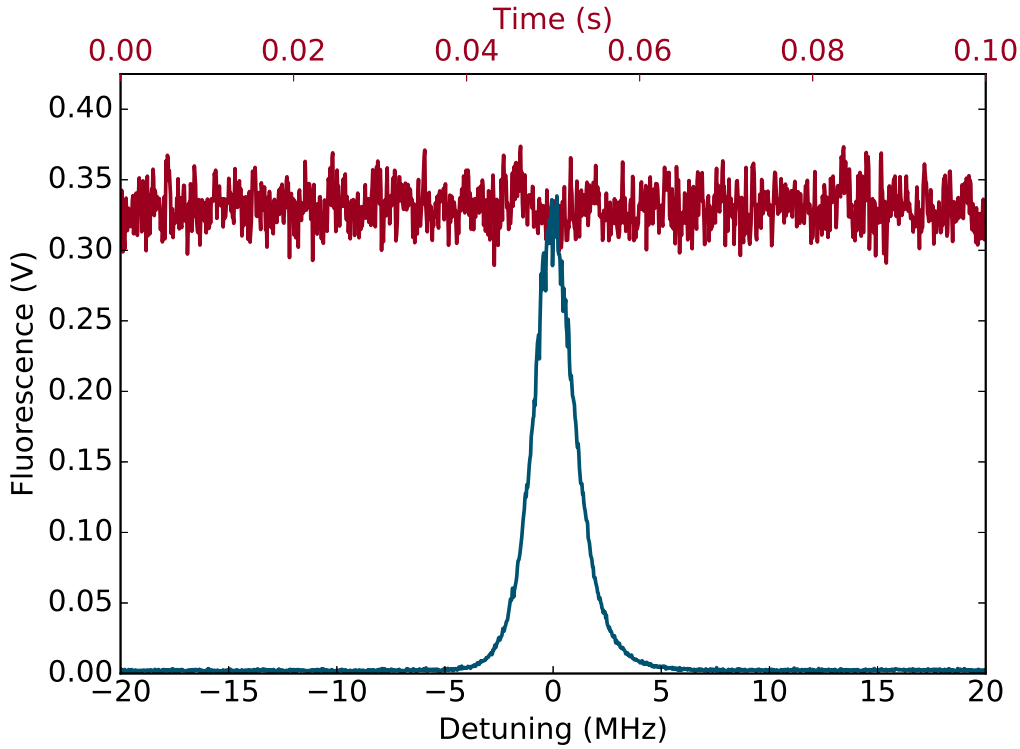

Figure 3.8: The blue curve shows a typical fluorescence signal obtained whilst scanning over the $^1S_0 \rightarrow {}^3P_1$ transition of ^{174}Yb with modulation applied to the probe beam by the spectroscopy AOM. The red signal shows the fluorescence whilst the laser is locked, with short term frequency fluctuations of less than 1 MHz.

an atomic beam at velocity, v, observes a Doppler shift in the frequency of a probe beam crossing the atomic beam at an angle, θ, of

$$\Delta\delta = \frac{v\cos\theta}{2\pi\lambda_0}, \tag{3.7}$$

where λ_0 is the resonant wavelength when the atom is at rest. Given the mean speed of an Yb atom effusing from a 470 °C oven is around 350 m s^{-1}, we can estimate that small departures of θ from a 90 ° crossing angle with the atomic beam will cause a frequency shift of around 11 MHz per degree. The impact of this effect in our system is discussed in more detail in section 4.5.

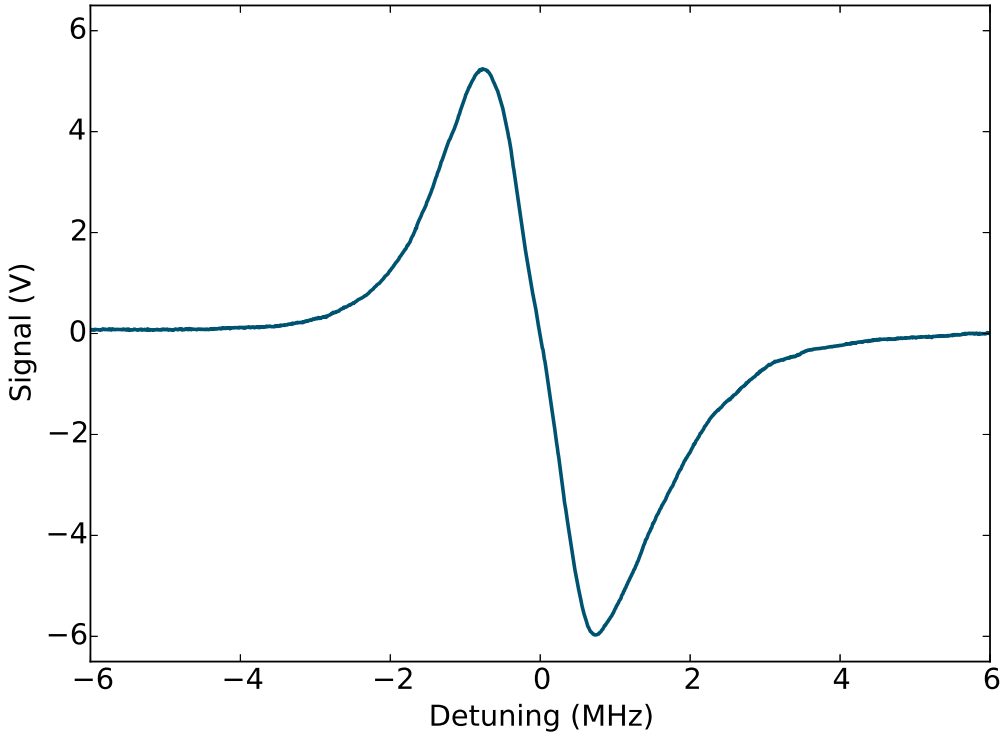

Figure 3.9: A typical error signal generated by demodulating the signal obtained in figure 3.8 using a lock-in amplifier. Despite not being a sub-Doppler feature, the level of frequency stabilisation of the 556 nm laser light is found to be beyond sufficient for producing Yb MOTs of a consistent temperature and atom number.

3.4 Summary

In this chapter we have presented a robust, reliable and inexpensive method of obtaining fluorescence spectra of ytterbium for use in laser frequency stabilisation. Whilst a passive cavity would be essential for addressing the ${}^1S_0 \rightarrow {}^3P_0$ clock transition in ytterbium, we have found that atomic beam spectroscopy for the purposes of creating ytterbium MOTs with a large number of atoms is more than sufficient. We have described the vacuum system used to create the high-flux collimated atom beam that is addressed by probe light, in addition to the high-gain photodiode used to detect the resulting fluorescence. Finally, we have demonstrated the removal of the bosonic isotopes of ytterbium from fluorescence spectra in order to produce a spectrum purely comprised of fluorescence peaks due to the hyperfine transitions in fermionic isotopes.

The next chapter looks at how we use this system alongside the experimental apparatus described in chapter 2 to produce large numbers of ytterbium atoms in a MOT. In addition to this, we detail how the control offered by the ytterbium spectroscopy setup described here allows the cooling of Yb atoms in a MOT to a temperature of 22 μK.

Chapter 4

The ytterbium MOT

The MOT is the starting point for the majority of ultracold atom experiments, utilising the scattering of resonant photons, the Zeeman shift of magnetic substates, and the Doppler effect, to trap and cool large numbers of atoms. The first realisation of the laser cooling of atoms lead to the 1997 Nobel Prize for Physics being awarded to Chu, Cohen-Tannoudji, and Phillips [2–4]. In this chapter we present a brief summary of laser cooling and the MOT, and how a similar approach may be used to describe Zeeman slowing. We then describe the optimisation and characterisation of our narrowband Yb MOT. Bosonic Yb has a single ground state and provides a good test of Doppler theory. The narrow linewidth regime of Doppler theory is compared to measurements of the Yb MOT temperature under a variety of conditions. A more complete description of MOTs and Doppler theory may be found in references [155–160].

4.1 Laser cooling and trapping

4.1.1 The molasses force

In simple terms the laser cooling of atoms is the reduction of the thermal energy of an atomic sample by the use of laser light. Consider a two-level atom with energy spacing $\hbar\omega_0$, where $\hbar$ is the reduced Planck constant and ω_0 is the resonant angular frequency of photons that drive the transition from

the ground state to the excited state. These photons have a wavelength, λ_0, and a momentum of $\vec{p} = \hbar\vec{k}$, where $\vec{k}$ is the wavevector of the photon, directed along the direction of light propagation and with magnitude $2\pi/\lambda_0$. Upon the absorption of a photon the atom is excited to the upper state and receives a momentum kick in the direction of light propagation, resulting in a change of the atom's momentum,

$$\vec{p}_{\text{atom}} = m\vec{v} \rightarrow m\vec{v} + \hbar\vec{k}, \tag{4.1}$$

where m is the mass of the atom and $\vec{v}$ is the initial velocity of the atom prior to the momentum kick. The finite lifetime of the transition leads to spontaneous decay of the atom back to the ground state. In such a decay, a photon of frequency ω_0 is re-emitted leading to further momentum kicks of magnitude $\hbar k$. However, since the decay process is symmetric, momentum kicks due to spontaneous emission will average to zero over many cycles of the absorption and re-emission process. Therefore the net change in momentum of the atom is in the direction of propagation of the absorbed photons.

In order to cool atoms in a gas, the velocity distribution of the gas must be compressed. To achieve this, it needs to be arranged for the atoms to preferentially absorb photons with a wavevector opposite to the direction of motion of the atom. To do this we consider an arrangement of a pair of counter-propagating laser beams. If the laser frequency ω is detuned from resonance by $\delta = \omega - \omega_0$, then only stationary atoms experience the same detuning from both beams. In the reference frame of the atom, the Doppler effect leads to a modified laser frequency of

$$\omega' = \omega - \vec{k} \cdot \vec{v} = \omega_0 + \delta - \vec{k} \cdot \vec{v}. \tag{4.2}$$

Provided the detuning of the laser is negative (red detuned) then the atoms will preferentially absorb photons that counter-propagate the motion of the atom.

Solving the optical Bloch equations in the steady state for such a two level

system yields an excited state population of

$$\rho_{\text{excited}} = \frac{\Omega^2/4}{\delta^2 + \Omega^2/2 + \Gamma^2/4}, \tag{4.3}$$

where Γ is the decay rate of the transition, and Ω is the Rabi frequency of the driving optical field. The Rabi frequency is related to the intensity of the laser, I, by

$$I = \frac{2\Omega^2 I_{\text{sat}}}{\Gamma^2}, \tag{4.4}$$

where I_{sat} is the saturation intensity of the transition. The rate at which photons are scattered is then $R = \Gamma\rho_{\text{excited}}$. Combining this rate with the momentum change due to each absorption yields the scattering force

$$\vec{F} = \frac{\hbar\vec{k}\Gamma}{2}\frac{I/I_{\text{sat}}}{1 + I/I_{\text{sat}} + 4\delta^2/\Gamma^2}. \tag{4.5}$$

If we consider two counter-propagating laser beams along a Cartesian axis as discussed above, then the detuning seen by the atom is modified for each beam by $\pm kv$. The resultant force on the atom is then given by

$$\begin{aligned} F_{\text{molasses}} &= F(\delta - kv) - F(\delta + kv) \\ &= \frac{\hbar k\Gamma}{2}\left[\frac{I/I_{\text{sat}}}{1 + 2\frac{I}{I_{\text{sat}}} + 4\left(\frac{\delta - kv}{\Gamma}\right)^2} - \frac{I/I_{\text{sat}}}{1 + 2\frac{I}{I_{\text{sat}}} + 4\left(\frac{\delta + kv}{\Gamma}\right)^2}\right]. \end{aligned} \tag{4.6}$$

The $2I/I_{\text{sat}}$ term in the denominator accounts for the fact that two beams, each of intensity I, are now contributing to the saturation of the transition. In the regime where the Doppler shift is much less than a linewidth [159] we may approximate the molasses force as

$$F_{\text{molasses}} \approx \frac{8\hbar k^2\delta}{\Gamma}\frac{I/I_{\text{sat}}}{\left(1 + 2I/I_{\text{sat}} + 4(\delta/\Gamma)^2\right)^2}v = -\alpha v, \tag{4.7}$$

where α is the damping coefficient. When the laser is red detuned from resonance, F_{molasses} opposes the direction of atomic motion; the force is frictional in nature, compressing the velocity distribution and cooling the gas. Figure 4.1 shows the net force exerted by a pair of counter-propagating laser beams on a moving atom in the circumstances described above.

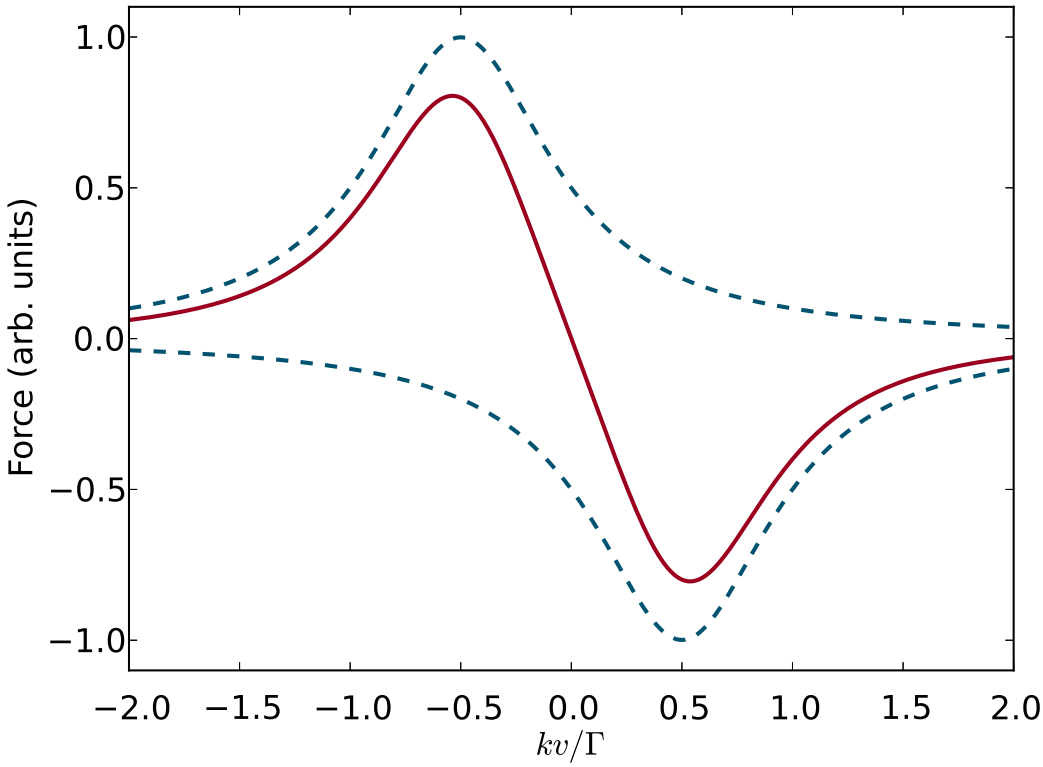

Figure 4.1: The red curve shows the net force exerted on an atom moving at a velocity of v by two counter-propagating laser beams detuned from resonance by $\delta = -\Gamma/2$. The case shown is for where $I/I_{\text{sat}} \ll 1$. The dashed blue curves show the force due to the individual laser beams. When the atom has a positive velocity, the force is negative (and vice-versa), the effect being frictional force acting against the atom's motion.

4.1.2 Doppler theory

The above is a description of optical molasses in one dimension. The treatment can be generalised to N dimensions by including the saturation induced by all the beams in the denominator of the damping coefficient, so that equation 4.7 becomes

$$\alpha_{3\text{D}} = -\frac{8\hbar k^2 \delta}{\Gamma} \frac{I/I_{\text{sat}}}{\left(1 + 2NI/I_{\text{sat}} + 4\left(\delta/\Gamma\right)^2\right)^2}. \tag{4.8}$$

It must be noted that this is only an approximation since it does not include the possibility that a photon may be absorbed from one laser beam, followed by the stimulated emission into another beam. A more complete description can be found in reference [161].

Whilst the damping force leads to a cooling rate of $-\alpha v^2$ there is also heating due to the random nature of the spontaneous emission, where each momentum kick of $\hbar k$ is part of a random walk in momentum space. Thus, after each step the mean square momentum grows by $\hbar^2 k^2$ [162]. The rate of change of the mean square momentum is given by

$$\frac{d\langle p^2\rangle}{dt} = 2\hbar^2 k^2 R = 2\mathscr{D}_p, \tag{4.9}$$

where we have defined a momentum diffusion coefficient, $\mathscr{D}_p$. This diffusion leads to a heating rate of $\hbar^2 k^2 R/m = \mathscr{D}_p/m$, where the scattering rate for N dimensions is now

$$R = \frac{\Gamma}{2}\frac{2NI/I_{\text{sat}}}{1 + 2NI/I_{\text{sat}} + 4\delta^2/\Gamma^2}. \tag{4.10}$$

At equilibrium the heating and cooling rates cancel and we may use the equipartition theorem [162] to define the thermal energy of gas of atoms, the result being

$$k_{\text{B}}T = \frac{\mathscr{D}_p}{3\alpha_{3\text{D}}} = \frac{\hbar\Gamma_P^2}{8|\delta|}\left(1 + 4\frac{\delta^2}{\Gamma_P^2}\right), \tag{4.11}$$

where k_{B} is Bolztmann's constant, T is the temperature, and $\Gamma_P = \Gamma\sqrt{1 + 6I/I_{\text{sat}}}$ is the power broadened linewidth for three dimensions (six beams, each of intensity I). For a given laser intensity this expression is minimised to $T_{\text{min}} = \hbar\Gamma_P/2k_{\text{B}}$ when the detuning is $\delta = -\Gamma_P/2$. In the case that $I/I_{\text{sat}} \ll 1$ we obtain the lowest temperature that can be achieved using Doppler cooling, the Doppler temperature [160]

$$T_{\text{D}} = \frac{\hbar\Gamma}{2k_{\text{B}}}. \tag{4.12}$$

The Doppler temperatures for the two Yb cooling transitions and the Cs cooling transition can be seen in table 4.1.

4.1.3 The magneto-optical trap

Without a spatially dependent force, the atoms cooled by the molasses force are not trapped. However, by introducing a magnetic quadrupole field centred on the intersection of the six laser beams, it is possible to engineer such a trapping force. Magnetic quadrupole fields are often produced using two coils positioned in the anti-Helmholtz configuration. In such a configuration, the magnetic field strength, B, cancels at the point between the two coils. Close to this point there is a uniform field gradient obeying

$$\frac{dB_x}{dx} = \frac{dB_y}{dy} = \frac{1}{2}\frac{dB_z}{dz}, \tag{4.13}$$

where z is the axis defined by the axial field direction of the coils, and x and y are the radial directions.

If we consider a simple $J = 0$ to $J = 1$ transition for the cooling cycle, then, in the region of low magnetic field strength about the field zero, the energy of the $m_J = 0, \pm 1$ magnetic sublevels will vary linearly with the magnetic field in space. By carefully choosing the correct handedness of circular polarisation for each of the six MOT beams, this spatially dependent Zeeman shift has the effect of the atoms being preferentially pushed towards the trap centre. Equation 4.6 is then modified to account for the Zeeman effect to give a net force of

$$\begin{aligned} \vec{F}(\vec{v},\vec{x}) &= \frac{\hbar\vec{k}\Gamma}{2}\frac{I/I_{\text{sat}}}{1 + I/I_{\text{sat}} + 4\left(\delta - \vec{k}\cdot\vec{v} - \mu\frac{d\vec{B}}{dx}\cdot\vec{x}\right)^2/\Gamma^2} \\ &- \frac{\hbar\vec{k}\Gamma}{2}\frac{I/I_{\text{sat}}}{1 + I/I_{\text{sat}} + 4\left(\delta + \vec{k}\cdot\vec{v} + \mu\frac{d\vec{B}}{dx}\cdot\vec{x}\right)^2/\Gamma^2}, \end{aligned} \tag{4.14}$$

where $\vec{x}$ is the position of the atom, $\mu = g_J\mu_{\text{B}}/\hbar$ is the effective magnetic moment the transition, g_J is the Lande g-factor, and μ_{B} is the Bohr magneton. This gives a restoring force in addition to the frictional force provided by optical molasses.

4.1.4 The capture velocity

It is clear from equation 4.14 that in the limit $I/I_{\text{sat}} \to \infty$, and when the laser is resonant with an atom, there exists a maximum acceleration that the atom can experience (from a single laser beam), given by

$$a_{\text{max}} = \frac{\hbar k \Gamma}{2m}. \tag{4.15}$$

If the MOT beams have a diameter, D, this can be used to give an upper limit on the capture velocity of the MOT; the maximum velocity an atom can have upon entering the MOT region and still be retained, where

$$v_{\text{c}} = \sqrt{a_{\text{max}} D}. \tag{4.16}$$

This is an upper limit as the expression doesn't incorporate decays to states outside the cooling cycle. It also makes the assumption that the atom remains on resonance across the entire trapping region. Nonetheless, it is a good rule of thumb.

Transition	λ (nm)	a_{max} (m s^{-2})	v_{c} (m s^{-1})	T_{D} (μK)
Cs: $6\,^2S_{1/2} \to 6\,^2P_{3/2}$	852.3	5.79×10^4	33.9	126
Yb: $6s^2\,^1S_0 \to 6s\,6p\,^1P_1$	398.9	5.06×10^5	100	673
Yb: $6s^2\,^1S_0 \to 6s\,6p\,^3P_1$	555.8	2.36×10^3	6.87	4.4

Table 4.1: A table summarising the key properties of MOTs of Cs and Yb for the transitions used in this apparatus. The capture velocity, v_{c}, has been calculated using equation 4.16 with a beam diameter of 20 mm.

Table 4.1 shows the relevant properties of MOTs of Yb and Cs using the available transitions. Cs only has one viable cooling transition - the $F = 4 \to F' = 5$ transition of the D_2 line. This transition has a good capture velocity for loading atoms into the MOT but has a relatively high Doppler temperature. However, Cs has the advantage of having hyperfine structure in its ground state, leading to sub-Doppler cooling during molasses. This mechanism has led to molasses of Cs with temperatures lower than ~ 10 μK being produced [163–165].

The Doppler theory discussed in section 4.1.2 should provide the ideal description of the temperature of a MOT of bosonic Yb: the available cooling transitions are of the form $J = 0 \rightarrow J' = 1$. The choice in MOT transition is between the 398.9 nm singlet transition from the ground state to the $^1\mathrm{P}_1$ state, or the 555.8 nm triplet transition from the ground state to the $^3\mathrm{P}_1$ state. At first glance, the singlet transition seems ideal for producing a MOT, with a large capture velocity and maximum acceleration. However, with no available sub-Doppler cooling mechanisms for this transition, the lower limit to the temperature is the Doppler temperature of 673 μK. This is vastly different to the expected Cs molasses temperature, and will be problematic for loading into an optical dipole trap later in the experimental sequence. An additional problem is that the $^1P_1$ state has a finite branching ratio to the $^3D_2$ and $^3D_1$ states: the cooling transition is not completely closed, limiting the lifetime of atoms in the MOT [110, 111]. The triplet $^1S_0 \rightarrow {}^3P_1$ transition has the advantage of being very narrow ($2\pi \times 180$ kHz), leading to a much lower Doppler temperature of 4.4 μK. However, the associated capture velocity for the transition is only 6.87 $\mathrm{m\,s^{-1}}$, even for a relatively large MOT beam diameter of 20 mm. This poses a problem; it is clear that the ideal situation would be to cool Yb using the triplet transition, yet the high temperature required to produce a significant vapour pressure of Yb means that a relatively low proportion of atoms will travel at a speed below the capture velocity of the MOT. One solution would be to load a singlet MOT from fast Yb, followed by transferring trapped Yb to a triplet MOT. However, a more elegant solution is to produce a slow Yb beam that can be trapped directly by a triplet MOT; a solution first implemented by the Kyoto group in 1999 [130].

4.2 Zeeman slowing of Yb

4.2.1 Ideal Zeeman slower theory

The most common approach for creating a MOT of Yb is to use a Zeeman slower in conjunction with an effusive oven, although other techniques such as a 2D MOT [117] and a thermal source [118] have also been used. In order

to load directly into a MOT on the triplet transition the atoms must be at a velocity below $v_c \approx 7\ \mathrm{m\,s^{-1}}$. The atoms must also not travel too slowly, as they will then fall too far under gravity prior to reaching the trapping region. For the geometry of our apparatus this lower limit is about $3\ \mathrm{m\,s^{-1}}$.

A Zeeman slower makes use of the scattering force in a similar way to a MOT, however in this method the atoms are only slowed in one direction, hence the necessity for a well-collimated atomic beam. For the Zeeman slower we elect to use the 398.9 nm transition since $a_{\max}$ is two orders of magnitude larger than for the 555.8 nm transition (see table 4.1), thus requiring a shorter Zeeman slower. We have seen previously that the maximum acceleration due to a resonant laser beam with $I \gg I_{\mathrm{sat}}$ is given by equation 4.15. Our Yb oven produces an atomic beam with a velocity of around $300\ \mathrm{m\,s^{-1}}$, meaning that at least 5.2×10^4 photons must be scattered for the average atom to be decelerated to a standstill. However, the linewidth of $2\pi \times 28$ MHz is equivalent to the Doppler shift for a Yb atom moving at just $11\ \mathrm{m\,s^{-1}}$: the atoms will be shifted out of resonance after only 1.9×10^3 scattering events. A Zeeman slower makes use of a magnetic field to cancel the Doppler shift of the laser frequency with the Zeeman shifted transition frequency. In the frame of the atom, the effective detuning, δ_z, at any velocity, v, at position, z, is then

$$\delta_z(z, v) = \delta + kv(z) + \mu B(z)/\hbar, \tag{4.17}$$

where δ is once again the detuning of the laser in the lab frame, and μ is the effective magnetic moment of the slowing transition. The resonance condition for a Zeeman slower is then that $\delta_z = 0$ at all points along the slower, which leads to a magnetic field profile of the form

$$B(z) = -\frac{\hbar}{\mu}\left[\delta + kv(z)\right]. \tag{4.18}$$

We assume a constant acceleration along the Zeeman slower of the form

$$a = \eta a_{\max}, \tag{4.19}$$

where η is the fraction of the maximum possible acceleration of the slower. It should be noted that this fraction is set by the laser intensity

$$\eta = \frac{I/I_{\text{sat}}}{1 + I/I_{\text{sat}}}. \tag{4.20}$$

It follows from Newton's laws that the velocity along the slower will take the form

$$v = \sqrt{v_0^2 - 2az} = v_0\sqrt{1 - z/L}, \tag{4.21}$$

where v_0 is the capture velocity of the Zeeman slower: the velocity above which atoms are not decelerated by the slower, and below which all atoms may be decelerated. Those atoms travelling with an initial velocity, u, that is less than v_0 will not be resonant with the laser beam, and will continue to travel unperturbed until they approach a distance $z = L\left[1 - (u/v_0)^2\right]$, at which point the atoms are resonant with the laser light. It can be seen from equations 4.19 to 4.21 that the choice of η determines the length, L, of the slower required for the atoms to come to rest where

$$L = \frac{v_0^2}{2a} = \frac{v_0^2}{2\eta a_{\text{max}}}. \tag{4.22}$$

Combining equation 4.22 with equations 4.21 and 4.18 then gives the magnetic field profile required for the Zeeman slower to maintain constant deceleration along its length for the laser intensity defined by η

$$B(z) = -\frac{\hbar}{\mu}\left(\delta + kv_0\sqrt{1 - z/L}\right) = B_0 + B_L\sqrt{1 - z/L}. \tag{4.23}$$

This equations shows that, over the length of the Zeeman slower, the field must change by an amount $B_L = -\hbar k v_0/\mu$. Note that the field may increase or decrease depending on the sign of μ. The term $B_0 = -\hbar\delta/\mu$ is a constant offset to the field determined by the laser detuning and μ, and corresponds to the magnetic field at the point where $z = L$.

4.2.2 Practical considerations

It is important to note that Zeeman slowers are not typically used to bring atoms to a standstill, but to decelerate the atoms to speeds that are within the MOT capture velocity. In our case this is an Yb velocity of between 3 and 7 $\mathrm{m\,s^{-1}}$ as discussed above. For Cs the capture velocity is typically 40 $\mathrm{m\,s^{-1}}$ and so the Zeeman slower release velocity is not so critical compared to that for Yb. Theoretically, the point along the slower at which the photon scattering is turned off defines the release velocity, v_{rel}. For example, if the magnetic field profile is truncated at a point $z_{\mathrm{rel}} = L\left[1 - (v_{\mathrm{rel}}/v_0)^2\right]$, then the atoms will be out of resonance with the laser beam and will continue at a velocity of v_{rel}. In practice it is impossible to engineer a perfectly sharp drop off in magnetic field, the gradual decay of the field towards zero means that atoms will continue to scatter photons for a finite time, and therefore the position at which the field is truncated needs to occur slightly further upstream than the value of z_{rel}.

The extent to which the end of the magnetic field profile must be tailored can be lessened by choosing $B_0 = 0$ as then a sharp change in the magnetic field is not required. However, this highlights a further problem: when B_0 is set to zero, then δ must also be zero. Since the Zeeman slower laser beam invariably goes through the MOT trapping region, this would cause significant pushing and heating of the atoms trapped in the MOT [166–168]. This is particularly problematic for Yb in a 555.8 nm MOT, where the trapping transition is very narrow.

The solution we have adopted is to use a zero crossing Zeeman slower, which is often called a spin-flip Zeeman slower in the case of the alkali elements. Matching v_0 to the mean Yb exit velocity of the effusive oven ($300\mathrm{m\,s^{-1}}$) requires a total magnetic field change of $B_L = 537$ G. The zero crossing field profile has an additional benefit: the large change in magnetic field can be split between two coils carrying current in the opposite sense, reducing the current required to produce the field profile. Since the linewidth of the 398.9 nm transition is 28 MHz, the detuning required to reduce the pushing and heating of the MOT is large. We elect to use a detuning in the region of -600 MHz, this corresponds to a magnetic field of 435 G at the release

position. Since the radial magnetic field gradient for a 555.8 nm Yb MOT is typically 1.5 $\mathrm{G\,cm^{-1}}$ it is crucial that the field profile is well nulled over the distance of 7.5 cm between the Zeeman slower exit and the MOT.

Given that the shape of the magnetic field profile required to slow any species is the same, with only B_L changing, it is possible for a single slower to decelerate multiple species. Of course this is only valid provided the length of the slower is long enough for η to be below a value of 1. Typically L is chosen so that η remains less than a value of 0.67, this allows some headroom against fluctuations away from the ideal configuration. Examples of these fluctuations include deviations from the designed field profile, photon shot noise, and laser intensity variations. If the local value of η is greater than 1 at any point along the slower, then atoms are lost from the deceleration process. Given that the mean exit velocity of Cs from the dual species oven is around 240 $\mathrm{m\,s^{-1}}$ we elect to build a slower that is 0.7 m long. This leads to a value of $\eta_{\mathrm{Cs}} = 0.5$, giving plenty of headroom against real-world fluctuations. A slower of this length gives $\eta_{\mathrm{Yb}} = 0.128$, meaning a 398.9 nm laser intensity of only 0.15 I/I_{sat} is required. It is possible to use a compromise field profile to slow some pairs of elements simultaneously [119], however this typically requires the ratio of the individual values of η to lie between 0.5 and 2. Thus, it is not ideal to load a MOT of Yb and Cs simultaneously from a single Zeeman slower. Instead we choose to switch the currents in the slower and load the MOTs sequentially.

For Cs the main complication is the multi-level structure of the D_2 transitions. The design of the Zeeman slower means that prior to the zero crossing the atoms are slowed on the $|F = 4, m_F = 4\rangle \rightarrow |F' = 5, m'_F = 5\rangle$ transition in the so-called σ^+ configuration. Following the zero crossing the atoms are slowed on the $|F = 4, m_F = -4\rangle \rightarrow |F' = 5, m'_F = -5\rangle$ transition in the σ^- configuration. Zeeman slowers in the σ^- configuration typically have the advantage that a large laser detuning is required as the atoms reach the exit of the slower in order to maintain the deceleration [166]. The disadvantage of using a purely σ^- slower in Cs is that, at magnetic fields of around 60 G, the Zeeman shift leads to the $|F' = 5, m'_F = -5\rangle$ state crossing the $F' = 4$ manifold, thus leading to large losses as atoms have an increased probability of being lost to the dark $F = 3$ ground state via the $F' = 4$ states. Figure 4.2

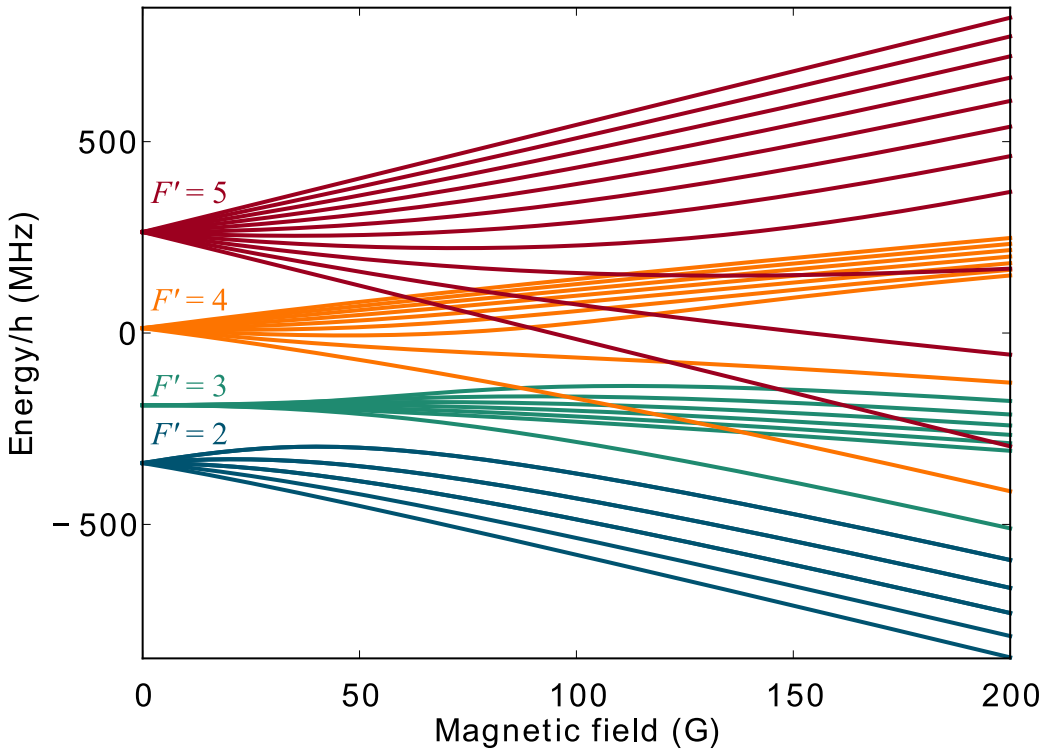

Figure 4.2: A Breit-Rabi diagram showing the Zeeman splitting of the $^2P_{3/2}$ state in Cs. The states are colour coded according to the F' manifold from which they originate. Of particular note is the crossing of the $|F' = 5, m'_F = -5\rangle$ state crossing the $F' = 4$ manifold at around 60 G.

shows a Breit-Rabi diagram of the $^2P_{3/2}$ state in Cs, illustrating the crossing of states at 60 G. To minimise this effect we ensure the zero crossing occurs towards the end of the Zeeman slower. To do so we set the laser detuning to be -50 MHz from the MOT cooling transition, ensuring perturbations of the MOT are minimised whilst loses via $F' = 4$ are minimised along the slower. Repumping is a complicated process in the Zeeman slower since the different Zeeman sublevels experience different frequency shifts along the slower, meaning that the repump light can only really be effective at the zero crossing and prior to the start of the Zeeman slower. We find that (2.8 ± 0.1) mW of repump light detuned by -50 MHz from the $F = 3 \rightarrow F' = 4$ transition optimises the slower. This detuning also corresponds to the expected Doppler shift of atoms in the zero crossing of the slower.

4.2.3 Zeeman slower design

With all of the above considerations in mind, a design summarised by the properties in table 4.2 was chosen. To generate these fields our design features hundreds of amp-turns. Designs utilising an array of permanent magnets [169] or windings of variable pitch [170] have also been used by other groups. The desired field profile is generated using five separate coils. A solenoid spanning the entire length of the slower is used to provide a magnetic field offset in order to match field profile to the chosen laser detunings for Yb and Cs. A H-bridge switch is used in order to reverse the direction of current flow within the coil. The overall shape of the field is provided by coils 1 and 2: these are two coils that are run in series but the current handedness is reversed between the two. Coils 3 and 4 are positioned at the end of the Zeeman slower, and are used with high currents in order to provide a sharp drop off in magnetic field prior to the MOT trapping region. The individual coils and their constituent turns are shown in figure 4.3 and the currents at which they are run for Cs and for Yb are summarised in table 4.3.

Property	Cs	Yb
Length, L (m)	0.7	0.7
Deceleration parameter, η	0.5	0.128
Capture velocity, v_0 ($\mathrm{m\,s^{-1}}$)	200	300
Magnetic field span, B_L (G)	167	537
Magnetic field offset, B_0 (G)	42	435
Detuning, δ (MHz)	59	609

Table 4.2: A table summarising the key properties of the dual species Zeeman slower, including the magnetic field profile and the corresponding detunings required. The values are shown for both Cs and Yb.

The Zeeman slower is wound in the following manner. The solenoid is first wound directly onto an 80 cm long steel former tube with an outer diameter of 38.1 mm. The solenoid consists of 177 turns using a 4.3×4.3 mm square cross section wire. This wire has a hollow bore running through it with a 2.75 mm diameter. This allows water to be used to cool the coil. The turns are wound by mounting the former tube in a lathe, which is turned

manually to spool wire onto the tube. As the turns are made the wire is coated with Araldite 2011. About 20 turns are added to the coil per day, with the solenoid being compressed axially overnight whilst the Araldite is allowed time to cure.

With the former tube still in the lathe, coils 1 and 2 are wound directly on top of the solenoid. These coils are made from a 3.08×1.19 mm cross section wire. Each of these coils are wound two layers at a time, starting from the middle of the Zeeman slower, where the trailing wire is clamped using toolmakers clamps and turns are wound towards one end of the slower. Here the wire is wound directly on top of the previous layer and the following windings are made back towards the middle of the slower. Following a curing time, the next pair of layers are wound on top of the previous layer. Once all layers have been wound, the layers or turns are then connected externally to create one continuous coil.

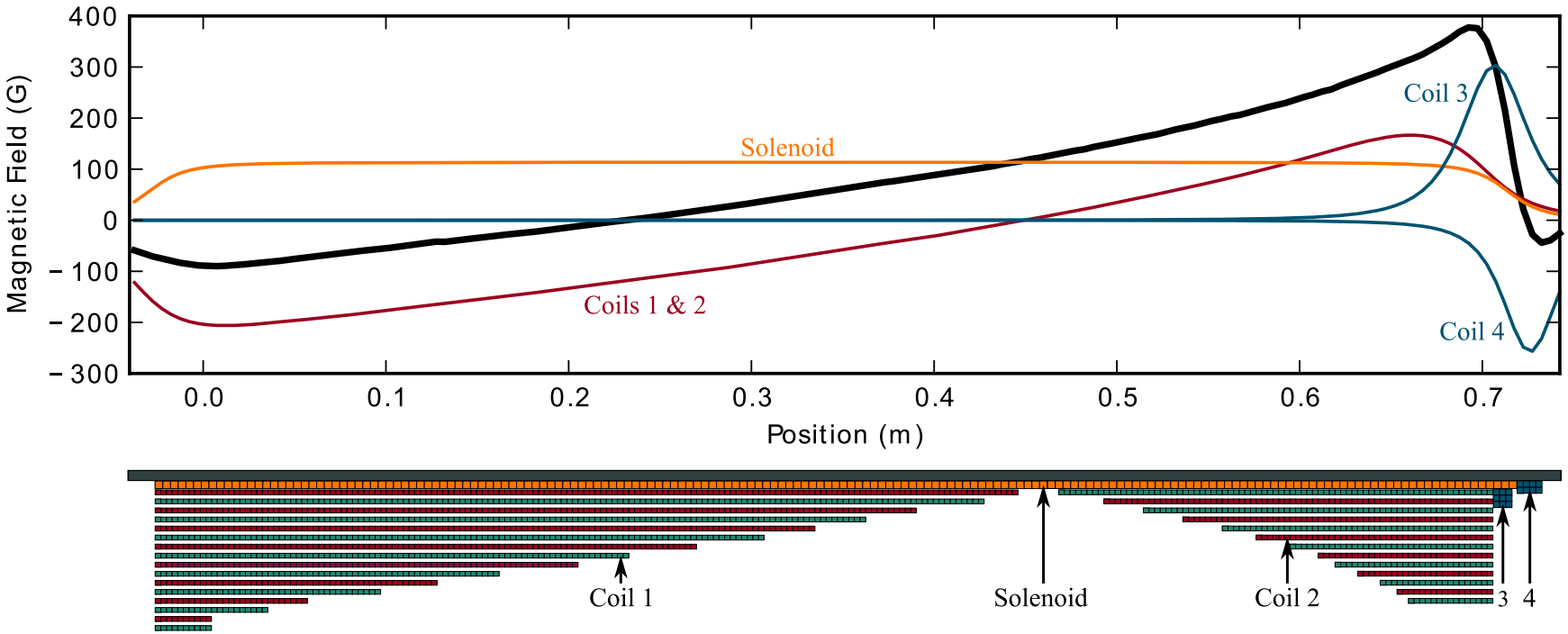

Figure 4.3: Plot showing the designed field profile of the Zeeman slower when running Yb currents (black curve). The position scale starts at the beginning of the ideal Zeeman slower profile. The lower part of the figure shows the designed coil windings of the Zeeman slower. The steel former tube is shown in grey. Turns made using the 4.3×4.3 mm cross section wire are shown in orange, those made using the 3.4×3.4 mm cross section wire are shown in blue, and those made from the 3.08×1.19 mm cross section wire are shown in red and teal. Those in red are wound from right to left from the viewport of the figure, those in teal are wound from left to right. The coloured curves in the main plot show the field produced by the individual coils, with the colours corresponding to the wire type in the schematic. The coils are labelled as they are described in this chapter.

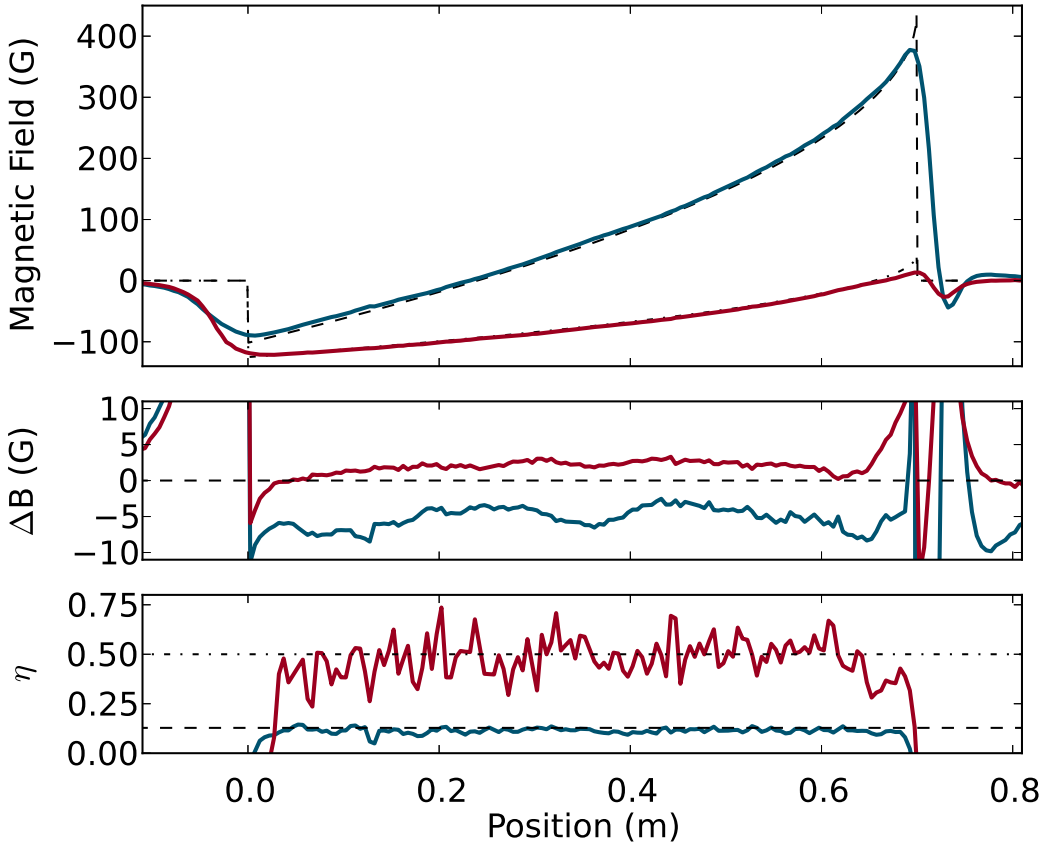

Figure 4.4: The top plot shows the axial magnetic field profile produced by the Zeeman slower when running in the Cs configuration (red solid curve) and the Yb configuration (blue solid curve). The dashed black curves show the field profile required by the ideal Zeeman slower theory. The middle plot shows the residuals of the measured field profiles from the ideal profiles, revealing small field offsets for each element. The bottom plot shows the experimentally determined value of η for each species, with the target values shown as dashed lines.

Coils 3 and 4 are wound using 3.4×3.4 mm cross section wire. This wire has a 2 mm diameter cooling channel. These coils are wound in their own formers that are mounted on the lathe. Coil 3 is then placed over the solenoid and secured using Araldite. This coil is positioned to be immediately adjacent to coil 2. Coil 4 is positioned next to the end of the solenoid and is secured directly to the former tube using Araldite.

An axial Hall probe is used to measure and fine tune the magnetic field profile produced by the Zeeman slower prior to the vacuum system being assembled. The field produced by each layer pair of coils 1 and 2 is tested and compared to the designed field profile. Turns are then added or removed

Coil	Cs Current (A)	Yb Current (A)
Solenoid	-20.5	38
Coils 1 & 2	1.25	3.95
Coil 3	28.1	149
Coil 4	23	121

Table 4.3: A table showing the currents at which the individual coils of the Zeeman slower are run. Shown are the currents used for slowing Cs and those for slowing Yb.

in order to tailor the field profile. The top plot of figure 4.4 shows the total magnetic field profile produced by the Zeeman slower when running with the Yb currents (blue curve) and Cs currents (red curve). The middle plot shows the residuals of the measured profiles from the ideal theory (shown as dashed lines in the top plot). For each species there is a small offset from the ideal profile along the tapered part of the the Zeeman slower. This offset is ~ 2 G for Cs, and ~ 5 G for Yb. These offsets are corrected for by the fine tuning of the solenoid current.

It is difficult to quantify how well a Zeeman slower will perform using the field profile alone. By differentiation of equation 4.23 and substituting equations 4.15 and 4.22 it is possible to show that, for an ideal slower, η must be related to the field profile by [169]

$$\eta = \frac{I/I_{\text{sat}}}{1 + I/I_{\text{sat}}} = -\frac{2m\mu}{\hbar^2 k^3 \Gamma}\left(\frac{\mu B}{\hbar} - \delta\right). \tag{4.24}$$

This relation must hold along the capture trajectory of the slower: the phase space trajectory followed by an atom entering the slower at a velocity of v_0. The expression shows that there exists an exact balance of laser intensity and magnetic field gradient for an atom travelling at the maximum velocity that can be decelerated by the slower. The consequence of this is that local deviations in the "wrong" direction for any of these parameters can result in insufficient local deceleration, causing atoms to escape the capture trajectory. Many real-world effects can cause such deviations: changes in laser intensity due to the Gaussian beam profile, increases in velocity from Poissonian noise,

and residual fields are three principal causes.

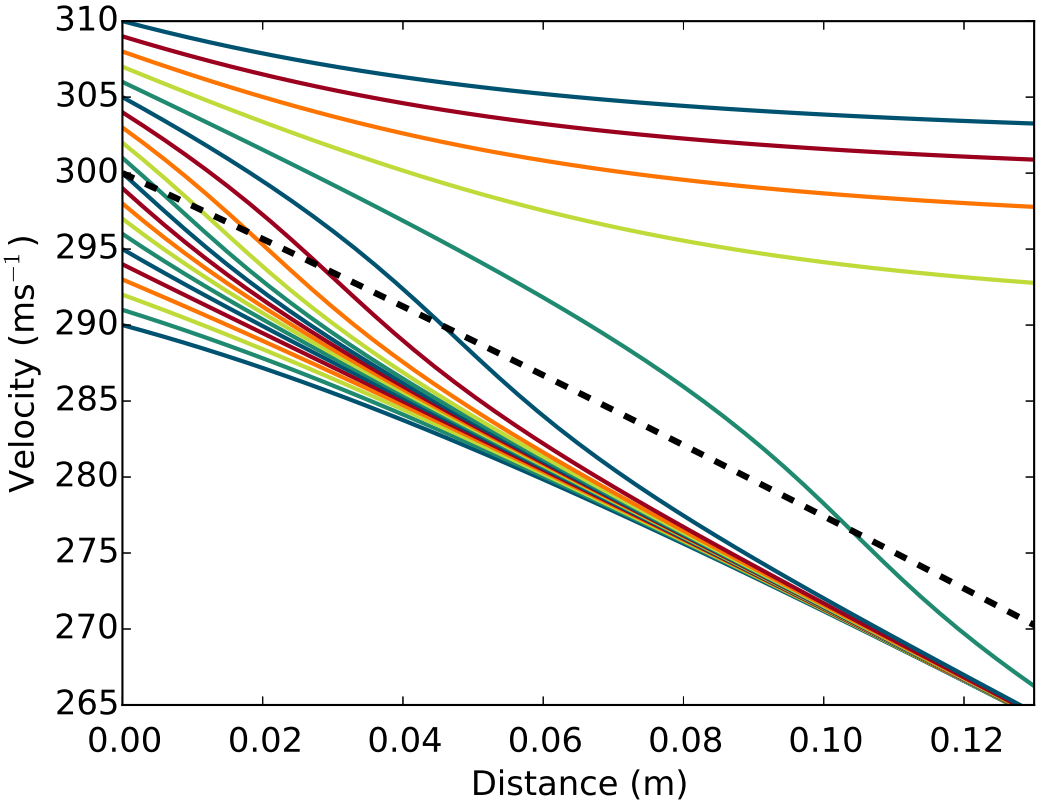

Figure 4.5: Atoms enter a Zeeman slower at a position of 0 m, where the Zeeman slower has a laser intensity higher than that defined by the value of η. In this example the intensity chosen fixes the offset, ϵ, at 6.3 m s^{-1}. Shown are velocity curves for 21 atoms entering the Zeeman slower, each with a different initial velocity, u. The dashed black curve shows the expected velocity for an atom entering the slower at the capture velocity of 300 m s^{-1}, as defined by equation 4.21.

The most effective solution to give headroom above such deviations is to increase the laser power above that defined by η whilst keeping the magnetic field profile the same. References [171, 172] originally derived the following ideas, and they were expanded upon by references [167, 173]. We consider the above scenario with a new saturation parameter, s', such that $s' > s$, where $s = I/I_{\text{sat}}$ is the saturation parameter defined by η in equation 4.24. This simple change increases the deceleration experienced by the atoms and leads to them following a stable trajectory along the slower. However, this is a cyclic process: by reducing the speed of the atom further than that defined by $B(z)$, the atom experiences a non-zero detuning, $\delta(z, v')$, and so

the atom starts to converge onto the original trajectory at which point it again experiences a greater-than-designed deceleration.

Intuitively one would expect these two effects to balance, such that the atom follows a new trajectory, $v'(z)$, which is offset below the original trajectory by a small amount

$$\epsilon(z) = v(z) - v'(z). \tag{4.25}$$

This idea is confirmed by our simulations; figure 4.5 shows the results of these simulations for atoms with 21 different initial velocities. It can be seen that, for the majority of the initial atom velocities, the atoms' velocities converge onto a velocity profile below and parallel to that of the ideal Zeeman slower. One can derive an analytic expression to this offset by taking equation 4.5 and inserting s' and the modified detuning $\delta = -k\epsilon$ from equation 4.17,

$$\frac{dv'}{dt} \equiv v'\frac{dv'}{dz} = -\frac{1}{1 + s' + 4(k\epsilon)^2/\Gamma^2} a_{\max}. \tag{4.26}$$

Using equations 4.25 and 4.26 we find

$$\epsilon = \frac{\Gamma}{2k}\left(\frac{s' - s}{s}\right)^{1/2}. \tag{4.27}$$

For more information on this derivation, see reference [174]. The increased saturation parameter, s', also means that atoms initially travelling at a velocity greater than the original capture velocity by an amount, ϵ, may also be decelerated. This effect is clearly seen in figure 4.5 where atoms entering the slower at velocities from 300 $\mathrm{m\,s^{-1}}$ to 306 $\mathrm{m\,s^{-1}}$ are decelerated and converge to the new velocity profile. The offset derived is enough to ensure the trajectory is stable: if the atom speeds up or hits a ripple in the magnetic field, it is shifted closer to resonance and is decelerated more; conversely, if the atom slows down it is decelerated less. The result of this is that the atom is always pushed back onto the new trajectory defined by the higher laser power. It is this mechanism that makes Zeeman slowers so robust.

4.3 Yb MOT loading

The setup for both the Cs and Yb MOT is the standard six-beam configuration. The cooling light is delivered to the experiment by means of three fibre coupled cage systems. Figure 4.6 shows the cage systems for the horizontal MOT beams for both Yb and Cs (viewed from above). There is one additional cage system below the science chamber for each of Cs and Yb; these vertical MOT beams are overlapped on a dichroic mirror before being directed through the re-entrant viewports of the science chamber. For Cs, the cage systems produce a collimated beam with a $1/e^2$ diameter of 18.0 ± 0.1 mm, whereas the Yb MOT beams have a diameter of 24.5 ± 0.2 mm. Generally, each cage system is followed by a quarter waveplate in order to create circularly polarised light of the correct handedness. The beams pass through the chamber, through a second quarter waveplate and are then retroreflected. In the case of the vertical MOT beams, the two wavelengths are first separated by a dichroic mirror before retroreflection in order to each pass through the appropriate quarter waveplate.

Figure 4.6 shows how the two imaging beams utilise the same viewports as two of the MOT beams. For Cs, PBS cubes are used to overlap and separate the beams before and after the chamber respectively, for Yb dichroic mirrors are used. In both instances the first lens for absorption imaging is placed in the MOT beam path. The Cs MOT beam that co-propagates with the imaging beam has a retroreflection mirror placed at the focus of the lens. In the case of Yb, a second lens is placed in the MOT beam in order to create a 1:1 telescope.

To load an Yb MOT, the Zeeman slower is set to the Yb currents shown in table 4.3, the shutter controlling the 399 nm Zeeman slowing beam, shown propagating from right to left in figure 4.6 is opened, and the MOT magnetic field gradient is set to the optimised value of 3.1 $\mathrm{G\,cm^{-1}}$. The atomic beam shutter in the vacuum system is rotated 45 ° and the MOT load is then recorded using fluorescence detection. We find that using the maximum amount of 556 nm light per MOT beam gives the best loading performance, typically around 15.0 ± 0.1 mW per beam. The optimum detuning is found to be -5.15 MHz as determined by the difference in frequency of the MOT

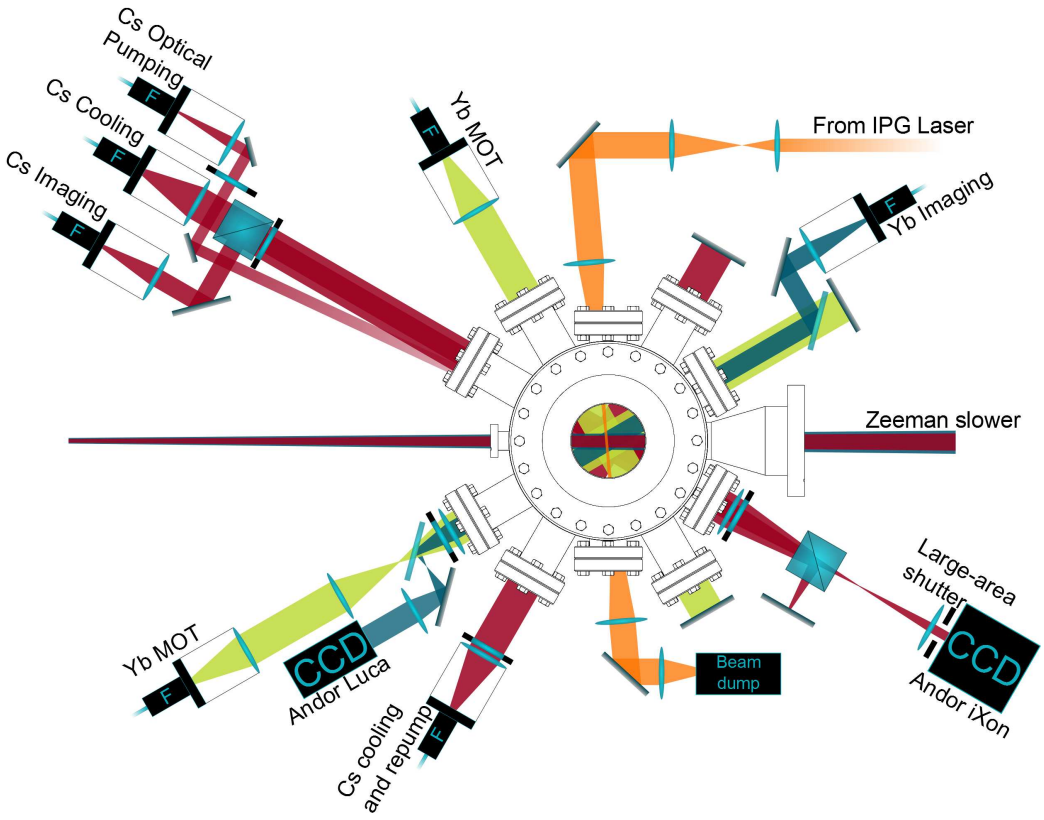

Figure 4.6: A schematic of the beams and optics on the science chamber breadboard. All of these beams pass horizontally through the science chamber. 852 nm light is shown in red, 556 nm light in green, 399 nm light in blue, and 1064 nm light in orange. The figure shows how the imaging beam for each species is overlapped and then split off from the MOT beams. The lenses located immediately before the CCD cameras may be changed to provide different magnifications for absorption imaging.

and spectroscopy AOMs shown in figure 2.7. However, it should be noted that this detuning is subject to an offset discussed below in section 4.5.

The magnetic field profile of the Zeeman slower was optimised incrementally by adjusting the current of each coil in turn. The loading performance was monitored by recording the average fluorescence signal from many MOT loads, each of a 3 s duration. This signal is proportional to the loading rate, which in turn depends on the flux of atoms arriving at the MOT with the capture velocity, thus giving a good measure of the Zeeman slower performance. Example measurements as each coil current is varied are shown in figure 4.7. The currents at which the peak load occurs are comparable to those in table 4.3 as predicted by our simulation during the design process.

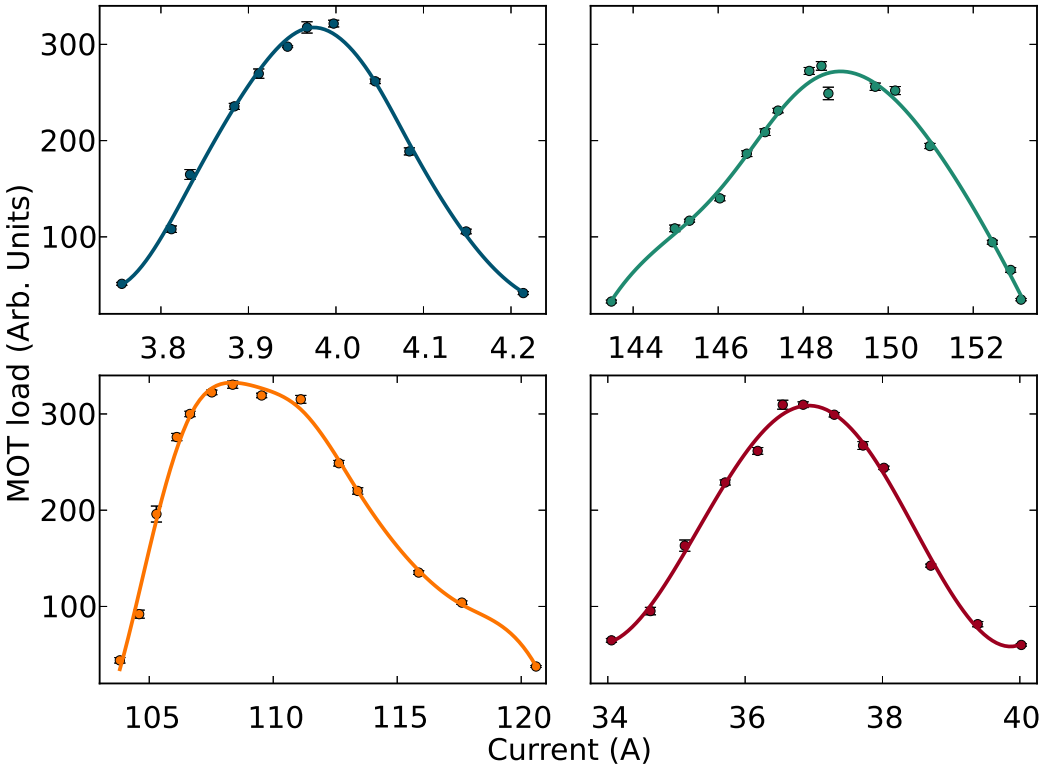

Figure 4.7: Plots showing the Yb MOT load as a function of the various Zeeman slower coil currents. The data shown is the average MOT fluorescence after 3 s loading time. The blue, teal, orange, and red data show the variation when changing the current in coils 1 and 2, coil 3, coil 4, and the solenoid respectively. The solid curves are guides to the eye only.

Figure 4.8 shows the effect of varying the detuning of the Yb Zeeman slower light for different intensities of the beam. For a given beam power there is a clear optimum in the detuning, and as the power of the beam increases the optimum detuning is further red detuned from resonance. This is very intuitive since the Zeeman slower requires a certain number of scattering events to bring the atoms within the capture velocity of the MOT: if there are too few photons scattered, the atoms will be too fast to be captured by the MOT; if there are too many, the atoms will drop under gravity prior to reaching the MOT. For a given power this fine control over the scattering rate is given by the detuning of the light. However, as discussed above, the power in the beam determines η for the Zeeman slower and hence we can expect the power in the beam to be the dominant factor for the loading rate, as evidenced by the high MOT loads at higher beam powers in figure 4.8. For peak loading performance we choose a power of 69 mW and a detuning

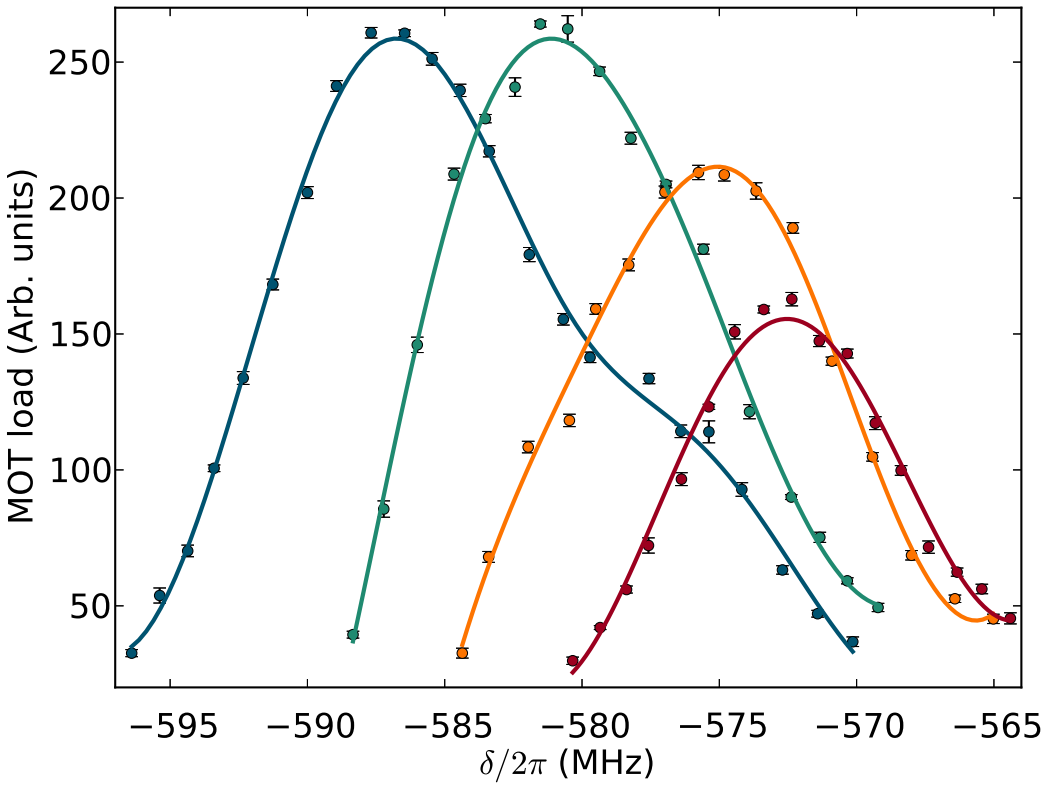

Figure 4.8: Plots showing the average Yb MOT atom number after a 3 s loading time as a function of Zeeman slower laser detuning. The red, orange, teal, and blue data show the loads for laser powers of 35 mW, 42.5 mW, 60.5 mW, and 69 mW respectively. The coloured solid curves are guides to the eye.

of -587.5 MHz from resonance.

Figure 4.9 offers further insight to the Zeeman slower behaviour. The MOT load is shown for different Zeeman slower beam powers at fixed detunings. This figure shows that when near the optimum detuning discussed above, the MOT load simply increases for the range of powers accessible. However, closer to resonance, as shown by the blue and orange curves, a peak load is reached before the MOT load starts to decrease as the amount of power is increased. This decrease is caused by the atoms becoming so slow that they drop below the trapping region as they traverse the distance between the exit of the slower and the MOT. Furthermore, the atoms still have a transverse velocity component. Despite efforts to minimise this through the collimation of the atomic beam, the transverse component can become dominant when the atoms are emerging from the slower at very slow axial velocities, again

causing the atoms to miss the trapping region.

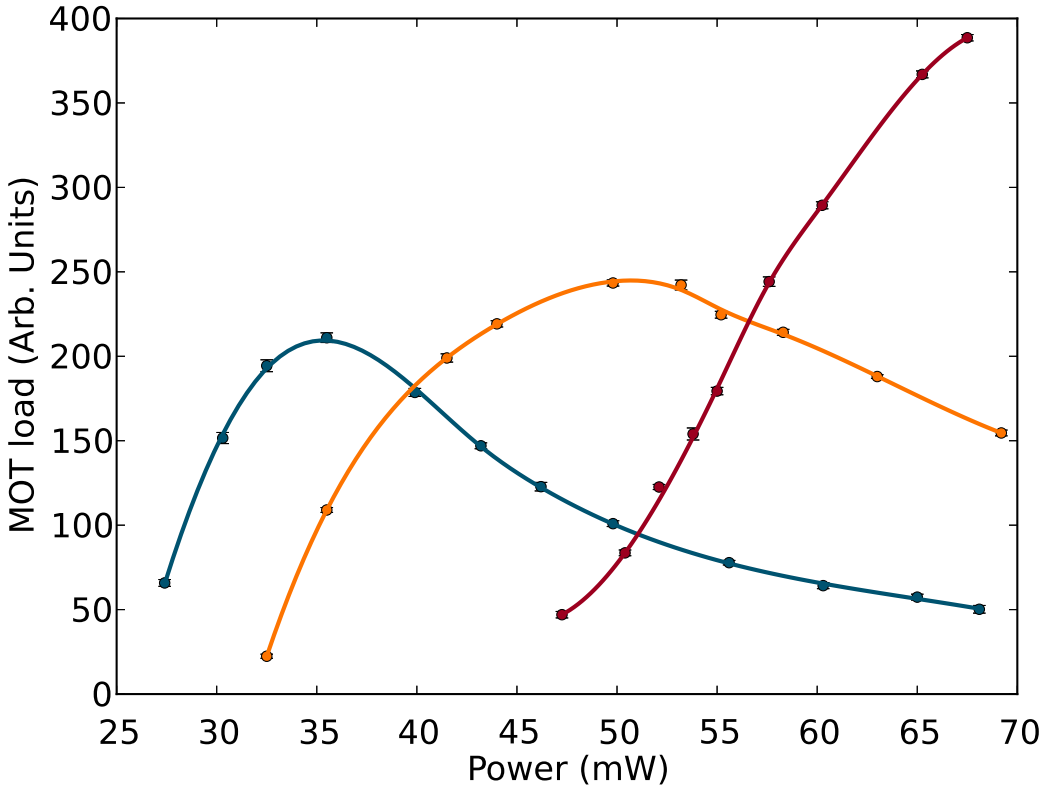

Figure 4.9: The loading rate of the Yb MOT typically increases when the Zeeman slower laser power is increased. However, at non-optimal detunings, a peak in the loading curve may be reached. This plot shows the loading rate of the MOT as a function of Zeeman beam powers for detunings of -571.3 MHz (blue data), -576.8 MHz (orange), and -587.0 MHz (red). For the two detunings closer to resonance a peak is observed in the loading rate, corresponding to atoms being slowed so much that the transverse spread of velocities upon leaving the slower becomes significant, or even causing atoms to be pushed back along the slower.

Following this optimisation process, we are able to load 3.7×10^9 Yb atoms into the MOT in a period of 40 s. The loading curve for this process, a fluorescence measurement calibrated to atom numbers from absorption imaging, is shown in figure 4.10. The loading curve is fit to a function of the form

$$N = \frac{R}{\gamma}\left[1 - \exp\left(-\gamma t\right)\right], \tag{4.28}$$

where N is the atom number, R is the loading rate, γ is the loss rate, and t is the time elapsed from the start of the MOT load [175]. From the fit

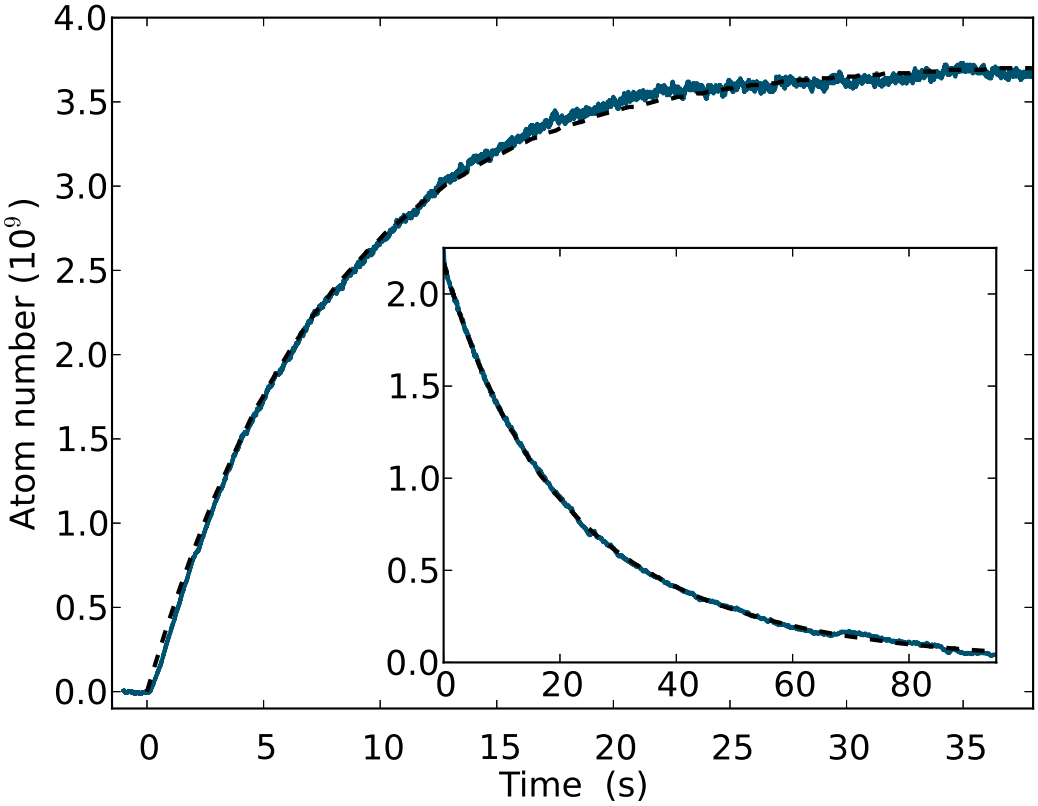

Figure 4.10: Optimised loading curves for the Yb MOT. The Yb MOT typically loads to a steady state of 3.7×10^9 atoms when the total beam intensity is 273 I_{sat} and the detuning is -5.15 MHz. The loading rate is 6.0×10^8 s^{-1}. The insets to the graph show the decay from the MOT when the source of atoms and Zeeman slower light is turned off. A single exponential fit to the Yb decay curve gives a lifetime of 28.50 ± 0.02 s.

we find $R = 6.0 \times 10^8$ s^{-1}. The high loading rate is due to the efficient loading rate from our tunable Zeeman slower [174] and using the full 15 mW of power per MOT beam: a single MOT beam of this intensity gives a power broadened linewidth of $\sim 40\ I/I_{\mathrm{sat}}$, increasing the capture velocity of the MOT. The inset to figure 4.10 shows the decay of the MOT fluorescence upon simultaneously turning off the MOT light and closing the atomic beam shutter. An exponential decay with a single characteristic decay rate is fit to the data to give a vacuum lifetime of 28.50 ± 0.02 s for this dataset.

4.3.1 Broadband Yb MOT loading

It has been reported that the artificial broadening of the MOT laser beam linewidth can increase the capture efficiency of an Yb MOT operating on the $^1S_0 \rightarrow {}^3P_1$ transition [130, 176]. This concept relies upon matching the frequency profile of the laser light to the Doppler broadened frequency profile of the atoms. This has the effect of increasing the capture velocity of the MOT. Figures 4.11 to 4.13 show the effects of broadening our MOT beams on the loading of the MOT. To broaden the light we sinusoidally modulate the MOT AOM using a function generator (Agilent E4421B), such that the resulting spectral profile is a comb where the modulation frequency gives the spacing of the comb.

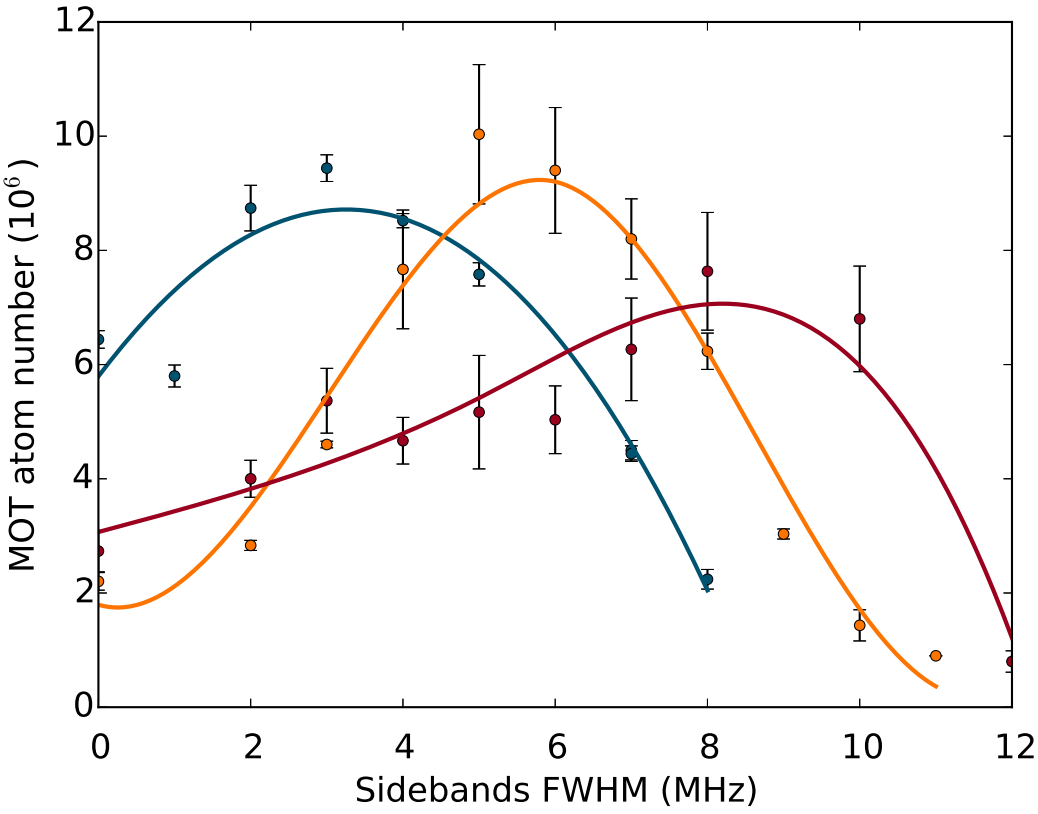

Figure 4.11: The atom number determined from absorption imaging after a 0.5 s atom load for a range of different MOT sideband FWHMs. The plot shows data for MOT detunings of -3 MHz (blue points), -5 MHz (orange), and -6 MHz (red). The solid curves are guides to the eye.

It is obvious that the setup described above offers a number of parameters to optimise: the MOT detuning, the linewidth of the broadened beams, and the

number of sidebands to name but a few. Here we present a brief account of the effect of the full width at half maximum (FWHM) of the sideband spectrum on the loading of the MOT. Clearly for each FWHM different numbers of sidebands will give the best results: if there are too many sidebands there will not be enough power in each sideband for it to make a considerable impact, if there are too few then there will be spatial regions in the MOT where few scattering events take place. Both of these extremes will reduce the MOT load. However, we find that this is only important for large sideband FWHM, which tend to be non-optimal.

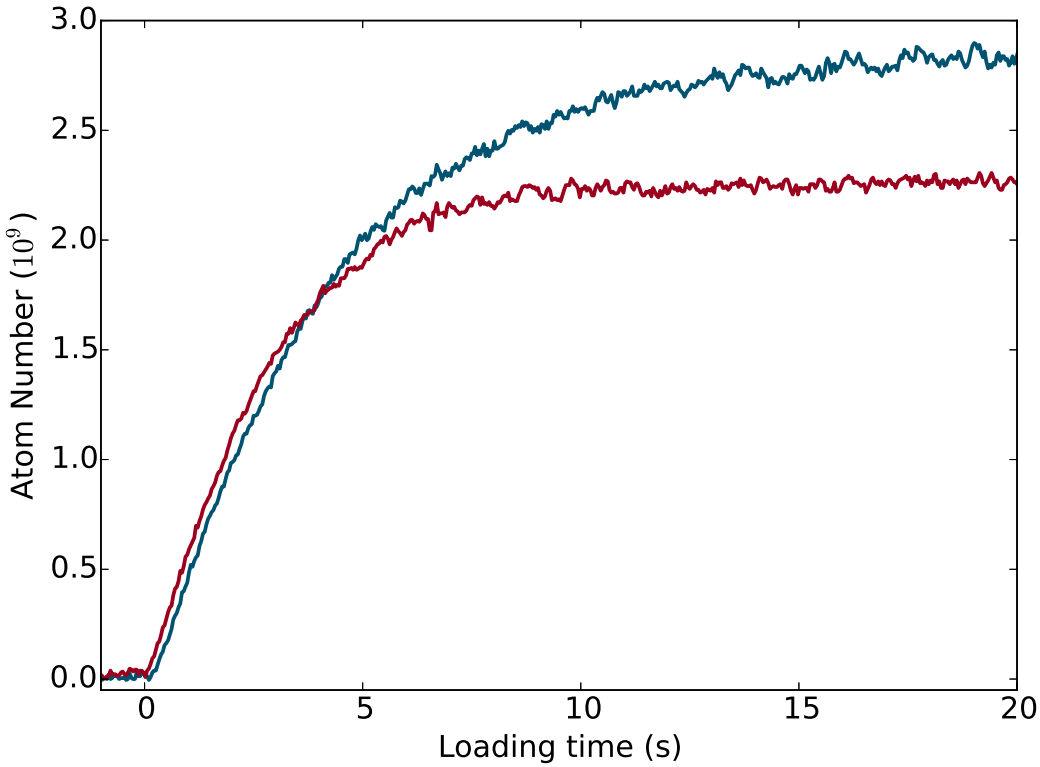

Figure 4.12: The loading curve in terms of MOT fluorescence for the case of no sidebands on the MOT beams (blue curve) and sidebands with a FWHM of 3 MHz (red curve). In both cases the MOT detuning was −5 MHz. Note that the fluorescence level with sidebands on the MOT beams has been calibrated separately using absorption imaging.

Figure 4.11 shows the effect of the sideband's FWHM on the atom number in the MOT after a 0.5 s loading time for a number of different MOT beam detunings. Here detuning refers to the central detuning of the MOT beam spectral profile. We typically find that the optimal sideband FWHM is equal to the magnitude of the MOT detuning. This is in line with optimum settings

in reference [117]. The absolute optimum for the parameter space observed is a sideband FWHM of 5 MHz for a MOT detuning of −5 MHz. In this case there are a factor of 5 more atoms captured by the MOT than if no sidebands are used. These parameters allow faster atoms to be captured by the MOT without significant heating of the trapped atoms. Increasing the FWHM beyond the optimum yields a sharp drop in atom number: some of the sidebands are close to, or even on, resonance, the result of which is significant heating and atom number loss.

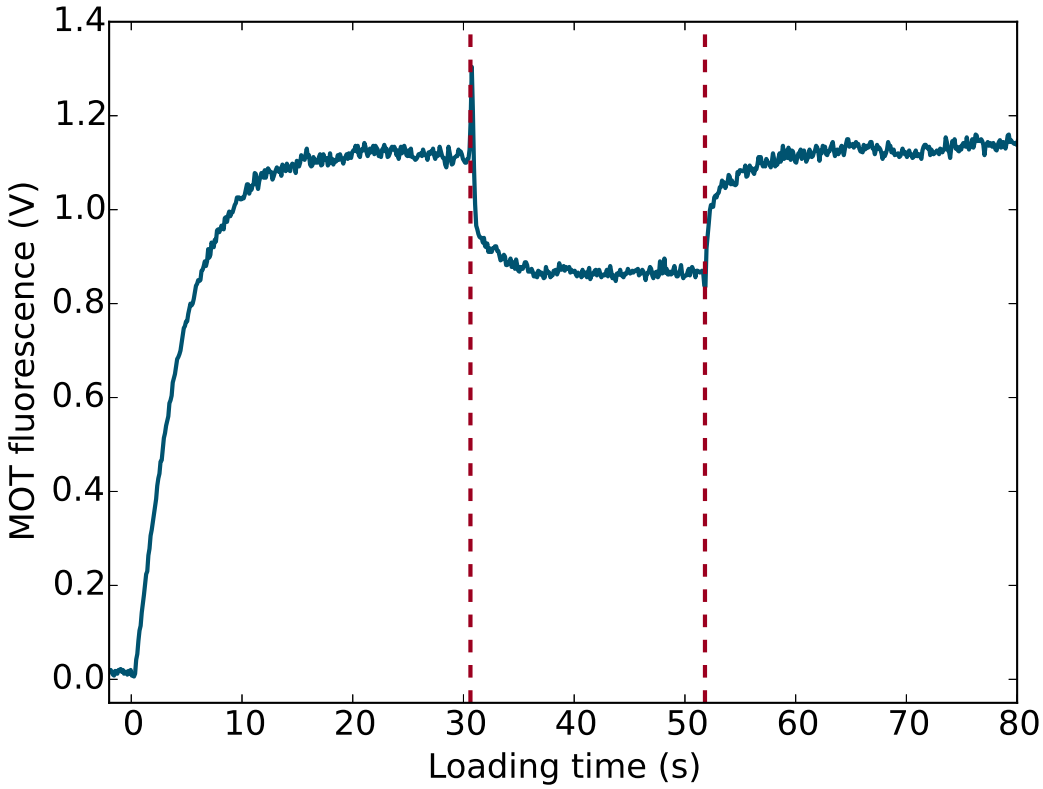

Figure 4.13: The loading of a standard MOT at an optimum detuning of −5 MHz with no sidebands is followed by turning on sidebands with a FWHM of 5 MHz. The time at which the sidebands are turned on is indicated by the first dashed vertical line. After stabilisation of the atom number in the MOT the sidebands are switched back off, as shown by the second dashed vertical line.

We also investigated the effect on the loading of the MOT for longer time periods at the settings that optimised the short term load. Figure 4.12 shows loading curves for Yb with and without the sidebands present on the MOT beams. As seen in figure 4.11, the loading rates are initially comparible with and without sidebands present on the MOT beams, however it is clear

that beyond a ~ 4 second loading time it is preferable to have no sidebands on the MOT beams if a large load is desired. It appears that whilst the sidebands increase the capture velocity of the MOT, they also increases the long term loses. This view is confirmed by figure 4.13 where the sidebands are only turned on after a 30 s MOT load (the point of which is shown by the first vertical line on the figure). At the instant of turning on the side bands there is a sharp increase in the fluorescence of the MOT followed by a decay. The instantaneous increase in fluorescence may be attributed to sidebands close to resonance causing increased photon scattering by the atoms close to the centre of the MOT. The decay that follows shows that the presence of sidebands is causing atoms to be lost from the trap. This is reaffirmed by turning the sidebands off: a loading curve follows the removal of sidebands from the MOT beams. This is in line with the findings of the Paris and Munich groups [177, 178] and it is possible that, as with these groups, sidebands are not needed due to the high power available in the cooling beams.

In light of these findings we have abandoned plans to use sidebands on the MOT light. For an experiment with a short duty cycle, sidebands would be a very useful feature, increasing the MOT loading by a factor of around 5. However, our experiment typically features a longer duty cycle where the maximum atom number is needed for transfer into the optical trap, and thus the extra complication is not necessary.

4.4 Yb MOT temperature

4.4.1 Comparison to standard Doppler theory

To measure the Yb MOT temperature, we first load the MOT for some time (typically 1 s) at the optimal loading settings discussed above. Following this, the atomic beam shutter is closed and the Zeeman slower light is turned off. Simultaneously the bias field along the Zeeman slowing axis is changed to compensate for the change in light forces induced by the Zeeman slowing beam, and hence keep the MOT stationary. The Zeeman slower magnetic field is then turned off and, once more, the bias field is adjusted to account

for the reduced residual field in the MOT location. These steps take a combined time of 100 ms. Then the MOT beam detuning, intensity, or both are ramped over a period of 200 ms to some final value, and is held at these settings for 100 ms. Finally, the MOT beams and the confining magnetic field gradient are switched off simultaneously, and the time of flight absorption imaging sequence discussed in section 2 begins. This is summarised as a timing diagram in figure 4.14.

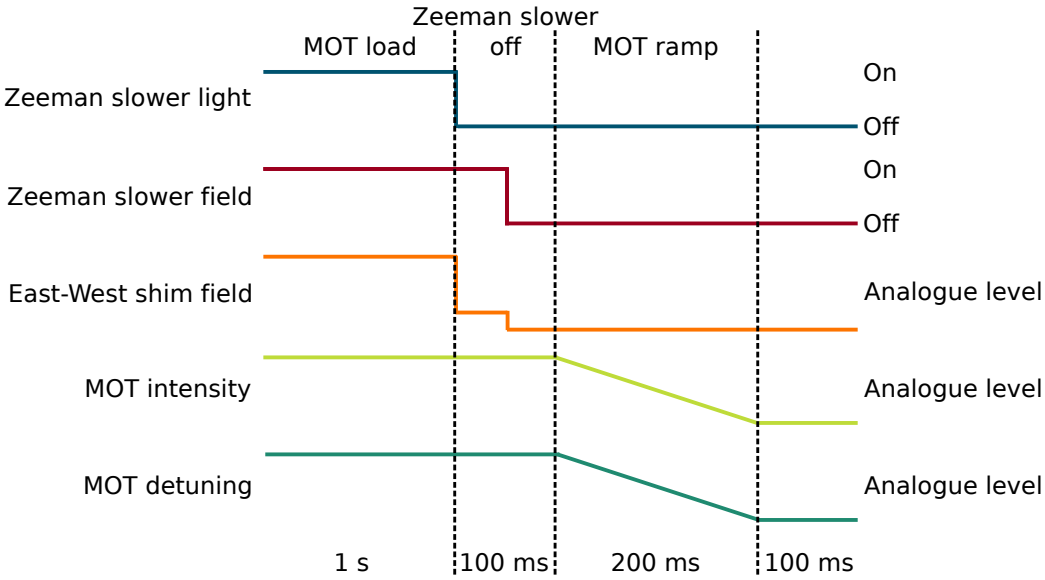

Figure 4.14: A timing diagram of the channels involved in measuring the Yb MOT temperature at different MOT beam intensities and detunings. Note that one or both of the MOT beam intensity or detuning may be changed in the MOT ramp step. A 100 ms wait period occurs after the ramp, with absorption imaging (not shown) as described in section 2.6.2 immediately following.

Figure 4.15 shows our initial findings when holding the MOT beam detuning at the loading setting of -4.2 MHz and varying the final six-beam intensity of the MOT. The dashed red curve in this figure shows the prediction of equation 4.11 for this detuning. One would naïvely expect the temperature of an Yb MOT to show excellent agreement to equation 4.11. However, it can be clearly seen that the temperature does not follow standard Doppler theory in any intensity regime. Only at high intensities does the temperature show the expected linear dependence on intensity, albeit with a much larger gradient than predicted. It is clear that at total intensities below $\sim 100\ I_{\mathrm{sat}}$ there is some mechanism giving rise to additional cooling, whereas above this

intensity additional heating is taking place.

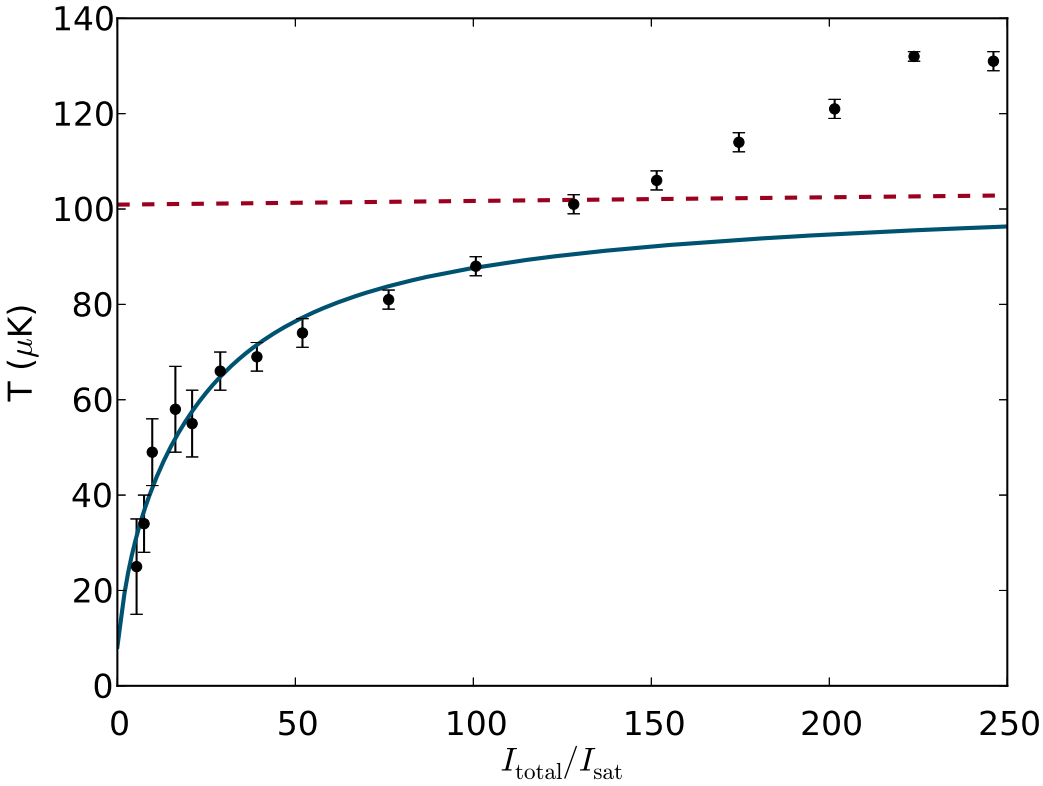

Figure 4.15: The black points show the temperature of the Yb MOT as a function of the total (six-beam) MOT beam intensity. Each point and its associated error bars are derived from a time of flight expansion measurement of the atomic cloud. These data are taken with a fixed MOT beam detuning of -4.2 MHz. The red dashed line shows the temperature predicted by simple Doppler theory (equation 4.11) for these intensities at this detuning. The solid blue curve shows the temperature predicted by the modified Doppler theory presented in section 4.4.2 at the same detuning. Note that this is not a fit, the temperature is calculated using the shifts shown in figure 4.19.

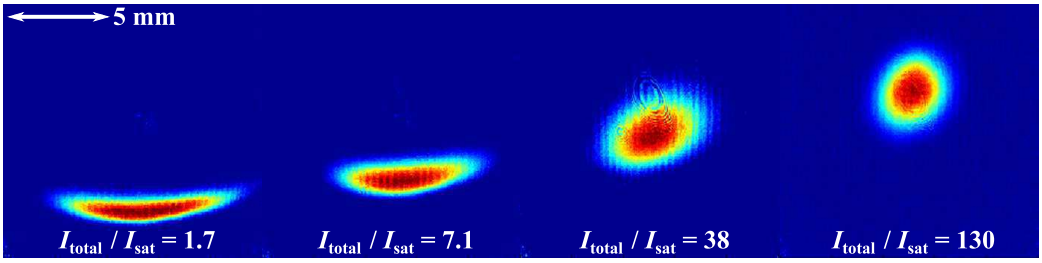

Figure 4.16: Absorption images of an Yb MOT taken with increasing final total MOT beam intensity from left to right. The atom cloud is seen to drop under gravity as the intensity is reduced.

Absorption images of the MOT at these low intensities give a significant clue

as to what is happening (figure 4.16). It can be seen that the position of the Yb cloud drops as the intensity of the MOT beams is reduced. Furthermore the optical depth profile can be seen to evolve from a Gaussian cloud at high intensities to an elongated "bowl" shape at low intensities. From these images it can be concluded that gravity is influencing the position of the atoms and, as such, the forces they experience.

4.4.2 Gravitational MOT shift

It is clear that we now have to modify equation 4.14 to include gravity, so that the force in the vertical direction becomes

$$\begin{aligned}\vec{F}\left(\vec{v},\vec{x}\right) &= \frac{\hbar\vec{k}\Gamma}{2}\frac{I/I_{\text{sat}}}{1+I/I_{\text{sat}}+4\left(\delta-\vec{k}\cdot\vec{v}-\mu\frac{d\vec{B}}{dx}\cdot\vec{x}\right)^2/\Gamma^2} \\ &- \frac{\hbar\vec{k}\Gamma}{2}\frac{I/I_{\text{sat}}}{1+I/I_{\text{sat}}+4\left(\delta+\vec{k}\cdot\vec{v}+\mu\frac{d\vec{B}}{dx}\cdot\vec{x}\right)^2/\Gamma^2} \\ &- m\vec{g}, \end{aligned} \tag{4.29}$$

where $\vec{g}$ is the acceleration due to gravity ($\sim 9.81\ \mathrm{m\,s^{-1}}$) [179].

In a broadband MOT, such as a Cs D_2 MOT or an Yb MOT on the $^1P_1$ transition, the maximum scattering force is much greater than the force due to gravity ($\frac{\hbar k\Gamma}{2mg} \sim 10^5$). However, for a MOT on the narrow $^3P_1$ transition, Γ is comparable to the recoil frequency, $\omega_{\text{R}} = 3.7$ kHz. A consequence of this is that the ratio of the maximum scattering force to the force exerted by gravity is only ∼24.

The effect this has on the force the atoms experience can be seen in figures 4.17 and 4.18. The effect of reducing the MOT beam intensity can be seen in figure 4.17 for two different detunings. As MOT beam intensity is reduced, the power broadening of the linewidth is also reduced. In the case where $\delta > \Gamma_P$ then there exists a region within the MOT where gravity is the dominant force. As a result the atoms will sag under gravity until the force due to the upwards propagating MOT beam balances the downwards force. The magnetic field gradient and detuning define an ellipsoid where the

atoms are resonant with the MOT beams. In the vertical direction the atoms interact with the upwards propagating beam alone, whereas in the horizontal directions the atoms undergo free flight until they reach the boundaries of the resonant ellipsoid. The extent of the gravitational sag may be seen in the inset to the figures, with the dashed black line indicating the position at which the force due to gravity is balanced by the vertical MOT beams. We can see that once I becomes comparable to I_{sat}, very large changes in position may be expected.

Figure 4.18 shows the effect of changing the MOT beam detuning at two different intensities. We can see from the inset that the expected change in MOT position is approximately linear with detuning at low intensities. This is due to the power-broadened linewidth of the transition being small enough for the atoms in the MOT to only be interacting with the upwards propagating MOT beam. At higher intensities the broadening of the transition results in the position shift being non-linear for small detunings. Considering that these positional shifts may be of the order of a few mm, considerations must be made to know the absolute detuning of the MOT beams at any given point during a cycle of the experimental sequence, especially when attempting to load atoms into a tightly focussed optical trap.

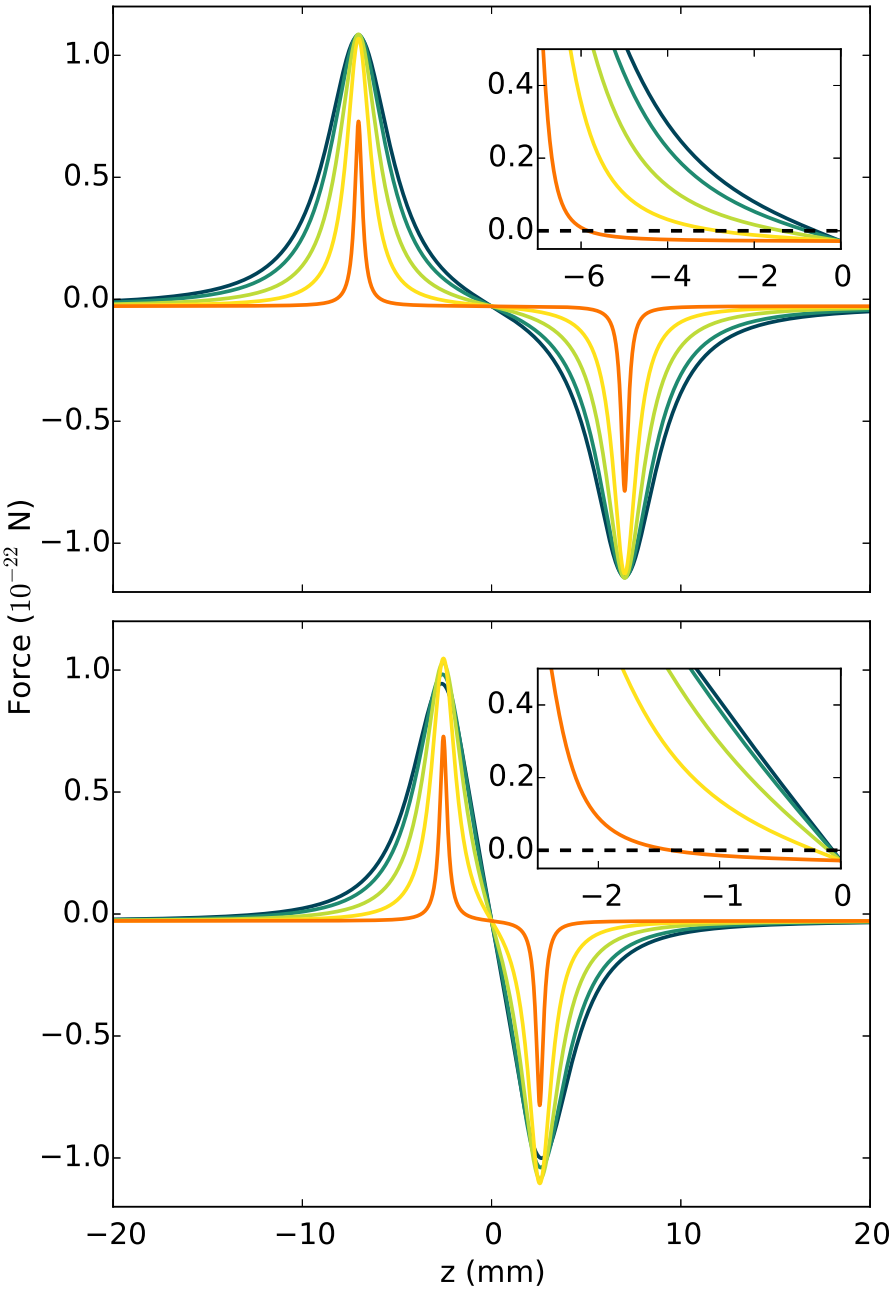

Figure 4.17: The force exerted by gravity and the vertical MOT beams operating on the $^3P_1$ transition at a detuning of -4.7 MHz (upper plot) and -1.7 MHz (lower plot). The axial magnetic field gradient is 3.1 G cm^{-1}. $I_{\text{total}}/I_{\text{sat}}$ is 2, 30, 85, 165, and 230 for the orange, yellow, green, teal and blue curves respectively. It is clear from both plots that as the MOT beam intensity tends to zero, the damping coefficient also tends towards zero and gravity becomes significant.

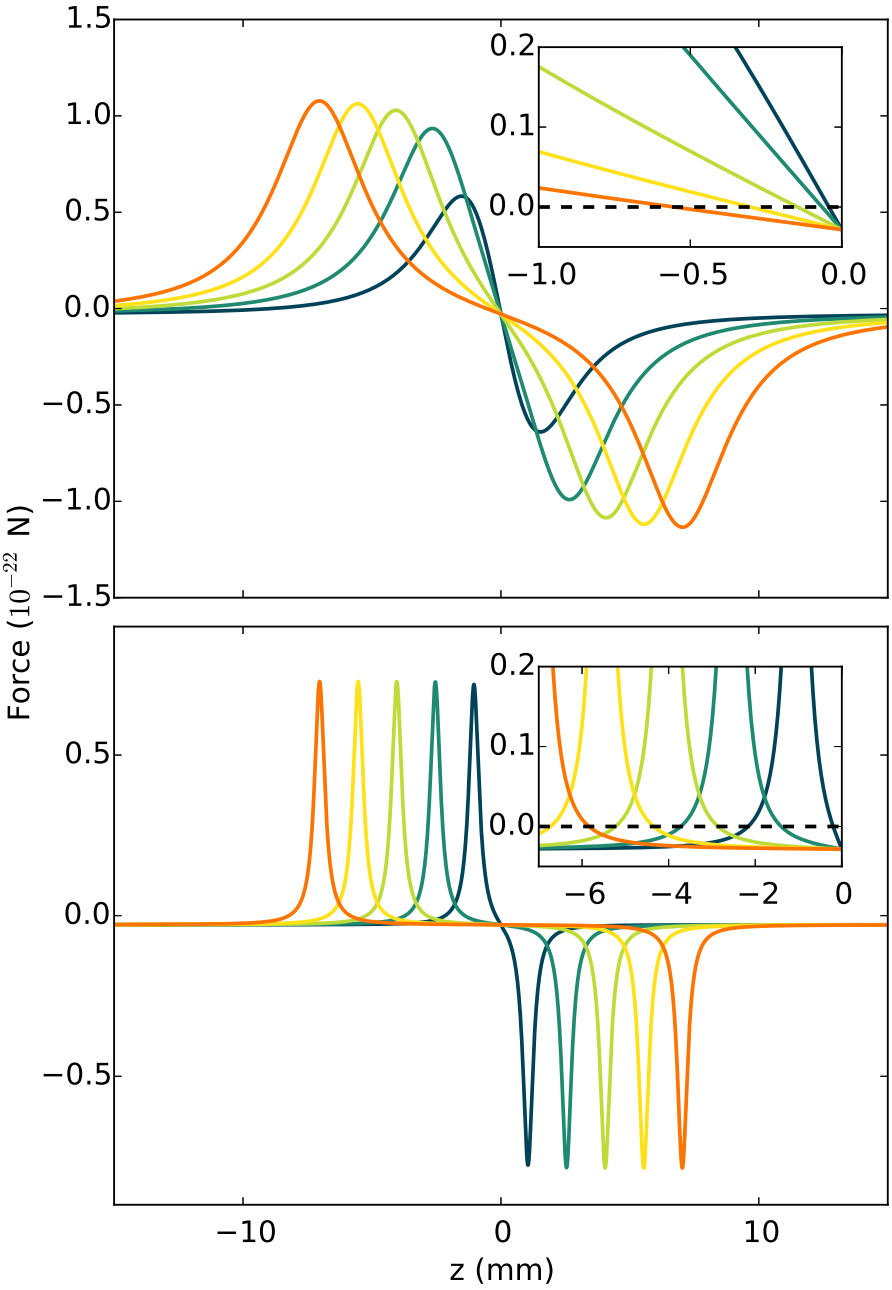

Figure 4.18: The force exerted by gravity and the vertical MOT beams operating on the $^3P_1$ transition at an $I_{\text{total}}/I_{\text{sat}}$ of 250 (upper plot) and 2 (lower plot). The axial magnetic field gradient is 3.1 G cm^{-1}. The MOT beams have a detuning of -4.7, -3.7, -2.7,-1.7, and -0.7 MHz for the orange, yellow, green, teal and blue curves respectively. The top curve shows that as we move to larger red detunings, the damping coefficient decreases as expected. However, at low intensities where gravity plays an important role, the Yb atoms are only resonant with the narrowband MOT beams at certain vertical positions that are determined by the detuning and the magnetic field gradient. The insets show the zero crossing of the net force, the point where the vertical MOT beams counteract gravity.

By performing absorption imaging on the MOT with zero time of flight (as in figure 4.16), the position that the atom cloud sags to can be extracted by using a Gaussian fit to the optical depth profile. Figure 4.19 shows the results of this measurement with a fixed MOT detuning of -4.6 MHz and varying intensity. The inset of figure 4.19 shows the effect of changing the detuning whilst at a fixed intensity of 2.1 I_{sat}. By solving for position where equation 4.29 is equal to zero we can predict the height at which the gravitational and scattering forces come into equilibrium. This calculation is fit to the data presented in figure 4.19 (and the inset) by using a vertical offset and small corrections to the intensity and detuning as free parameters.

The consequence of the atoms falling to a new equilibrium position, z_g, is the interplay of the MOT beams and magnetic field to Zeeman shift the atoms closer to resonance. The effective detuning that the atoms experience is

$$\delta_{\text{eff}} = \delta - \frac{\mu_0}{\hbar}\frac{dB_z}{dz}z_g. \tag{4.30}$$

As the intensity of the MOT beams is reduced, the power broadening decreases and the closer atoms must come to resonance with the upwards propagating beam to be supported against gravity. It is then immediately apparent from equation 4.11 that as the intensity is decreased, the temperature does not just decrease linearly but decreases further as $|\delta|$ comes closer to resonance. The blue curve on figure 4.15 shows the result of inserting the value of δ_{eff}, obtained when solving equation 4.29 for $\vec{F} = 0$ to find z_g, into equation 4.11. The curve shows the temperature predicted as a function of intensity for the MOT detuning of -4.2 MHz at which the data was taken. It can be seen that, unlike the standard Doppler theory, the modified theory predicts the temperature at low intensities very well. However, at high intensities the atom temperature is still increasing at a rate larger than either theory predicts. This is an effect that has been seen before in MOTs of atoms with two valence electrons [143, 180] and a number of theories have been proposed to explain its origin [181, 182].

Figure 4.20 shows a similar set of data to figure 4.15. Here the final temperature of the MOT is shown for different final MOT detunings at a constant total intensity of 57.6 I_{sat}. The blue curve again shows the predictions of the

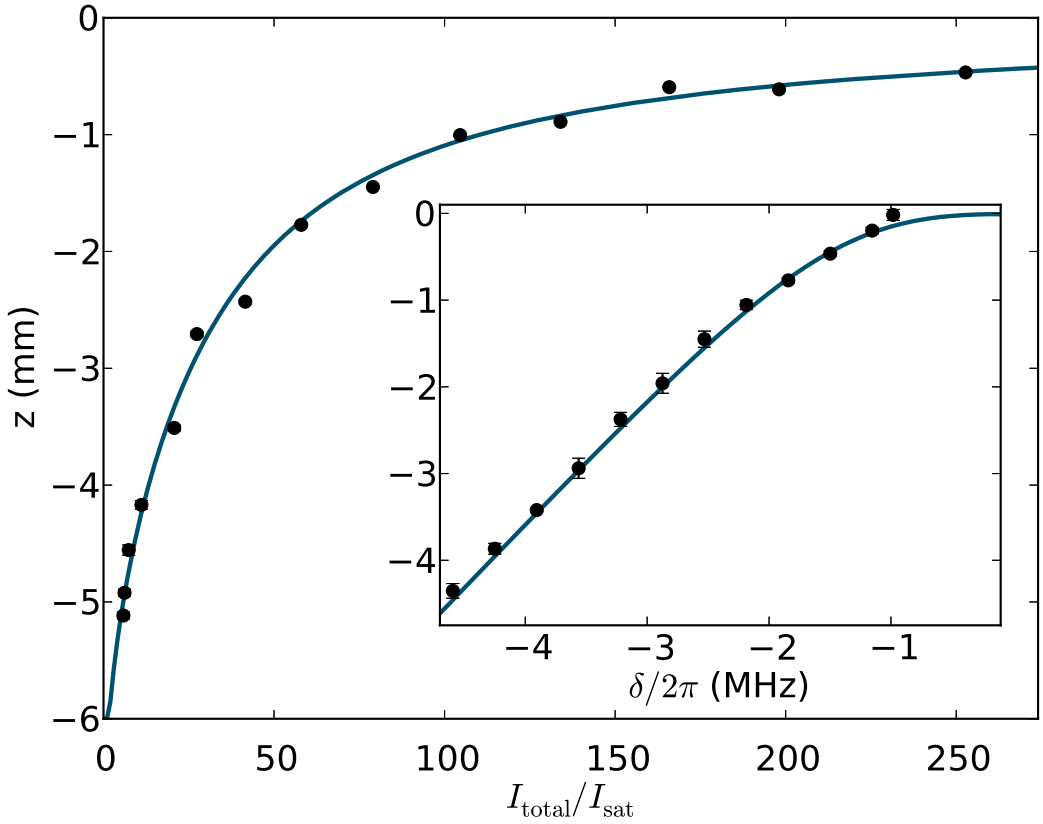

Figure 4.19: Main figure: the vertical position of the narrowband Yb MOT as a function of the total intensity of the MOT beams at a constant detuning of -4.6 MHz. The position is determined by the centre of a Gaussian fit to the optical depth obtained from absorption imaging. Inset: the vertical position of the narrowband MOT as a function of the detuning of the MOT beams at a constant total intensity of 2.1 I_{sat}. The blue curves show the position at which the scattering force from the vertical MOT beam balances the force due to gravity. The curves are fit to the data using a vertical offset, and small adjustments to $I_{\mathrm{total}}/I_{\mathrm{sat}}$ and the detuning as free parameters. The insets show the zero crossing of the net force, the point where the vertical MOT beams counteract gravity.

modified Doppler theory. Here the curve is fit to the data using a detuning offset and a constant scaling of the temperature as free parameters. The detuning offset is fairly large at 1.8 MHz, and is likely a systematic error resulting from a small misalignment of the 556 nm spectroscopy probe through the beam machine (see section 3): assuming a root mean squared velocity of 300 $\mathrm{m\,s^{-1}}$ a 1° misalignment of the probe beam from orthogonal would lead to a 9 MHz shift in the detuning. Following these measurements further investigation into the MOT beam detuning was undertaken (see section 4.5).

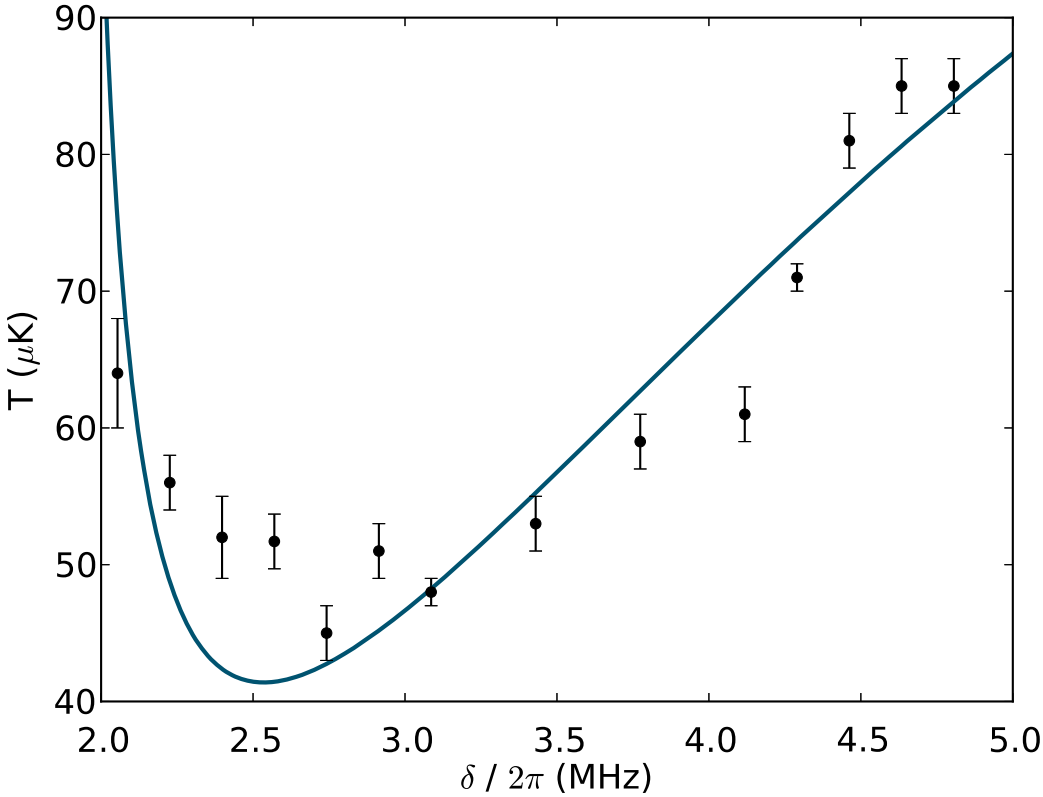

Figure 4.20: Yb MOT temperature as a function of detuning, with a total MOT beam intensity of 57.6 I_{sat}. The data points and error bars are calculated using time of flight expansion of the atom cloud. The blue curve shows a fit to equation 4.11.

The temperature scaling factor of the fit was 1.26. This could be due to a number of factors including misalignment of the camera, uncertainty in the magnification, and radiation pressure from multiple photon scattering events within the MOT. Further measurements could be undertaken by varying the density of the MOT, however the overall goal of this investigation was to minimise the temperature of the atom cloud. By optimising the final intensity and detuning of the MOT beams we are able to achieve a MOT temperature of 22 μK.

4.5 Absolute MOT detuning

It became clear in the above investigations into the MOT temperature that the absolute detuning of the MOT beams needed to be clarified. We began

by ensuring that the 555.8 nm spectroscopy beam going through Yb beam machine was as close to orthogonal with the atomic beam as possible. This was achieved by using a pair of apertures on the spectroscopy beam. The sensitivity to this angle could be seen when the laser was locked: the slightest movement of the final mirror in the set up caused the MOT to change location, as the position is sensitively determined by a balance between the MOT beam detuning and the pushing from the Zeeman slower beam.

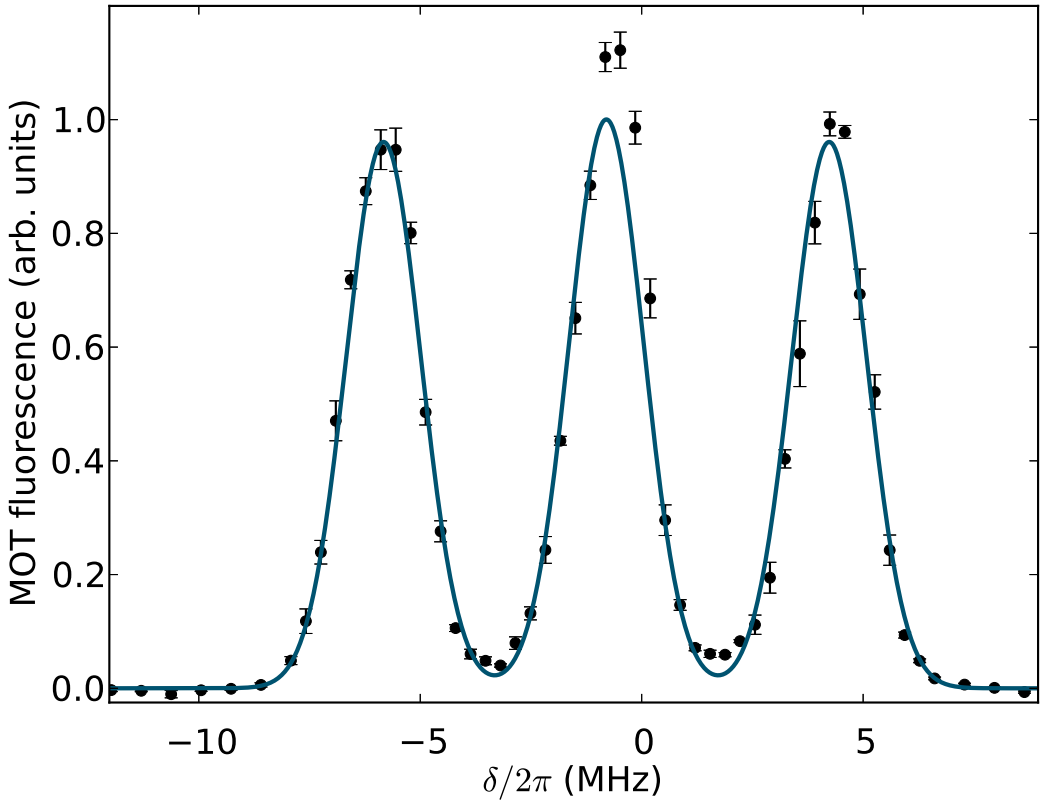

Figure 4.21: Fluorescence of the Yb MOT as a function of detuning in a 2.4 G bias field. The points are determined using the average fluorescence of the MOT across a region of interest in fluorescence imaging. The blue curve shows a triple Gaussian fit to the data, where we find a detuning shift of -0.72 MHz for the central peak. The data points and the curve are normalised to the fit.

The cold atoms in the Yb MOT itself were used to calibrate the detuning of the MOT beams by use of Zeeman shifts as follows. The camera (Andor Luca) was moved from its position in the absorption imaging setup to the dipole trapping viewports. The fluorescence of the atoms in the MOT was collected and focussed onto the camera using a 75 mm focal length lens.

Because the camera was now picking up fluorescence from the 555.8 nm MOT beams, the interference filter was removed from the camera and replaced with the large area shutter used for Cs absorption imaging.

To record the fluorescence, a MOT was loaded with the optimal conditions discussed above for 1 s. By ramping the detuning and the intensity of the MOT beams the MOT was then compressed and cooled to 22 μK. The magnetic field gradient and the MOT beams were then simultaneously switched off, and the camera shutter was opened immediately afterwards. Whilst the shutter was opening, the vertical shim coils were used to apply a 2.4 G bias field. This bias field remained on for the duration of the sequence. After the camera was fully open (11 ms) the MOT beams were pulsed on for 100 μs with a total intensity of $15I_{\text{sat}}$ and the fluorescence of the atoms was recorded on the CCD. A second image of the MOT beams being pulsed on for the same duration, but with no atoms present, was then recorded. The second image was subtracted from the first to obtain a background corrected image of the fluorescence.

The detuning of the MOT beam pulse during the imaging sequence was varied to map out the fluorescence due to the $m_J = 0, \pm 1$ magnetic substates of the the $^3P_1$. A region of interest was defined on the CCD and the average pixel counts across this region was recorded several times for each detuning. The $m_J = 0$ state is magnetically insensitive: the state experiences no Zeeman shift. Figure 4.21 shows the fluorescence recorded against the detuning given by the difference between the MOT and spectroscopy AOM frequencies. Clearly visible are the three peaks associated with the three states. Also shown is a triple Gaussian fit to the data, yielding an offset that shows the 555.8 nm locking signal is offset from resonance by 0.72 ± 0.06 MHz. The most likely source for this systematic offset in the MOT detuning is the crossing angle of the spectroscopy probe beam with the atomic beam of the beam machine. Given that, for an oven temperature of 470 °C, the mean speed of the atoms in the atomic beam is 350 m s^{-1}, this offset in detuning implies a deviation of 0.070 ± 0.006 ° from 90 ° in the crossing angle of the probe and atomic beam. We note that this offset is not consistent with that observed in the detuning dependence of the MOT shown in figure 4.20. This is due to the realignment of the beam machine following its use in another experient

and, given the detuning sensitivity demonstrated here, such a difference in offset detuning is to be expected.

4.6 Summary

In this chapter we have given a brief overview of the scattering force and its use in Zeeman slowing and the laser cooling of atoms. We have described in detail the design, construction and calibration of a dual-species Zeeman slower for sequentially loading ytterbium and caesium MOTs. A model of Zeeman slower performance is also presented, explaining how increased laser intensity allows the deceleration of atoms using a Zeeman slower magnetic field profile that is not "perfect". We have also shown the calibration of the ytterbium MOT itself, optimising the loading conditions including an investigation of the impact of frequency sidebands on the MOT beams.

We have also presented an investigation into the enhanced Doppler cooling seen in MOTs on narrow-linewidth transitions. The force due to gravity must not be ignored in such systems, and the significant movement of the MOT under gravity observed is the major contributor to producing samples of atoms cooler than one would intuitively expect given the MOT beam detuning and intensity. In the next chapter we look at how this effect may be used to efficiently load optical dipole traps with cold ytterbium for the purposes of cooling to quantum degeneracy.

Chapter 5

Optical trapping of ytterbium

Unlike the scattering force used in conjunction with magnetic field gradients to produce cold atoms in a MOT, an optical dipole trap utilises tightly focussed laser beams far-detuned from resonance, resulting in a scenario where photon scattering from trapped atoms is minimal compared to the dipole force. In this chapter we discuss the nature of the optical dipole potential and its use in the all-optical trapping and evaporative cooling to quantum degeneracy. We describe the design of an optical dipole trap for Yb, first investigating the alignment and loading of a single-beam optical trap and then using a crossed trap for the purpose of cooling Yb to create a Bose-Einstein condensate.

5.1 Optical trapping

Here we present a simple overview of the physics underlying the optical dipole potential as the technique will ultimately be pivotal for the creation of ultracold samples of CsYb molecules. More comprehensive reviews of optical trapping may be found in references [159, 183]. This thesis mostly concentrates on the implementation of an optical trap for ^{174}Yb, however we will also discuss the considerations for trapping of Cs here.

Optical trapping relies on the interaction between an electric dipole (the ground state atom) and laser light, providing a confining force due to gradients in the intensity of the laser beam. We shall see that in the situation

where the detuning of the laser light is far from the resonant frequency of transitions from the ground state, the dipole force dominates over the radiation force resulting from the scattering of photons. However, off-resonant scattering is still a limitation in the performance of an optical dipole trap. A result of the large detuning is that the resulting dipole potential is weak in comparison to that of a magnetic trap, for example. As such the depth of a typical trap is only ∼1 mK.

5.1.1 The classical harmonic oscillator model

In this model we will consider the atom as an oscillating dipole, interacting with an oscillating electric field, $\mathbf{E}(\mathbf{r},t)$, with an angular frequency, ω. Such an electric field induces an electric dipole moment, $\mathbf{d}(\mathbf{r},t)$. The oscillating field is defined as,

$$\mathbf{E}(\mathbf{r},t) = \hat{\mathbf{e}}\tilde{E}(\mathbf{r})\exp(-i\omega t) + c.c., \tag{5.1}$$

and the associated oscillating dipole moment is given by,

$$\mathbf{d}(\mathbf{r},t) = \hat{\mathbf{e}}\tilde{d}(\mathbf{r})\exp(-i\omega t) + c.c., \tag{5.2}$$

where $\hat{\mathbf{e}}$ is the unit polarisation vector. The oscillation amplitude, $\tilde{d}$, of the dipole moment is related to the amplitude of the driving field, $\tilde{E}$, by

$$\tilde{d} = \alpha(\omega)\tilde{E}, \tag{5.3}$$

where $\alpha(\omega)$ is the complex polarisability of the ground state at frequency ω. Assuming the response of the atom to the field is linear, we may write the interaction potential as

$$U_{\text{dipole}} = -\frac{1}{2}\mathbf{d}\cdot\mathbf{E}. \tag{5.4}$$

The factor of 1/2 results from the fact that this is an induced dipole moment [183]. Taking the time average and writing in terms of intensity, $I = 2\epsilon_0 c|E|^2$, gives

$$U_{\text{dipole}} = -\frac{\text{Re}\,(\alpha)\, I}{2\epsilon_0 c}. \tag{5.5}$$

Note that this expression is equivalent to the light shift of the ground state of the atom. If we consider the dipole potential for a Gaussian beam of power, P, and waist, w_0, this gives a maximum trap depth at the focus of the beam of

$$U_{\text{max}} = -\frac{\text{Re}\,(\alpha)\, P}{\epsilon_0 c \pi w_0^2}. \tag{5.6}$$

The dipole force is then given by the gradient of the dipole potential,

$$\mathbf{F}_{\text{dipole}} = -\nabla U_{\text{dipole}} = -\frac{1}{2\epsilon_0 c}\text{Re}\,(\alpha)\,\nabla I\,(\mathbf{r})\,, \tag{5.7}$$

which is a conservative force and is proportional to the gradient in the intensity of the laser light.

The dipole force arises from the dispersive properties of the atom-light interaction, which are characterised by the real part of the atomic polarisability. Conversely, the imaginary part of the atomic polarisability results in the absorption and re-emission of photons: the scattering force [183]. This cycle of absorption and re-emission leads to a scattering rate defined as

$$\Gamma_{\text{scattering}} = \frac{1}{\hbar\epsilon_0 c}\text{Im}\,(\alpha)\, I\,(\mathbf{r})\,. \tag{5.8}$$

The expressions in this section are completely general for induced dipole moments in laser fields, as such they apply to Yb, Cs, and even the CsYb molecule. However, it is clear that the polarisabilities of the atoms or molecules under investigation are required in order to model the dipole force experienced.

5.1.2 The polarisability

The atomic polarisability may be considered as the distortion, by means of an electromagnetic field, of the charge distribution defined by the nucleus

and electrons of the atom. Classically, the atom may be approximated as a negatively charged valence electron bound elastically to a positively charged core, resulting in a polarisability defined by the following [183]

$$\alpha = \frac{e^2}{m_e} \frac{1}{\omega_0^2 - \omega^2 - i\omega\Gamma_\omega}, \tag{5.9}$$

where ω_0 is the resonant oscillation frequency, ω is the driving frequency of the laser field, m_e is the mass of the electron, and

$$\Gamma_\omega = \frac{e^2\omega^2}{6\pi\epsilon_0 m_e c^3}, \tag{5.10}$$

is a damping rate due to the radiative energy loss. If we define an on-resonant damping rate, $\Gamma = \frac{\omega_0^2}{\omega^2}\Gamma_\omega$, then the polarisability takes the following form

$$\alpha = 6\pi\epsilon_0 c^3 \frac{\Gamma/\omega_0^2}{\omega_0^2 - \omega^2 - i\left(\omega^3/\omega_0^2\right)\Gamma}. \tag{5.11}$$

In the limit of a large detuning from the atomic resonance and low saturation, combining this formulation with equation 5.5 yields a dipole interaction energy of

$$U_{\text{dipole}} = -\frac{3\pi c^2}{2\omega_0^3}\Gamma\left(\frac{1}{\omega_0 - \omega} + \frac{1}{\omega_0 + \omega}\right) I\left(\mathbf{r}\right). \tag{5.12}$$

A semi-classical approach may also be considered but produces largely the same result, with the on resonance damping rate replaced by the spontaneous decay rate for the transition

$$\Gamma \equiv A_{i,f} = \frac{\omega_0^3}{3\pi\epsilon_0\hbar c^3}|\langle i|\mathbf{d}|f\rangle|^2, \tag{5.13}$$

where $|i\rangle$ and $|f\rangle$ are the ground and excited states respectively. In the case of low saturation, this dipole interaction energy is equivalent to the light shift of the ground state when considering the so-called dressed state picture. However, even a simple atom such as Cs cannot be considered as a simple two-level system: all allowed transitions contribute to the polarisability and hence the dipole interaction energy. By summing over all electric-dipole

allowed transitions we obtain an expression for the total dipole interaction energy or light shift of the ground state,

$$U_{\text{dipole,i}} = -\frac{3\pi c^2}{2} \sum_{f \neq i} \frac{A_{i,f}}{\omega_{0,f}^3} \left(\frac{1}{\omega_{0,f} - \omega} + \frac{1}{\omega_{0,f} + \omega} \right) I(\mathbf{r}) . \tag{5.14}$$

Hence the real part of the polarisability is given as

$$\text{Re}(\alpha) = 3\pi\epsilon_0 c^3 \sum_{f \neq i} \frac{A_{i,f}}{\omega_{0,f}^3} \left(\frac{1}{\omega_{0,f} - \omega} + \frac{1}{\omega_{0,f} + \omega} \right) . \tag{5.15}$$

This model does not account for the polarisability due to all electrons in the atom; this requires a difficult calculation involving random phase approximations to account for the non-valence electrons [184]. However, for the scope of this work the above approximation is valid for use in determining polarisabilites to within a few percent.

5.1.3 Gaussian beams

From equation 5.12 it is clear that the spatial intensity profile of the laser beam defines the optical trap, and so in order to have a well-defined trap potential it is paramount to have an intensity profile that is a good approximate to a functional form. Whilst spatial light modulators are increasingly being used to produce arbitrary trap potentials and create interesting dynamics [185–187], we are fortunate that most laser beam profiles approximate a Gaussian beam. The fundamental Gaussian beam mode propagating along the z-direction is completely described by

$$E(x, y, z) = E_0 \frac{w_0}{w(z)} e^{-\frac{-r^2}{w^2(z)}} e^{-i\frac{kr^2}{2R(z)}} e^{-i[kz - \phi(z)]}, \tag{5.16}$$

where k is the wavevector, $r = \sqrt{x^2 + y^2}$ is the radial distance from the propagation axis, $w_0 = \sqrt{\frac{2z_{\text{R}}}{k}}$ is the beam waist, here defined to be at $z = 0$, z_{R} is the Rayleigh range, and $\phi(z)$ is the so-called Gouy-phase [188]. The curvature of the beam is given by

$$R(z) = z\left(1 + \frac{z^2}{z_{\mathrm{R}}^2}\right), \tag{5.17}$$

and the width of the beam is given by

$$w(z) = w_0\sqrt{1 + \left(\frac{z}{z_{\mathrm{R}}}\right)^2}. \tag{5.18}$$

Generalising to allow for an elliptical beam profile by defining beam waists $w_{0,x}$ and $w_{0,y}$ for the x and y directions respectively, the intensity profile of a Gaussian beam is

$$I(x, y, z) = I_0\left(\frac{w_0}{w(z)}\right)^2 e^{-\frac{2x^2}{w_x^2(z)}} e^{-\frac{2y^2}{w_y^2(z)}}, \tag{5.19}$$

where

$$I_0 = \frac{2P}{\pi w_{0,x} w_{0,y}}, \tag{5.20}$$

is the peak intensity for a beam of total power, P. This leads to a useful property of Gaussian beams; given that the trapping potential is proportional to I, then a trap with depth U_0 may be approximated as a harmonic potential

$$U_{\mathrm{dipole}} \approx -U_0\left(1 - 2\frac{x^2}{w_{0,x}^2} - 2\frac{y^2}{w_{0,y}^2} - \frac{z^2}{z_{\mathrm{R}}^2}\right), \tag{5.21}$$

for small deviations from the trap centre, with trap frequencies in x, y, and z directions respectively of [189]

$$\omega_x = 2\sqrt{\frac{U_0}{m w_{0,x}^2}}, \omega_y = 2\sqrt{\frac{U_0}{m w_{0,y}^2}}, \omega_z = \sqrt{\frac{2U_0}{m z_{\mathrm{R}}^2}}. \tag{5.22}$$

The second feature of a Gaussian beam is that its properties at all points along its propagation, given a waist at position z_w, may be determined from the complex beam parameter, $q = z - z_w - iz_{\mathrm{R}}$, implying that q is entirely defined by the Rayleigh range. This parameter may be used with ray-tracing matrices to determine q after optical transformations. For a position z_a where q is known, the value of q at a position of interest, z_b, following an

optical transformation (and hence new values of $w(z)$, z_w, and z_R) may be determined using

$$\begin{pmatrix} q_{z_b}/n \\ 1 \end{pmatrix} = \begin{pmatrix} A & B \\ C & D \end{pmatrix} \begin{pmatrix} q_{z_a}/n \\ 1 \end{pmatrix}, \tag{5.23}$$

where the so-called ABCD matrix determines the optical operation. For example, for a thin lens with focal length, f, the ABCD matrix is defined as

$$\begin{pmatrix} 1 & 0 \\ -1/f & 1 \end{pmatrix}. \tag{5.24}$$

Further examples of ABCD matrices may be found in [190]. These transformations were used in the design of the optical setup of both incarnations of the optical trap used in this work, primarily to design optical systems giving the desired waist at the trap centre.

5.2 Optical trap design

5.2.1 Polarisability of Cs and Yb

Tables 5.1 and 5.2 outline the wavelengths and A-coefficients for selected ground state transitions of Cs and Yb respectively. It is worth noting the further allowed transitions exist, but their contributions to the ground state light shift are negligible due to large detunings or small linewidths. Figure 5.1 shows the polarisability of Cs and Yb, in units of Bohr radius cubed, for a range of wavelengths. The curves in this figure are calculated using equation 5.15 and the transition data in tables 5.1 and 5.2. For Cs, equation 5.15 is modified to allow for the fine structure splitting by weighting the A-coefficients by the angular momentum of the states involved.

The two most commonly used optical trapping wavelengths are 1070 nm and 532 nm owing to the ease of access to high-power fibre lasers at such wavelengths. Figure 5.1 includes dashed vertical lines at these wavelengths to illustrate the disparities in polarisability for Cs and Yb. At 532 nm the polarisability is approximately -226 a_0^3 and 264 a_0^3 for Cs and Yb respec-

Transition	λ_{vac} (nm)	A-coefficient (s^{-1})
6s $^2S_{1/2} \rightarrow$ 6p $^2P_{1/2}$	894.5929600	2.862×10^7
6s $^2S_{1/2} \rightarrow$ 6p $^2P_{3/2}$	852.3472759	3.279×10^7
6s $^2S_{1/2} \rightarrow$ 7p $^2P_{1/2}$	459.44880	7.93×10^5
6s $^2S_{1/2} \rightarrow$ 7p $^2P_{3/2}$	455.65844	1.84×10^6
6s $^2S_{1/2} \rightarrow$ 8p $^2P_{1/2}$	388.9710415	8.99×10^4
6s $^2S_{1/2} \rightarrow$ 8p $^2P_{3/2}$	387.72473	3.86×10^5
6s $^2S_{1/2} \rightarrow$ 9p $^2P_{1/2}$	361.83400	2.23×10^4
6s $^2S_{1/2} \rightarrow$ 9p $^2P_{3/2}$	361.25014	1.43×10^5
6s $^2S_{1/2} \rightarrow$ 10p $^2P_{1/2}$	348.1057	6.33×10^3
6s $^2S_{1/2} \rightarrow$ 10p $^2P_{3/2}$	347.7805	6.27×10^4
6s $^2S_{1/2} \rightarrow$ 11p $^2P_{1/2}$	340.0955	2.36×10^3
6s $^2S_{1/2} \rightarrow$ 11p $^2P_{3/2}$	339.8941	3.61×10^4

Table 5.1: Table taken from [107] showing the transition wavelengths and A-coefficients considered in calculating the ground state polarisability of Cs. The values are sourced from [191] and converted to vacuum wavelengths.

Transition	λ_{vac} (nm)	A-coefficient (s^{-1})
$4f^{14}6s^2\ ^1S_0 \rightarrow 4f^{14}6s6p\ ^3P_1$	555.80236	1.15×10^6
$4f^{14}6s^2\ ^1S_0 \rightarrow 4f^{14}6s6p\ ^1P_1$	398.91142	1.92×10^8
$4f^{14}6s^2\ ^1S_0 \rightarrow 4f^{13}5d6s^2\ (7/2, 5/2)_1$	346.53620	6.83×10^7
$4f^{14}6s^2\ ^1S_0 \rightarrow 4f^{13}5d^26s$	267.2754	1.43×10^7
$4f^{14}6s^2\ ^1S_0 \rightarrow 4f^{14}6s7p\ ^1P_1$	246.5242	1.00×10^8

Table 5.2: A table of the 5 transitions considered in the calculation of the ground state polarisability of the Yb atom. The wavelengths and A-coefficients are taken from [124].

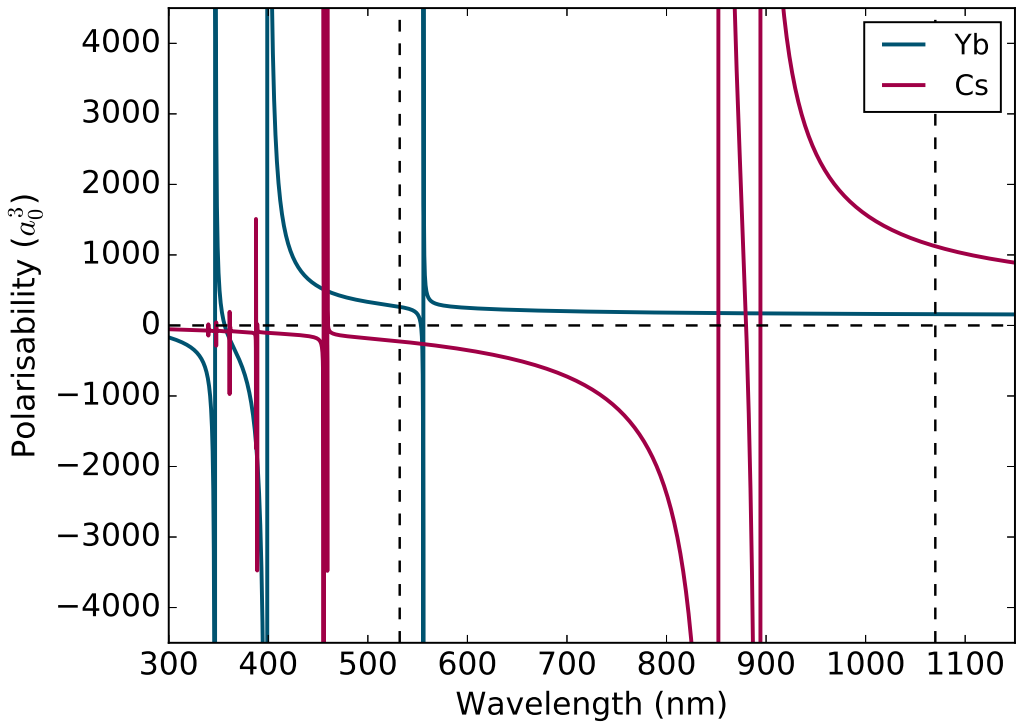

Figure 5.1: The ground state polarisability as a function of the trapping wavelength for both Yb (blue curve) and Cs (red curve). The intersection with with the dashed vertical lines show the polarisability at 532 nm and 1070 nm, the wavelengths of the available trapping lasers. The curves are calculated using equation 5.15 (or a modified form to account for hyperfine states in the case of Cs) with the transition wavelengths and A-coefficients in tables 5.1 and 5.2.

tively, where a_0 is the Bohr radius. Whereas at 1070 nm the polarisability is approximately 1123 a_0^3 and 160 a_0^3 for Cs and Yb respectively. Therefore a trapping wavelength of 532 nm would produce a repulsive barrier for Cs in its ground state and form an attractive potential well for Yb. This clearly rules out using a pure 532 nm trap for the purposes of producing ultracold Cs and Yb in a mutual trap. Conversely, the dipole interaction is attractive for both species at 1070 nm, however the trap will be around seven times deeper for Cs than for Yb, potentially resulting in any ultracold Yb being "boiled" out of the trap by the Cs that will have a naturally higher equilibrium temperature.

One possible solution to producing a equal trap depths for the two species would be to implement a bichromatic dipole trap; by using both trapping wavelengths it would be possible to engineer a situation whereby 532 nm

light in addition to 1070 nm light would reduce the Cs trap depth and increase the trap depth for Yb. A similar method has previously been used by the Düsseldorf group [192], although here magnetically trapped Rb is used to sympathetically cool Yb in a bichromatic optical dipole trap. Such a potential is very sensitive to pointing and focussing instabilities; the Düsseldorf group have since abandoned this approach in the latest version of their apparatus.

The approach we have taken, at least initially, is to use a single optical trap operating at 1070 nm. Whilst the polarisability is much larger for Cs than for Yb, the relative ease of imaging small amounts of cold Cs means that it may be possible to load a small amount of Cs into an Yb trap for measurements of the interspecies scattering length using the rethermalisation of the two species. The experiments and optimisation presented in this thesis are performed in two different trap configurations: a single beam trap, used initally to optimise the loading from a Yb MOT into an optical trap and to investigate the impact of loading a Cs MOT in the presence of optically trapped Yb; and a two-beam crossed optical dipole trap, which has subsequently been used to cool Yb to quantum degeneracy. The following sections describe the design and operation of these trap configurations.

5.2.2 Modelling the optical trap

To model the optical trap, we consider the contribution of three potentials: the dipole potential, the gravitational potential, and the magnetic potential. The dipole potential contribution is modelled using the calculated value of the polarisability at the trap's operating wavelength by

$$U_{\text{dipole}}(\mathbf{r}) = -\frac{\text{Re}(\alpha)\,\text{I}(\mathbf{r})}{2\epsilon_0 c}. \tag{5.25}$$

Given the polarisability for the trapped state and the Gaussian profile of the trapping beam, the trap depth and frequencies are easily computed using equations 5.6 and 5.22 respectively. It follows that the trap depth scales with the power of the optical trapping beam, and the trap frequencies scale as the square root of this power.

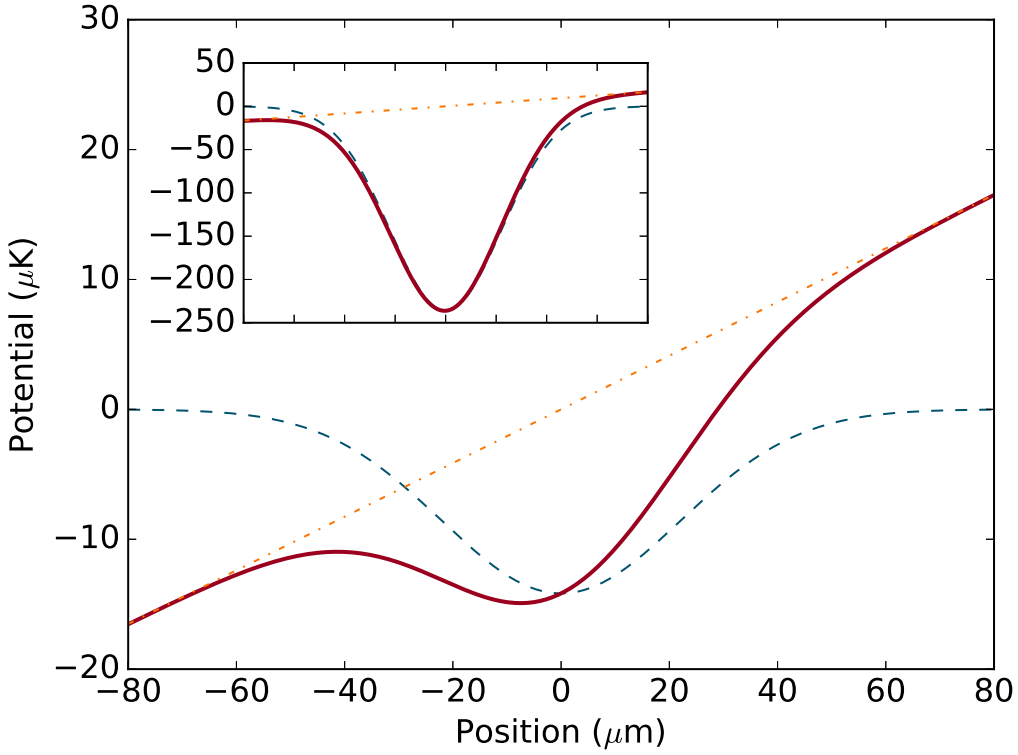

Figure 5.2: The main figure shows the total potential energy for a single beam dipole trap with a waist of 44 μm and a power of 0.1 W as a function of vertical position, with 0 μm being the location of the maximum in trap beam intensity. The orange dot-dashed curve shows the potential energy due to gravity, whilst the blue dashed curve shows that due to the dipole interaction. The solid red curve shows the combined potential energy, including the tilting of the trap due to gravity. The inset to the figure shows the same system with a power of 20 W in the trapping beam. Here the effect of tilting is much less significant and the harmonic part of the trap could be modelled by the dipole potential alone.

For large intensities it is often sufficient to simply scale the known trap depths and frequencies with a change in power, however at lower intensities gravity has a significant effect. For an atom of mass m, the gravitational contribution to the overall potential is simply

$$U_{\text{Grav}} = mgz, \tag{5.26}$$

where z is taken to be the vertical direction in the lab frame, and is usually perpendicular to the trapping beam. This contribution acts as to reduce the total depth of the trap by making the combined potential barrier lower on

the underside of the trap. Whilst insignificant at large trapping intensities, this contribution to the overall potential can have a big impact in the final stages of evaporative cooling to quantum degeneracy. This occurs because the gravitational tilting of the trap potential becomes so pronounced that the evaporating atoms experience a lower trap depth in the vertical direction compared to escaping along one of the trapping beams. Figure 5.2 shows this affect for two beam powers in a trap consisting of a single beam with a 44 μm waist.

In some cases the tilting of the trap can be beneficial since the trap frequencies have a weak dependence on the trap depth in this regime: the trap depth can be lowered with less of a reduction in the elastic collision rate [193]. This effect can be controlled further for the alkali atoms using the magnetic potential arising from a combination of a magnetic field gradient and a bias field [194]. Our code for modelling the optical trap incorporates all three of these potentials, including the state dependant magnetic potential, in order to produce a total potential

$$U_{\text{total}} = U_{\text{dipole}} + U_{\text{grav}} + U_{\text{mag}}. \tag{5.27}$$

However, Yb atoms in the ground state do not have a magnetic moment and so the magnetic potential is of no significance when modelling the trap for this species. The magnetic trapping of Cs is briefly discussed in appendix A. From the total potential we are able to extract the trap depth, along with the trap frequencies along the principal axes of the trapping volume by fitting the harmonic region of the trap to a function of the form

$$U_j = \frac{1}{2} m \omega_j^2 j^2, \tag{5.28}$$

where j is the direction in consideration. In some instances we are able to measure the trap frequencies in certain directions and compare to the model. Once we have confidence in the model, we use its predicted trap frequencies for use in determining the temperature and phase-space densities of the atomic sample.

5.3 The single beam optical trap

5.3.1 Optical setup

The light for optical dipole trapping is derived from a multi-mode fibre laser operating at 1070 nm (IPG, YLR-100-AC-MM). The maximum power output from the fibre laser head is 100 W. Figure 5.3 shows the typical setup of one of our dipole trap configurations. The laser output first passes through a $\lambda/2$ waveplate before entering a PBS cube. The reflected output of the PBS is dumped into a fire brick. This combination of waveplate and PBS is primarily used for alignment purposes; the waveplate is used to dump most of the laser power into the brick and allow for safe working conditions when aligning the main beam. In normal operation the waveplate is set to maximise transmission through the PBS. This is not simply to achieve the maximum intensity possible in the trap, but there is also a higher purity of the Gaussian beam mode under these conditions. This is because the fibre laser has an unpolarised "speckle" surrounding the main mode of the beam, resulting from laser light transmitted through the fibre cladding. By optimising the transmission we have the highest ratio of power in the main mode to power in the speckle, giving a better focus downstream.

The beam is then resized through a telescope before entering a high-power water-cooled AOM (Isomet, M1135-T80L-3). The first-order light from the AOM is incident on a motorised flipper mirror. When the flipper mirror is in the upright position, the first-order light is dumped into a beam dump. The zeroth-order light is also dumped into the same beam dump using a pick off mirror. When the flipper mirror is down the first-order light continues on to the focussing optics specific to the trap being used.

The final element in the system is an achromat with a focal length of 300 mm. This lens is mounted on a translation stage to allow for precise alignment of the waist of the trapping beam to the atoms. Prior to this lens is a telescope used to change the beam size before the final lens. This configuration allows the trap waist to be changed simply by changing the lenses in this telescope. The single beam setup used in the rest of this section is designed to have a waist at the atoms of $\sim$40 μm. A mirror is used between the telescope and

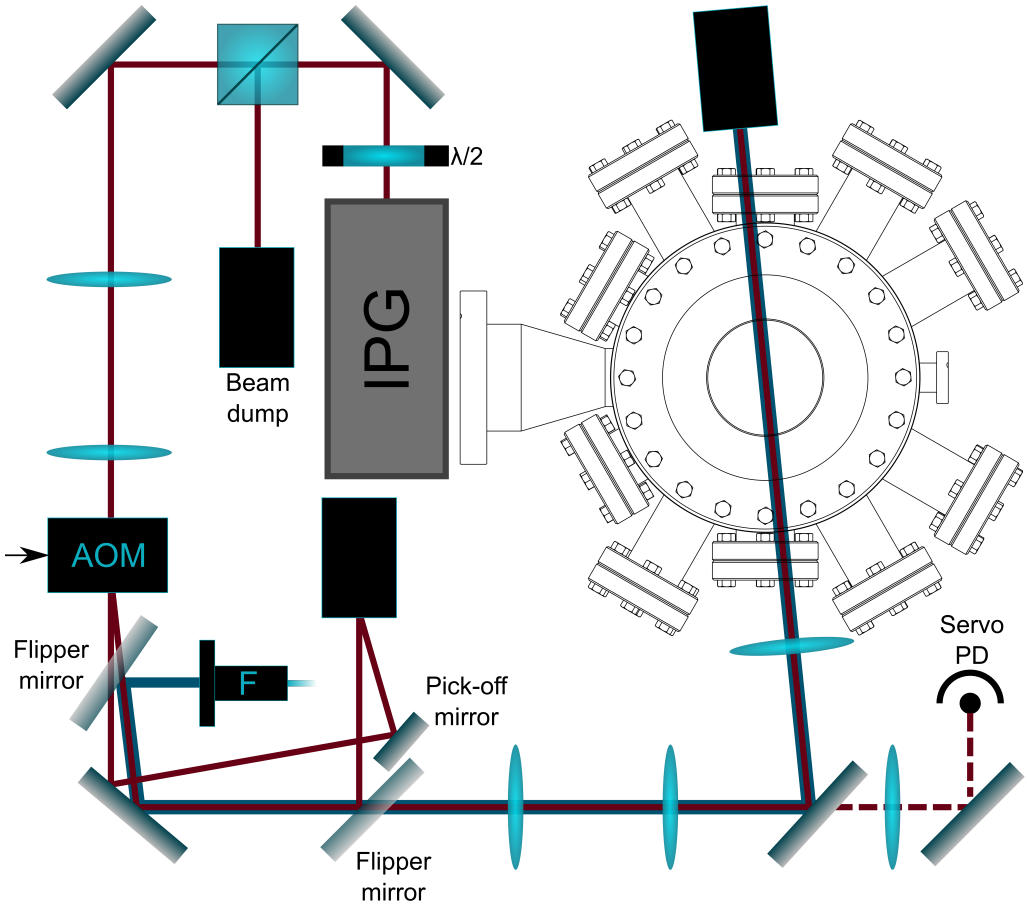

Figure 5.3: A schematic (not to scale) showing the standard setup of the dipole trapping laser. The power of the trapping beam is controlled using a water-cooled AOM and a flipper mirror is used for quick dumping of the beam (red line). A typical single beam setup is shown. A telescope is used to resize the beam profile before an achromat is used to focus the beam into the science chamber. A drawing of the science chamber is included for reference, showing the beam path through the chamber and into the final beam dump. Also shown is a fibre coupler and flipper mirror combination that are used to align the dipole trap to the MOT by using resonant 399 nm light (blue line).

the final lens, this is used to set the single beam trap to pass through the allocated dipole trap viewports at an angle of 5 ° from normal incidence, and is the basis of most of our optical traps.

The power of the trapping beam is controlled in two ways. Coarse tuning of the power in the beam is provided by use of an analogue input to the fibre laser control panel, allowing direct control of the output power at the fibre laser head. This control is typically only for setting the starting power of the dipole beams or for the start of power ramps in our sequences. We find

that changing the power of the fibre laser output has a small effect on the size of the beam waist at the focus, an effect possibly attributed to thermal lensing in the fibre head itself. The RF power input of the AOM is used as a finer control over the trapping beam power. The light transmitted through the final mirror in figure 5.3 is focussed onto a photodiode and used to servo the light level. An analogue control voltage is supplied from the LabVIEW control software to the servo, and the resulting negative feedback is sent to the input of the AOM RF amplifier.

We have also found that thermal lensing can cause the waist position of the single-beam trap to move by up to 20 mm when using a simple high-power plano-convex lenses as the final optic. However, this is minimised to around a 1 mm displacement when using an achromatic doublet as the final optic; this is within the Rayleigh range of our beam focus and as such is negligible. Despite this improvement, we still found that the trap waist would evolve over time as the dipole trap laser was turned on. Eventually we established that all of the high-power plano-convex lenses needed replacing with achromatic doublets to minimise this effect, the first lens after the fibre head in the setup in particular proved crucial to the focussing stability of the beam.

5.3.2 Alignment of the trap

Light from the 399 nm probe fibre is used to align the dipole trap to the cold Yb atoms in the MOT. By using a combination of a fibre output coupler and a flipper mirror, the resonant probe light can be aligned to follow the same path as the dipole trapping light. Although the optics in the system are not AR coated for 399 nm, enough light reached the science chamber to observe a "hole" being burnt through the MOT by the probe light. The starting point was to see a visible effect of the probe light on the MOT in loading conditions. Following this, a sequence was set up to ramp the power of the MOT light down to the value used for optimal gravitational sag cooling of the MOT, as discussed in section 4.4.2. The ramp was set to occur over an interval of several seconds as opposed to the 100 ms used in the actual MOT cooling process. By repeating this sequence we were able to trace the MOT's movement with the dipole beam by adjusting the final mirror of the

dipole trap until a hole was burnt through the MOT in its final position. This process was repeated by adding the detuning ramp that optimises the cooling and compression of the MOT. Again the probe beam was walked with the MOT position using the dipole trap optics until aligned with the MOT at the end of the detuning ramp. At this point the MOT was so small and cool that the probe light would destroy the MOT. This method provides a visible way of aligning a tightly focussed trap to the cold Yb atoms; once the probe beam is aligned the flipper mirror is retracted and only small adjustments to the final optics are required to optimise the number of Yb atoms transferred to the optical trap.

5.3.3 Characterisation of the trap

Beam profiling

To measure the intensity profile of the dipole laser beam at various points in the setup, we use a CCD camera (Thorlabs, DCC1645C) to capture images of the beam and fit equation 5.19 to the images, following a subtraction of an image measuring the background light. This process uses single images to extract both $w_x(z)$ and $w_y(z)$ for a particular point in the beam path, or a series of images along the beam path, to use the beam widths to find the waist of the beam. Where the beam size is too large for the CCD camera, a knife edge is incrementally passed across the beam and the power remaining in the beam is recorded on a power meter. A fit to the integrated power in a Gaussian beam is then performed to find the beam width in the corresponding direction.

The obvious issue with using these methods to measure the dipole beam are the high powers involved; even in low power operation there is likely to be a power on the order of 100 mW focussed to a few tens of micrometers. To overcome this issue, and to check the operation of the beam at different powers, we insert a high-power mirror into the optical setup to dump the powerful beam and use the light transmitted through the mirror to make our measurements. These techniques were crucial in aligning the final telescope in the system to provide a well-collimated beam prior to the final lens. This

allowed some flexibility in measuring the focus of the beam after the final lens, since the waist would not be affected by small translations of the lens. We found the horizontal waist of the single beam trap to be (44 ± 1) μm and the vertical waist to be (43 ± 1) μm. The waist was approximately 295 mm from the final lens in the system. By using a translation stage to mount the final optic, small adjustments to the position of the waist relative to the atom cloud can be made to improve loading of the trap.

Trap depth

With the trap waists measured and the polarisability calculated, it is possible to estimate the trap depth of the single beam trap. For the trap operating at full power we would expect the depth to be around $U_0 = 500.6$ μK. One method to measure the approximate depth of the dipole potential is to perform a series of measurements of the Yb temperature for different hold times in the trap. We would expect to see plain evaporation as the hotter atoms escape, causing the remaining atoms to rethermalise and eventually reach equilibrium in the trap. We can define an evaporation parameter, η, relating the equilibrium temperature of the cloud to the trap depth

$$U_0 = \eta k_{\mathrm{B}} T. \tag{5.29}$$

In a single beam trap the evaporation surface tends to be from the bottom of the cloud, as seen in figure 5.2, whereas at high intensities crossed beam traps atoms may evaporate along one of the individual beams. In this single beam scenario it is found empirically that the equilibrium temperature reached is typically a factor of $\eta \approx 10$ times lower than the depth of the trap [189].

Figure 5.4 shows the dependance of Yb temperature on the hold time in the single beam trap for loading powers of 43.8 W and 21.9 W. Following the loading of the Yb MOT for 20 s and gravity assisted cooling by reduction of the MOT beam power and detuning, the dipole trap is switched on at one of these powers for a loading time of 1 s. After this loading period the MOT beams and magnetic field are switched off and the atoms are held in the optical trap for a period of time before measuring their temperature

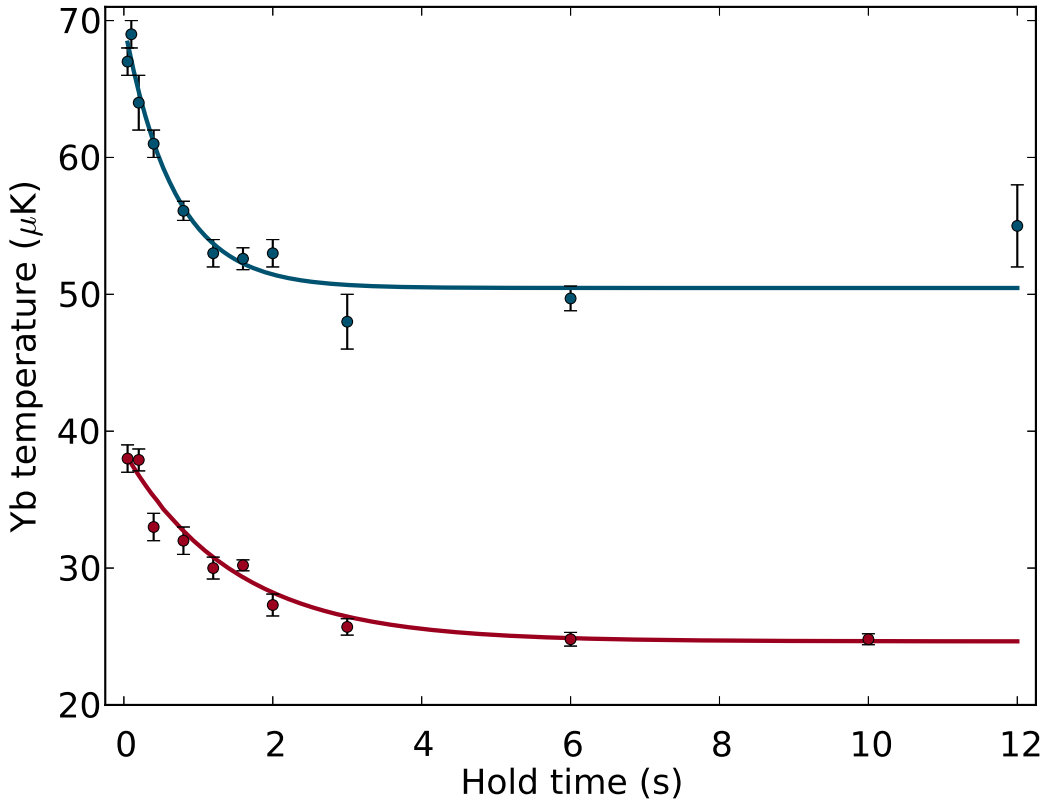

Figure 5.4: The data points show the evolution of the temperature of the trapped cloud of Yb as it is held in the single beam trap. The blue points show the temperature of the Yb when the trap is loaded at 43.8 W, whereas the red points show the temperature of the Yb when the trap is loaded at 21.9 W. The curves are exponential fits to the data. The Yb loaded into the 43.8 W trap stabilises to a temperature of 50.5 ± 0.6 μK over a $1/e$ time of 0.67 ± 0.09 s. The cloud in the 21.9 W trap reaches equilibrium at 24.6 ± 0.3 μK, with a $1/e$ time of 1.5 ± 0.1 s.

through time of flight expansion. By performing an exponential fit to the Yb temperature's temporal evolution, we find the atoms reach a temperature of (50.5 ± 0.6) μK with a characteristic time of (0.67 ± 0.09) s. By comparing this temperature to our modelled trap depth of 500.2 μK, we obtain $\eta = 9.9 \pm 0.1$. Similarly, at 21.9 W we measure a temperature of (24.6 ± 0.6) μK with a characteristic time of (1.5 ± 0.1) s. Using our model, we expect the trap depth to be around 249 μK. This gives a value of $\eta = 9.9 \pm 0.2$: both of the observed values of η are in line with the typical factor of 10. Note that the trap depth more than halves due to tilting by gravity, an effect that becomes even more pronounced at lower trap depths. We also find that the lifetime of Yb trapped in the single beam trap at full power is 12.3 ± 0.1 s

in this instance. More discussion of lifetimes in this trap will be presented in the following chapter.

Trap frequencies

Whilst our model is able to determine the trap frequencies of our optical trap configurations based on the power and waists of the beams, along with the polarisability of the species at the trapping wavelength, it remains useful to measure the trap frequencies in experiment to confirm the performance of both the model and the trapping beam itself. Throughout the work covered in this thesis we use one of two methods to measure trap frequencies: by parametric heating or by setting the trapped cloud into oscillation.

For the single beam trap we used parametric heating to determine the radial trap frequency. This method involves adding a sinusoidal modulation to the trap depth. This is achieved by using an arbitrary function generator to add a sine wave modulation to the AOM RF power in order to add modulation to the power of the optical trapping beam. To perform the measurement, Yb atoms were first cooled in the MOT and transferred to the dipole trap via the standard ramp of the MOT beam power and detuning. The transfer occurs with the dipole beam on at full power. This corresponds to 43.8 W with a servo control voltage of 10 V. A ramp of the dipole trap power down to 7.2 W occurs over the period of 1 s in order to further cool the atoms. Following this, the dipole trap power is then ramped back up to the desired value over 1 ms. The AOM servo is then modulated for 1 s at a set frequency. After a 50 ms hold time the atoms are released from the trap and their temperature is measured through standard time of flight expansion. This process is repeated to form a sweep of modulation frequencies for each trap power.

When the modulation frequency matches the second harmonic of the trap frequency (i.e. $\nu_{\mathrm{mod}} = 2\nu_{\mathrm{radial}}$), atoms in the trap are heated parametrically and a drop in the number retained in the trap is observed [195]. This is due to intensity fluctuations at twice the trapping frequency causing an exponential growth in the energy of the atoms in the trap [196]. It is also possible to observe sub-harmonic excitations at frequencies corresponding to $2\nu_{\mathrm{radial}}/n$, where n is a positive integer [197]. Figure 5.5 shows the heating

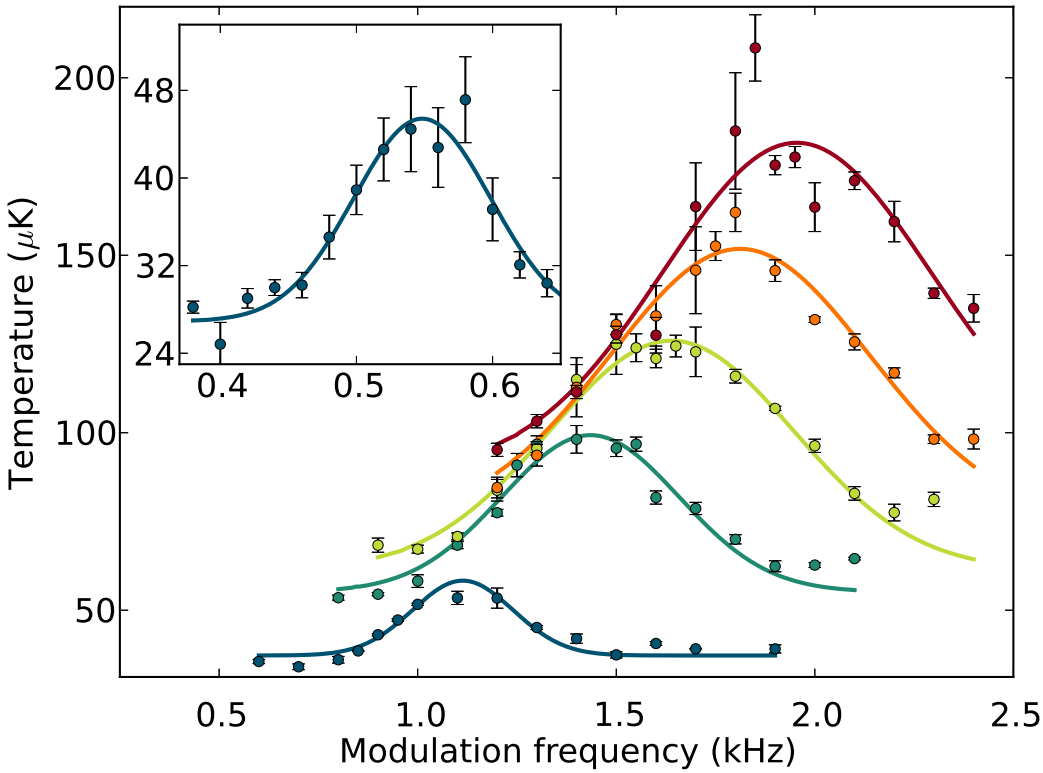

Figure 5.5: The main figures shows the temperature as a function of modulation frequency follow 1 s of parametric heating in the single beam trap. The powers used were 13.1 W (blue points), 21.9 W (teal), 27.6 W (green), 33.3 W (orange), and 39.4 W (red). The solid curves shows the result of Gaussian fits to the data from which the harmonic of the radial trap frequency is extracted. For these data the modulation peak-to-peak amplitude was 12 % of the central beam power. The inset shows the heating observed at the fundamental excitation frequency for atoms in the beam at 13.1 W. These data were obtained using a modulation amplitude of 20 %.

observed at a number of beam powers in the single trap, including Gaussian fits to the peaks in the temperature to determine the harmonic of the trap frequency. For these measurements a modulation with a peak-to-peak amplitude of 12 % of the central servo value was used. Also shown in the inset to figure 5.5 is the fundamental excitation for a AOM servo value of 3 V (13.1 W beam power). The observed value of (0.55 ± 0.02) kHz is in good agreement with the observed value of the corresponding harmonic frequency of (1.11 ± 0.06) kHz. Figure 5.6 summarises the measured trap frequencies and shows a fit of the form $\nu_{\mathrm{trap}} = \nu_{\mathrm{trap,max}}\sqrt{P/P_{\mathrm{max}}}$, where P is the beam power and $\nu_{\mathrm{trap,max}}$ is the trap frequency at the maximum beam power of $P_{\mathrm{max}} = 43.8$ W. The fitted value of $\nu_{\mathrm{trap,max}}$ is 1.02 ± 0.03 kHz, this is within

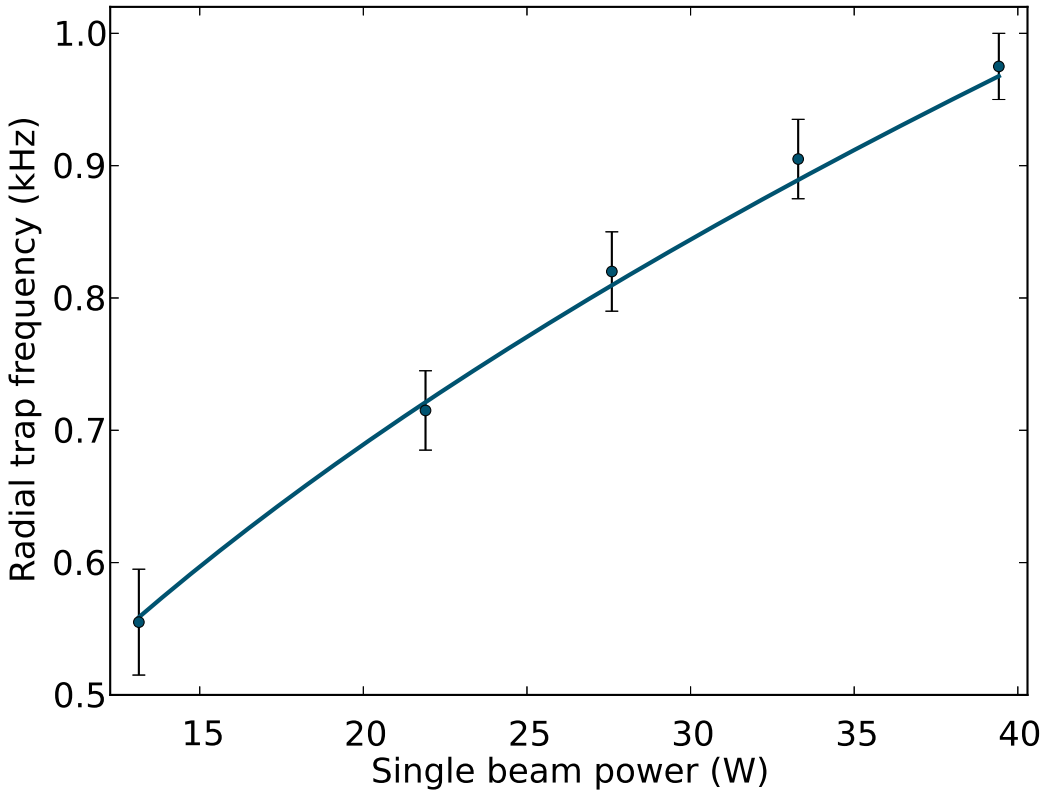

Figure 5.6: The fitted trap frequencies from the data presented in figure 5.5. The frequencies plotted are half the measured harmonic frequencies in order to estimate the trap frequencies. The solid curve shows a fit to the expected square root growth of the trap frequency with dipole trap beam power.

4 % of the expected value from our model. Note that it was not possible to observe the low axial trapping frequency for this beam. However, given the similarity between the observed and measured radial frequencies we were confident that our model will produce suitable estimates.

5.3.4 Optimising trap loading

Given that ground state Yb has no magnetic moment to allow magnetic trapping to tighten the trap along the dipole beam axis, the low axial trap frequency will significantly limit the elastic collision rate within the trap. It follows that the creation of quantum degenerate gases of Yb is more suited to a crossed trap with higher trapping frequencies in all directions. However, the single beam trap forms one of the beams of the crossed trap and presents an opportunity to easily optimise the transfer of atoms from the MOT to the

optical trap. The following sections present a series of figures showing the optimisation of the transfer for a variety of MOT parameters, resulting in a maximum transfer of 1.4×10^7 atoms into the single beam trap.

In each section the basic experimental sequence remains the same. As one might expect, we find loading the MOT for a longer period of time results in more atoms being transferred to the dipole trap, owing to the losses incurred when the MOT power and detuning are changed. As a result, we choose to load the MOT for 20 s. This is followed by a simultaneous linear ramp of the MOT beam power and detuning over 200 ms. The single beam dipole trap beam is then turned on at full power (43.8 W) via the AOM, whilst the MOT remains at the final beam power and detuning for a hold time before both the MOT beams and field gradient are switched off. Following a 50 ms hold in the dipole trap, the atoms are released from the trap by rapid switching of the dipole beam AOM, and the atom number is measured by absorption imaging. In relation to section 5.3.2, we find that the atom number transferred to the trap is highest when the final shim fields for the MOT are set so that the MOT is slightly displaced along the optical trapping beam. This can be observed by imaging with and without the dipole trap turning on and finding the difference in centres of the MOT and the centre of the optical trap. Owing to the imaging geometry and the large discrepancy in the size of the MOT and optically trapped atoms, the exact distance is hard to quantify. However, we estimate that it is approximately 5 mm, which is comparable to the Rayleigh range of the trapping beam and is in line with the results presented in reference [198]. This corresponds to a point where the relative size of the equipotential surfaces of the trapping potential produce greater spatial overlap with the MOT.

MOT hold time and initial trap depth

The first parameter optimised in the experimental sequence is the time the MOT is held whilst the dipole trap is turned on following the detuning and power ramps of the MOT beams. The main graph of figure 5.7 shows the variation of the atom number trapped following the 50 ms hold in the optical trap as the hold time of the MOT is varied. In this instance the MOT beam

detuning and total intensity are at their optimum values as determined in the following two sections: -1.25 MHz and 4.6 I/I_{sat} respectively.

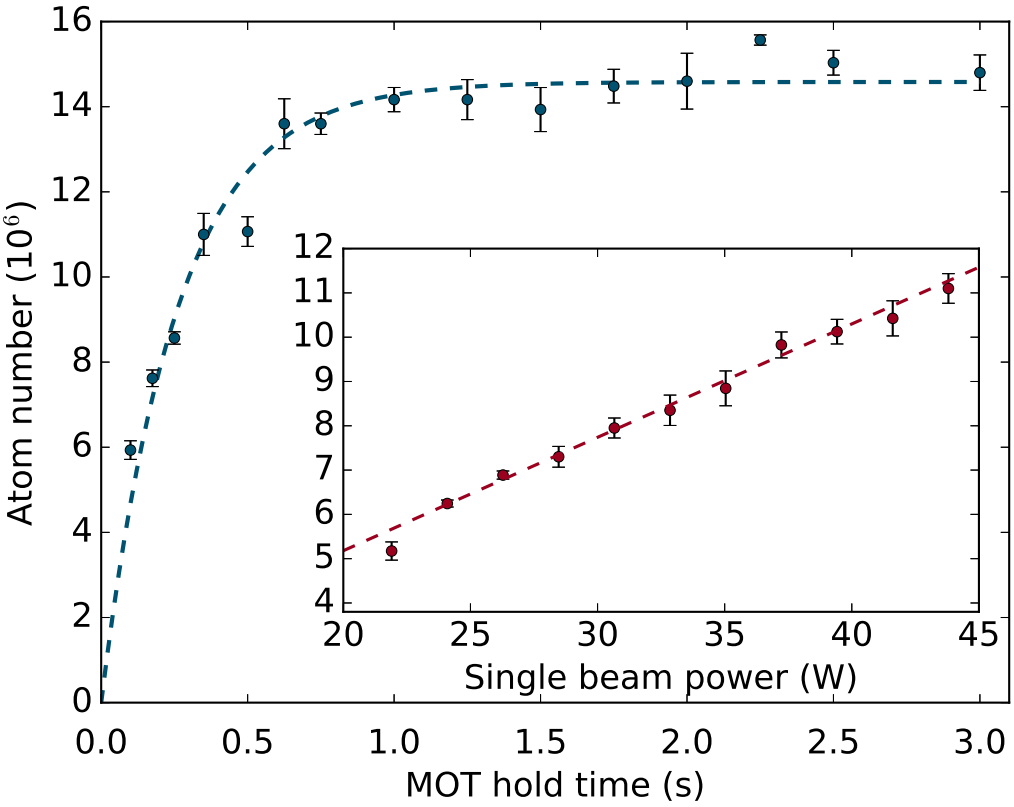

Figure 5.7: The main figure shows the atom number transfer to the single beam trap as the MOT hold time is varied following a ramp of the MOT beam intensity and detuning to 4.6 $I_{\mathrm{total}}/I_{\mathrm{sat}}$ and -1.25 MHz. The blue curve is a guide to the eye, showing a saturation of the atom number after 1 s of hold time. The inset shows the atom number loaded to the single beam trap as the "turn-on" power of the trapping beam is varied. The power of the trapping beam is determined by a measurement after the beam has passed through the chamber. The line shows a linear fit to the data.

We observe a sharp increase in the number of trapped atoms up until around half a second of trap loading, following which we observe the saturation of the atom number after 1 s. This sharp increase is likely due to the timing of the optical trap being turned on: the optical trap potential will take some time to settle into its final position and beam waist due to thermal lensing effects. Saturation is expected due to the reduced loading rate of the MOT from the atomic beam at this combination of intensity and detuning, and loss mechanisms in the trap will start to overcome the loading rate [199]:

at longer hold times we would expect to see the atom number start to fall. However, the figure shows that the transfer to the trap is fairly stable for MOT hold times between 1 and 3 s. We chose to hold the MOT for 2 s in our experimental sequences; whilst this may be longer than necessary to saturate the trap loading under typical conditions, it still allows optimal optical trap loading even in runs where MOT loading is less than optimal.

The inset to figure 5.7 shows the variation of the number of atoms transferred to the single beam trap as the trapping beam power is changed. As expected, the atom number increases as the beam power, and hence the trap depth increases. We observe no saturation effects as the beam power is increased, implying that the limit to the transfer to the optical trap is the beam power available. The solid red line in the inset of the figure shows that a linear increase in atom number occurs in this regime of the optical trap beam power.

MOT beam intensity and detuning

As we saw in section 4.4.2, both the MOT beam intensity and detuning have a significant effect on the temperature of the atoms. We have also seen that at low MOT beam intensities, the position of the MOT becomes incredibly sensitive to either of these parameters. It is for this reason that we attempted to align the dipole trap to the position of the MOT at the end of the intensitiy and detuning ramps using the techniques outlined in section 5.3.2. As we shall see when discussing the crossed dipole trap, the so-called "mode-matching" of the cold atoms to the optical trap can have a dramatic impact on the efficiency of evaporative cooling [200]. As such the final position and density of the MOT can affect both the number and temperature of the atoms transferred to the dipole trap [198, 201].

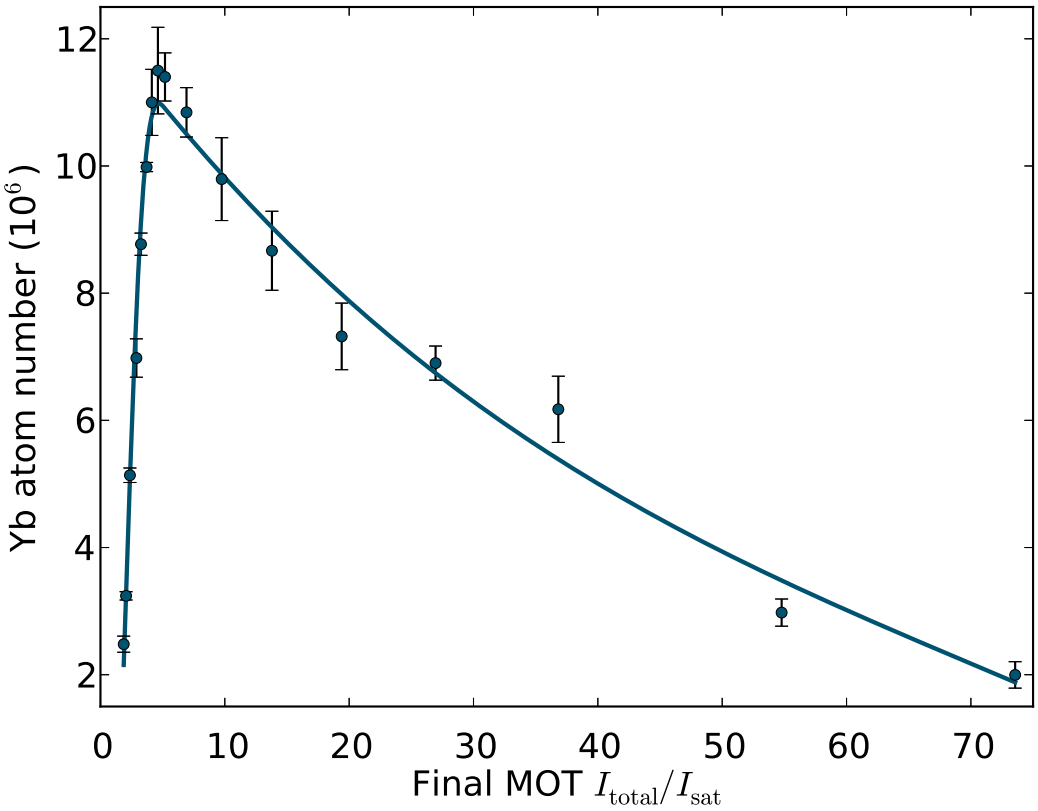

Figure 5.8: The number of atoms transferred to the single beam optical trap with a 20 s MOT loading time, followed by a 200 ms linear ramp of the MOT beam detuning to -1.25 MHz and a simultaneous ramp of the MOT beam intensity. The MOT is held at these parameters for 2 s before the beams and magnetic field gradient are turned off. The dipole trap remains on for a further 50 ms before absorption imaging is used to measure the atom number. The blue points show the variation of the trapped atom number with the final intensity to which the MOT beams are ramped. The blue curve shows a guide to the eye, indicating that the optimal transfer to the dipole trap occurs at around 4.6 $I_{\text{total}}/I_{\text{sat}}$

Figure 5.8 shows the impact on the atom number transferred from the MOT to the single beam trap as the final intensity of the MOT beam ramp is varied. The final detuning of the MOT beams is -1.25 MHz for all points in the figure. We observe a very sharp increase as the final MOT total beam intensity is increased from zero, with a maximum in atom number transferred occurring for a total beam intensity of 4.6 $I_{\text{total}}/I_{\text{sat}}$. At final ramp intensities greater than this value, the transfer to the single beam optical trap falls, albeit at a much lesser rate than for intensities lower than the optimum.

Figures 4.16 and 4.19 provide an explanation of the behaviour observed.

The maximum transfer occurs at an intensity that produces our optimum MOT temperatures. This is as expected since the dipole trapping beam was aligned to the MOT position with these detuning ramps in place. The figures show that as the intensity reduces further we can expect a very large shift in the vertical MOT position and more dramatic flattening on the shape of the MOT. Both of these effects will result in a vastly reduced overlap with the optical trap, causing the atom transfer to reduce considerably. In addition to this, at very low MOT beam intensities the linewidth of the transition is very narrow, and the MOT becomes unstable due to intensity and detuning noise, further reducing transfer to the optical trap. We can see from figures 4.16 and 4.19 that, for intensities higher than that for optimum transfer, the loss is not going to be as significant. This is because the spatial extent of the MOT increases and the rate of displacement of the MOT is lessened at higher MOT beam intensities. The result of this is that there is likely to always be some overlap of the Yb MOT with the optical trap at higher MOT beam intensities, allowing for transfer of atoms. However, at these higher intensities the higher temperatures of the atoms and the misalignment between the MOT and trap centre result in lower than optimal transfer.

Similarly, at low MOT beam intensities the detuning of the beams can cause a significant effect in the position of the MOT. This is illustrated in the inset of figure 4.19. Whilst the displacement is not as significant as for a change in intensity, it may still be considered large compared to the waist of the trapping beam.

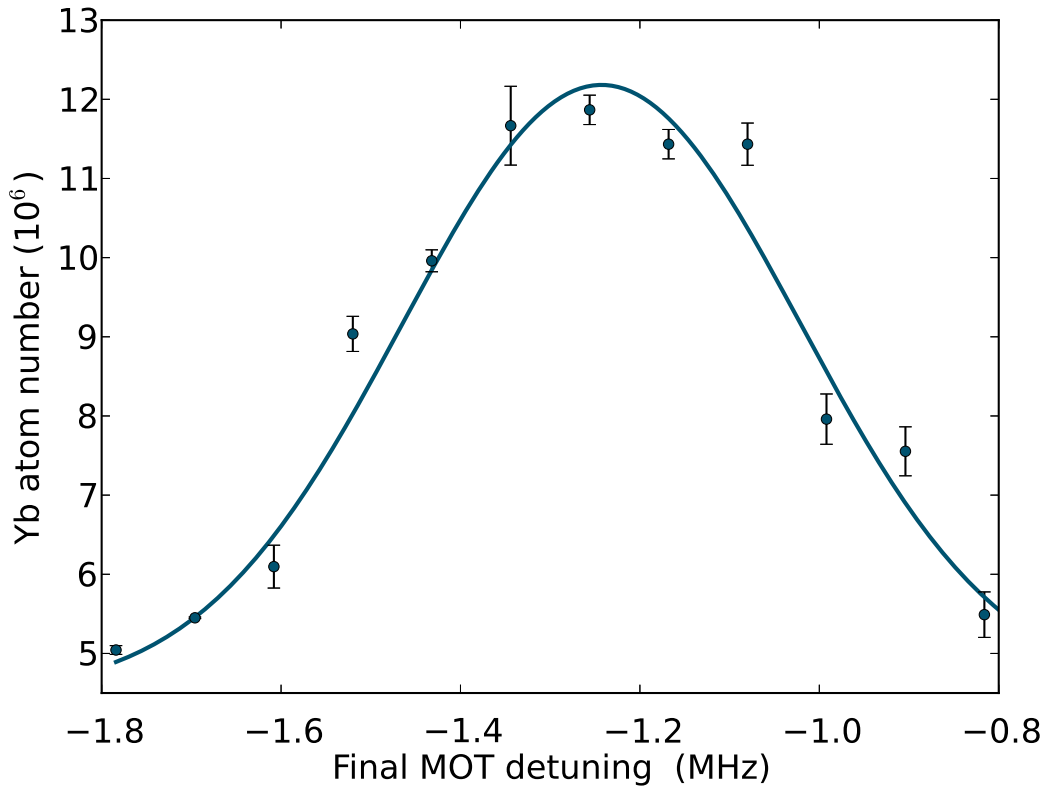

Figure 5.9: The Yb MOT is loaded for 20 s, followed by a 200 ms ramp of both the MOT beam power and detuning. During this step the total MOT beam intensity is ramped from the maximum available down to 4.6 $I_{\text{total}}/I_{\text{sat}}$ and the final MOT beam detuning is varied. The MOT is then held for 2 s whilst the dipole trap is loaded, after which the MOT beams and magnetic field gradient are turned off. After a 50 ms hold in the dipole trap, the number of Yb atoms remaining is determined using absorption imaging. The blue points show the number of Yb atoms in the trap as a function of the final Yb MOT detuning. The blue curve shows a Gaussian fit to the data, which yields and optimum detuning of -1.25 ± 0.05 MHz.

Figure 5.9 shows the impact of the final MOT beam detuning on the atom number transferred from the MOT to the single beam optical trap. As with the MOT beam intensity there is a clear optimum in the transfer efficiency. This occurs at a MOT detuning of $-(1.25 \pm 0.05)$ MHz and compares again to the value of the detuning used in the MOT ramp when aligning the trap. In this instance the reduction in the transfer to the optical trap is fairly symmetric. In figure 4.16 we can see that for a fixed MOT beam intensity the change in vertical MOT position for a given change in MOT beam detuning is approximately linear. This suggests that the variation of transfer efficiency due to changes in MOT beam detuning is predominately due to changes in

the spatial overlap between the MOT in its final state and the optical trap. Following these two investigations we choose to set the MOT beam intensity and detuning at 4.6 $I_{\text{total}}/I_{\text{sat}}$ and -1.25 MHz respectively for all experiments with the single beam optical trap.

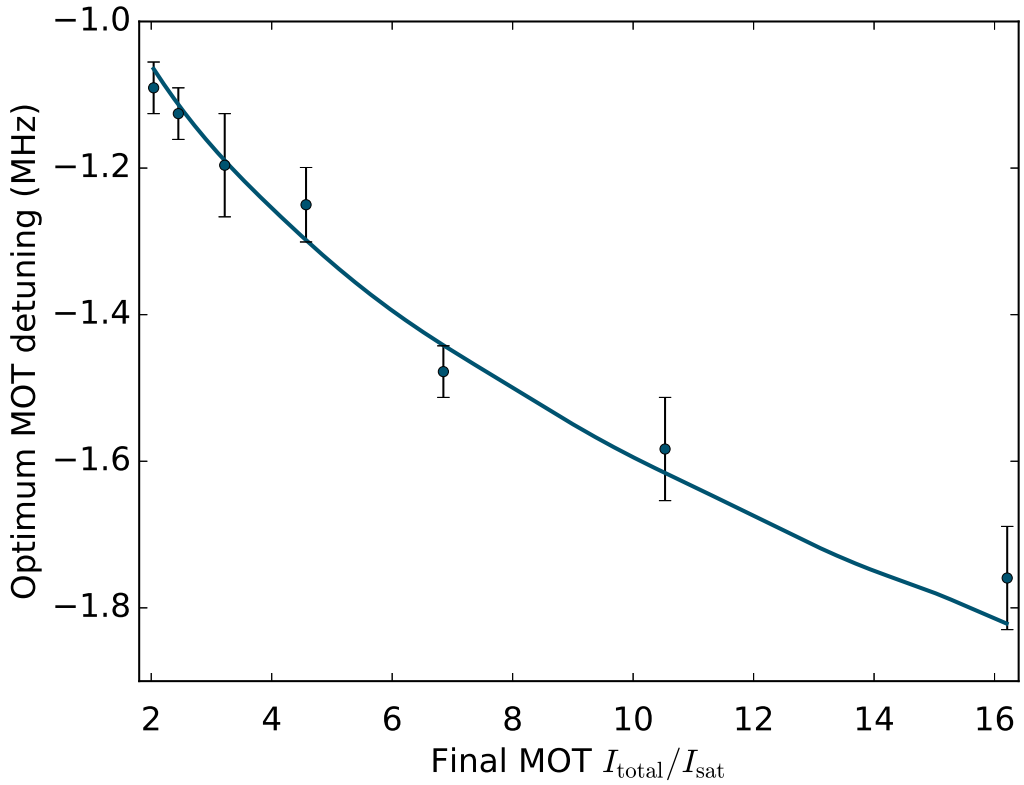

Figure 5.10: The blue points show the optimum final MOT detuning for loading Yb into the single beam dipole trap. These are determined from fits similar to those in figure 5.9 at various final MOT beam intensities. The blue curve is a prediction of the optimal detuning based upon the point at 3.26 I_{sat} and using equation 4.29 to solve for the detuning at which the Yb MOT is at the same vertical position as for this point.

To further investigate the implied correlation between the final vertical position of the MOT and the loading into the single beam trap, we have performed an experiment to find the optimum final MOT detuning for a number of final MOT intensities, extracting the optimum from fits to data such as that shown in figure 5.9. Figure 5.10 shows the the results of this experiment, with the magnitude of the detuning found to increase with the final MOT beam intensity as we would expect from our findings in section 4.4.2. The curve in the figure is a prediction from the code used to produce figure 4.16.

We take one point on the graph and use the recorded MOT detuning and intensity to calculated the position where the forces due to the up-down MOT beams and gravity balance. The code is then used to find the detuning that gives this vertical MOT position for the range of MOT beam intensities considered. The excellent agreement between this curve at the data suggests that the extent of the MOT sag under gravity is pivotal in determining the efficiency of the transfer to the optical trap. We should note that this graph shows the optimum detuning for a given intensity, we still find the global optimum to be at a MOT intensity and detuning of 4.6 $I_{\text{total}}/I_{\text{sat}}$ and -1.25 MHz respectively, corresponding closely to the parameters used to produce our coldest Yb MOT.

5.3.5 Light shift of the $^1S_0 \rightarrow {}^3P_1$ transition at 1070 nm

As we have seen previously, a red-detuned dipole trap requires a positive ground state polarisability in order to trap atoms in an intensity maximum. However, the excited state will have a polarisability too, which may be different to that of the ground state. Such a differential shift in the ground and excited state energies will consequently mean a change of the detuning required to excite trapped atoms from the ground state to the excited state. The wavelength at which this shift in energy is zero is termed a "magic wavelength" [202].

To calculate the excited state polarisability, one can proceed exactly as for calculating the approximate ground state polarisability: using equation 5.15 with the transition frequencies and Einstein A-coefficients for the possible transitions from the excited state. It has been difficult to find literature in which direct measurements of the A-coefficients have been made, and so for some transitions calculated values have been used [203]. We have based our calculation of the $^3P_1$ state on 31 transitions from references [203, 204]. These are summarised in table 5.3.

λ_{vac} (nm)	A-coefficient (s^{-1})
1540.0	9.2×10^5
1480.0	1.6×10^5
1032.4	1.5×10^5
678.4	2.5×10^7
609.8	3.45×10^6
555.8	-1.15×10^6
495.5	8.33×10^6
489.5	8.33×10^6
457.5	6.18×10^6
456.9	1.3×10^7
405.6	7.14×10^6
494.3	1.47×10^7
395.8	1.17×10^7
395.2	1.62×10^7
393.1	3.85×10^7
391.5	5.49×10^5
389.6	7.14×10^6
387.4	7.14×10^6
387.2	8.33×10^6
386.4	8.44×10^7
384.2	2.0×10^7
380.8	2.22×10^6
379.2	1.12×10^7
377.9	4.55×10^7
377.7	8.66×10^7
368.1	4.0×10^6
360.5	1×10^4
357.6	1.89×10^7
356.2	2.5×10^6
337.9	8×10^6
259.5	5×10^5

Table 5.3: A table of the 31 transitions considered in the calculation of the $^3P_1$ state polarisability of the Yb atom. The wavelengths and A-coefficients are taken from [203, 204]. Note that the A-coefficient for the $^3P_1 \rightarrow {}^1S_0$ transition is negative to represent the fact that it is a decay as opposed to an excitation.

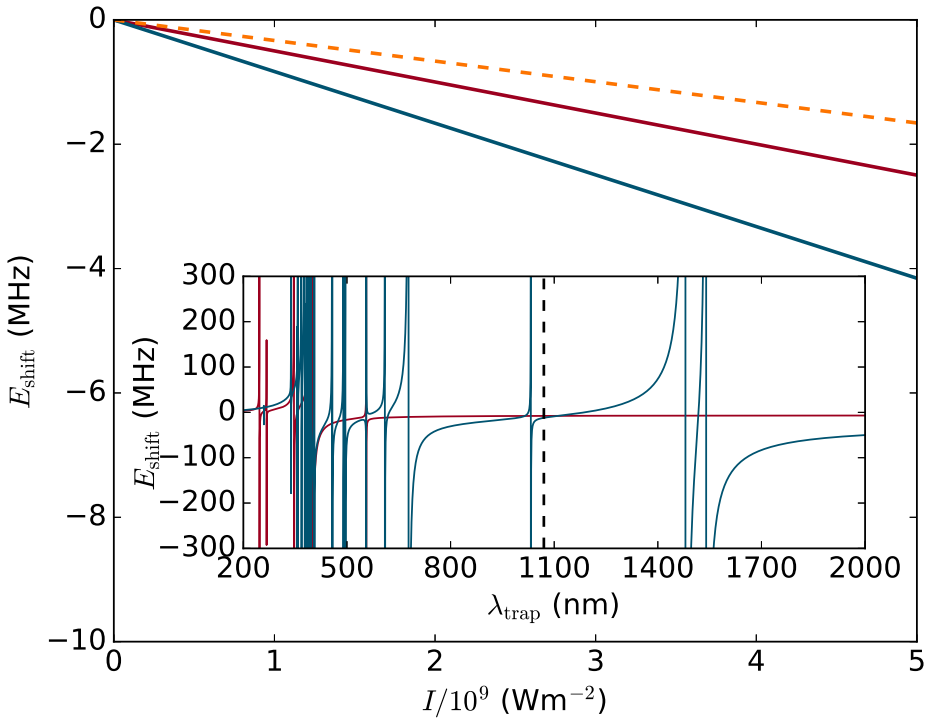

Figure 5.11: The main figure shows the expected light shift in the energy of the $^1S_0$ state (red curve), the $^3P_1$ state (blue), and the resulting change in the transition frequency (orange dashed). These curves are calculated for a trap wavelength of 1070 nm. The inset to the main figure shows the calculated light shift of the two states as a function of trap wavelength for a typical single beam trap intensity of 1.5×10^{10} W m^{-2}.

Figure 5.11 shows the calculated energy shift for the ground and excited states as a function of dipole trap intensity for a wavelength of 1070 nm. These are calculated using the values in tables 5.2 and 5.3. Both states are found to decrease in energy as the intensity of the laser field increases, with the light shift greater for the excited state. This scenario results in the reductions of the resonant frequency for the $^1S_0 \rightarrow {}^3P_1$ transition; the effective detuning from the undressed transition will become red-shifted. From the calculation used in figure 5.11 we estimate a light shift at 1070 nm of around 3.3×10^{-10} MHz W m^{-2}.

The region of the cloud of trapped atoms with the highest density will naturally align itself with the highest intensity region of a red-detuned optical trap. For a single beam trap, the intensity in this location is very well de-

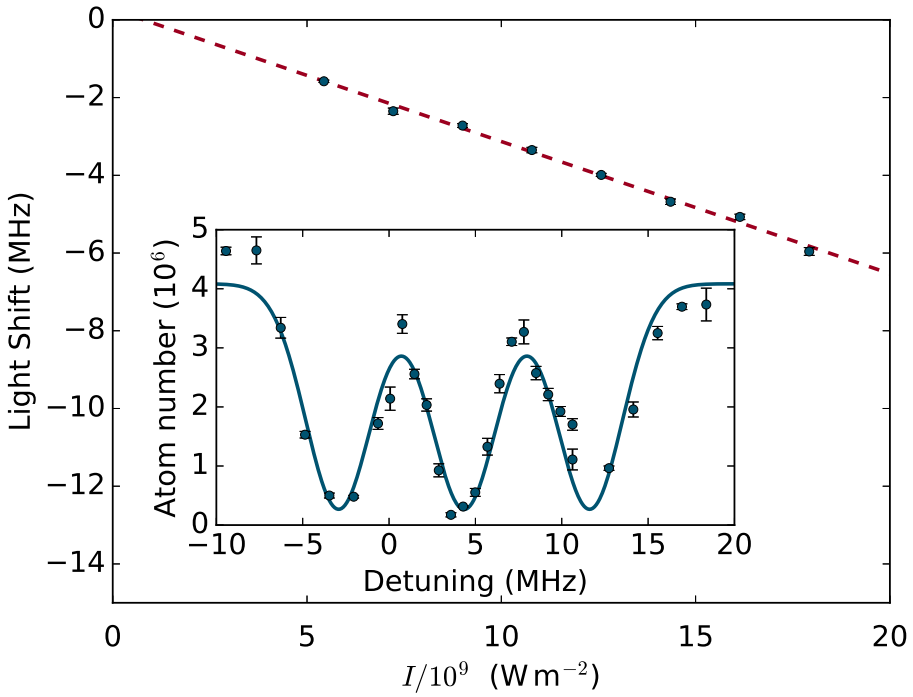

Figure 5.12: The main figure shows the measured light shift from the resonant frequency of the undressed $^1S_0 \rightarrow {}^3P_1$ transition at different intensities. The red dashed line is a fit to the data, yielding a light shift of $(3.34 \pm 0.04) \times 10^{-10}$ MHz W m^{-2}. The inset to the figure shows an example of how the light shift was extracted from the number of atoms remaining in the single beam trap following a pulse of the 556 nm MOT light at different detunings.

fined and offers an opportunity for measuring the light shift of the $^1S_0 \rightarrow {}^3P_1$ MOT transition in a trap with $\lambda_{\text{trap}} = 1070$ nm. Furthermore, this is another test of the detuning of the 556 nm MOT laser. To measure the light shift we load the Yb MOT for 20 s, cool the atoms further using the gravitational sag method, and then switch the dipole trap on at 47.3 W. The atoms from the MOT are loaded into the single beam trap for 2 s before switching the MOT beams and magnetic field gradient off. The dipole trap power is then ramped to a known value in 50 ms. At this point a 3.5 G bias field is applied. Following this the MOT beams are set to a detuning and flashed on for 50 ms with a total intensity of 5.9 I_{sat}. The atom number remaining is then measured using absorption imaging. This process is repeated, varying the detuning of the MOT beam flash enables the mapping out of the hyperfine substates of the $^3P_1$ state. By fitting a triple Gaussian to the data we are able to obtain

the light shift of the transition by finding the centre of the magnetically insensitive transition to the $m'_J = 0$ state. The inset to figure 5.12 shows the spectrum obtained after a ramp to a single beam trapping power of 33.2 W.

Figure 5.12 shows the result of this experiment when the intensity in the dipole trap is varied. We obtain a light shift for the triplet transition of $(3.34 \pm 0.04) \times 10^{-10}$ MHz W m^{-2}. This value appears to be in excellent agreement with the light shift calculated above. However, the calculation is extremely sensitive to the number of states used and their associated transition strengths. Given the doubt over the reliability of the values used in the polarisability calculation, we will not claim that the model agrees with the result observed.

5.4 The crossed dipole trap

Setup of the crossed trap

Whilst the single beam optical trap provided a suitable testing ground for our first attempts at optically trapping ^{174}Yb, the lack of confinement along the beam is not conducive to the evaporative cooling to quantum degeneracy. To provide confinement in all directions, we have opted to use a crossed beam trap based on the previous single beam trap. In this trapping geometry, atoms are typically trapped within the two individual beams and transferred collisionally to the small region at the crossing of the beams. In this "dimple" of the trap potential, trap frequencies are high and lead to fast rethermalisation of the ensemble of atoms.

The primary beam of the crossed trap is still setup as for the single beam trap shown in figure 5.3, with the exception of one change to the optics. Previous successful attempts at making quantum degenerate Yb in other groups worldwide have utilised tighter traps with narrower beam waists than that used in our large-volume single beam trap [117, 176, 205]. For this reason we have opted to change the optics in the final telescope in the beam path to those in figure 5.13, allowing a beam waist for beam 1 of $w_{1,x} = 33$ μm in the horizontal plane and $w_{1,y} = 28$ μm in the vertical plane. The final focussing lens to achieve this waist remains a 300 mm focal length achromat, which is

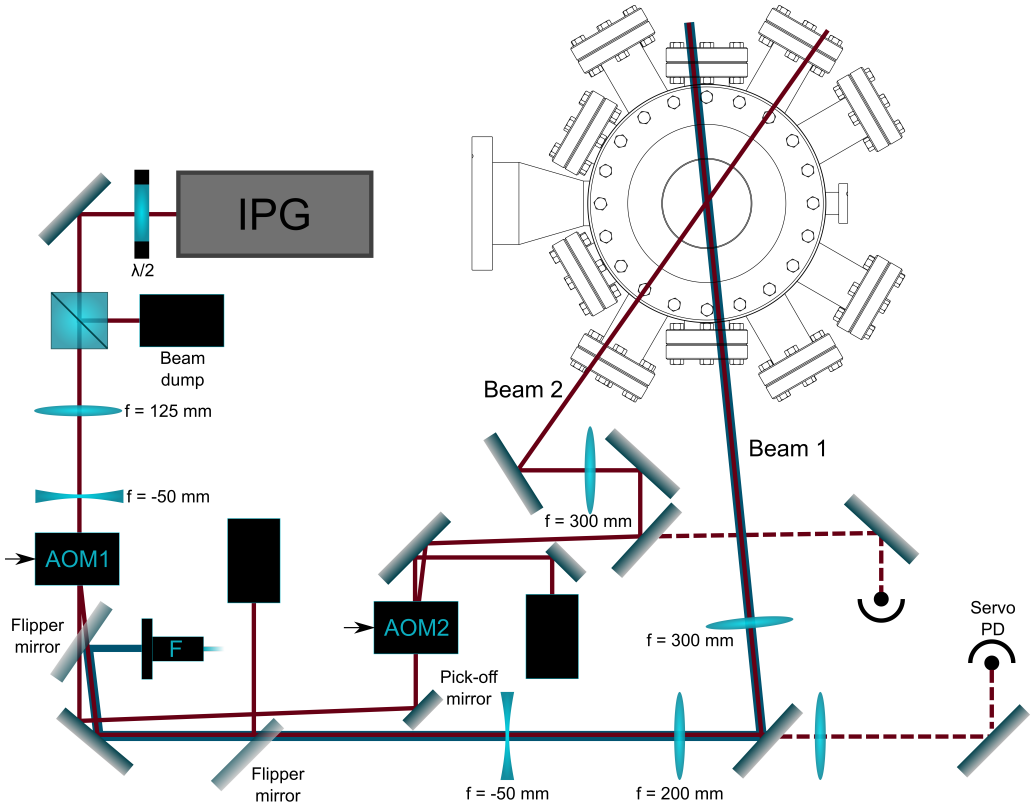

Figure 5.13: Schematic showing the optical setup for the crossed dipole trap. Beam 1 has the narrower waist of the two beams at 33 and 28 μm in the horizontal and vertical directions respectively. The optical path for this beam is unchanged from that used in the single beam trap, with the exception of the beam size being expanded further in the final telescope before the focussing of the trap. Beam 2 has a waist of 73 and 76 μm in the horizontal and vertical directions respectively. The powers in the beams are controlled by a series of two AOMs. The 300 mm focal length achromatic lenses used for focussing the beams into the science chamber are both mounted on translation stages. The beams are dumped after passing through the chamber (not shown on the figure). Note that for convenience the setup is not shown to scale and simplified beam paths are shown.

mounted on a translation stage to allow the focus to be precisely tuned.

Instead of dumping the zeroth-order light from the AOM as in figure 5.3, we now use this light to form the second beam of the crossed trap. A pick-off mirror is used to pass the zeroth-order light from AOM1 through a second AOM (AOM2 in figure 5.13). The resulting first-order diffracted beam from this AOM is used in order to control the power in beam 2. Once more, the light passing through the back of a mirror in the beam path is focussed onto a

photodiode in order to servo the power in the beam. This setup of two AOMs obviously restricts the relative power available for each of the two trapping beams. We have set the system of AOMs and photodiode servos such that there are 50 W available in beam 1 at maximum power with 40 W available for beam 2. Once more, a 300 mm focal length achromatic doublet is used to focus this beam to a waist of 73 and 76 μm in the horizontal and vertical directions respectively at the location of the atoms. This lens is mounted on a translation stage so that the focus of beam 2 may be precisely aligned to the focus of beam 1. Originally we attempted to use a small crossing angle of the two beams by passing both through the dipole trap viewports of the system, however this setup did not provide enough confinement along the axis of beam 1. Instead we have aligned beam 2 to pass through one set of the Cs MOT viewports, creating a 40° crossing angle for the trap. At full power we model this trap to have trap frequencies of 137 Hz, 2430 Hz, and 2070 Hz along the principal axes of the crossed trap region, and a trap depth of approximately 950 μK.

Alignment of the crossed trap

The 399 nm resonant probe light is again used to align the two beams to the atoms in the MOT at the end of it's intensity and detuning ramp. The fibre collimator shown in figure 5.13 can be used to copropagate the probe light with either beam in the setup by alignment of the collimator and the flipper mirror. The iterative process described in section 5.3.2 is used to walk the two beams towards the final position of the MOT after cooling through the gravitation sag method discussed in section 4.4.2.

Trap frequencies

We measure the trapping frequencies of the crossed dipole trap by setting the trapped atoms in motion and measuring the frequency of oscillation of the cloud in the trap. This is achieved by cooling the atoms in the trap using evaporation ramps, and then jumping the dipole trap beam powers up to some predetermined value, setting the cloud in oscillation. Owing to the gravitational tilt at low beam powers, this method is particularly

effective in measuring the vertical trap frequency. Following the jump in the trap depth, the atoms are held for a time before the vertical position of the cloud is measured using absorption imaging. When using this method, it is important the oscillation amplitude is small compared to the size of the cloud of atoms ($\sim$ 60 μm) and the waist of the trap [206]. This ensures that the atoms are only sampling the harmonic region of the trap and thus undergoing harmonic motion, allowing a sinusoidal fit to the oscillation and extraction of the trap frequency.

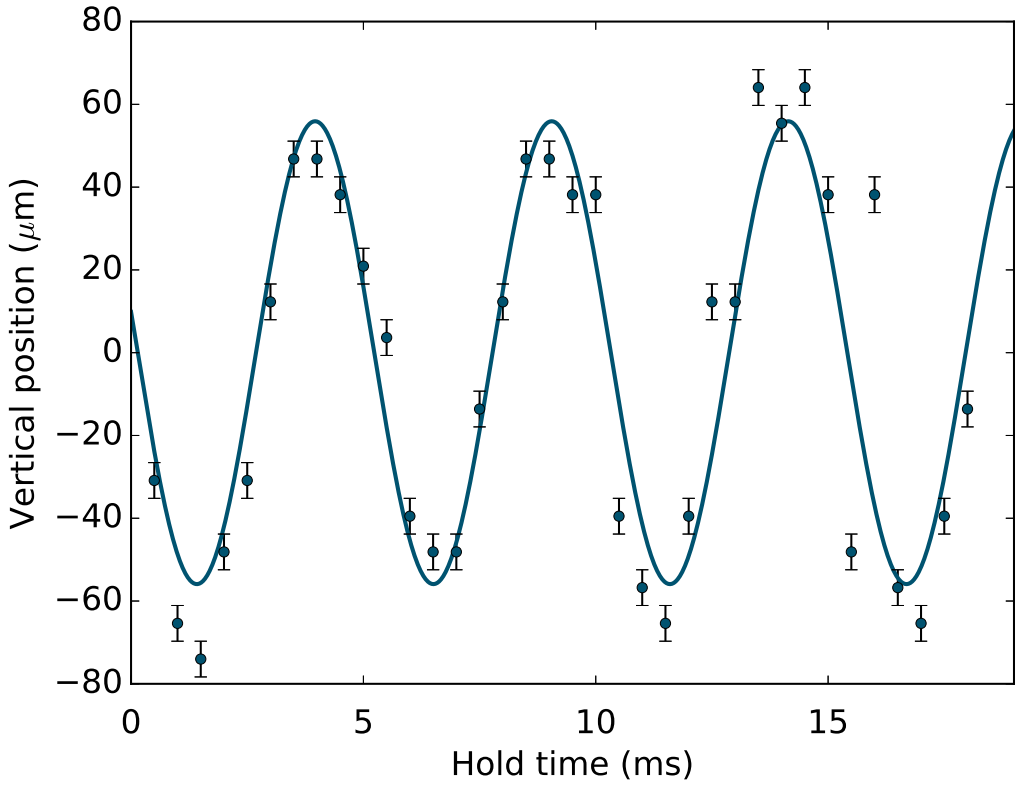

Figure 5.14: Measurement of the vertical trap frequency using the oscillation of the cloud of atoms. The atoms are first cooled evaporatively in the crossed dipole trap and then the trap is jumped back up to a power of 0.44 W and 0.73 W in beam 1 and beam 2 respectively. The vertical position of the cloud is shown as the hold time after the jump is varied. The blue curve shows a sinusoidal fit to the data, yielding a vertical trap frequency of $\omega_z = 2\pi \times (196 \pm 2)$ s^{-1}.

Figure 5.14 shows the vertical oscillation of atoms in the crossed dipole trap after the power in beams 1 and 2 have been simultaneously jumped to 0.44 W and 0.73 W respectively. From our model of the optical trap, we expect a

frequency of $2\pi \times 199$ Hz in this direction. The sinusoidal fit to these data gives a measured value of $\omega_z = 2\pi \times (196 \pm 2)$ s^{-1}, giving us confidence in the model. Similar comparisons to the model trap frequencies are found at different trap depths. Unfortunately, owing to the location of the camera we have not been able to measure the other two trap frequencies with confidence. The angle the absorption imaging probe makes to the optical trap beams means that the horizontal position of the cloud will be coupled to oscillations in the directions of both principal axes in the horizontal plane. In particular the larger trap frequency will contribute very little to the horizontal position of the cloud as seen by the camera. However, given that the model of the trap gives sensible results for the vertical trap frequency, we are confident in its ability to predict the remaining two trap frequencies.

5.5 Evaporative cooling in an optical trap

Evaporative cooling is a technique originally proposed by Hess for the cooling of hydrogen in a magnetic trap [207], but the technique may be readily applied to any form of trapped gas. The technique involves an initial thermal ensemble of atoms with a temperature T, and selectively removing atoms with energies at the high-energy tail of the thermal distribution. This leaves an ensemble with fewer atoms, but with a lower average energy per atom. By the process of rethermalising elastic collisions, the remaining atoms come into thermal equilibrium with a new temperature $T' < T$. By continuously removing high-energy atoms in a controllable manner it is possible to increase the phase-space density (PSD) of the ensemble by many orders of magnitude but with fewer atoms as a consequence.

For a non-quantum degenerate gas, the maximum PSD, $\mathcal{D}$, is given by [200]

$$\mathcal{D} = n_0 \lambda_{\mathrm{dB}}^3, \tag{5.30}$$

where n_0 is the maximum atomic density of the ensemble. λ_{dB} is the thermal de Broglie wavelength, defined as

$$\lambda_{\mathrm{dB}} = \sqrt{\frac{2\pi\hbar^2}{mk_{\mathrm{B}}T}}, \tag{5.31}$$

where m is the mass of the particle, and T is the temperature of the ensemble. For a harmonic trap with a geometric mean trap frequency of $\bar{\omega} = (\omega_x\omega_y\omega_z)^{1/3}$ the peak density is given by

$$n_0 = N\bar{\omega}^3 \left(\frac{m}{2\pi k_{\mathrm{B}}T}\right)^{3/2}. \tag{5.32}$$

This leads to a peak PSD of

$$\mathcal{D} = \frac{N\hbar^3\bar{\omega}^3}{(k_{\mathrm{B}}T)^3}, \tag{5.33}$$

and a peak elastic scattering rate of

$$\Gamma_{\mathrm{elastic}} = \frac{\sqrt{2}Nm\sigma\bar{\omega}^3}{\pi^2 k_{\mathrm{B}}T}, \tag{5.34}$$

where $\sigma = 8\pi a_s^2$ is the scattering cross section in the ultracold limit for an s-wave scattering length, a_s.

Figure 5.15 illustrates the concept of evaporative cooling in an optical trap. By reducing the power in the beams making up the optical trap, the trap depth is lowered and the atoms with the most energy are able to escape the trapping region. The remaining atoms are then able to rethermalise collisionally to a lower temperature. This technique has been used to efficiently cool atoms and create quantum degenerate gases of ytterbium, caesium, and many other species [5, 13, 17, 18, 20, 35, 117, 176, 201, 208, 209]. However, the stiffness of a pure optical dipole trap also reduces as the laser intensity is reduced. This results in the reduction of trap frequencies, causing the elastic scattering rate to fall, leading to longer rethermalisation time-scales as the trap depth reduces. As such in a standard optical trapping evaporation ramp, one does not achieve the concept of runaway evaporation, whereby the elastic collision rate increases during the evaporation process [193, 210]. However, for atoms with a ground state magnetic moment such as Cs, tilting the trap potential by using a magnetic field gradient can allow such a process

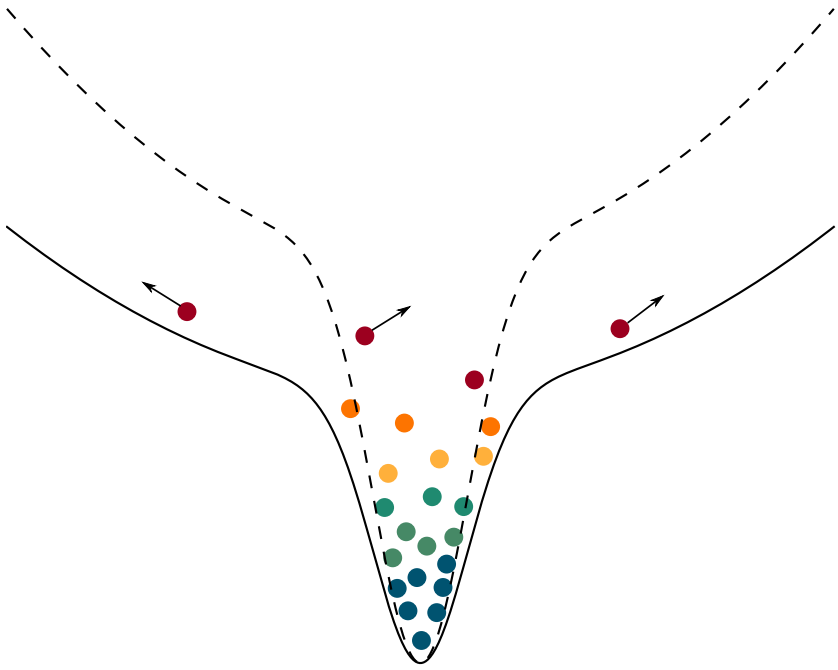

Figure 5.15: A illustrative drawing of an arbitrary crossed dipole trap potential. The dashed line indicates the potential in a horizontal direction for the trap at full power, whereas the solid line shows the potential after the trap beams have been ramped down to half power. By performing this ramp, the most energetic atoms are able to exit the crossed trap region, leaving an ensemble with a lower average energy. The trap frequencies are also reduced by lowering the optical trap intensity.

to occur. Despite this, the use of dynamic optical traps for fast evaporation of Yb to quantum degeneracy has recently been demonstrated [211]. With all of this in mind, one would expect that ramping infinitely slowly would allow the retention of a large number of atoms in the process. However, background collisions and inelastic loss mechanisms within the ensemble place a limit on how slow an evaporation ramp can feasibly occur.

In our experiment we use linear evaporation ramps of increasing length to produce condensed Yb. These ramps are realised by changing the power in the first-order diffracted beams of the AOMs in figure 5.13 by use of the photodiode servos. The following section discusses the optimisation of the loading into the crossed dipole trap by utilising evaporation ramps.

5.6 Optimal loading of the crossed trap

Optimisation of the transfer to the crossed dipole trap follows a similar approach to that used in section 5.3.4. However, with the crossed trap aligned, we attempt to optimise the phase-space density following two evaporation ramps for each of the MOT parameters. Due to mode-matching arguments [212], the phase-space density at the end of an evaporation ramp is sensitive to the phase-space density at the beginning of the ramp. To determine the phase-space density, we measure the atom number and temperature using time of flight absorption imaging, along with estimates of the final trap frequencies extracted from our model of the crossed trap.

MOT loading time

Figure 5.16 shows that, as expected, the number of atoms remaining in the crossed dipole trap after evaporation increases in line with the MOT loading time. These data are collected by loading the MOT for varying amounts of time, followed by the standard detuning and intensity ramps of the MOT beams. The crossed dipole trap is then turned on at full power for 2 s before the MOT is released. A series of two linear evaporation ramps follow in which the final powers in the dipole trap are 1.2 W and 3.4 W in beam 1 and beam 2 respectively, giving an expected trap depth of 14.4 μK in the vertical direction. Time of flight imaging is then used to extract the number of atoms remaining and their temperature. A fitted exponential loading curve has a characteristic time of 6.1 s, which compares well with the measured loading time of the MOT in figure 4.10 of 6.3 s, suggesting the number remaining in the trap strongly depends on the number in the MOT prior to transfer.

The associated temperatures of the atom clouds are also shown in figure 5.16. We can see that for short loading times the final temperature of the atoms in the crossed dipole trap are around a factor of 1.8 hotter than those at longer times. The final cloud temperature stabilises to around 1.6 μK after around 5 s of MOT loading, which is in line with what we would expect given the trap depth. Given that the phase-space density is PSD $\propto NT^{-3}$, this implies that after $\sim$ 5 s of MOT loading the resulting phase-space density at the end

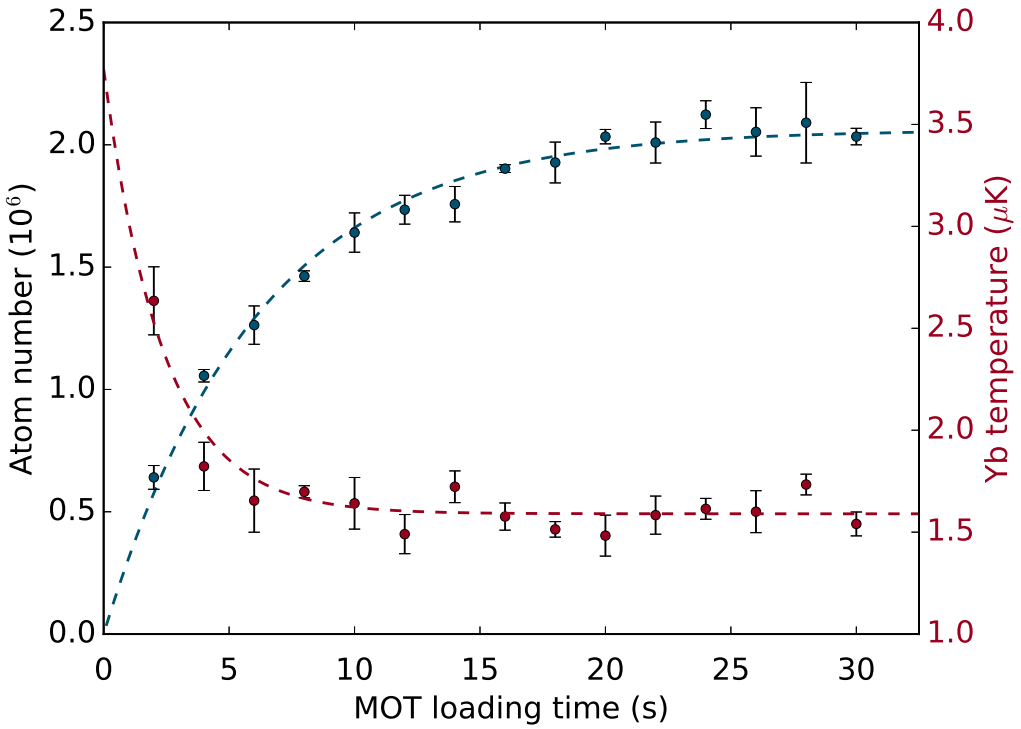

Figure 5.16: The atom number remaining (blue points) in the crossed trap following the second of the three evaporation ramps used for producing ^{174}Yb BECs is plotted against the loading time of the MOT prior to transfer to the dipole trap. We find that the transfer to the dipole trap is an increasing function of the number of atoms in the MOT. The blue curve shows an exponential fit with a characteristic time of 6.1 s; a similar trend to the MOT loading curve shown in figure 4.10. The associated temperature of the atomic clouds are shown by the red points, with the red curve being a guide to the eye.

of the evaporation ramp is only dependant on the number of atoms in the trap, hence we choose to continue loading the MOT for 20 s as for the single beam trap discussed previously.

Final MOT detuning and intensity

As for the single beam trap, the final detuning and intensity can have a dramatic impact on not just the atom number, but also the phase-space density of the atomic cloud after the evaporation ramps. In the figures that follow the MOT is loaded for 20 s, followed by a single 200 ms ramp of the detuning and intensity of the MOT beams, the final values of which are

varied in turn. The MOT remains at these settings for 2 s whilst the dipole trap is turned on at full power, before the MOT beams and field gradient are turned off. The dipole trap beams then undergo the same evaporation ramp as in the previous section before the atom number and temperature are inferred by absorption imaging.

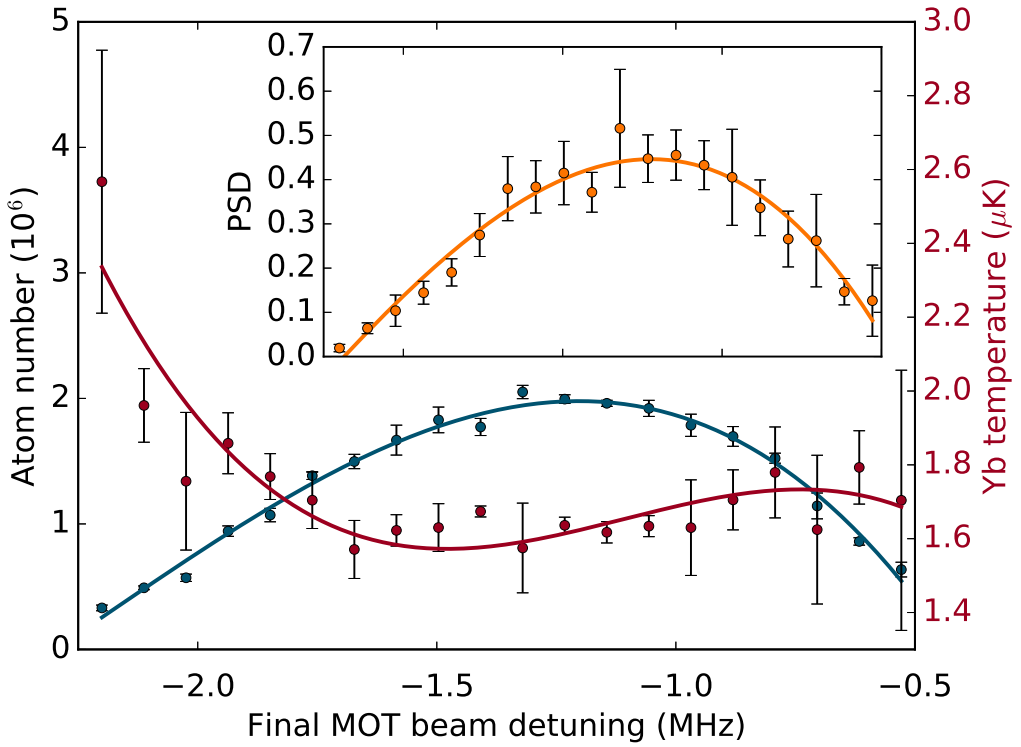

Figure 5.17: The blue points show the atom number remaining in the crossed dipole trap following two evaporation ramps as the final detuning of the MOT beams is varied. The red points show the corresponding temperature measured at each MOT detuning. Using the estimated trap frequencies at the end of the second evaporation ramp, the phase-space density is inferred and plotted in the inset. The solid lines are guides to the eye.

Figure 5.17 shows that the number of atoms remaining in the crossed dipole trap following the evaporation ramps follows a similar trend to that found for the single beam trap (figure 5.9), i.e. it shows a maximum, with the final MOT beams being 1.25 MHz red-detuned from resonance. The data recorded for this figure used a final MOT beam intensity of $\sim 8.3\ I_{\mathrm{total}}/I_{\mathrm{sat}}$. The red points on the figure show the corresponding temperature of the atom cloud after the evaporation ramps for each final MOT beam detuning studied. As we saw in our studies of the narrowband Yb MOT, at larger red detunings

from resonance the temperature of the cloud increases, showing that there is a residual of this effect in the dipole trap itself. The minimum temperature achieved is around 1.6 μK, and corresponds to the detuning that also gives the maximum atom number remaining in the trap. As such, the phase-space density is maximised at around 1.25 MHz red-detuned from the $^1S_0 \rightarrow {}^3P_1$ transition, as shown in the inset to the figure.

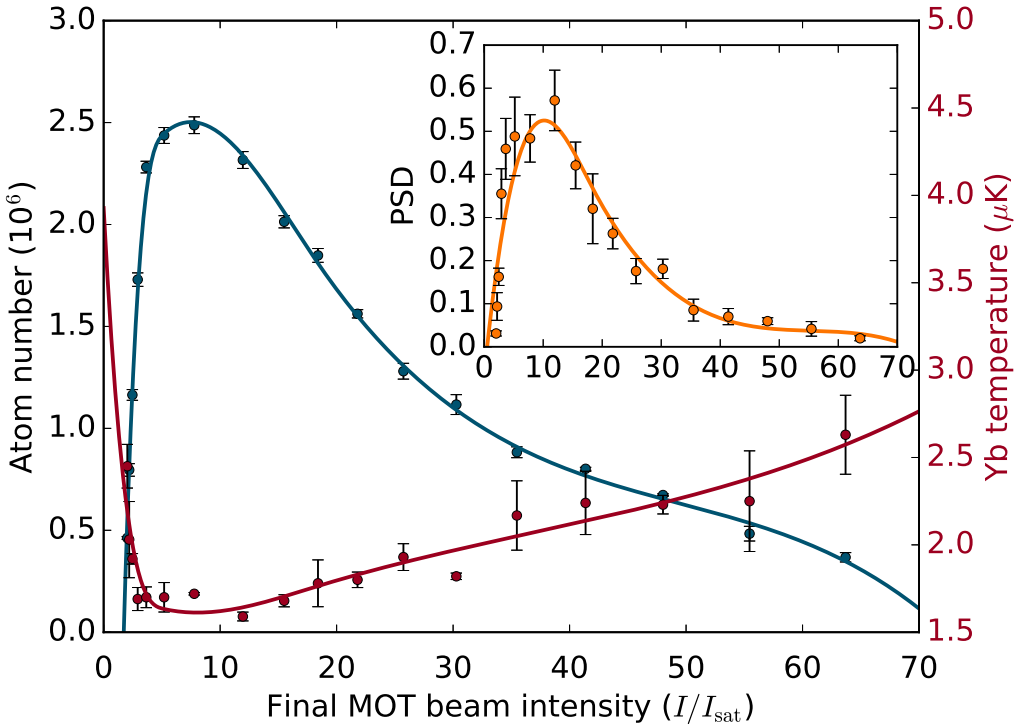

Figure 5.18: The number of atoms remaining in the crossed trap as the final six-beam MOT intensity is varied are shown by the blue points. The corresponding temperature of the Yb cloud is shown by the red points. The numbers and temperatures are recorded following the second evaporation ramp in the experimental sequence. The phase-space density inferred by the estimated final trap frequencies is shown in the inset of the figure. The solid curves are guides to the eye.

In comparison to our studies of the Yb MOT when varying the final intensity of the MOT beams, figure 5.18 shows that we find a similar result. Here the data were taken with a final MOT detuning of -1.25 MHz. In a parallel to our optimisation of the single beam trap, we notice that there is a sharp rise in atom number remaining in the trap, and a corresponding fall in the temperature, as the final MOT beam intensity is raised from 0 to around 7 $I_{\mathrm{total}}/I_{\mathrm{sat}}$. This can be associated with the sensitivity in the position of the

MOT at low MOT beam powers, and the fact that the dipole trap was aligned to the vertical position of the MOT when its parameters are set to produce the coldest atom clouds. Increasing the final MOT beam intensity from this point results in a fall in the number and an increase in the temperature of the atoms remaining in the trap after the evaporation ramps. This results in a peak in the phase-space density at MOT intensities of 7-10 $I_{\mathrm{total}}/I_{\mathrm{sat}}$. Note that the phase-space density in both of these plots is estimated using inferred trap frequencies from our model.

5.7 Bose-Einstein condensation

The phenomenon of Bose-Einstein condensation occurs when the temperature of a gas of indistinguishable bosons (or composite bosons) falls below a critical temperature, T_{c}. Close to this temperature quantum effects take over and the atoms may be described as matter waves with wavelengths given by the de Broglie wavelength (equation 5.30). From equations 5.30 and 5.31 it can be seen that as the temperature decreases, the de Broglie wavelength increases. As the temperature of the ensemble continues to fall the de Broglie wavelength reaches a regime in which it is comparable to the atomic separation. Below T_{c} the wavefunctions start to overlap and a form a coherent matter-wave. This process corresponds to the onset of a macroscopic ground state population, hence the term condensation. This process of condensation may be characterised by the phase-space density exceeding a critical value

$$\mathcal{D} \geq 2.612. \tag{5.35}$$

The first experimental observation of the transition to a Bose-Einstein condensate occurred in 1995 [5, 6], however the phenomenon was first predicted collaboratively by Bose and Einstein in 1924 [213, 214]. Einstein extended Bose's work on the statistical treatment of photons to the case of an ideal gas comprising a fixed number of non-interacting bosons. From this work, it may be shown that below the critical temperature the ground state occupation will be a non-zero fraction of the atom number; the atoms condense into the ground state.

Statistical consideration of an ideal Bose gas

For a system of N non-interacting indistinguishable bosons in thermal equilibrium, the occupation of state i with corresponding energy ϵ_i is given by [159]

$$N_i = \frac{1}{e^{(\epsilon_i - \mu)/k_{\mathrm{B}}T} - 1}, \tag{5.36}$$

where μ is the chemical potential, governed by the condition of the conservation of the total number of bosons in the gas

$$N = \sum_i N_i. \tag{5.37}$$

In order to prevent the non-physical negative occupation of the ground state, with energy ϵ_0, it is clear that the condition $\epsilon_0 > \mu$ must be placed on the chemical potential. Thus at high temperatures, the state energies are such that $\epsilon_i >> \mu$, and consequently the chemical potential may be ignored, except for the ground state population, and the distribution becomes

$$N_{i\neq 0} = \frac{1}{e^{\epsilon_i/k_{\mathrm{B}}T} - 1}. \tag{5.38}$$

This leads to a reformulation of the condition on the number of bosons in the system

$$N = \sum_i \frac{1}{e^{(\epsilon_i - \mu)/k_{\mathrm{B}}T} - 1} \approx N_0 + \sum_i \frac{1}{e^{\epsilon_i/k_{\mathrm{B}}T} - 1}, \tag{5.39}$$

where N_0 is the ground state occupation. This equation implies that as the temperature drops, the chemical potential increases in order to conserve the atom number. As we approach the critical temperature $\mu \to \epsilon_0$ and so the ground state occupation can become macroscopic (comparable to N). Considering the case of a harmonic trap with trap frequencies $\omega_{x,y,z}$, and where the particle number is large, we may replace the sum with an integral to find

$$N - N_0 = \zeta(3)\left(\frac{k_B T}{\hbar\bar{\omega}}\right)^3, \tag{5.40}$$

where $\zeta(n)$ is the Riemann ζ function [215]. By setting $N_0 = 0$ at temperatures greater than T_c, we obtain an expression for the critical temperature in a harmonic trap

$$k_B T_c \approx 0.94\hbar\bar{\omega}N^{1/3}. \tag{5.41}$$

Note that for an optical trap this expression sets a limit on the number of atoms remaining in the trap required for the onset of BEC for a given set of trap frequencies. By combining equations 5.40 and 5.41 we can find an expression for the condensate fraction for temperatures below T_c

$$\frac{N_0}{N} = 1 - \left(\frac{T}{T_c}\right)^3. \tag{5.42}$$

Interactions in dilute Bose gases

The typical density of a Bose-Einstein condensate is of the order 10^{13} - 10^{15} cm^{-3}, making it far more dilute than the molecules in air at room temperature. However, despite the diluteness of a BEC, there are still interactions between the particles comprising a real Bose gas, requiring a modification of our treatment thus far. At these densities, interactions in a Bose gas mainly take the form of two-body interactions, making the treatment of interactions more tractable. Such systems are well-described by the Gross-Pitaevskii mean field formalism.

Condensates consisting of N interacting particles, each with a spatial coordinate, $\mathbf{r}$, can be described by a many-body Hamiltonian. However, for large numbers of particles this formalism becomes impractical. Instead a mean-field approach may be taken by defining a mean-field operator

$$\hat{\Psi}(\mathbf{r}, t) = \Phi(\mathbf{r}, t) + \hat{\Psi}'(\mathbf{r}, t), \tag{5.43}$$

where $\Phi(\mathbf{r}, t)$ is defined as the expectation value of the field operator and is

often called the condensate wavefunction or order parameter. $\hat{\Psi}'(\mathbf{r},t)$ is a first-order perturbation term [216]. The density of the condensate may be expressed in terms of the order parameter [217]

$$n_0(\mathbf{r},t) = |\Phi(\mathbf{r},t)|^2. \tag{5.44}$$

In such dilute systems we may take the approximation that the atomic interactions occur over distances smaller than the atomic separation, represented as an effective interaction potential between atoms at points $\mathbf{r}$ and $\mathbf{r}'$

$$V(\mathbf{r}-\mathbf{r}') = g\delta(\mathbf{r}-\mathbf{r}'), \tag{5.45}$$

where g is a coupling constant representing the strength of the point interaction given by

$$g = \frac{4\pi\hbar^2 a_s}{m}. \tag{5.46}$$

At temperatures lower than T_c we may neglect the $\hat{\Psi}'$ term in equation 5.43 and write $\hat{\Psi} = \Phi$ [215, 217]. From this it is possible to arrive at the time-dependant Gross-Pitaevskii equation (GPE)

$$i\hbar\frac{\partial}{\partial t}\Phi(\mathbf{r},t) = \left(\frac{-\hbar^2}{2m}\nabla^2 + U_{\text{trap}} + g|\Phi(\mathbf{r},t)|^2\right)\Phi(\mathbf{r},t). \tag{5.47}$$

Given that $n_0(\mathbf{r},t) = |\Phi(\mathbf{r},t)|^2$, the time-dependant GPE gives the time evolution of the condensate density. If we use the trial wavefunction $\Phi(\mathbf{r},t) = \phi(\mathbf{r})\,e^{-i\mu t/\hbar}$, one can obtain the time-independent GPE,

$$\left(\frac{-\hbar^2}{2m}\nabla^2 + U_{\text{trap}}(\mathbf{r}) + g|\psi(\mathbf{r})|^2\right)\psi(\mathbf{r}) = \mu\psi(\mathbf{r}), \tag{5.48}$$

where the condensed state wavefunction is given by

$$\psi(\mathbf{r}) = N^{1/2}\phi(\mathbf{r}). \tag{5.49}$$

The time-independent GPE takes the form of a non-linear Schrödinger equa-

tion, however it can be seen that by switching off the interactions between the atoms (i.e. $g = 0$), we revert to the typical Schrödinger formalism.

The Thomas-Fermi approximation

Much of the properties of a condensate are set by an atomic interaction energy, E_{int}, which is determined by the s-wave scattering length, a_s, and is proportional to the square of the atomic density. If $a_s > 0$, the interactions between particles are repulsive and as such $g > 0$. By introducing a characteristic radius, a_{ho}, for the ground state wavefunction in a harmonic trap with geometric mean trap frequency, $\bar{\omega}$, where

$$a_{\text{ho}} = \sqrt{\frac{\hbar}{m\bar{\omega}}}, \tag{5.50}$$

the ratio of the interaction energy to the kinetic energy is approximately [159]

$$\frac{E_{\text{int}}}{E_{\text{kin}}} \approx \frac{Na_s}{a_{\text{ho}}}. \tag{5.51}$$

For large condensates $E_{\text{int}}/E_{\text{kin}} >> 1$, and we can neglect the kinetic term in the time-independent GPE. This is the so-called Thomas-Fermi regime. We now obtain a density profile for the condensed fraction of the form

$$n_0\left(\mathrm{r}\right) = \left|\psi\left(\mathrm{r}\right)\right|^2 = \frac{\mu - U_{\text{trap}}\left(\mathbf{r}\right)}{g}, \mu - U_{\text{trap}} > 0. \tag{5.52}$$

Elsewhere the density of the condensate is zero, this occurs where the trap potential is equal to the chemical potential. From this expression it may be seen that the density profile of a condensate will take the form of an inverse parabola for a harmonic trap, with a radius determined by the chemical potential. By considering the normalisation of the wavefunction, $\psi\left(\mathbf{r}\right)$, the relation between the number of atoms and the chemical potential is obtained [215]

$$\mu = \frac{\hbar\bar{\omega}}{2}\left(\frac{15Na_s}{a_{\text{ho}}}\right)^{2/5}. \tag{5.53}$$

It follows that for the trap frequency directions $i = x, y, z$ in a harmonic trap, the Thomas-Fermi radius of the condensate along one of these principal trapping axes is given by

$$R_{\mathrm{TF,i}} = \sqrt{\frac{2\mu}{m\omega_i^2}} = \frac{\bar{\omega}}{\omega_i} a_{\mathrm{ho}} \left(\frac{15Na_s}{a_{\mathrm{ho}}}\right)^{1/5}. \tag{5.54}$$

From this it follows that one of the observable features at the onset of condensation is the appearance of a bi-modal density profile, with the condensed fraction taking the form of a Thomas-Fermi parabola, whilst the remaining thermal atoms follow a Gaussian density distribution [200].

5.8 Bose-Einstein condensation of ^{174}Yb

Upon the loading of the crossed dipole trap, the PSD of the thermal cloud of around $(1.52 \pm 0.06) \times 10^7$ Yb atoms is approximately 4×10^{-3}; an increase of three orders of magnitude is required for the onset of condensation. However, it important to note that at this stage the atoms are loaded into both the crossed region and along the individual beams, hence this figure is only an estimate based on the fit to the Gaussian density profile of the atoms in the crossed region after time of flight expansion. To reach quantum degeneracy we employ forced evaporation by ramping the individual beam intensities down in order to lower the trap depth.

Whilst some experiments utilise optimised exponential ramps to produce BECs of ^{174}Yb [177], we find approximating an exponential by using three linear intensity ramps is sufficient to produce nearly pure BECs. As we have seen previously, $\bar{\omega} \to 0$ as the trap depth reduces in a pure optical trap, for this reason we evaporate in the crossed region of the optical trap to maintain the stiffness of the trap as far as possible in the evaporation ramps. Furthermore, the rate at which the power in the dipole beams changes, which is approximately equivalent to the rate of change of the trap depth, is slower in each subsequent ramp to account for the reduction in the elastic scattering rate. Figure 5.19 illustrates the ramps used to produce ^{174}Yb BECs. Also shown for comparison are the final stages of the MOT operation. Following

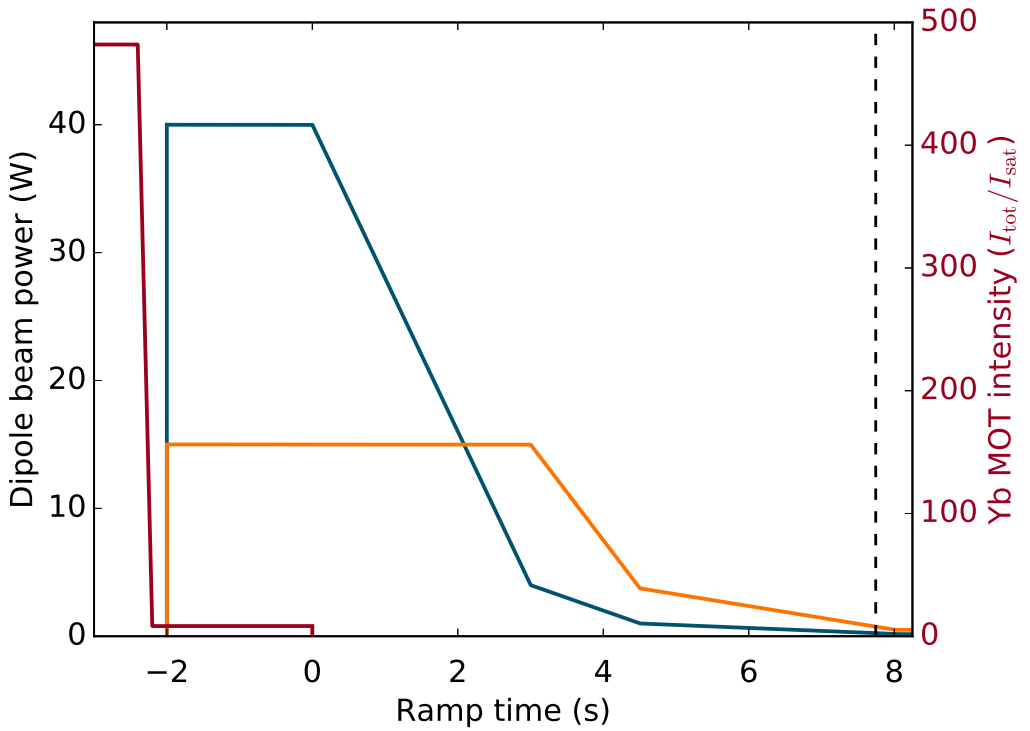

Figure 5.19: The timings of the evaporation ramps for producing a nearly pure BEC of ^{174}Yb. The evolution of the power in beam 1 (2) is shown in blue (orange), with the time scale chosen so that 0 s corresponds to the start of the first evaporation ramp in which beam 1 is ramped alone to transfer atoms into the crossed part of the trap. After 8.25 s nearly-pure BECs consisting of $\sim 10^5$ atoms are produced. The time at which the onset of BEC occurs is roughly indicated by the dashed vertical line. For reference the final evolution of the total MOT beam intensity (red curve) is also shown, with the dipole beams switching on following the reduction in MOT intensity.

the 200 ms ramp of the MOT beam intensity and detuning, the MOT remains in this state for a further 200 ms before the dipole trap turns on at full power. This corresponds to 40 W in beam 1, and 15 W in beam 2. The MOT and dipole trap remain in this state for 2 s whilst atoms are loaded into the dipole trap before the MOT beams and magnetic field gradient are switched off. Following this the evaporation ramps begin.

The evaporation sequence is optimised by choosing a cut in the trap depth and varying the time of the ramp. The figure of merit used to measure the performance of the ramp is the efficiency, γ, which takes into account the relative increase between the initial and final PSD, and the reduction of the atom number, N.

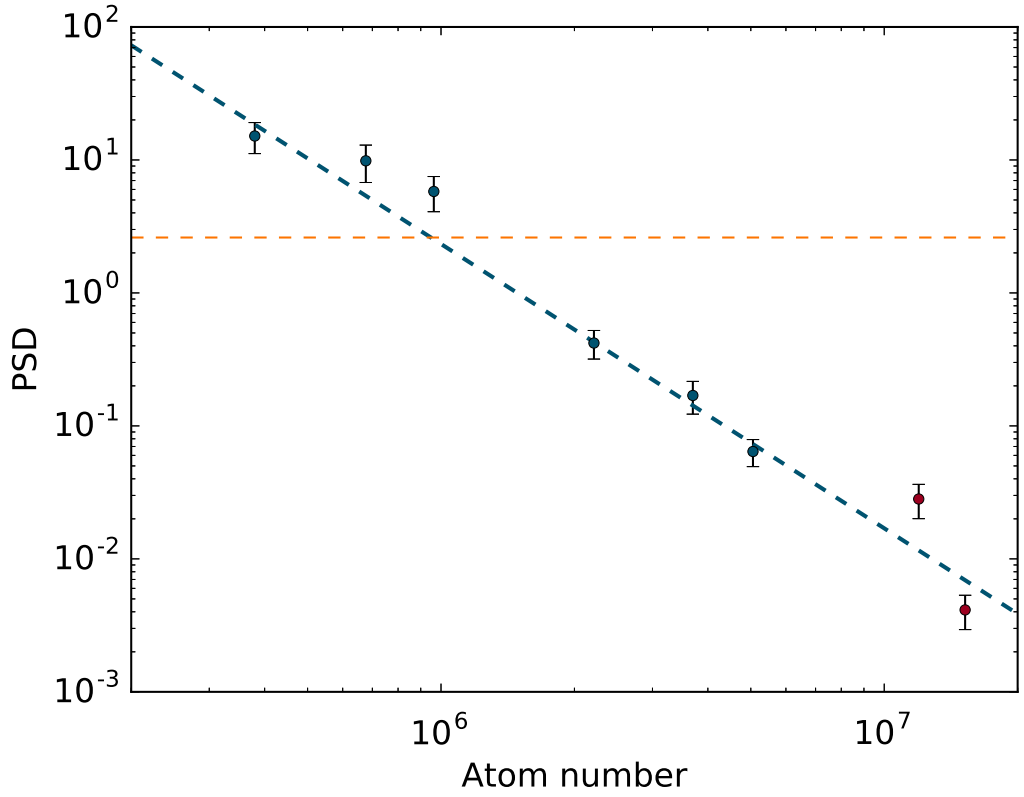

Figure 5.20: Evaporation trajectory of ^{174}Yb in the crossed dipole trap. The estimated phase-space density is plotted against the number of trapped atoms remaining at different points during the evaporation sequence, showing the increase in phase-space density as atoms are lost from the trap. Shown by the orange dotted line is the BEC transition point (PSD = 2.61). The blue points correspond to measurements when the atoms are located entirely in the crossed region of the trap, the points in red correspond to estimates in phase-space density when the atoms are not entirely in the crossed region, and may be less reliable. The blue dashed line shows a fit to the trajectory, yielding an evaporation efficiency of 2.1 ± 0.1.

$$\gamma = -\frac{\log_{10}\left(\mathrm{PSD}_f/\mathrm{PSD}_i\right)}{\log_{10}\left(N_f/N_i\right)}. \tag{5.55}$$

The first stage of evaporation shown in figure 5.19 shows only beam 1 ramping from 40 W down to 4 W in 3 s, whilst beam 2 remains at 15 W. The purpose of this ramp is to equalise the trap depths of the individual beams and to collisionally load atoms into the crossed region of the trap. Following the first ramp the PSD increases to $(6.4 \pm 0.8) \times 10^{-2}$ with $(5.1 \pm 0.2) \times 10^6$ atoms remaining in the trap. We should note here that the PSD is determined from

estimates of the trap frequencies using our model of the crossed trap, with which we assign a 5 % error estimate. We should also note that, in these early stages of the evaporation ramps, some atoms may be spilling into the "arms" of the crossed trap, making meaningful measurements of the PSD difficult. The second evaporation ramp occurs over 1.5 s, during which the power in each of the trapping beams is ramped down by 75 % to 1 W and 3.75 W for beam 1 and beam 2 respectively. Following this ramp the PSD is $(4.2 \pm 0.6) \times 10^{-1}$, with $(2.21 \pm 0.08) \times 10^{6}$ atoms remaining in the trap. The final evaporation ramp takes 3.5 s, during which time the power in beam 1 is ramped to 0.17 W and the power in beam 2 is ramped to 0.5 W. The dashed vertical line in figure 5.19 shows the approximate point in the evaporation ramp at which the onset of BEC occurs. By introducing a 250 ms hold time after this final ramp, evaporation continues and nearly pure BECs with $\sim 2 \times 10^{5}$ atoms are produced. The critical temperature based on this trap, T_{c}, is found to be (0.56 ± 0.02) μK when calculated for the non-interacting case (equation 5.41). Using this 8.25 s routine of forced evaporation from the crossed trap we regularly produce large BECs of ^{174}Yb.

Figure 5.20 shows the trajectory to BEC in terms of the increase in PSD at the expense of atom loss. The points are found by halting evaporation at various points in the ramps described above. The line on figure 5.20 shows a power-law fit to the change in PSD as the atom number changes. From this fit we obtain an average evaporation efficiency of $\gamma = 2.1 \pm 0.1$. It should be noted that we exclude the data points where the atoms were not exclusively in the crossed region of the trap from the fit (red points on figure 5.20). In this regime the spatial extent of the atom cloud means the trap is not harmonic, as such the PSDs shown as red points in the figure are estimates only.

Figure 5.21 show the density profile in terms of optical depth, after a 27.5 ms time of flight, for three different points in the evaporation ramps covering the onset of BEC. The lower frames of the figure show the cross cut of the density profiles and fits to them. The left image shows the atomic cloud at the onset of BEC, at which point the density profile can still be approximated by a Gaussian profile. By cutting further into the final evaporation ramp, we obtain the centre image. Here the bimodal distribution is clear, with

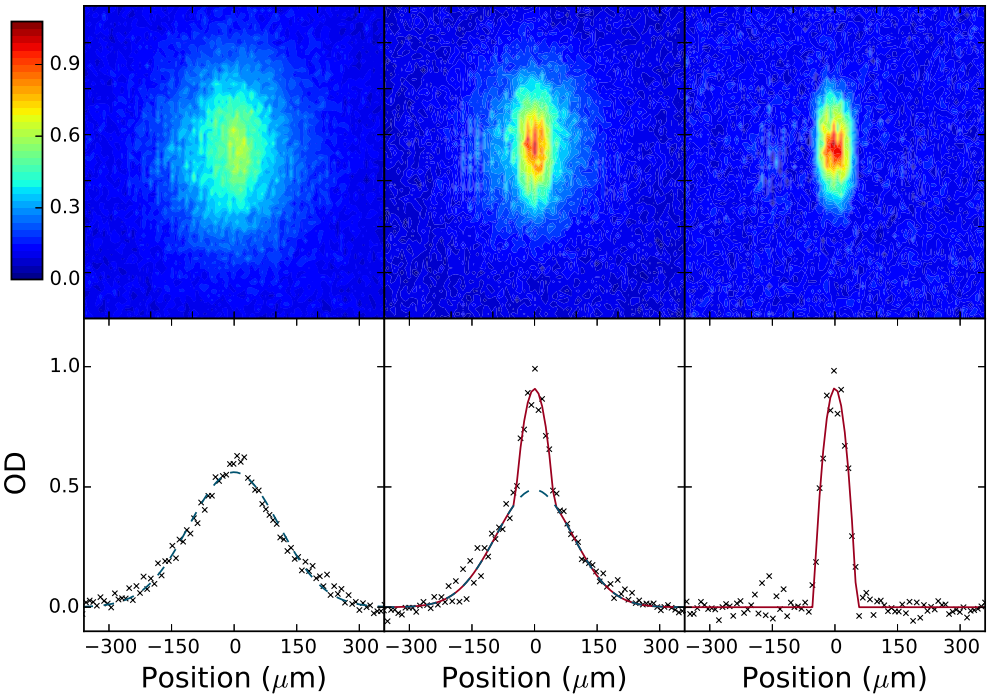

Figure 5.21: The top row shows two-dimensional colour maps of the optical depth for thermal (left), bimodal (centre), and purely condensed (right) samples. The corresponding horizontal cross-sections of the density profiles are shown in the bottom row. The dashed blue curves show Gaussian fits to the thermal sample, and the Gaussian component of a bimodal fit to the centre density profile. The solid red curves show the overall bimodal fit to the bimodal condensate, and a Thomas-Fermi fit to the pure condensate.

the condensed fraction having a parabolic profile and the remaining thermal component being described by a Gaussian. It is from the fit to the residual Gaussian component of the cloud density profile that allows the extraction of a temperature. Following the end of our evaporation ramp and the hold time of 250 ms, we obtain the nearly-pure BEC shown in the right image. Here the condensate density is entirely described by a Thomas-Fermi parabola. Any remaining thermal component of the cloud is too low in optical depth to provide a good fit.

By holding the trap at the final parameters we are able to observe the decay of the BEC. Figure 5.22 shows the number of atoms remaining as the hold time is increased, along with an exponential decay fit to the data. We find that the lifetime of the BEC is (6.3 ± 0.2) s in this instance. Since the scattering rate

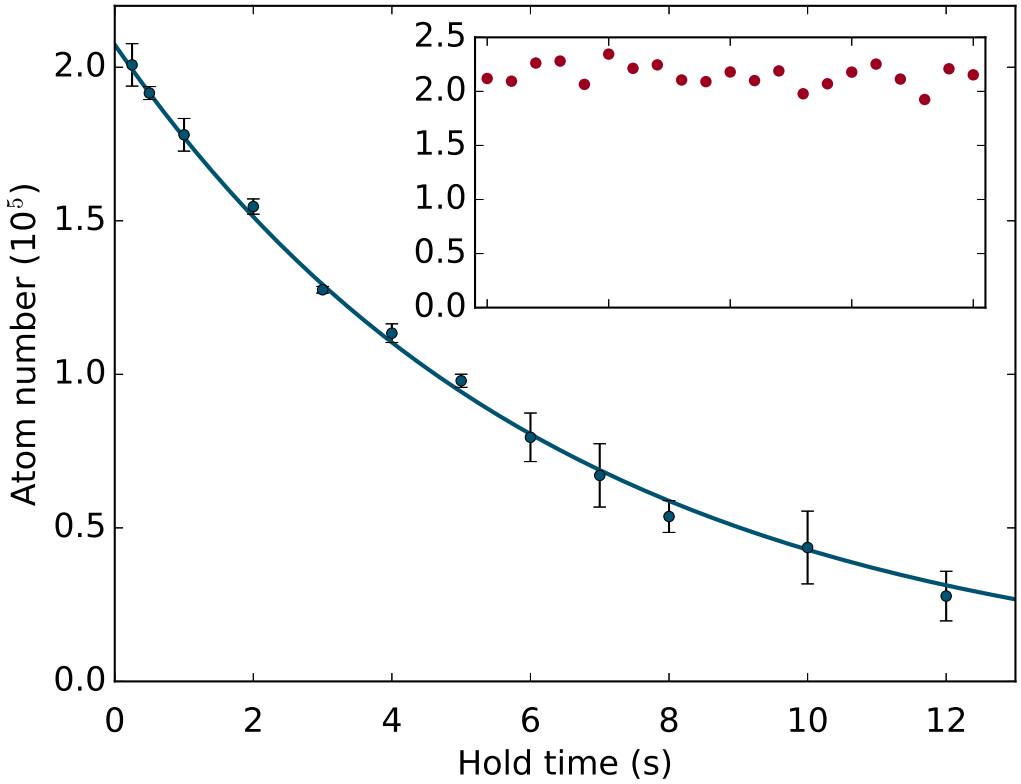

Figure 5.22: The blue points show number of atoms remaining in a pure BEC for hold times of different durations following the final evaporation ramp. The blue curve shows an exponential fit to number remaining as a function of hold time, yielding a BEC lifetime of 6.3 ± 0.2 s. The inset shows the reproducibility of the production of a pure ^{174}Yb condensate. Each red point denotes the number of atoms in the condensate immediately after the final evaporation ramp for 21 runs of the experimental sequence.

due to the trapping light is only $\sim 2 \times 10^{-3}$ s^{-1}, we expect that the lifetime is limited by background collisions in the vacuum system. Along with the lifetime of both MOTs, this has led us to question the vacuum quality in the science chamber. Improvements to the system are suggested in the following chapters. The inset to figure 5.22 shows the ability to reproduce the BEC during 21 runs of the experimental sequence. Each run takes approximately 31 s from the start of the MOT load to the beginning of the absorption imaging sequence. Here we show that the number of atoms in the BEC is highly reproducible; the average atom number is 2.2×10^5, with an rms error of less than 5 %.

5.9 Summary

In this chapter we have presented the addition of a crossed optical dipole trap to the experiment that enables the reliable production of Bose-Einstein condensates of $\sim 2 \times 10^5$ ^{174}Yb atoms. The optical setup of this trap was described, along with some of the difficulties in producing a consistent trap depth. In particular, the issue of thermal lensing at high powers in spherical lenses was highlighted. We also discussed the optimal loading of this trap to ensure higher phase-space densities following evaporation ramps. This involved optimising the intensity and detuning of the MOT beams, along with the loading time of the MOT. The method of evaporative cooling has been outlined, and its implementation in the cooling of ^{174}Yb to quantum degeneracy was described.

We have also set out a series of measurements using a single beam optical trap. This trap ultimately formed the basis of the later crossed trap. Using this well-defined trap, we tested a model of the trap depth and trap frequencies of dipole traps for Yb operating at a trapping wavelength of 1070 nm. We confirmed the validity of this model using parametric heating and measurements of the final atom temperature. This trap was also used to measure the light shift on the $^1S_0 \rightarrow {}^3P_1$ MOT transition. This was achieved by probing the trapped atoms with the MOT beams and measuring the detuning of the magnetically insensitive $m_J = 0$ excited state.

Cooling Yb to quantum degeneracy is not a necessity for this experiment, however having the control offered with a BEC will make future measurements easier. In particular, BECs offer many advantages when loading atoms into optical lattices. This is only half of the story for this experiment. In the next chapter we will reintroduce Cs, and look towards making measurements that will enable the production of ultracold CsYb molecules: an ultracold mixture of Yb and Cs is required.

Chapter 6

Towards ultracold mixtures of Yb and Cs

In order to produce ultracold molecules by the association of ultracold atoms we need to first understand how Cs and Yb interact. In this chapter we investigate the progress and development of the techniques and laser systems to measure the scattering length for Yb-Cs mixtures. We first address progress towards rethermalisation measurements with Cs and Yb in a common conservative trap, before moving on to the development of a photoassociation laser system that uses photons detuned from the Cs $6^2P_{1/2}$ asymptote. These systems are tested and outstanding issues preventing measurements of the interspecies scattering length are discussed.

6.1 Routes to ultracold molecules

As we saw in chapter 1, there are generally two categories that experiments attempting to produce ultracold molecules fall into: direct cooling of molecules or indirect cooling of molecules. In this experiment we take the indirect path, attempting to associate ultracold CsYb molecules from ultracold samples of Yb and Cs. However, it is unclear as to what the most efficient route for molecule production will be, and even if such a route is known it will still be necessary to have knowledge of the molecular potential for CsYb.

6.1.1 The scattering length

As we have already seen in the previous chapter, favourable elastic collisions between atoms in a harmonic trap are fundamental in creating quantum degenerate gases. Further to this, an understanding of ultracold collisions in a system is crucial in determining a route to the creation of ultracold molecules. In order to produce deeply bound molecular states in the ground electronic state, a thorough knowledge of the positions of the bound states in the ground, and indeed excited, electronic molecular potentials is required. Since the shape of the potentials involved are often well-known, ultimately a measurement of the binding energy of the least bound vibrational state is required, which is in effect a measurement of the scattering length. This section is not intended as a review of quantum scattering nor of the association of molecules, instead serving to introduce important terms and techniques. For reference, many review articles provide a comprehensive review of this subject [83, 218–220].

Elastic scattering theory

Elastic collisions in which kinetic energy is conserved are the process by which trapped atoms rethermalise, resulting in a decrease in the temperature of the trapped atoms following the removal of the hottest atoms from the ensemble by reducing the trap potential. In the ultracold limit, these collisions may be characterised by the s-wave scattering length, which follows as a result of comparing the wavefunction of the free atom pair to the wavefunction in the presence of the molecular interaction potential, $V(\mathbf{r})$, where $\mathbf{r} = \mathbf{r_1} - \mathbf{r_2}$ is the relative separation of atoms 1 and 2. Under the assumption that $V(\mathbf{r})$ is spherically symmetric, the Hamiltonian describing the collision process is

$$H = \frac{\hbar^2}{2\mu}\left(\frac{1}{r^2}\frac{d}{dr}\left(r^2\frac{d}{dr}\right) - \frac{l(l+1)}{r^2}\right) + V(r), \tag{6.1}$$

where l is the orbital angular momentum quantum number, and $\mu = \frac{m_1 m_2}{m_1+m_2}$ is the reduced mass of the two-atom system. With the assumption that the potential vanishes as $r \to \infty$, unbound eigenfunctions of this Hamiltonian take the form

$$\psi_k(r) = e^{ikz} + f(\mathbf{k})\frac{e^{ikr}}{r}, \tag{6.2}$$

where $\mathbf{k}$ is the wavevector of the scattered wave. The first term of equation 6.2 represents an incoming plane wave, and the second term represents the scattered wave, determined by the scattering amplitude $f(\mathbf{k})$. The elastic scattering cross section may now be defined as

$$\sigma(\mathbf{k}) = \int |f(\mathbf{k})|^2 d\Omega. \tag{6.3}$$

Again making the assumption that the interaction is spherically symmetric, the scattering amplitude may be assumed to depend only on θ, and can be written in terms of the Legendre polynomials, $P_l(\cos\theta)$, giving

$$f(\theta) = \frac{1}{2ik}\sum_{l=0}^{\infty}(2l+1)\left(e^{2i\delta_l}-1\right)P_l(\cos\theta), \tag{6.4}$$

where $l = 0, 1, 2, \ldots$ are the terms associated with the $s, p, d, \ldots$ partial waves, and δ_l is the associated phase shift for each partial wave. By integrating over the full solid angle we obtain

$$\sigma = \frac{4\pi}{k^2}\sum_{l=0}^{\infty}(2l+1)\sin^2\delta_l. \tag{6.5}$$

For indistinguishable bosons, the wavefunction ψ_k, must be symmetric on the exchange of the coordinates of the two particles, so that $\mathbf{r} \to -\mathbf{r}$, $\phi \to \pi + \phi$, and $\theta \to \theta - \pi$. Under this consideration equation 6.2 becomes

$$\phi_k = e^{ikz} \pm e^{-ikz} + \left(f(\theta) \pm f(\theta-\pi)\right)\frac{e^{ikr}}{r}. \tag{6.6}$$

To avoid double counting we must change the limits of equation 6.3 to only integrate over half the solid angle. The resulting cross section for indistinguishable bosons is double that for classical particles

$$\sigma = \frac{8\pi}{k^2}\sum_{l=\text{even}}^{\infty}(2l+1)\sin^2\delta_l. \tag{6.7}$$

Note that the sum now only contains partial waves with even values of l, fulfilling the condition on the symmetry of the wavefunction, due to the $(-1)^l$ parity of the Legendre polynomials. This implies that p-wave collisions are suppressed in bosonic gases. However, when a second species is introduced, as is the case for Yb and Cs, the particles are no longer indistinguishable and odd order partial waves contribute once more.

Ultracold scattering

The Hamiltonian introduced in equation 6.1 contains a term for the centrifugal barrier experienced for those partial waves with $l \neq 0$. At low temperatures, the kinetic energy of the two-atom system is not sufficient to overcome this barrier. The result of this is that the s-wave channel completely determines the scattering behaviour. The cross section then becomes

$$\sigma = \frac{8\pi}{k^2} \sin^2 \delta_0. \tag{6.8}$$

The s-wave phase shift is often parameterised in the form of the scattering length, a_s, which is defined as

$$k \cot \delta_0 \approx -\frac{1}{a_s}. \tag{6.9}$$

The scattering cross section becomes

$$\sigma = \frac{8\pi a_s^2}{1 + k^2 a_s^2}. \tag{6.10}$$

It is now possible to define two scattering regimes. The ultracold limit occurs where $ka_s << 1$; the de Broglie wavelength is much larger than the scattering length. In this regime the cross section saturates to a value of

$$\sigma_{\mathrm{uc}} = 8\pi a_s^2, \tag{6.11}$$

where the cross section is independent of the energy and temperature of the particles.

Conversely, when $ka_s >> 1$, we enter the unitary regime, in which σ is entirely limited by the de Broglie wavelength and hence the temperature of the ensemble,

$$\sigma_{\mathrm{u}} = \frac{8\pi}{k^2} \tag{6.12}$$

These are important results, ensuring that at ultracold temperatures the cross section, and hence the s-wave scattering length, are constant. These parameters then define the collisional properties of the sample in this regime.

The impact of the scattering length

The free-atom wavefunction is a plane wave defined by the de Broglie wavelength. When a molecular potential is introduced at short range, this free-atom wavefunction is perturbed. The potential serves to increase the energy of the scattering pair and a result of this is that, in the range of the interaction, the wavelength and oscillation amplitude of the wavefunction are reduced. This effect is illustrated in figure 6.1. These fast oscillations of the wavefunction, combined with the continuous and continuous differentiable properties of wavefunctions, results in a long-range phase shift from the free-atom wavefunction. It is this phase shift that determines the scattering length for the particular energy of the colliding atoms, defining the maximum separation at which the atoms begin to interact with one another. The sign of the scattering length determines the nature of the interactions: a positive scattering length implies that the collisions are repulsive, whereas the collisions are attractive when the scattering length is negative.

As yet we have neglected to discuss the form of the molecular potential. Typically the shape of the potential is that of a Lennard-Jones potential

$$V(r) = \frac{C_{12}}{r^{12}} - \frac{C_6}{r^6}, \tag{6.13}$$

with C_6 describing the Van-Der-Waals interaction, and C_{12} serving as a quantum defect term. Small changes to the potential can have a significant effect on the scattering length: the number of bound states, and specifically the

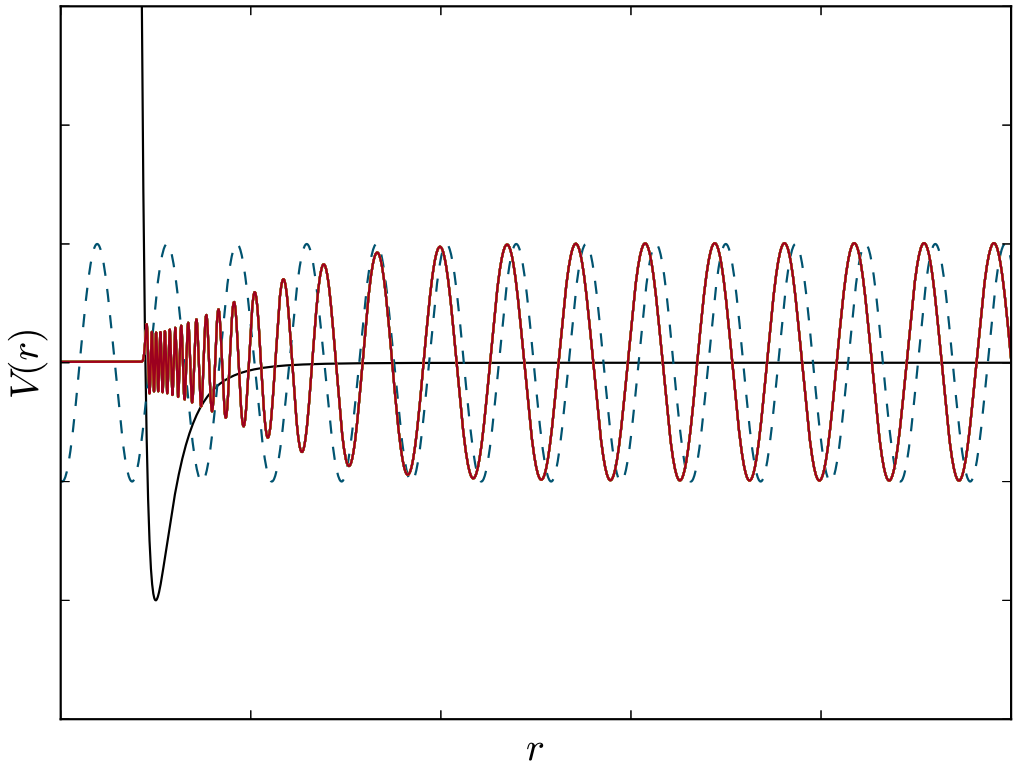

Figure 6.1: In the absence of a potential, the scattering wavefunction is simply a plane wave with a frequency determined by the de Broglie wavelength (blue dashed curve). The black curve shows the form of an arbitrary molecular potential, with a nearly-bound state of the potential shown in red. The characteristic decrease in the scattering wavefunction's amplitude and wavelength in the region of the potential are clear. At long range the scattered wavefunction approximates the free-atom wavefunction with a small phase shift. The sign and magnitude of this phase shift determines the scattering length.

position of the least bound state within the potential directly determines the scattering length. As the potential deepens and a new bound state is close to being added, the scattering rate becomes large and positive. As the new bound state appears, there is a pole in the scattering length and it becomes infinite before becoming large and negative as the state becomes more bound. As the binding energy increases, the scattering length remains negative but approaches zero. Known changes to the molecular potential, such as those due to magnetic fields or changes in the reduced mass of the system, therefore have an impact on the scattering length. This implies that if the scattering length can be measured, the long-range molecular potential can be inferred,

from which the location of bound molecular states can be calculated.

6.1.2 Magneto-association

Feshbach resonances

Initially predicted in 1958 [221], Feshbach resonances were first observed in a sodium BEC in 1998 [222]. They have since become an invaluable tool in controlling the scattering length in ultracold atomic gases for a multitude of purposes, including the formation of molecules [92, 95, 223, 224], and the production of bright solitary matter waves [29–31]. Feshbach resonances are best understood by considering two molecular potentials, $V_{\text{entrance}}(r)$ and $V_{\text{closed}}(r)$ – known as the entrance and closed channels respectively. The resonance occurs when colliding atoms with energy E_c in the entrance channel couple resonantly to a bound vibrational state in the closed channel. Typically the states in the entrance and closed channels will have different magnetic moments, allowing a magnetic field to be used to tune the bound molecular state across the dissociation threshold of the entrance channel. These principals are outlined in figure 6.2.

A virtual bound state exists when the bound state is more energetic than the entrance channel threshold, corresponding to a negative perturbation on the background scattering length. As the virtual state crosses the threshold energy, the scattering length tends to infinity and becomes positive as the bound state dips below threshold. As the energy of the bound state continues to reduce relative to the threshold, the positive scattering length tends to zero. This process will be repeated in the event of a new virtual bound state approaching the threshold energy. This pole in the scattering length is shown in figure 6.2. It is this feature in the scattering length behaviour that is known as a Feshbach resonance. This impact on the scattering length makes Feshbach resonances relatively easy to detect: the a^4 dependence on the three-body collision rate means that inelastic trap losses are enchanced [131].

The form taken by the scattering length as a function of the bias magnetic field strength, B, is described by

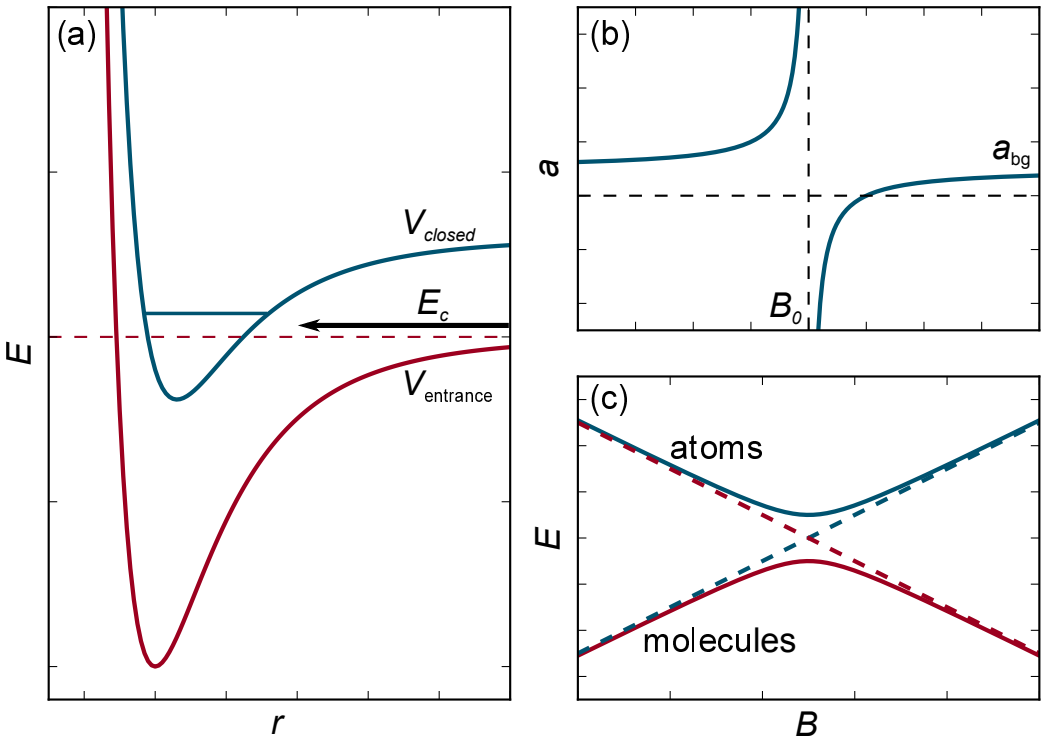

Figure 6.2: (a) Two atoms colliding with energy E_c may resonantly couple to a bound state in the closed channel, which may be tuned relative to the atomic threshold of the entrance channel by use of a magnetic bias field. (b) As the bound state is tuned towards the threshold from above, the scattering length reduces to less than its background value, a_{bg}, and tends to negative infinity as it approaches the atomic threshold. As the bound state crosses the threshold energy, the scattering length becomes positive and reduces in magnitude as the state becomes more bound. (c) In the presence of coupling between the molecular and atomic states, there exists an avoided crossing. This may be used in an adiabatic magnetic field sweep to transfer colliding atomic states to loosely bound Feshbach molecule states.

$$a = a_{\mathrm{bg}}\left(1 - \frac{\Delta B}{B - B_0}\right), \tag{6.14}$$

where a_{bg} is the scattering length in the absence of the Feshbach resonance, determined by the position of the least bound state in the entrance channel as described in the previous section. B_0 is the position of the Feshbach resonance: the magnetic field strength at which the bound state in the closed channel crosses the threshold of the entrance channel. ΔB parametrises the width of the resonance, and is the additional magnetic field strength on B_0 that must be applied for the scattering length of the system to be zero.

Molecule formation

Feshbach resonances are often utilised in homonuclear or heteronuclear systems of alkali elements. These atoms have a ^2S ground state and as such their spins can pair up to give either a singlet or triplet molecular potential. As previously discussed, for a Feshbach resonance to occur a crossing between a bound molecular state in the closed channel and the atomic threshold is required when the magnetic field strength is ramped. However, a coupling between the atomic and molecular states is also required. In systems of alkali atoms, it is the different form of the singlet and triplet potentials that give rise to the required coupling.

By ramping the magnetic bias field strength adiabatically across the Feshbach resonance, colliding pairs of atoms efficiently form weakly bound molecular states known as Feshbach molecules, whilst preserving the phase-space density of the original ensemble. However, these molecules are extremely weakly bound; for bosonic molecules this results in short trap lifetimes limited by atom-molecule and molecule-molecule collisions. Thus, the process of Stimulated Raman Adiabatic Passage (STIRAP) is often employed to coherently transfer molecules to the absolute ground state via an intermediate excited state [60, 62]. The fact that both STIRAP and Feshbach association are reversible is extremely useful: deeply bound molecules can be converted back to the same Feshbach state and disassociated by reversing the adiabatic sweep of the magnetic field, enabling atomic imaging systems to effectively image the molecules.

Magneto-association of CsYb

As we have seen in the above sections, the existence of a magnetically tunable Feshbach resonance requires a coupling between a bound molecular state and an atom pair continuum state and that the two states can cross when a magnetic field is applied. In systems of alkali atoms it is the existence of both singlet and triplet potentials and the magnetic dipolar interactions between electron spins that give rise to the required coupling. However, in a system consisting of an alkali and a ^1S atom such as Yb, neither of these effects exist. In such a system all of the molecular potentials are doublet

states, and so all of the potentials for the different states lie parallel to one another, shifted in terms of atomic hyperfine energy [106]. Note that there are still crossings of molecular states with the atomic threshold, however in this simple picture there is no coupling between the states. We can see this by writing the molecular Hamiltonian

$$H = K + V(\mathbf{r}) + \xi I_{\mathrm{Cs}} \cdot S_{\mathrm{Cs}} + H_{\mathrm{Zeeman}}, \tag{6.15}$$

where K is the kinetic energy term, ξ is the hyperfine coupling constant for Cs, I_{Cs} and S_{Cs} are the nuclear and electron spin operators for Cs, and H_{Zeeman} represents the Zeeman interaction. Because there is only one form of potential and there is no hyperfine interaction for Yb, there is nothing to couple atomic states to bound molecular states.

However, this is only a simplified picture since ξ depends on the internuclear separation. The hyperfine coupling constant is predicted to change significantly in the presence of another atom, in this case Yb, and has since been observed in photoassociation spectroscopy of RbYb [225]. This effect can be thought of as being due to the perturbing effect of the second atom's electron cloud. The change in the hyperfine coupling constant as a function of the internuclear separation gives rise to the coupling necessary for non-zero width Feshbach resonances in an Yb and Cs mixture.

The work of Brue and Hutson [106, 132] show that the widths of such resonances can be given as

$$\Delta B = \frac{\pi I_{m_F,a}^2 I_{nk}^2}{k a_{\mathrm{bg}} \delta\mu_{\mathrm{res}}}, \tag{6.16}$$

where $I_{m_F,a}$ is the matrix element of $I \cdot S$; I_{nk} is the radial matrix element of $\Delta\xi(r)$, the separation dependence of the modification to the hyperfine coupling constant between the bound and continuum states; $\delta\mu_{\mathrm{res}}$ is the difference in magnetic moments of the bound and continuum states; and k is the wavevector. These factors should yield favourable results for the CsYb molecule. For example, both $I_{m_F,a}$ and I_{nk} will be favourably large for the heavy choice of alkali element. A small value of $\delta\mu_{\mathrm{res}}$ can be thought of as a "glancing blow" where the molecular state and atomic state cross

at a shallow "angle", giving a larger range of magnetic field strength in which the effect of the Feshbach resonance will be apparent. The seven stable isotopes of Yb increase the chances of finding one of these resonances at favourable field strengths. Crucially, for weak magnetic field strengths ($\lesssim$ 4000 G), $I_{m_F,a}$ increases linearly with magnetic field strength, and so the expected width of the Feshbach resonances will be proportional to B^2. It is predicted that resonances of usable width will only be accessible at large magnetic fields ($\sim$ 2000 G). As a result of this, magneto-association of CsYb will pose a serious challenge. We have incorporated space for high-magnetic field coils within the experiment, however stability will be an issue, and searching for sub-m G resonances will be akin to finding the proverbial needle. Whilst not ruling out the possibility of associating CsYb through Feshbach resonances, we have decided to develop a photoassociation system in parallel to the proposed search for Feshbach resonances.

6.1.3 Photoassociation

An alternative method for associating cold atoms into molecules is that of photoassociation, a technique first demonstrated by Thorsheim et al [226]. The process is illustrated in figure 6.7. Two colliding atoms, A and B, are excited to a molecular bound state, $(AB)^*$, within the potential of an excited electronic state of the molecule. The excitation occurs by the absorption of a photon with energy $\hbar\omega_1$, corresponding to the difference in energy of the bound molecular state and the colliding atoms, which is generally red detuned from an atomic transition with energy $\hbar\omega_0$. As such the absorption process is generally given by

$$A + B + \hbar\omega_1 \rightarrow (AB)^* . \tag{6.17}$$

The molecular state $(AB)^*$ produced in this process is electronically excited, and will often dissociate back to a pair of free atoms

$$(AB)^* \rightarrow A + B + \hbar\omega', \tag{6.18}$$

where ω' is the angular frequency of a photon emitted during the decay process. However, sometimes the excited molecular bound state will decay to a bound state in the electronic ground state of the molecule, AB,

$$(AB)^* \rightarrow AB + \hbar\omega_2, \tag{6.19}$$

where ω_2 is the energy of the photon emitted in this process. It is clear that when the molecule decays into the least bound state of the ground electronic potential of the molecule, the difference between ω_1 and ω_2 will give the binding energy of the molecule formed, which may be used to determine the scattering length of the system.

The issue with photoassociation is that the experimenter has relatively little control over the molecular states in the ground electronic potential that are produced in this process. This is the polar opposite of association via a Feshbach resonance, in which the atoms are coherently transferred to a single vibrational state, albeit a high-lying one. The distribution of the bound states formed in the decay process are determined by Franck-Condon factors: the overlap of the wavefunctions corresponding to the bound state in the excited electronic potential and the various bound states in the ground electronic potential of the molecule.

In Franck's semi-classical consideration of transition strengths for transitions between vibrational states of molecules, the vibration between the nuclei in the molecule is considered to be quantised, whereas the motion is considered to be classical [227]. It is assumed that the time scale of nuclear motion is much shorter than that of an electronic transition, and that the kinetic energy gained by the nuclei is minimal. This implies that the transitions most likely to occur are those in which the changes in kinetic energy and internuclear separation are minimal. Such transitions are the so-called "vertical" transitions, as in the instant of the transition the internuclear separation is unchanged.

Condon formalised this with a fully quantum mechanical approach in which the nuclear positions are described by a wavefunction [228]. In a similar approach to the transition strength for an electric dipole transition in an atom, we may consider the transition strength under the Born-Oppenheimer

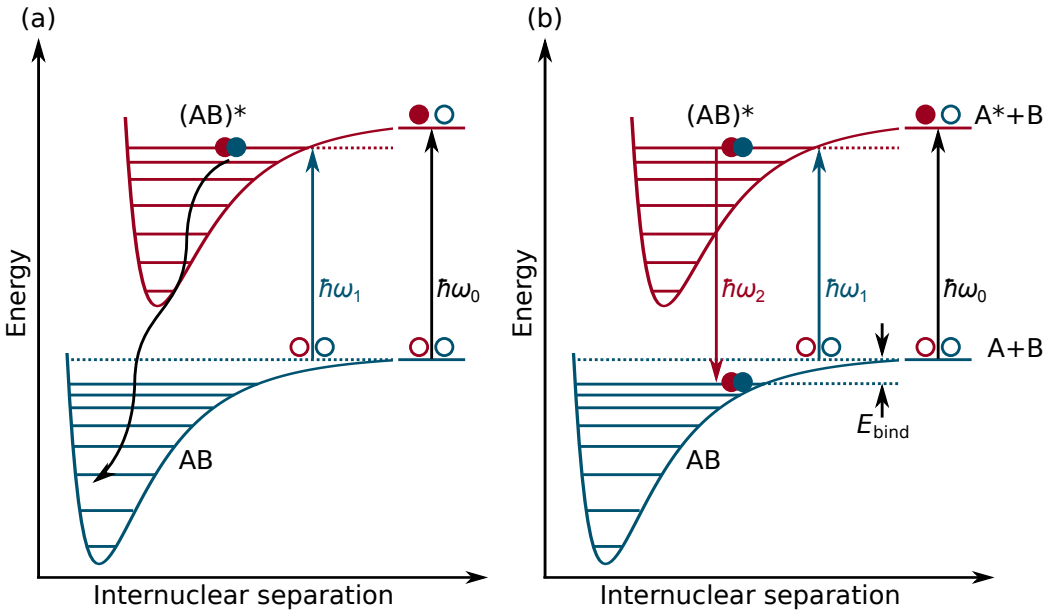

Figure 6.3: (a) An illustration of the one-photon photoassociation process. In the absence of the scattering potential, or equivalently at large internuclear separations, an excitation corresponds to a free-atom making an electronic transition. At smaller separations a laser with driving frequency ω_1 results in a transition to an electronically excited state (AB)*. This molecule may then dissociate or decay into a bound state within the ground electronic potential. (b) A second laser of angular frequency ω_2 may couple excited molecules to bound states in the ground electronic manifold. When the second photon is resonant with the topmost bound state, the difference in photon energy gives the binding energy of the molecule, and hence the scattering length.

approximation to be [229]

$$\langle \psi' | \mathbf{d} | \psi'' \rangle = \langle \psi^N_{1,\nu'} | \langle \psi^e_1 | \mathbf{d} | \psi^e_0 \rangle | \psi^N_{0,\nu''} \rangle, \tag{6.20}$$

where the ground electronic state is denoted 0 and the excited electronic state is denoted 1. It is assumed that the wavefunction of a particular state may be written as the product of an electronic (e) and a nuclear (N) wavefunction. Convention dictates that the vibrational quantum number of the state in the ground electronic state is denoted ν'', whilst that in the excited electronic state is denoted ν'. Another assumption made is that the dipole moment operator can be split into the linear combination of a dipole operator for the electrons, $\mathbf{d_e}$, and for the nuclei, $\mathbf{d_N}$, such that $\mathbf{d} = \mathbf{d_e} + \mathbf{d_N}$. Following the treatment in [228], we arrive at the transition strength

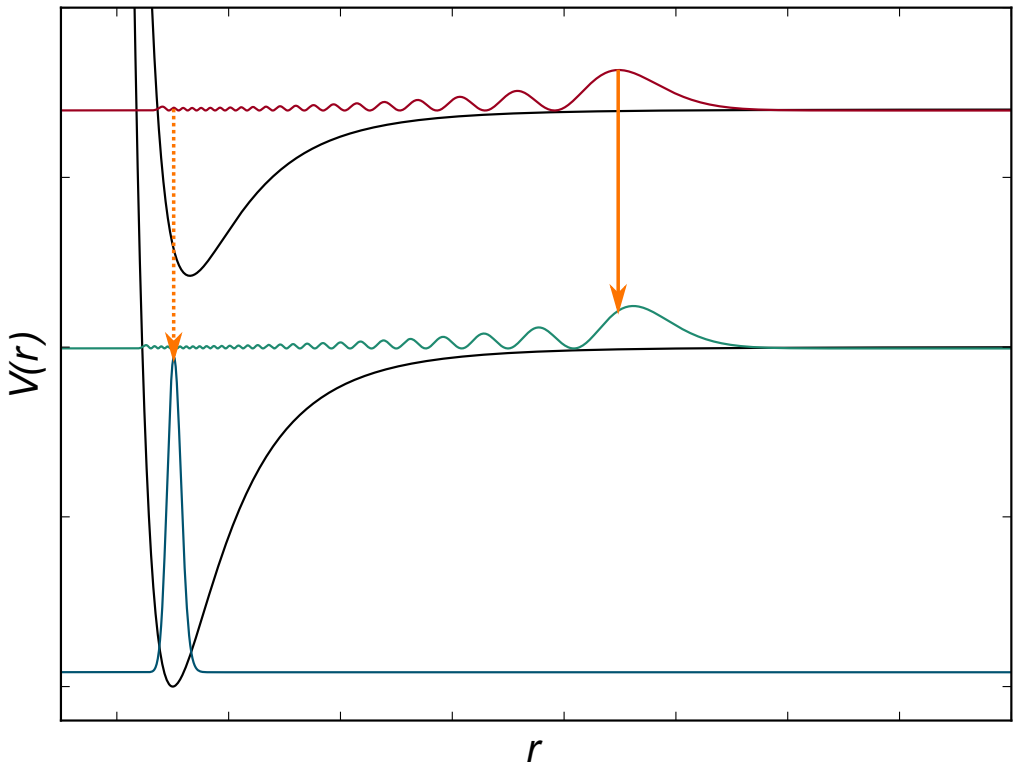

Figure 6.4: A bound state in an excited electronic state of the molecule may decay to a number of bound states in the ground electronic state. The probability density of the initial state is shown in red, with the probability density of the absolute ground state and another bound state of the ground electronic state shown in blue and teal respectively. The overlap of the initial state's wavefunction with the weakly bound ground state is much larger than that with the absolute ground state, hence the transition shown by the solid orange arrow is much more likely to occur than that shown by the dashed arrow.

$$\langle \psi' | \mathbf{d} | \psi'' \rangle = \langle \psi^N_{1,\nu'} | \psi^N_{0,\nu''} \rangle \langle \psi^e_1 | \mathbf{d} | \psi^e_0 \rangle, \tag{6.21}$$

this is simply the atomic transition strength, $\langle \psi^e_1 | \mathbf{d} | \psi^e_0 \rangle$, multiplied by the spatial overlap of the wavefunctions of the two vibrational states, $\langle \psi^N_{1,\nu'} | \psi^N_{0,\nu''} \rangle$. This factor is known as the Franck-Condon factor, and shows that the transition probability between two vibrational levels is proportional to the spatial overlap of their wavefunctions.

Figure 6.4 provides an illustrative guide to the Franck-Condon principle. A molecule in a bound state of an excited electronic state has a probability

density shown in red. The overlap between this state's wavefunction and a loosely bound state in the ground state electronic potential (teal) is comparatively large when compared to the overlap with the absolute ground state of the system (blue), in which $\nu'' = 0$. The Franck-Condon principal states that the decay to the state in teal is far more likely to occur than a decay to the $\nu'' = 0$ state. However for this initial state, the overlap will likely be large for several of the high-lying vibrational states in the ground electronic state. As such molecules excited to the state shown in red will decay to an incoherent mixture of loosely bound vibrational states in the electronic ground state. From this it can be seen that the "vertical" transition condition is effectively maintained: the amplitude of a vibrational state's wavefunction is greatest at the classical turning point, and as such the average internuclear separation will reflect this. The Franck-Condon principal means that transitions will likely occur between states with large wavefunction overlap, and hence similar turning points, implying the average internuclear separation typically only changes by a small amount in an electronic transition.

This process also applies to the upward transition from a pair of free atoms to an excited molecular bound state. As such the states accessible in the excited electronic potential of the molecule will depend on the average separation of the colliding atoms. For photoassociation from a MOT, molecular states with internuclear separation on the order of microns are likely. In this case the example from above is recovered, with the excited bound state favouring decays to loosely bound states in the ground electronic potential. Having said this, it is possible that some systems exhibit a large overlap with the absolute ground state. The fortuitous double-well structure in the excited state potential of the Cs_2 dimer, leads to a case where the internal turning point of some excited vibrational levels have good transition strength to the ground state. However, this is not a typical case, and usually the incoherent population of high-lying vibrational states and leads to centre of mass heating of the sample. Despite this, ultracold molecules of many homonuclear and heteronuclear combinations have been produced using this technique [230–237]. However, transferring these molecules to the absolute ground state will require a more sophisticated approach.

Irrespective of the route chosen to indirectly produce the CsYb molecule

from cold samples of Cs and Yb, we require a knowledge of the scattering length. By measuring the scattering length we obtain information about the molecular potential. Whilst the general form of this potential is known, the bound state structure is extremely sensitive to details that only measurement can provide. Once the potential is determined, the binding energies and wavefunctions of the bound states can be estimated, allowing a route to produced ground state molecules to be identified.

6.2 Rethermalisation

6.2.1 Finding the scattering length

As we have previously seen, for s-wave scattering the elastic collision cross section is given as

$$\sigma = \frac{8\pi a^2}{1 + k^2 a^2}. \tag{6.22}$$

If the orbital angular momentum quantum number for the collision, l, is greater than zero, the long-range part of the scattering potential will include a term for the resulting centrifugal barrier experienced

$$V(r) = -\frac{C_6}{r^6} + \frac{\hbar^2 l(l+1)}{2\mu r^2}. \tag{6.23}$$

The height of this barrier will determine an upper limit on the temperatures required for scattering to be exclusively due to s-wave collisions. For d-wave collisions ($l = 2$) in Cs and ^{174}Yb the height of the barrier is 180 μK and 228 μK respectively [150, 238]. However, the C_6 coefficient for the scattering potential between Cs and Yb has yet to be measured, and forms one of the ongoing aims of this experiment.

It seems reasonable that the collisional properties of an ultracold mixture of two species could be inferred from their behaviour in a shared trap, and indeed by studying the timescales for rethermalisation between species 1 and 2 the interspecies collision rate, $\Gamma_{1,2}$ can be inferred [239, 240]. This collision rate will depend on the spatial overlap of the density profiles, n_1 and n_2, of

the two species within the trap

$$\Gamma_{1,2} = \sigma_{1,2}\bar{v} \int n_1(\mathbf{r})\, n_2(\mathbf{r})\, d\mathbf{r}, \tag{6.24}$$

where the overlap will depend on the temperatures of the species and, in the case of a harmonic trap, the trap frequencies for each species. Here $\sigma_{1,2}$ is the interspecies elastic collision cross section, and $\bar{v}$ is the mean relative velocity

$$\bar{v} = \left[\frac{8k_\mathrm{B}}{\pi}\left(\frac{T_1}{m_1} + \frac{T_2}{m_2}\right)\right]^{1/2}, \tag{6.25}$$

where $m_{i=1,2}$ and $T_{i=1,2}$ are the mass and temperature of the species respectively. It can then be shown that each species will equilibrate in the trap at a temperature [239, 240]

$$\bar{T} = \frac{N_1 T_1 + N_2 T_2}{N_1 + N_2}, \tag{6.26}$$

which is the average of the initial temperatures, weighted by the number N_i of each species. This final temperature is approached exponentially with a time constant

$$\tau^{-1} = \frac{4\sqrt{2\xi}\,(N_1 + N_2)\,\sigma_{1,2}\alpha_{x,1}\alpha_{y,1}\alpha_{z,1}}{3\pi^2 k_\mathrm{B}\bar{T}\,(m_1 + m_2)^{1/2}}\left(1 + \beta^{-1}\right)^{-3/2}, \tag{6.27}$$

where $\xi = 4m_1m_2/(m_1 + m_2)^2$ is the reduction in the energy transfer per collision compared to two colliding particles with equal mass. Here we are assuming the mutual trap is harmonic for both species, with $\alpha_{i,1} = \sqrt{m_1\omega_{i,1}^2}$ being the force constant along trap axis i for species 1. The force constants for species 2 are those for species 1 scaled by a factor β. For more information on this derivation see [239, 240]. This reasoning implies that by preparing a mixture of two species in a common trap, in which there exists an initial temperature difference between the species, measuring the time constant of the rethermalisation process allows the interspecies elastic scattering cross section to be inferred [241]. It is important to note that it is the scattering length that we desire, which is proportional to the square root of the cross section, since this gives information as to whether the collision is attractive

or repulsive. However, since the scaling of the scattering length with the reduced mass of the system is well known, by making measurements the cross section with different isotopic combinations (where available) the sign of the scattering length can also be inferred.

We should however note that using rethermalisation to measure the scattering length is likely to be less accurate than using photoassociation, as will be discussed in section 6.3. This is because photoassociation gives a direct measurement of the binding energy of the least bound state in the molecular potential, which directly determines the sign and size of the scattering length. In addition to this, there are other factors that may lead to statistical or systematic uncertainty on the rethermalisation measurements. For example, the above treatment assumes the suppression of partial waves above s-wave scattering. However, despite being at temperature below that imposed by the centrifugal barrier, phenomena such as shape resonances can cause partial waves with $l > 0$ to contribute to the scattering cross section [218]. It is for these reasons that photassociation is the more desirable method for the determination of the scattering length, however rethermalisation arguably requires fewer systems to be implemented on the main experiment compared to the additional laser systems required for photoassociation.

6.2.2 Optically trapped Yb in the presence of a Cs MOT

Whilst we have been unable to carry out a measurement of the background scattering length for Yb-Cs using either rethermalisation or photoassociation, we have been able to carry out initial measurements to test the concepts and to develop the systems required for these measurements. These tests also provide insights into what might be the ideal route towards making CsYb molecules, and are discussed further in section 6.4.

One such experiment carried out is to look at the impact of loading a Cs MOT in the same location as Yb atoms trapped in a dipole trap. These experiments were carried out using a cloud of Yb loaded into the single beam optical trap. The Yb MOT is loaded for a period of 20 s before the standard ramps of the Yb MOT intensity and detuning are carried out. At

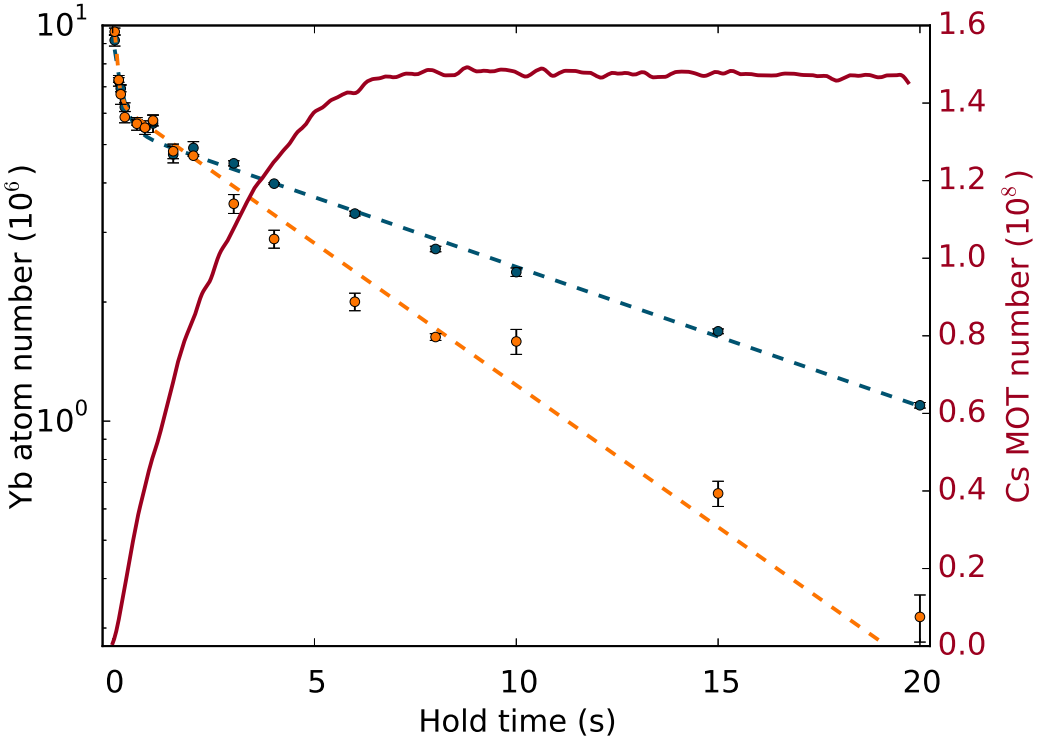

Figure 6.5: The influence of a Cs MOT on the number of trapped Yb atoms in the single beam optical trap. The blue data points show the number of Yb atoms remaining after a given hold time. The dashed blue curve shows a double exponential fit to the data. The orange data points show the Yb atom number remaining in the same optical trap when a Cs MOT, which is aligned to the optical trap, starts loading at the beginning of the hold time. The Cs MOT number over this time period is shown in red. The dashed orange line shows a significant reduction in the lifetime of the trapped Yb due to the presence of the Cs. We find that by loading the MOT in a different location by use of a small magnetic bias field, a lifetime similar to the blue curve is restored.

this point the single beam optical trap is turned on at full power with a transfer period of 1 s from the MOT to the dipole trap. The Yb atoms are then held for a predetermined time before absorption imaging is used to to determine the number of atoms remaining within the trap and their temperature. In the absence of any Cs atoms, a double exponential fit to the number of atoms remaining in the trap at different hold times leads to a short lifetime of 0.21 ± 0.02 s and a longer lifetime of 12.3 ± 0.1 s. The shorter of the two lifetimes can be attributed to the initial plain evaporation of the more energetic atoms from the trap, with the longer lifetime being due to losses associated with collisions with background gas in the vacuum

system. The blue curves in figures 6.5 and 6.6 show the decay of the atom number and the fall in the temperature respectively. We can see that the temperature of the Yb in the absence of Cs equilibrates to around 50 μK, in line with figure 5.4 which was taken under similar conditions.

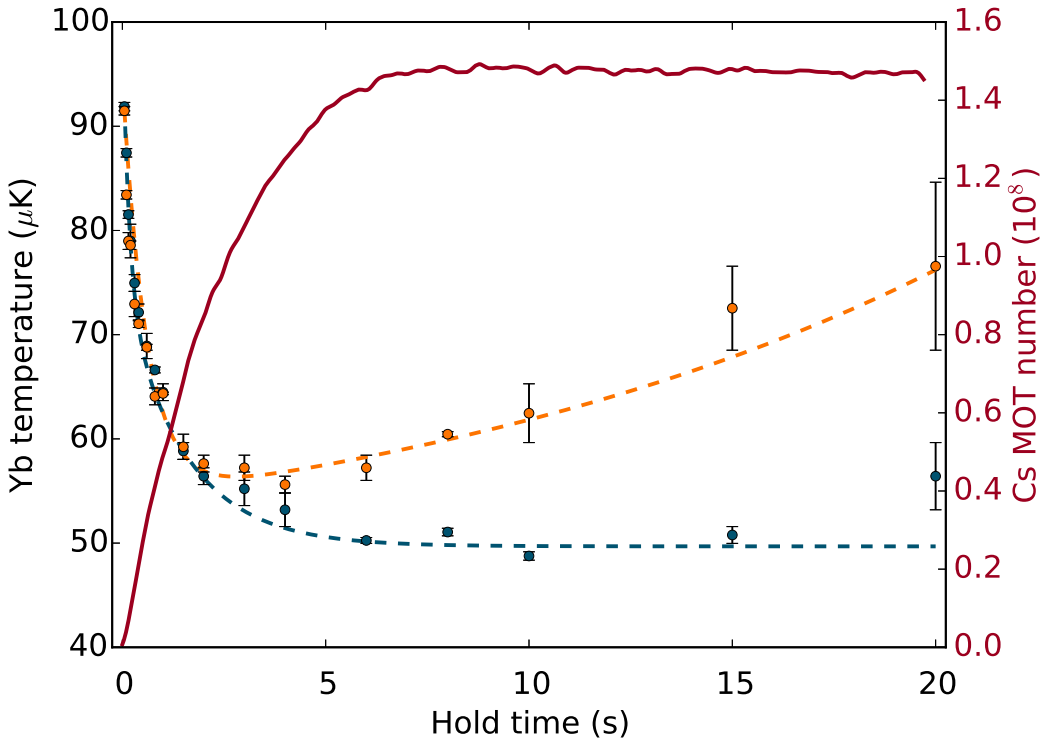

Figure 6.6: The impact of a Cs MOT on the temperature of Yb atoms held in the single beam optical trap. The blue points show the temperature evolution of the Yb clouds used to produce figure 6.5 as the hold time is increased. In the presence of the Cs MOT the plain evaporation of the Yb atoms is overcome by heating due to the Cs atoms, seen as an increase in the temperature at long hold times (orange data points). For reference the Cs loading curve is shown in red. The dashed curves are guides to the eye.

We now introduce a MOT of Cs to the routine. This is achieved by following the routine above, with the exception that following the transfer of Yb to the single beam optical trap, the oven's atomic beam shutter remains open and the beams and magnetic fields for the Cs Zeeman slower and MOT are turned on. The result is that whilst the Yb cloud is held within the dipole trap, the Cs atom number in the vicinity of the optical trap is increasing. For reference, the loading curve for the Cs MOT over this hold time can be seen as the red curve in figures 6.5 and 6.6.

The optical trap will be loaded with Cs atoms directly from the MOT, owing

to the fact that the trap depth is approximately an order of magnitude deeper for Cs than it is for Yb. In figure 6.5 we can see that the presence of the MOT has a detrimental effect on the lifetime of optically trapped Yb. The presence of Cs reduces the longer trap lifetime by a factor of two to 6.05 ± 0.09 s. We can also see in figure 6.6 that the temperature of the trapped Yb no longer reaches an equilibrium temperature of 50 μK. Whilst we still observe the rapid reduction in temperature resulting from the plain evaporation of Yb from the trap over the first 2 s of holding, the Yb then begins to heat at times later than this as the Cs MOT load increases. Over the timescales studied, which are limited by the number of atoms remaining in the optical trap, we observe an increase in the temperature to around 75 μK.

It is not possible to infer the scattering cross section from these measurements for a number of reasons: given the presence of a MOT, the Cs and Yb are not strictly speaking in the same trap; the density overlap of the Cs and Yb is unknown; and, most importantly, the Cs atoms will be in a mixture of hyperfine states, Zeeman sublevels, and even optically excited states owing to the pumping processes occuring in the MOT. Nevertheless this experiment does have implications. This experiment demonstrates that the routine of sequentially loading the two species into a common trap is viable. This will allow temperature differences between the species to be produced and the rethermalisation process to be observed. This is provided we are able to transfer Cs in its absolute ground state to the same trap, a process that is given more discussion in the next section. We can also see that we need to load the Cs MOT in a different location to the optical trap in order to avoid both losses and heating of the trapped Yb and the unwanted transfer of unpolarised Cs to the optical trap. In a similar experiment to the above, we have loaded the Cs MOT at a different location by applying a magnetic bias field using the shim coils. In this situation the lifetime of the Yb in the optical trap is restored and no residual heating is observed.

6.2.3 Outlook

It is clear that to be able to extract a meaningful scattering length from rethermalisation we need to load ultracold Cs in a single magnetic state,

namely $|F = 3, m_F = 3\rangle$, into a shared trap with ultracold Yb. Throughout this thesis we have not discussed in detail the performance of the Cs setup. This is because the performance and techniques have been well-established elsewhere [105, 107, 108]. However, some improvements and developments to the existing setup are discussed in appendix A. A relevant development of the Cs setup for the purposes of rethermalisation is that of optical pumping. Following the optical molasses stage of the experiment in which the Cs atoms experience sub-Doppler cooling to temperatures around 14 μK, we turn the repump beam off and use detuned cooling photons to depump the molasses into the $F = 3$ hyperfine manifold of the ground state. At this point the optical pumping beam is turned on for 200 μs along with a quantisation magnetic field in order to pump the atoms into the $|F = 3, m_F = -3\rangle$ state. This process can easily be reversed to pump to the $|F = 3, m_F = 3\rangle$ state.

Following the implementation of this routine, we have attempted to load this polarised sample of Cs into an optical trap already containing cold Yb. However, because the Cs MOT needs to be separated from the trapped Yb, the resulting Cs atom transfer to the optical dipole trap is not efficient enough to perform rethermalisation measurements with the trapped Yb. Clearly another approach is needed. Following the work of Weber et al [10], degenerate Raman sideband cooling (DRSC) is a good tool to produce clouds of polarised Cs with a high PSD; an ideal starting point for the creation of a Cs BEC. The higher PSD will enable more efficient transfer to an optical trap and allow rethermalisation measurements to be carried out. However, we would still need to repeat this process for a number of isotopic combinations in order to extract the scattering length as opposed to the cross section. For this reason work is ongoing to implement DRSC and create routines for optically trapping different isotopes of Yb. Such repeated measurements are unnecessary when using two-photon photoassocation, as a single measurement extracts the scattering length directly. It is for this reason, along with the aim of producing ultracold molecules, that we have been developing a photoassociation system in parallel with our attempts at rethermalisation.

6.3 Photoassociation

6.3.1 Finding the scattering length

Whilst photoassociation may not be the ideal method for producing ultracold molecules in the ground state, photoassociation spectroscopy can be an invaluable tool for finding the scattering length of a system. Unlike rethermalisation, photoassociation provides a direct measurement of the binding energy, and hence the background scattering length as opposed to the cross-section. Furthermore, this process may be undertaken in a MOT and has been used by the Düsseldorf group to measure the binding energy of the RbYb molecule [100, 242, 243]. The first stage in this process is to locate and identify the bound states within the excited state molecular potential. This can be achieved by scanning the frequency, ω_{L1}, of a laser that is focussed onto the trapped atoms. This frequency will be red-detuned from the corresponding free-atom transition of interest. When the frequency is resonant with a molecular bound state, a reduction in the trapped atom number will be observed. This is either due to the molecule dissociating to free atoms with enough kinetic energy to escape the atom trap, or the molecule may decay to a bound state in the ground electronic potential of the molecule and is thus not resonant with the atom imaging laser system. Whilst this simple application of one-photon photoassociation spectroscopy may be applied to determine the scattering length in homonuclear systems, certain assumptions underlying this technique break down for heteronuclear systems [82].

Once the spectrum of bound states in the electronically excited molecular potential has been identified, two-photon photoassociation spectroscopy may be used. This process is outlined in figure 6.3 (b). The excitation laser is stabilised to a photoassociation resonance at a frequency, ω_1, and a second laser's frequency, ω_{L2}, is scanned. When ω_{L2} is resonant with a downwards transition from the excited bound state to a bound state in the ground electronic potential of the molecule, a light shift of the excited state occurs and causes a lower rate of production of molecules by the first laser. As such the number of atoms lost from the trap is partly restored. This process is analogous to Autler-Townes spectroscopy [244].

In order to extract the scattering length from two-photon photoassociation spectroscopy, we first need to use the locations of the bound states to extract the long-range form of the molecular potential. This requires finding the C_6 coefficient for the system, which can be achieved by fitting the binding energies of the last few bound states of the ground state electronic potential to the LeRoy-Bernstein formula [245]

$$\Delta_{\text{bind}} = -\frac{1}{hc}\left[\left(\nu_D - \nu\right)\hbar\sqrt{\frac{2\pi}{\mu}}\frac{\Gamma\left(7/6\right)}{\Gamma\left(2/3\right)}\frac{4}{C_6^{1/6}}\right]^3, \tag{6.28}$$

where ν is the vibrational quantum number, ν_D is the non-integer value of the vibrational quantum number at the dissociation threshold, and μ is reduced mass of the system. C_6 and ν_D can be used as the fitting coefficients. Using the fitted value of C_6, a Lennard-Jones potential of the form

$$V\left(r\right) = \frac{C_{12}}{r^{12}} - \frac{C_6}{r^6}, \tag{6.29}$$

can be modelled with the Schödinger equation, using C_{12} as a fitting parameter to find a good approximation of $V\left(r\right)$ that replicates the observed bound states. The scattering length is then given by

$$a = \bar{a}\left[1 - \tan\left(\phi - \frac{\pi}{8}\right)\right], \tag{6.30}$$

where $\bar{a}$ is the mean scattering length given by

$$\bar{a} = 2^{-3/2}\frac{\Gamma\left(3/4\right)}{\Gamma\left(5/4\right)}\left(\frac{-2\mu C_6}{\hbar^2}\right)^{1/4}. \tag{6.31}$$

The phase, ϕ, is found by integrating the potential from the classical turning point of the last bound state, r_0, outwards to infinity

$$\phi = \frac{\sqrt{2\mu}}{\hbar}\int_{r_0}^{\infty}\sqrt{\left|V\left(r\right)\right|}dr. \tag{6.32}$$

From the mass scaling of μ it is then possible to predict the scattering lengths for all isotropic combinations from only one measurement of the scattering length. As such, two-photon photoassociation spectroscopy is a very powerful

technique for determining the scattering length of a heteronuclear system.

6.3.2 Optical setup

Whilst the method of two-photon photoassociation spectroscopy is very simple in principle, two stringent conditions are placed on the laser systems used in the process. Firstly, the more deeply bound vibrational states of the molecular potential can be more than 50 cm^{-1} detuned from the free atom threshold. The laser systems therefore need to be highly tunable, ideally with a large scan range in order to produce spectra with more than one molecular feature. Secondly, the Franck-Condon overlap between the continuum of free atom states and bound vibrational states is generally poor, and since the rate of photoassociation is proportional to intensity this implies that usable spectra will require high laser powers. To meet these requirements, we use an ECDL with a large scan range to seed a tapered amplifer (Toptica, BoosTA Pro) with a maximum output power of $\sim$ 1.5 W, and a distributed Bragg reflector (DBR) laser (Photodigm, 895nm Mercury Packahe) with a 200 mW output power. Both of these laser systems have peak operating wavelengths of 895 nm, making them ideal to produce photoassociation spectra in the vicinity of the Cs D_1 lines.

Figure 6.7 shows the photoassociation setup, although it should be noted that at the time of writing only the DBR laser setup is fully operational. The output wavelength of the DBR laser is highly tunable by the control of the diode's temperature. This makes it a good choice for the "first-photon" – the laser providing the excitation from the free atom state to a bound state within the electronically excited molecular potential. The ECDL can be continuously tuned over a typical range of $\sim$ 30 GHz, and paired with the TA provides a good choice in system with which to search for bound-bound transitions to the electronic ground state of the molecule.

A small portion of the output power from the ECDL and DBR lasers is combined on a PBS cube and fibre coupled to a wavemeter and a compact saturation absorption spectroscopy setup on the D_1 lines. The spectroscopy setup is primarily for diagnostics, but the wavemeter is used for an absolute frequency calibration. Some light from each laser is also fibre

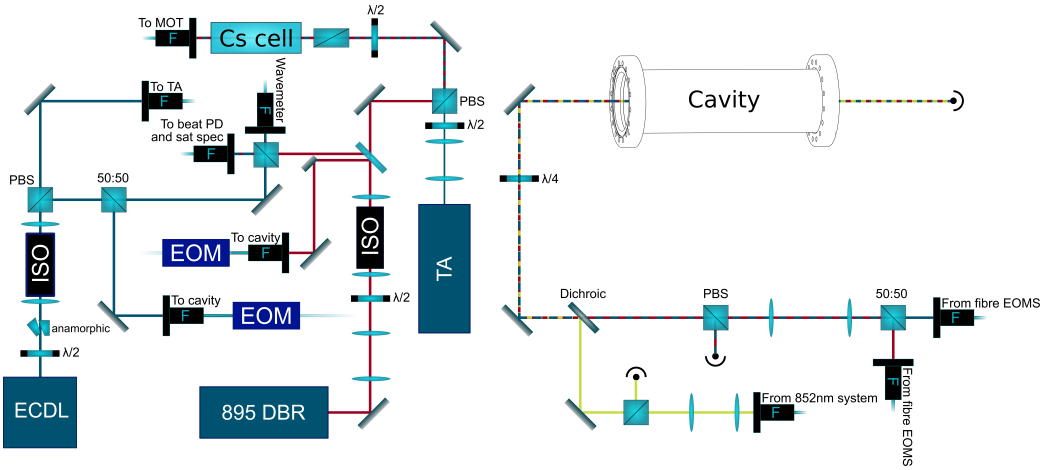

Figure 6.7: Schematic diagram of the photoassociation laser setup in its current form. An external cavity diode laser (ECDL) and a distributed Bragg reflector laser (DBR) are used as sources of 895 nm light, with the ECDL being used to seed a tapered amplifier (TA). Both lasers are stabilised by referencing a sideband from fibre EOMs to a high-finesse optical cavity in a Pound-Drever-Hall (PDH) locking scheme. The cavity itself is stabilised to 852 nm light from the Cs MOT setup. Beams from the ECDL and DBR are also sent to a wavemeter and saturated absorption spectroscopy setup to provide absolute frequency references. Beams combined from the TA and the DBR laser are fibre coupled to the main table of the experiment.

coupled to a high-finesse optical cavity using broadband optical fibre EOMs (EOSPACE, PM-0S5-10-PFU-PFU-895). The cavity itself is a homebuilt system, originally intended for the STIRAP of RbCs Feshbach molecules to the rovibrational ground state, featuring a zerodur spacer that keeps two resonator mirrors at a fixed distance. This setup gives a free spectral range of 750 MHz [144]. The zerodur spacer has a thermal expansion coefficient that leads to a drift in frequency that is too large for reproducible results. For this reason the cavity length is actively stabilised with reference to 852 nm light from the frequency stabilised Cs MOT setup, using a PZT behind one of the cavity mirrors to provide feedback. Further details on the optical cavity can be found in appendix B.

The purpose of this cavity in our setup is to stabilise the laser systems using a Pound-Drever-Hall locking scheme. By choosing to stabilise one of the sidebands from the fibre EOM to a cavity peak, we are effectively able to set the laser output frequency arbitrarily by changing the RF frequency input of the fibre EOM. This will ultimately be used to fix the first photon to

resonance with a molecular bound state, whilst the second laser is scanned to find downwards transitions. The locking signal is maximised by correctly mode-matching the beams to the cavity to ensure the maximum amount of light in the TEM_{00} mode as possible. This is achieved by a combination of a pair of lenses with focal lengths of 100 mm and -100 mm respectively, the positions of which are moved until the position and size of the beam waist matches the cavity geometry. An example of this process can be seen in figure B.1.

The vast majority of the power outputs of the DBR laser and the TA are coupled to the main table of the experiment for use in photoassociation via a high-power optical fibre. Prior to the fibre a heated Cs cell is used as a filter in order to eliminate resonant D_1 light reaching the MOT or optical trap. The output of the fibre is focussed to a waist of 150 μm at the MOT location, using the dipole trapping viewports for optical access. By retroreflecting the photoassociation beam we obtain a peak intensity of 250 $\mathrm{W\,cm^{-2}}$.

6.3.3 Photoassociation of Cs_2 in a MOT

As a first test of the 895 nm photoassociation system, we perform one-photon photoassociation spectroscopy of the Cs MOT using the DBR laser. Using the wavemeter as a guide, the DBR laser is red-detuned from the $6^2S_{1/2} \rightarrow 6^2P_{1/2}$ free atom transition. As we have seen previously, any excited Cs_2 molecules that are produced will either decay into a bound state of the ground electronic molecular potential or dissociate back into a pair of free atoms. It follows that our detection scheme for molecular production is the loss of atoms from the MOT – either the molecule decays to another state and remains a molecule that is lost from the MOT cooling cycle, or the molecule dissociaties into atoms with velocities greater than the capture velocity of the MOT. For this experiment we monitor the Cs MOT number continuously by measuring the fluorescence of the atoms in the MOT using one of the detectors described in chapter 3.

Before searching for photoassociation spectra of Cs_2, there are a number of parameters that must be considered in order to produce a useful signal of molecular association. This is because the detection is strongly dependent

on the loading and loss properties of the Cs MOT. Consider the modified rate equation for the Cs MOT when photoassociative loss is included

$$\frac{dN}{dt} = R - \gamma N - (\beta + \beta_{\mathrm{PA}}) \int n^2 (\mathbf{r})\, d\mathbf{r}, \tag{6.33}$$

where N is the Cs atom number in the MOT with $n(\mathbf{r})$ the corresponding atom density, R is the loading rate, γ is the background loss rate, and β is the loss rate due to binary collisions between Cs atoms (non-photoassociative). β_{PA} is the loss rate due to photoassociative collisions forming molecules that do not then decay back to trappable atoms. The average rate of photoassociative loss, $\mathcal{B} = \beta_{\mathrm{PA}}\bar{n}$, where $\bar{n}$ is the average atom density, can be expressed as [246]

$$\mathcal{B} = A \left(\frac{3}{2\pi}\right)^{3/2} \frac{h}{2} n \lambda_{\mathrm{th}}^3 e^{-E_r/k_{\mathrm{B}}T} \Omega^2 S^2, \tag{6.34}$$

where A is an angular momentum factor, λ_{th} is the de Broglie wavelength of the scattering atoms, $E_r = \hbar\Delta_\nu$ is the energy associated with the detuning from the state with vibrational quantum number ν, Ω is the Rabi frequency, and S^2 is the Franck-Condon overlap between the scattering state and the bound molecular state.

This treatment implies that we need to engineer a Cs MOT where photoassociative loss becomes significant compared to the other forms of trap loss. The reason we reteroreflect the photoassociation beam to give intensities of 250 $\mathrm{W\,cm^{-2}}$ at a tightly focussed waist of 150 μm is to increase the Rabi frequency and thus increase photoassociative loss. We also load the Cs MOT with a magnetic field gradient of 25 $\mathrm{G\,cm^{-1}}$ as opposed to the usual 8.53 $\mathrm{G\,cm^{-1}}$. This creates a higher Cs density in the high intensity region of the photoassociation beam, and crucially reduces the capture velocity of the MOT, making dissociating Cs_2 molecules less likely to be recaptured by the MOT and increasing our loss signal. We also reduce the background collisions in the MOT by operating with the atomic beam partially shuttered off. This also reduces the MOT loading rate, R, but we find the reduced γ to have a significant impact on the signal. Finally, the MOT is operated at a total cooling intensity of 10 $\mathrm{mW\,cm^{-2}}$. This has the effect of reducing binary

collisions between excited Cs atoms in the MOT, and reducing the loss rate β.

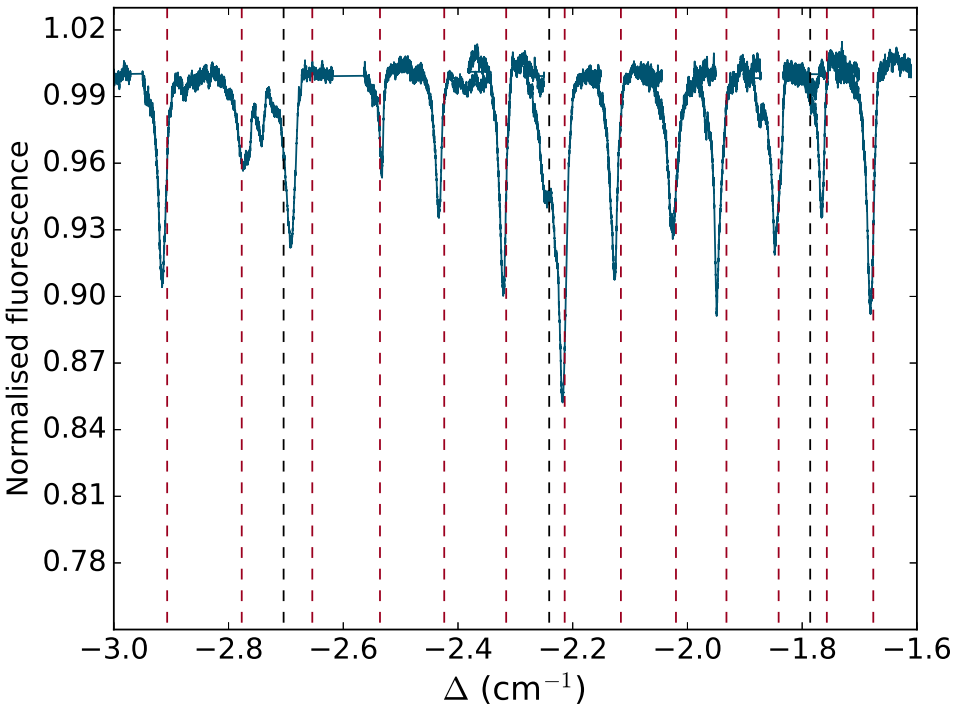

Figure 6.8: One-photon photoassociation spectrum of Cs_2 from a Cs MOT. The detuning is measured from the $5S_{1/2}\,(F = 4) \rightarrow 6P_{1/2}\,(F' = 4)$ transition. The reductions in MOT fluorescence correspond to the excitation of different vibrational states in the excited electronic state of the Cs_2 molecule. The dashed red (black) vertical lines correspond to previously measured values of the binding energies of 0_u^+ $\left(0_g^-\right)$ vibrational levels.

Figure 6.8 shows a sample one-photon photoassociation spectrum for Cs_2 red detuned from the $6^2P_{1/2}$ atomic asymptote. The figure is built up by making 3.5 GHz scans of the DBR laser whilst the Cs MOT is continuously loaded with the parameters outlined above. The start point of the scan is determined using the wavemeter, and each scan is performed three times and averaged. A total of 36 separate 3.5 GHz scans were used to build up the spectrum shown in figure 6.8. The dashed vertical lines show the expected positions of the resonances taken from the measurements of Pichler et al [247]. In total we observe 16 transitions to vibrational states, these correspond to vibrational states $\nu_\mathrm{d} - \nu = 122$ – 136 of the 0_u^+ potential, and $\nu_\mathrm{d} - \nu = 14$ – 16 of the 0_g^- potential. Here ν is the vibrational quantum number of the state, and

ν_d is the quantum number of the last vibrational bound state supported by the potential. To obtain spectra such as this, we need to scan the photoassociation laser frequency slowly – here 2 GHz/min was used – this allows the photoassociation beam to be resonant for approximately the response time of the MOT, which is around 2 s in this case. It is for this reason that the lineshapes of the loss features are asymmetric. When the photoassociation beam is resonant with transitions to bound states a rapid depletion of the MOT occurs, corresponding to $\mathcal{B}$ increasing close to resonance. As the detuning of the photoassociation beam departs from resonance, $\mathcal{B}$ reduces and is accompanied by an increase in the atom number in the MOT. The rate of increase is limited by the MOT properties, and as such the linewidths of the features will inherently be linked to the scan rate of the laser frequency. We notice that there is typically a systematic error between our loss features and those observed in [247]. This may be due to this lag in the response of the MOT, however over such long scans there may also be thermal noise on the DBR laser diode contributing to the uncertainty.

6.3.4 Towards photoassociation spectroscopy of CsYb

Producing Cs_2 spectra has been a good test of the first laser in our photoassociation scheme, however the intention is to use this setup to measure the binding energy of the CsYb molecule. Photoassociation spectroscopy of a mixture of species, in both its one- and two-photon varients, is perfectly possible in a dual species MOT. Indeed, this is the method the Düsseldorf group used to find the scattering length for s-wave scattering of Yb and Rb [100]. Performing these experiments in a MOT is in some ways preferable to using a conservative trap, as it is possible to obtain a continuous signal from the fluorescence of the atoms in the MOT. If we were to proceed with this approach, we would monitor the fluorescence of the Yb molecules in the MOT as opposed to the D_2 fluorescence scheme used above. In this scenario we would be measuring photoassociative loss of Yb from the MOT. Because we will still be associating molecules with photoassociation energies red detuned of the Cs $6^2P_{1/2}$ asymptote, the only photoassociative loss of Yb will be due to the excitation of CsYb molecules. Cs_2 will still be excited at detunings

resonant with transitions such as those in figure 6.8, however they result in no loss of Yb and so will no longer be detected.

Whilst it is perfectly possible to produce a dual-species MOT in our exeriment [105, 107, 108], there are some important details to note. Firstly, given the vastly different conditions required for the Zeeman slowing of Yb and Cs, it is not currently possible to simultaneously load MOTs of both species at once. Instead we load the MOTs sequentially, partially loading the Yb MOT with one Zeeman slower field configuration, and then switching to the configuration for Cs. This method is repeated so that the Yb MOT is always loading whilst the Cs MOT is decaying and vice versa. Whilst this would produce a varying background fluorescence signal, it does not rule out photoassociation spectroscopy on the MOT. However, we have observed that the Yb Zeeman slowing beam enhances losses from the Cs MOT, possibly due to the ionisation of excited Cs. When operating in the conditions presented in section 6.3.3 this will cause a large reduction in the Cs MOT density, limiting the photoassociation rate, $\mathcal{B}$. Furthermore, given the long length of the photoassociation laser scans, the loading conditions will have to be switched several times. The large changes in magnetic field profiles required for sequential loading, and in particular the beam pushing of the Yb MOT by the Yb Zeeman slower light, make it very hard to maintain an overlapped dual species MOT. These factors significantly reduce the likelihood of performing photoassociation spectroscopy of CsYb in a dual species MOT in our system.

These considerations leave loading Yb and Cs into a common optical dipole trap as our best route towards determining the background scattering length, which should enable rethermalisation measurements to also take place. This scenario is not as ideal as performing photoassociation in a MOT. The techniques remain the same by scanning the frequency of an intense photoassociation beam that is aligned to the atoms in the trap. An increased density will also improve photoassociation rates. However, the loss will not be observed continuously as we will have to use destructive absorption imaging techniques to measure losses. This process will be more time consuming than the simple method of observing loss from the MOT. The atoms in the optical trap will not be continuously loaded and will decay with time limiting the scan range of the photoassociation laser system. Furthermore, we will have to identify

losses and then reduce the scan ranges to pinpoint the detuning of a resonance, at which point shot-by-shot measurements will have to be made to map out the lineshape of the resonance.

6.4 Towards ultracold CsYb molecules

As we have explored throughout this chapter, there exist a number of possible routes to explore in the creation of ultracold CsYb. In choosing a method there are a number of factors to consider that will be outlined here. We have seen that Feshbach resonances in a mixture of Yb and Cs only arise due to the weak coupling of the hyperfine coupling constant to the internuclear separation of the Cs and Yb atoms. The result is that Feshbach resonances are likely to be very narrow until magnetic bias fields exceed ~ 2000 G [106]. In addition to these fields the level of precision required in controlling the magnetic field is likely to be 10^5. At present our setup is not capable of producing these magnetic fields, although it is possible that, given the 7 isotopic combinations available, we may find a fortuitously wide Feshbach resonance if a bound state and atomic threshold have a small difference in their magnetic moments, giving rise to a "glancing blow"-type resonance. This compounds the need for a measurement of the scattering length in order to proceed with any study with CsYb molecules, so that we may predict where such resonances lie. We have purposefully designed the experiment so that the magnetic coil arrays can easily be replaced, and continue to look into methods of creating large and controllable bias fields such as through the use of bitter coils [133].

It has been shown that broader Feshbach resonances occur between ground state alkali atoms and Yb atoms excited to the metastable $^3P_2$ [248]. This is also a possibility for our sytem, but would require the development of a new laser system to populate Yb in the metastable state. All of this information points to the fact that whilst magneto-association is the preferred choice for preparing ultracold CsYb molecules, owing to the coherent production of molecules in a single vibrational state, we must prepare for the possibility that the method is not available, or not possible, for our system.

This leaves photoassociation in its various forms as the technique for producing ultracold CsYb molecules that is most likely to succeed, at least in the short-term. The disadvantage of photoassociation is that it typically forms an incoherent mixture of molecule states in the ground electronic potential of the molecule. As we have seen, some systems are able to obtain significant transfer to the absolute ground state due to favourable Franck-Condon factors arising from the shape of the molecular potentials [85]. Unfortunately the molecular potentials in CsYb will lie parallel to one another, with separations given by the energy of free atom transitions. As such, a weakly bound state in the excited potential formed by photoassociation will be unlikely to decay to the absolute ground state, instead favouring decay to a series of weakly bound vibrational states or dissociation back to free atoms.

There could be a solution to these problems by performing photoassociation in an optical lattice. Furthermore CsYb is not stable to exchange reactions of the form $2\mathrm{CsYb} \rightarrow \mathrm{Cs_2}+\mathrm{Yb_2}$, and so any molecules produced will need to be localised in an optical lattice to prevent losses of this form. Since an optical lattice will ultimately be needed for the furtherance of the experiment, it seems to be a good avenue to explore to aid the production of the molecules themselves. By producing Cs and Yb BECs it will be possible to form a Mott insulator state in an optical lattice, with a single Yb and Cs atom in each site [36]. From this point, we would need to perform photoassociation and search for states exhibiting decay to only a few bound states in the ground potential. Here STIRAP may be used to transfer atoms to the ground state. The reduced internuclear separation in a lattice may even allow STIRAP to be used to coherently transfer free atomic states directly to a molecular state [88]. Ultimately the path to producing CsYb molecules is not set in stone, and is an ongoing problem for groups studying systems of alkali and alkaline-earth-like atoms. What is clear is that we must first characterise the system and identify the leading contenders for efficient production of ground state CsYb.

6.5 Summary

In this chapter we have presented the progress towards a measurement of the background scattering length of mixtures of Yb and Cs. This measurement is of crucial importance as it will determine the route we take to produce ultracold molecules, and which isotopic combination is the most favourable. We have described the two techniques with which we intend to measure the scattering length: rethermalisation in a conservative trap, and photoassociation. The progress made on each of these techniques has been reported alongside some of the difficulties we face in obtaining the measurement and in the long-term goal of producing CsYb molecules.

It has been shown that rethermalisation can be used to obtain the elastic cross section, from which the magnitude of the scattering length can be inferred. Thus by performing this process with a few isotopic combinations the sign of the scattering length could also be found. To date we have seen the impact that loading a Cs MOT has on optically trapped Yb. If the MOT overlaps the optical trap then we observe significant loss and heating of the trapped Yb atoms. By loading the Cs MOT in a location below the optical trap, the trap lifetime and equilibrium temperature of Yb is restored. For this reason, in future sequential loading routines we will separate the location of the loading phase of the MOTs and the optical dipole trap. We have attempted to load polarised Cs in the $|F = 3, m_F = -3\rangle$ state into a single beam optical trap containing Yb by simply optically pumping the Cs into this state from optical molasses. However, we are unable to efficiently load these atoms into the optical trap and will instead pursue degenerate Raman sideband cooling in future experiments to polarise and further cool the Cs atoms prior to loading them into the optical dipole trap.

We have also reported the development of a photoassociation spectroscopy setup using the Cs $6^2P_{1/2}$ asymptote. The current purpose for this setup is to infer the scattering length by measuring the binding energy of the least bound state in the ground electronic potential of the CsYb molecule. We have described the optical setup for this system and demonstrated the ability to perform one-photon photoassociation spectroscopy of Cs_2 as a test of the system's performance. Ultimately photoassociation spectroscopy of Yb-Cs

will have to be performed in an optical dipole trap, owing to the fact that we can only sequentially load MOTs of Cs and Yb in our current apparatus.

The next chapter looks ahead to the future of the experiment and provides a conclusion for this thesis.

Chapter 7

Conclusions and outlook

During the course of this work a number of improvements and developments have been made to the CsYb experiment. There have been considerable changes made to the Yb laser systems and the vacuum system, improving the reliability and reproducibility of the experiment. We have used these new systems to characterise a fluorescence detection system on an atomic beam of Yb, and the cooling of atoms in a Yb MOT at narrow linewidths. An optical dipole trap has also been implemented, allowing the regular production of nearly pure ^{174}Yb BECs containing $\sim 10^5$ atoms. Finally, we have made significant steps towards a measurement of the background scattering length of Yb-Cs mixtures, which should be undertaken in the near future, allowing for possible routes to the creation of ultracold CsYb to be discovered. In the remainder of this chapter we will summarise the work presented in this thesis and outline future upgrades to the apparatus and experiments that may be performed.

7.1 Summary

During the course of this work a number of upgrades have been made to the original CsYb apparatus [107, 108]. The vacuum system has been updated with a new oven design. This design replaces the Cs dispensers used in the previous incarnation with a 1 g ampoule of Cs placed in a small vacuum bellows and heated with a band heater. This design has allowed far greater

control over the Cs beam flux than in the previous design and with a greater longevity. The Yb and Cs sources within the oven are now separated by a valve. This allows Yb to be studied independently of Cs, without the appreciable room temperature vapour pressure of Cs creating a low-flux Cs beam. Another major advantage this offers is the ability to service and replenish the Yb oven without bringing the Cs source up to air.

The second addition to the main experiment is the implementation of a new coil array positioned in the reentrant flanges of the science chamber. This array includes a quadrupole pair of coils and fast bias coil pair. This is the partial implementation of a larger array of coils that include two further bias coil pairs with the capability of producing $\sim$ 1800 G bias fields. We have not implemented the full set of coils thus far, as we first wish to study the scattering properties of the Yb-Cs mixture before making an informed decision of the magnetic fields required based on the likely location and widths of Feshbach resonances.

The modification to the experiment with the biggest impact has been the overhaul of the Yb laser system. We have replaced the previous master-slave setup of homebuilt ECDL lasers that address the 399 nm transition with a single high-power commercial diode laser (Toptica, DL Pro HP). This laser outputs up to 100 mW of tunable single-mode light, meaning a separate slave laser is no longer required. As before, the majority of the power output is sent to form the Zeeman slower beam for Yb, with the remaining power fibre-coupled to a spectroscopy setup. This setup has also changed dramatically – we now use a system of double passed AOMs to produce the detuning required for the Zeeman slower beam, using fluorescence spectroscopy on an atomic beam to stabilise the laser frequency. This system has allowed the implementation of resonant absorption imaging on the cold Yb atoms produced in the experiment. The same approach is also used to stabilse the 556 nm laser used to produce the MOT beams for Yb; a frequency modulated probe beam passes through an Yb beam and the fluorescence signal is demodulated to provide a signal with which to stabilise the laser frequency.

To produce the fluorescence spectra for laser frequency stabilisation we use a "beam machine" – a miniature atomic oven – with homebuilt fluorescence

detectors. These detectors give excellent signal to noise ratios without the use of photomultiplier detectors, instead using relatively inexpensive high-gain photodiode circuits. The detectors are battery powered and enclosed within a Faraday cage to reduce RF pickup. This simple approach to laser frequency stabilisation allows us to load Yb MOTs on the $^1S_0 \rightarrow {}^3P_1$ transition, trapping $\sim 10^9$ atoms without the use of frequency sidebands on the MOT beams. We have also demonstrated that the dipolar spontaneous emission pattern may be used to separate the spectra of the fermionic and bosonic isotopes of Yb.

The combination of the new 399 nm laser system and laser frequency stabilisation using the fluorescence on the atom beam, has lead to highly reproducible MOTs of Yb allowing for the characterisation of the cooling processes in a narrow linewidth MOT. In such systems the force due to gravity on the atoms within the MOT cannot be ignored, as it becomes comparable to the scattering force from the MOT photons. In situations where the MOT beam intensities are low, the power broadening of the transition decreases and atoms in the MOT must fall to experience a force from the upwards propagating MOT beam that allows them to be supported against gravity. This change in the position results in a Zeeman shift that effectively brings the atoms closer to resonance with the upward propagating MOT beam, resulting in temperatures up to a factor of 5 lower than the predictions of standard Doppler cooling. This process has allowed for efficient direct loading of Yb MOTs into an optical dipole trap. We have also used the cold MOT as a method of calibrating the fluorescence spectroscopy of the $^1S_0 \rightarrow {}^3P_1$ transition. By cooling the MOT using the above gravitational sag technique, we release the MOT with a bias field applied before pulsing the MOT beams to produce fluorescence spectra of the magnetic field insensitive $m_J = 0 \rightarrow m'_J = 0$ transition. This technique has allowed the measurement of systematic detuning offsets created by non-orthogonal crossing of the probe and atomic beam in the fluorescence spectroscopy setup.

The implementation of a crossed optical dipole trap has enabled the efficient loading of Yb into a conservative trap, with the final Yb MOT parameters found to be crucial in increasing the initial phase-space density. Evaporative cooling has resulted in the reliable production of ^{174}Yb Bose-Einstein

condensates containing $\sim 10^5$ atoms. This represents the first realisation of a lanthanide or alkaline-earth BEC in the UK. This reliable production of Yb BECs should allow for controllable loading of Yb into optical lattices for future association with Cs into ultracold molecules.

Finally, we have made significant progress towards the measurement of the Yb-Cs interspecies scattering length. We have focussed on two approaches: the rethermalisation of Cs and Yb in a common conservative trap, and direct measurement of the binding energy through two-photon photoassociation spectroscopy. Rethermalisation measurements have proved troublesome without the use of degenerate Raman sideband cooling (DRSC), since efficient transfer of Cs atoms in the $|F = 3, m_F = 3\rangle$ state to an optical trap containing Yb has not been possible using optically pumped molasses. However, these measurements have shown that the presence of a Cs MOT nearby optically trapped Yb severely impacts the lifetime and heating of the Yb cloud, necessitating an experimental routine in which the Cs MOT is formed away from the trapped Yb. We have also described the development of a photoassociation spectroscopy system and its testing in producing one-photon photoassication spectra of Cs_2. Given that it is difficult to produce overlapped Cs and Yb MOTs continuously with this system, there is further evidence that our immediate goal is to produce optically trapped samples of polarised Cs that can be combined with our optically trapped Yb. Once achieved this will allow us to proceed with photoassociation or rethermalisation measurements of the interspecies scattering length.

7.2 Outlook

Future upgrades to the apparatus

There are a number of potential upgrades and additions that could be made to the apparatus in order to access new physics with ultracold atoms and molecules. Whilst we could perform the majority of planned experiments in our science chamber, optical access is now at a premium. For this reason it has been proposed that we attach a glass cell to one of the dipole trap viewports on the science chamber. This would include an additional vacuum

pump, potentially a model combining a NEG and ion pump, in order to address our limited background lifetime. This extended glass cell would likely contain in-vacuum electrodes for use in measuring the electric dipole moment of CsYb molecules. In order to transport atoms to the glass cell we would ideally optically trap the atoms in the current science chamber, and optically transport the ultracold atoms into the glass cell using a translational optical stage. The addition of the glass cell would then provide much more optical access for optical lattice beams as well as allowing multiple-axis absorption imaging. Such a proposal is shown in figure 7.1.

Short-term

In the short-term, the biggest priority is to obtain a measurement of the interspecies scattering length. If this is achieved through photoassociation, mass scaling could be applied to estimate the scattering length for all isotopic combinations. Using rethermalisation, only the cross section is obtained, and so this experiment would be repeated for a few isotopic combinations in order to extract the sign of the scattering length. Once the scattering length is known, the long-range molecular potential is also known and may be used to predict the locations and widths of Feshbach resonances, along with the positions of the various bound states supported by the potential.

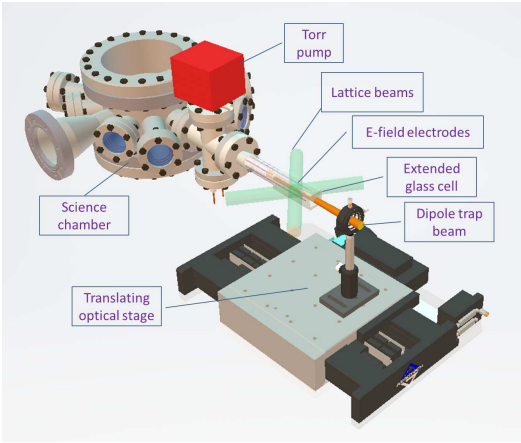

Figure 7.1: An illustration of a potential upgrade to the apparatus, in which an extended glass cell with in-vacuum electrodes and additional pumping station are added to the science chamber. A translating optical table would enable a simple optical tweezer setup to be realised, allowing optical access for lattice beams.

Following on from the work presented in this thesis, the first stage to measuring the scattering length will be to obtain a spin-polarised sample of optically trapped Cs. One possible method for achieving this is to implement degenerate Raman sideband cooling prior to the loading of the optical trap. [1] By transferring the resulting sub-Doppler cooled Cs atoms into a trap already containing Yb, rethermalisation or photoassociation measurements of the scattering length can follow. Given the large polarisability of Cs at 1070 nm, it is also desirable to produce an optical trap with larger volume (i.e. larger waist at the trap centre) than our existing trap that produces BECs of Yb. This trap will create a "reservoir" of Cs, which can then be used to load a "dimple" trap of smaller volume by elastic collisions. This may be the trap that is already employed for Yb. This method has proven to be an efficient way to produce BECs of Cs [10]. Whilst BECs are not strictly necessary for a cold molecule experiment, they will add a certain degree of control in loading an optical lattice. By loading both species as BECs it may be possible to access a two-species Mott insulator transition with near unity filling of each species in the lattice sites.

Long-term

In the long-term our main aim is to implement the techniques required to produce ground state CsYb molcules. At present we do not know what the ideal route will be, however we know that we will need to form the ultracold molecules in lattice sites in order to prevent loss by reactive collisions. Measurements of the scattering length will reveal whether suitable Feshbach resonances occur for magneto-association, however it is quite likely that these resonances will be too narrow or occur at magnetic fields too large to address. Should this be the case we will explore further routes. One such route is to create metastable Yb, denoted Yb*, by populating the long-lived $^3P_2$ state. This would be achieved by exciting Yb to the $^3D_2$ state using laser light at a wavelength of 404 nm. It has been shown in other systems that collisions between atoms and Yb* have much stronger coupling between the molecular bound states and the free atom states, resulting in broader Feshbach resonances [248, 249]. Should either of these approaches to magneto-association

[1] Over the course of writing, this process has been implemented in the experiment.

work, the molecules will be in a excited state of the ground state molecular potential and we would need to implement STIRAP for coherent transfer to the absolute ground state. It is entirely possible that by accessing the two-species Mott insulator state in a lattice, we will be able to directly associate free atoms to molecular states using STIRAP by following the scheme demonstrated for Sr_2 by Stellmer et al [88]. Investigations into accessing the two-species Mott insulator will be carried out using a lattice at a wavelength of around 880 nm using a Ti:sapphire laser. At this wavelength the relative polarisabilities of Cs and Yb are highly tunable as can be seen in figure 7.2, allowing the relative lattice potentials to be tuned for Cs and Yb.

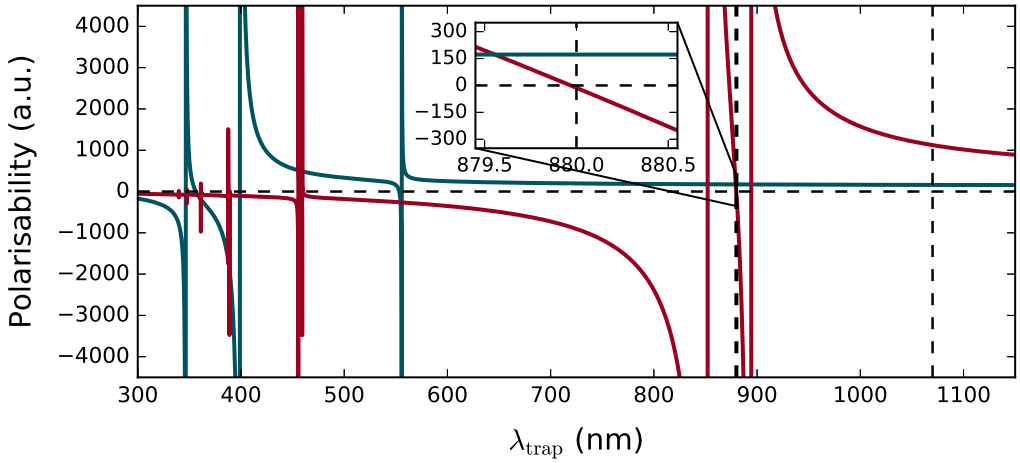

Figure 7.2: The calculated polarisability for Yb (blue) and Cs (red) in their respective ground states is shown for a variety of wavelengths. The inset to the figure shows the tunability of the relative polarisability between the D_1 and D_2 lines of Cs. It can be seen that the polarisability of Cs is zero at approximately 880 nm whilst the polarisability of Yb remains positive, opening the door to the possibility of a Cs-blind lattice potential.

Whilst the primary aim for this experiment is to associate ultracold Yb and Cs to CsYb molecules in an optical lattice, the wavelength tunability of a Ti:sapphire lattice offers many interesting opportunities for atomic experiments. Figure 7.2 shows that in between the D_1 and D_2 lines of Cs at around 880 nm it would be possible to engineer a Cs-blind lattice, in which Yb atoms feel the lattice potential whilst the Cs atoms are unperturbed. By producing a lattice with near unity Yb filling immersed in a Cs BEC, we would engineer a system of a superfluid with impurities in the form of Yb atoms pinned by the lattice sites. This would allow a number of interesting

experiments to be carried out. For example, the dephasing and clustering of the impurities [250], novel lattice cooling schemes [251], and the transport of polarons on the lattice [252] could be performed in such a system.

7.3 Concluding remarks

The work presented in this thesis outlines the large steps forward this experiment has made towards producing ultracold CsYb molecules. Molecules of this form are extremely valuable for quantum simulation due to their ground state magnetic dipole moment, allowing the investigation of lattice spin models. A number of the tools required for producing CsYb molecules in their ground state follow from their counterparts in the creation of bi-alkali dimers in their rovibrational ground state. However, it is the method of association for CsYb and similar molecules that is unknown and challenging. Two forms of magneto-association have been proposed, and it is possible that photoassociation in one of its various forms will be favourable for this system. The experiment has been developed with an approach that allows multiple directions to be pursued, and the upcoming modifications to the experiment will extend this further. These plans, alongside the developments presented here, ensure an exciting future for the CsYb experiment.

Appendix A

The Cs MOT

The work to date regarding Cs in this experiment has been well-reported, using techniques that are well-established in Durham. Here we present an overview of the improved performance of the Cs MOT, as well as studies of the optical molasses and optical pumping. As discussed in the main body of this thesis, upgrades to the Cs system are planned including the introduction of degenerate Raman sideband cooling (DRSC) and a reservoir optical dipole trap, both designed to aid the cooling of Cs to quantum degeneracy. In the long-term further updates are planned such as the addition of a glass cell to the vacuum system and an optical tweezer system. The purpose of these is to allow greater optical access for an optical lattice to be produced and to improve lifetimes from background collisions.

Figure A.1 shows the typical performance of the Cs MOT. Here the MOT loads to around 5.5×10^8 atoms in approximately 30 s, corresponding to a loading rate of 7.5×10^7 s^{-1}. This loading rate is limited mainly by the modest temperature used by the Cs oven. The inset to the figure shows a typical decay curve for the Cs MOT. Two decay rates are observed, with a shorter lifetime of 17.44 ± 0.03 s corresponding to two-body collisions, and a longer lifetime of 40.04 ± 0.02 s corresponding to background collisions in the vacuum system. The conditions used for these curves were: a total beam intensity of 12.5 I/I_{sat}, a MOT cooling beam detuning of -5.6 MHz, and a magnetic field gradient of 8.53 $\mathrm{G\,cm^{-1}}$.

Figure A.2 shows the temperature of the Cs optical molasses as a function

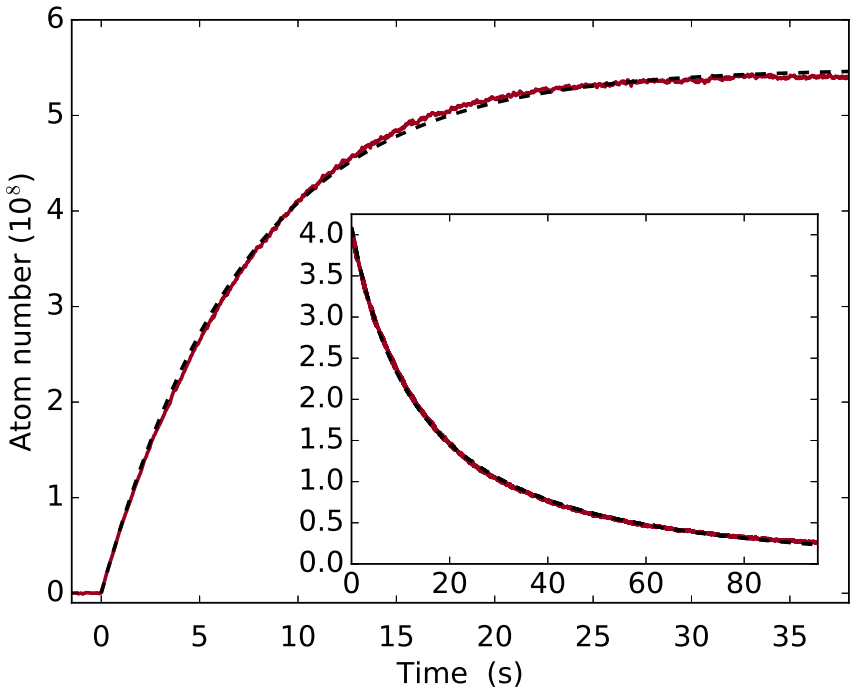

Figure A.1: The main figure shows a typical loading curve for the Cs MOT. The atom number is inferred from absorption imaging calibrated fluorescence imaging. The loading rate is extracted from a fit to equation 4.28 to give a rate of 7.5×10^7 s^{-1}. In this instance the MOT loads to a steady state atom number of 5.5×10^8 atoms. The inset to the main figure shows a typical decay curve for the Cs MOT. Here a two-component exponential fit gives lifetimes of the Cs MOT and is shown as a dashed black curve.

of the dimensionless light-shift parameter $\Omega^2/\Gamma_0|\Delta|$, where Ω is the Rabi-frequency of the MOT cooling beams, Δ is the detuning from resonance, and Γ_0 is the natural linewidth of the transition. In this sequence the MOT is first loaded, followed by the magnetic field gradient switching to zero. At this point Ω and Δ are set to new values for the molasses process. The molasses occurs for 15 ms before time-of-flight absorption imaging is used to determine the temperature obtained. As the light-shift parameter is reduced, the temperature of the molasses falls until a minimum temperature of 13.3 ± 0.9 μK is reached. At light-shift parameters smaller than this, the temperature rises sharply, this occurs when the detuning and intensity imbalances in the molasses region are too large for sub-Doppler cooling to work effectively [253].

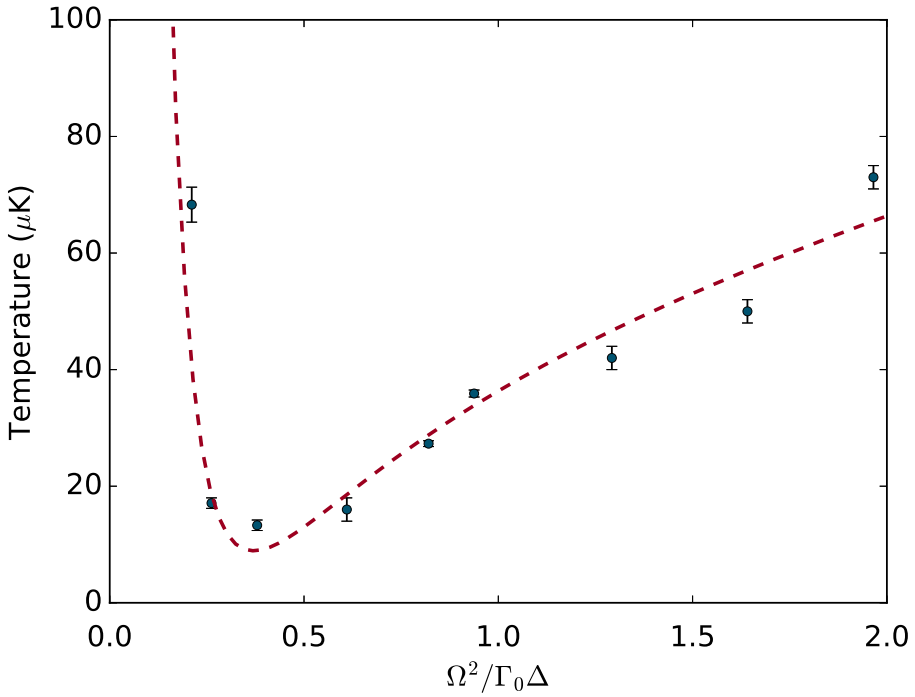

Figure A.2: The temperature of the Cs optical molasses as a function of the dimensionless light shift parameter. The red dashed curve is a guide to the eye. The lowest temperature achieved is 13.3 ± 0.9 μK

In our implementation of optical pumping we used a magnetic trap as a diagnostic of the performance of the pumping process. A magnetic trap works by selectively trapping m_F states by the use of a magnetic field gradient. The state $|F, m_F\rangle$ has a magnetic moments $\mu = g_F m_F \mu_B$. As such the magnetic field gradient can be used to counterbalance gravity for certain states, and the force in the vertical direction is given by

$$F = \mu |\frac{dB}{dz}| - mg = 0 \tag{A.1}$$

The addition of a vertical bias field allows either high field seeking states or low field seeking states to be levitated; using the bias field to move the field zero above the atom cloud traps high field seeking states, whereas moving the field zero below the atoms traps low field seeking states. For Cs, the states with $F = 3$ and $m_F = -3, -2,$ and -1 can be levitated using field gradients of 31.1, 46,7 and 93.4 G cm^{-1} respectively.

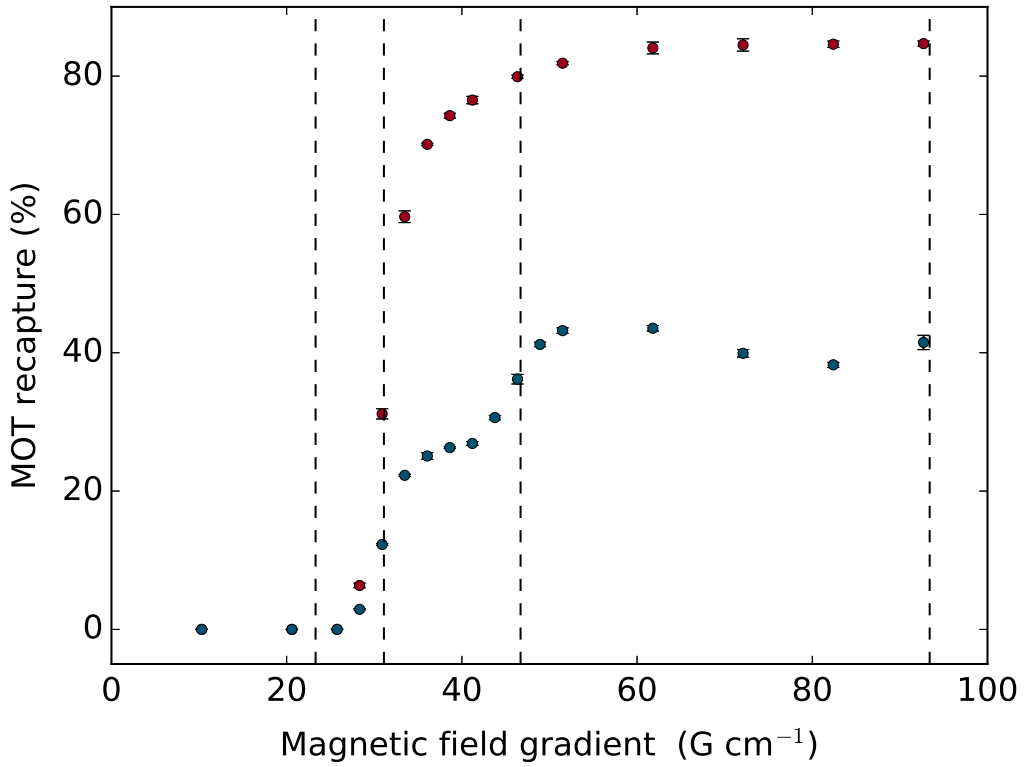

Figure A.3: The blue data points show the MOT recapture as the magnetic trap gradient is increased for atoms that are depumped into the $F = 3$ hyperfine ground state manifold prior to trapping in the magnetic trap. The characteristic step-like recapture is observed as increasing the trapping gradient levitates more m_F states. The levitation gradients required to levitate the $m_F = -3, -2, \text{and} -1$ states. The red points show the recapture percentage when optical pumping is performed in the $F = 3$ manifold before transfer to the optical trap.

To polarise the Cs in the $|F = 3, m_F\rangle$ state we employ optical pumping. In this process a 2 ms pulse of detuned MOT cooling light is used to depump all of the atoms to the $F = 3$ manifold. This is observed when no atoms are counted using absorption imaging, which is based on transitions from the $F = 4$ manifold. At this point a quantisation field of around 4 G is turned on along the direction of the circularly polarised optical pumping beam. The optical pumping beam is turned on 200 μs in order to pump the atoms to $m_F = -3$. The magnetic trap can be used to test this procedure by using a low field seeking state configuration. Following optical pumping the magnetic trap is turned on and atoms are held for 0.2 s. After this period the atoms are released and the Cs MOT beams and field gradient are turned

back on. The number of atoms in Cs MOT is compared to the original MOT load. In the absence of optical pumping, step-like features are observed in the MOT recapture as the magnetic field, these correspond to the trapping of each subsequent m_F state. This effect can be seen with the blue data points in figure A.3. Note that we are currently able to produce magnetic field gradients large enough to see the onset of $m_F = -1$ atoms being trapped. When optical pumping is successfully employed we observe a single step at the gradient required to trap $|F = 3, m_F\rangle$ atoms, implying that the optical pumping has successfully transferred atoms to this state.

Appendix B

The high-finesse cavity

The homebuilt high-finesse cavity, used for the frequency stabilisation of the photoassociation lasers, was originally intended for the stabilisation of the pump and Stokes STIRAP lasers for transferring Feshbach molecules of RbCs into the rovibrational ground state. The cavity is formed of an evacuated chamber containing a Zerodur spacer. The spacer is designed to keep a plane mirror and concave mirror at a fixed separation of 20 cm, giving a free spectral range of 750 MHz. Because the thermal drift of the cavity is of the order of $\mathrm{MHz\,K^{-1}}$, a ring PZT stack is used to actively stabilise the cavity length to a frequency stabilised 852 nm beam. The mirrors are coated to give high reflectivities for 852 nm light and the STIRAP wavelengths of 980 nm and 1556 nm. At our photoassociation wavelength of 895 nm the reflectivity is approximately 99.92 %.

In this cavity design, many Gauss-Hermite beam modes may be supported. In order to couple as much light as possible into the $\mathrm{TEM_{00}}$ mode, the beam profiles need to be mode-matched to the cavity geometry. The concave mirror has a radius of curvature of 50 cm. For the 895 nm beams to be mode matched to this cavity their Gaussian beam radius must be 50 cm at the position of this mirror. This requires the waist to be positioned at the surface of the plane mirror and the size of the waist to be 264 μm. Figure B.1 shows an example of when the cavity is well mode-matched (red), coupling a large portion of the laser light into the $\mathrm{TEM_{00}}$ mode. An example of a waist misaligned to the cavity geometry (black) is also shown, and several higher-order

transverse modes can be seen to be supported.

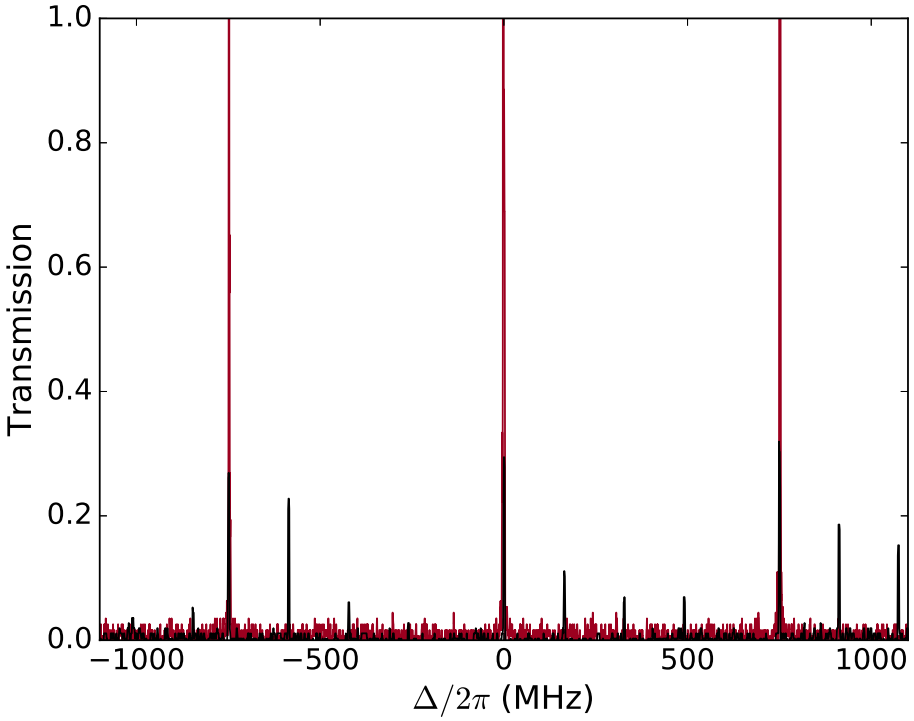

Figure B.1: The red line shows the transmission through the optical cavity as a function of detuning for a beam that is well mode-matched to the cavity. Zero detuning is arbitrarily chosen to be at one of the transmission peaks, and the scan is linearised using the known free spectral range of the cavity. The black signal shows the same scan range for a laser beam that is not as well-mode matched to the optical cavity. Here higher-order transverse modes are visible between the main peaks.

Bibliography

[1] L. D. Carr, D. DeMille, R. V. Krems, and J. Ye, *Cold and ultracold molecules: science, technology and applications*, New J. Phys. **11**, 055049 (2009).

[2] S. Chu, *Nobel lectures in physics 1997*, Rev. Mod. Phys. **70**, 685 (1998).

[3] C. Cohen-Tannoudji, *Manipulating atoms with photons*, Rev. Mod. Phys. **70**, 707 (1998).

[4] W. Phillips, *Nobel lectures in physics 1997*, Rev. Mod. Phys **70**, 721 (1998).

[5] M. H. Anderson, J. R. Ensher, M. R. Matthews, C. E. Wieman, and E. A. Cornell, *Observation of Bose-Einstein condensation in a dilute atomic vapor*, Science **269**, 198 (1995).

[6] K. B. Davis *et al.*, *Bose-Einstein condensation in a gas of sodium atoms*, Phys. Rev. Lett. **75**, 3969 (1995).

[7] C. Bradley, C. Sackett, J. Tollett, and R. Hulet, *Evidence of Bose-Einstein condensation in an atomic gas with attractive interactions*, Phys. Rev. Lett. **75**, 1687 (1995).

[8] S. Cornish, N. Claussen, J. Roberts, E. Cornell, and C. Wieman, *Stable 85 Rb Bose-Einstein condensates with widely tunable interactions*, Phys. Rev. Lett. **85**, 1795 (2000).

[9] G. Modugno *et al.*, *Bose-Einstein condensation of potassium atoms by sympathetic cooling*, Science **294**, 1320 (2001).

[10] T. Weber, J. Herbig, M. Mark, H.-C. Nägerl, and R. Grimm, *Bose-Einstein condensation of cesium*, Science **299**, 232 (2003).

[11] A. Marchant, S. Händel, S. Hopkins, T. Wiles, and S. Cornish, *Bose-Einstein condensation of 85 Rb by direct evaporation in an optical dipole trap*, Phys. Rev. A **85**, 053647 (2012).

[12] S. Kraft, F. Vogt, O. Appel, F. Riehle, and U. Sterr, *Bose-Einstein Condensation of Alkaline Earth Atoms: Ca 40*, Phys. Rev. Lett. **103**, 130401 (2009).

[13] S. Stellmer, M. K. Tey, B. Huang, R. Grimm, and F. Schreck, *Bose-Einstein condensation of strontium*, Phys. Rev. Lett. **103**, 200401 (2009).

[14] P. Mickelson, Y. M. De Escobar, M. Yan, B. DeSalvo, and T. Killian, *Bose-Einstein condensation of Sr 88 through sympathetic cooling with Sr 87*, Phys. Rev. A **81**, 051601 (2010).

[15] M. K. Tey, S. Stellmer, R. Grimm, and F. Schreck, *Double-degenerate Bose-Fermi mixture of strontium*, Phys. Rev. A **82**, 011608 (2010).

[16] Y. Takasu *et al.*, *Spin-singlet Bose-Einstein condensation of two-electron atoms*, Phys. Rev. Lett. **91**, 040404 (2003).

[17] T. Fukuhara, S. Sugawa, and Y. Takahashi, *Bose-Einstein condensation of an ytterbium isotope*, Phys. Rev. A **76**, 051604 (2007).

[18] T. Fukuhara, S. Sugawa, Y. Takasu, and Y. Takahashi, *All-optical formation of quantum degenerate mixtures*, Phys. Rev. A **79**, 021601 (2009).

[19] K. Aikawa *et al.*, *Bose-Einstein condensation of erbium*, Physical review letters **108**, 210401 (2012).

[20] A. Griesmaier, J. Werner, S. Hensler, J. Stuhler, and T. Pfau, *Bose-Einstein condensation of chromium*, Phys. Rev. Lett. **94**, 160401 (2005).

[21] M. Lu, N. Q. Burdick, S. H. Youn, and B. L. Lev, *Strongly dipolar Bose-Einstein condensate of dysprosium*, Physical review letters **107**, 190401 (2011).

[22] M. Matthews *et al.*, *Vortices in a Bose-Einstein condensate*, Phys. Rev. Lett. **83**, 2498 (1999).

[23] K. Madison, F. Chevy, W. Wohlleben, and J. Dalibard, *Vortex formation in a stirred Bose-Einstein condensate*, Physical Review Letters **84**, 806 (2000).

[24] J. Abo-Shaeer, C. Raman, J. Vogels, and W. Ketterle, *Observation of vortex lattices in Bose-Einstein condensates*, Science **292**, 476 (2001).

[25] A. Rakonjac *et al.*, *Measuring the disorder of vortex lattices in a Bose-Einstein condensate*, Physical Review A **93**, 013607 (2016).

[26] M.-O. Mewes *et al.*, *Output coupler for Bose-Einstein condensed atoms*, Physical Review Letters **78**, 582 (1997).

[27] I. Bloch, T. W. Hänsch, and T. Esslinger, *Atom laser with a cw output coupler*, Physical Review Letters **82**, 3008 (1999).

[28] W. Ketterle, *Nobel lecture: When atoms behave as waves: Bose-Einstein condensation and the atom laser*, Rev. Mod. Phys. **74**, 1131 (2002).

[29] L. Khaykovich *et al.*, *Formation of a matter-wave bright soliton*, Science **296**, 1290 (2002).

[30] K. E. Strecker, G. B. Partridge, A. G. Truscott, and R. G. Hulet, *Formation and propagation of matter-wave soliton trains*, Nature **417**, 150 (2002).

[31] S. L. Cornish, S. T. Thompson, and C. E. Wieman, *Formation of bright matter-wave solitons during the collapse of attractive Bose-Einstein condensates*, Phys. Rev. Lett. **96**, 170401 (2006).

[32] A. Marchant *et al.*, *Controlled formation and reflection of a bright solitary matter-wave*, Nature communications **4**, 1865 (2013).

[33] E. A. Donley *et al.*, *Dynamics of collapsing and exploding Bose–Einstein condensates*, Nature **412**, 295 (2001).

[34] J. Billy *et al.*, *Direct observation of Anderson localization of matter waves in a controlled disorder*, Nature **453**, 891 (2008).

[35] M. Barrett, J. Sauer, and M. Chapman, *All-optical formation of an atomic Bose-Einstein condensate*, Phys. Rev. Lett. **87**, 010404 (2001).

[36] I. Bloch, *Ultracold quantum gases in optical lattices*, Nature Physics **1**, 23 (2005).

[37] I. Bloch, J. Dalibard, and W. Zwerger, *Many-body physics with ultracold gases*, Reviews of Modern Physics **80**, 885 (2008).

[38] M. Greiner, O. Mandel, T. Esslinger, T. W. Hänsch, and I. Bloch, *Quantum phase transition from a superfluid to a Mott insulator in a gas of ultracold atoms*, Nature **415**, 39 (2002).

[39] M. Zaccanti *et al.*, *Control of the interaction in a Fermi-Bose mixture*, Phys. Rev. A **74**, 041605 (2006).

[40] S. Ospelkaus, C. Ospelkaus, L. Humbert, K. Sengstock, and K. Bongs, *Tuning of heteronuclear interactions in a degenerate Fermi-Bose mixture*, Phys. Rev. Lett. **97**, 120403 (2006).

[41] S. Papp, J. Pino, and C. Wieman, *Tunable miscibility in a dual-species Bose-Einstein condensate*, Phys. Rev. Lett. **101**, 040402 (2008).

[42] H. Cho, D. McCarron, D. Jenkin, M. Köppinger, and S. Cornish, *A high phase-space density mixture of 87 Rb and 133 Cs: towards ultracold heteronuclear molecules*, The European Physical Journal D-Atomic, Molecular, Optical and Plasma Physics **65**, 125 (2011).

[43] E. Altman, W. Hofstetter, E. Demler, and M. D. Lukin, *Phase diagram of two-component bosons on an optical lattice*, New Journal of Physics **5**, 113 (2003).

[44] M. Lewenstein, L. Santos, M. Baranov, and H. Fehrmann, *Atomic Bose-Fermi mixtures in an optical lattice*, Physical review letters **92**, 050401 (2004).

[45] A. Micheli, G. Pupillo, H. Büchler, and P. Zoller, *Cold polar molecules in two-dimensional traps: Tailoring interactions with external fields for novel quantum phases*, Phys. Rev. A **76**, 043604 (2007).

[46] J. M. Hutson and P. Soldan, *Molecule formation in ultracold atomic gases*, International Reviews in Physical Chemistry **25**, 497 (2006).

[47] J. Hudson *et al.*, *Improved measurement of the shape of the electron*, Nature **473**, 493 (2011).

[48] J. Baron *et al.*, *Order of magnitude smaller limit on the electric dipole moment of the electron*, Science **343**, 269 (2014).

[49] S. Truppe *et al.*, *A search for varying fundamental constants using hertz-level frequency measurements of cold CH molecules*, Nature communications **4** (2013).

[50] S. Truppe, R. J. Hendricks, E. Hinds, and M. Tarbutt, *Measurement of the lowest millimeter-wave transition frequency of the CH radical*, The Astrophysical Journal **780**, 71 (2013).

[51] S. Sainis *et al.*, *Detailed spectroscopy of the Cs 2 a 3 Σ u+ state and implications for measurements sensitive to variation of the electron-proton mass ratio*, Physical Review A **86**, 022513 (2012).

[52] S. Cahn *et al.*, *Zeeman-tuned rotational level-crossing spectroscopy in a diatomic free radical*, Physical review letters **112**, 163002 (2014).

[53] S. V. Alyabyshev, M. Lemeshko, and R. V. Krems, *Sensitive imaging of electromagnetic fields with paramagnetic polar molecules*, Physical Review A **86**, 013409 (2012).

[54] R. V. Krems, *Cold controlled chemistry*, Phys. Chem. Chem. Phys. **10**, 4079 (2008).

[55] G. Quemener and P. S. Julienne, *Ultracold molecules under control!*, Chem. Rev. **112**, 4949 (2012).

[56] J. Hwang and E. Hinds, *Dye molecules as single-photon sources and large optical nonlinearities on a chip*, New Journal of Physics **13**, 085009 (2011).

[57] D. DeMille, *Quantum computation with trapped polar molecules*, Phys. Rev. Lett. **88**, 067901 (2002).

[58] A. Micheli, G. Brennen, and P. Zoller, *A toolbox for lattice-spin models with polar molecules*, Nat. Phys. **2**, 341 (2006).

[59] T. Lahaye, C. Menotti, L. Santos, M. Lewenstein, and T. Pfau, *The physics of dipolar bosonic quantum gases*, Reports on Progress in Physics **72**, 126401 (2009).

[60] K.-K. Ni *et al.*, *A high phase-space-density gas of polar molecules*, Science **322**, 231 (2008).

[61] T. Takekoshi *et al.*, *Ultracold Dense Samples of Dipolar RbCs Molecules in the Rovibrational and Hyperfine Ground State*, Phys. Rev. Lett. **113**, 205301 (2014).

[62] P. K. Molony *et al.*, *Creation of Ultracold Rb 87 Cs 133 Molecules in the Rovibrational Ground State*, Phys. Rev. Lett. **113**, 255301 (2014).

[63] M. Guo *et al.*, *Creation of an Ultracold Gas of Ground-State Dipolar Na 23 Rb 87 Molecules*, Physical review letters **116**, 205303 (2016).

[64] J. W. Park, S. A. Will, and M. W. Zwierlein, *Ultracold Dipolar Gas of Fermionic Na 23 K 40 Molecules in Their Absolute Ground State*, Physical review letters **114**, 205302 (2015).

[65] M. T. Hummon *et al.*, *2D magneto-optical trapping of diatomic molecules*, Phys. Rev. Lett. **110**, 143001 (2013).

[66] J. Barry, D. McCarron, E. Norrgard, M. Steinecker, and D. DeMille, *Magneto-optical trapping of a diatomic molecule*, Nature **512**, 286 (2014).

[67] D. McCarron, E. Norrgard, M. Steinecker, and D. DeMille, *Improved magneto–optical trapping of a diatomic molecule*, New Journal of Physics **17**, 035014 (2015).

[68] V. Zhelyazkova *et al.*, *Laser cooling and slowing of CaF molecules*, Phys. Rev. A **89**, 053416 (2014).

[69] D. Egorov *et al.*, *Buffer-gas cooling of NH via the beam loaded buffer-gas method*, The European Physical Journal D-Atomic, Molecular, Optical and Plasma Physics **31**, 307 (2004).

[70] N. Bulleid *et al.*, *Characterization of a cryogenic beam source for atoms and molecules*, Physical Chemistry Chemical Physics **15**, 12299 (2013).

[71] H. L. Bethlem, G. Berden, and G. Meijer, *Decelerating neutral dipolar molecules*, Physical Review Letters **83**, 1558 (1999).

[72] M. R. Tarbutt *et al.*, *Slowing heavy, ground-state molecules using an alternating gradient decelerator*, Physical review letters **92**, 173002 (2004).

[73] S. Y. van de Meerakker, P. H. Smeets, N. Vanhaecke, R. T. Jongma, and G. Meijer, *Deceleration and electrostatic trapping of OH radicals*, Physical review letters **94**, 023004 (2005).

[74] S. Hoekstra *et al.*, *Electrostatic trapping of metastable NH molecules*, Physical Review A **76**, 063408 (2007).

[75] S. Y. van de Meerakker, H. L. Bethlem, N. Vanhaecke, and G. Meijer, *Manipulation and control of molecular beams*, Chemical Reviews **112**, 4828 (2012).

[76] E. Lavert-Ofir *et al.*, *A moving magnetic trap decelerator: a new source of cold atoms and molecules*, New Journal of Physics **13**, 103030 (2011).

[77] A. Trimeche, M. N. Bera, J.-P. Cromières, J. Robert, and N. Vanhaecke, *Trapping of a supersonic beam in a traveling magnetic wave*, The European Physical Journal D **65**, 263 (2011).

[78] S. Chervenkov *et al.*, *Continuous centrifuge decelerator for polar molecules*, Physical review letters **112**, 013001 (2014).

[79] A. O. Wallis and J. M. Hutson, *Production of ultracold NH molecules by sympathetic cooling with Mg*, Physical review letters **103**, 183201 (2009).

[80] S. K. Tokunaga *et al.*, *Prospects for sympathetic cooling of molecules in electrostatic, ac and microwave traps*, The European Physical Journal D **65**, 141 (2011).

[81] A. O. Wallis, E. J. Longdon, P. S. Żuchowski, and J. M. Hutson, *The prospects of sympathetic cooling of NH molecules with Li atoms*, The European Physical Journal D **65**, 151 (2011).

[82] K. M. Jones, E. Tiesinga, P. D. Lett, and P. S. Julienne, *Ultracold photoassociation spectroscopy: Long-range molecules and atomic scattering*, Rev. Mod. Phys. **78**, 483 (2006).

[83] C. Chin, R. Grimm, P. Julienne, and E. Tiesinga, *Feshbach resonances in ultracold gases*, Rev. Mod. Phys. **82**, 1225 (2010).

[84] A. Fioretti *et al.*, *Formation of cold Cs 2 molecules through photoassociation*, Physical Review Letters **80**, 4402 (1998).

[85] J. Deiglmayr *et al.*, *Formation of ultracold polar molecules in the rovibrational ground state*, Physical review letters **101**, 133004 (2008).

[86] K. Aikawa *et al.*, *Toward the production of quantum degenerate bosonic polar molecules, 41K87Rb*, New J. Phys. **11**, 055035 (2009).

[87] K. Aikawa *et al.*, *Coherent transfer of photoassociated molecules into the rovibrational ground state*, Physical review letters **105**, 203001 (2010).

[88] S. Stellmer, B. Pasquiou, R. Grimm, and F. Schreck, *Creation of ultracold Sr 2 molecules in the electronic ground state*, Physical review letters **109**, 115302 (2012).

[89] K. E. Strecker, G. B. Partridge, and R. G. Hulet, *Conversion of an atomic Fermi gas to a long-lived molecular Bose gas*, Physical Review Letters **91**, 080406 (2003).

[90] M. W. Zwierlein *et al.*, *Observation of Bose-Einstein condensation of molecules*, Physical review letters **91**, 250401 (2003).

[91] K. Xu *et al.*, *Formation of quantum-degenerate sodium molecules*, Physical review letters **91**, 210402 (2003).

[92] C. A. Regal, C. Ticknor, J. L. Bohn, and D. S. Jin, *Creation of ultracold molecules from a Fermi gas of atoms*, Nature **424**, 47 (2003).

[93] E. A. Donley, N. R. Claussen, S. T. Thompson, and C. E. Wieman, *Atom–molecule coherence in a Bose–Einstein condensate*, Nature **417**, 529 (2002).

[94] S. Dürr, T. Volz, A. Marte, and G. Rempe, *Observation of molecules produced from a Bose-Einstein condensate*, Physical review letters **92**, 020406 (2004).

[95] J. Herbig *et al.*, *Preparation of a pure molecular quantum gas*, Science **301**, 1510 (2003).

[96] C.-H. Wu, J. W. Park, P. Ahmadi, S. Will, and M. W. Zwierlein, *Ultracold fermionic Feshbach molecules of Na 23 K 40*, Physical review letters **109**, 085301 (2012).

[97] M.-S. Heo *et al.*, *Formation of ultracold fermionic NaLi Feshbach molecules*, Physical Review A **86**, 021602 (2012).

[98] P. J. Zabawa, *Production of ultracold, absolute vibrational ground state NaCs molecules*, PhD thesis, University of Rochester, 2012.

[99] J. Ulmanis, S. Häfner, E. D. Kuhnle, and M. Weidemüller, *Heteronuclear Efimov resonances in ultracold quantum gases*, National Science Review , nww018 (2016).

[100] F. Münchow, *2-Photon-Photoassociation spectroscopy in a mixture of Ytterbium and Rubidium*, PhD thesis, Universitäts-und Landesbibliothek der Heinrich-Heine-Universität Düsseldorf, 2012.

[101] H. Hara, H. Konishi, S. Nakajima, Y. Takasu, and Y. Takahashi, *A Three-Dimensional Optical Lattice of Ytterbium and Lithium Atomic Gas Mixture*, J. Phys. Soc. Jpn. **83**, 014003 (2013).

[102] R. Roy *et al.*, *Photoassociative production of ultracold heteronuclear YbLi* molecules*, arXiv preprint arXiv:1606.03120 (2016).

[103] M. Gröbner *et al.*, *A new quantum gas apparatus for ultracold mixtures of K and Cs and KCs ground-state molecules*, Journal of Modern Optics , 1 (2016).

[104] B. Pasquiou *et al.*, *Quantum degenerate mixtures of strontium and rubidium atoms*, Phys. Rev. A **88**, 023601 (2013).

[105] S. Kemp *et al.*, *Production and characterization of a dual species magneto-optical trap of cesium and ytterbium*, Review of Scientific Instruments **87**, 023105 (2016).

[106] D. A. Brue and J. M. Hutson, *Prospects of forming ultracold molecules in* 2Σ *states by magnetoassociation of alkali-metal atoms with Yb*, Phys. Rev. A **87**, 052709 (2013).

[107] K. L. Butler, *A dual species MOT of Yb and Cs*, PhD thesis, Durham University, 2014.

[108] R. Freytag, *Simultaneous Magneto-Optical Trapping of Ytterbium and Caesium*, PhD thesis, Imperial College London, 2015.

[109] P. S. Żuchowski and J. M. Hutson, *Reactions of ultracold alkali-metal dimers*, Phys. Rev. A **81**, 060703 (2010).

[110] K. Honda *et al.*, *Magneto-optical trapping of Yb atoms and a limit on the branching ratio of the 1 P 1 state*, Physical Review A **59**, R934 (1999).

[111] K. Honda *et al.*, *Erratum: Magneto-optical trapping of Yb atoms and a limit on the branching ratio of the 1 P 1 state [Phys. Rev. A 59, R934 (1999)]*, Physical Review A **60**, 2603 (1999).

[112] D. A. Steck, *Cesium D Line Data,* available online at `http://steck.us/alkalidata` (revision 2.1.4), 2010.

[113] C. Alcock, V. Itkin, and M. Horrigan, *Vapour pressure equations for the metallic elements: 298–2500K*, Canadian Metallurgical Quarterly **23**, 309 (1984).

[114] S. Haendel, A. Marchant, T. Wiles, S. Hopkins, and S. Cornish, *Magnetic transport apparatus for the production of ultracold atomic gases in the vicinity of a dielectric surface*, Rev. Sci. Instrum. **83**, 013105 (2012).

[115] M. Harris, P. Tierney, and S. Cornish, *Magnetic trapping of a cold Rb–Cs atomic mixture*, J. Phys. B: At., Mol. Opt. Phys. **41**, 035303 (2008).

[116] A. Camposeo *et al.*, *A cold cesium atomic beam produced out of a pyramidal funnel*, Opt. Commun. **200**, 231 (2001).

[117] S. Dörscher *et al.*, *Creation of quantum-degenerate gases of ytterbium in a compact 2D-/3D-magneto-optical trap setup*, Review of Scientific Instruments **84**, 043109 (2013).

[118] U. D. Rapol, A. Krishna, A. Wasan, and V. Natarajan, *Laser cooling and trapping of Yb from a thermal source*, The European Physical Journal D-Atomic, Molecular, Optical and Plasma Physics **29**, 409 (2004).

[119] E. Wille, *Preparation of an optically trapped Fermi-Fermi mixture of ^{6}Li and ^{40}K atoms and characterization of the interspecies interactions by Feshbach spectroscopy*, PhD thesis, Universität Innsbruck, Austria, 2009.

[120] C. Stan and W. Ketterle, *Multiple species atom source for laser-cooling experiments*, Rev. Sci. Instrum. **76**, 063113 (2005).

[121] K. Ross and B. Sonntag, *High temperature metal atom beam sources*, Rev. Sci. Instrum. **66**, 4409 (1995).

[122] N. F. Ramsey, *Molecular beams* (Clarendon Press Oxford, 2007).

[123] D. A. Steck, *Cesium D Line Data,* available online at `http://steck.us/alkalidata` (revision 2.1.4), 2010.

[124] *NIST Basic Atomic Spectroscopic Data.*

[125] P. Arora, A. Agarwal, and A. S. Gupta, *Simple alignment technique for polarisation maintaining fibres*, Review of Scientific Instruments **82**, 125103 (2011).

[126] D. McCarron, S. King, and S. Cornish, *Modulation transfer spectroscopy in atomic rubidium*, Meas. Sci. Technol. **19**, 105601 (2008).

[127] J. H. Shirley, *Modulation transfer processes in optical heterodyne saturation spectroscopy*, Opt. Lett. **7**, 537 (1982).

[128] M. Gehrtz, G. C. Bjorklund, and E. A. Whittaker, *Quantum-limited laser frequency-modulation spectroscopy*, JOSA B **2**, 1510 (1985).

[129] G. C. Bjorklund, *Frequency-modulation spectroscopy: a new method for measuring weak absorptions and dispersions*, Opt. Lett. **5**, 15 (1980).

[130] T. Kuwamoto, K. Honda, Y. Takahashi, and T. Yabuzaki, *Magneto-optical trapping of Yb atoms using an intercombination transition*, Phys. Rev. A **60**, R745 (1999).

[131] T. Weber, J. Herbig, M. Mark, H.-C. Nägerl, and R. Grimm, *Three-body recombination at large scattering lengths in an ultracold atomic gas*, Physical review letters **91**, 123201 (2003).

[132] D. A. Brue and J. M. Hutson, *Magnetically tunable Feshbach resonances in ultracold Li-Yb mixtures*, Phys. Rev. Lett. **108**, 043201 (2012).

[133] D. O. Sabulsky, C. V. Parker, N. D. Gemelke, and C. Chin, *Efficient continuous-duty Bitter-type electromagnets for cold atom experiments*, Review of Scientific Instruments **84**, 104706 (2013).

[134] T. Luan, T. Zhou, X. Chen, and Z. Ma, *A modified Bitter-type electromagnet and control system for cold atom experiments*, Review of Scientific Instruments **85**, 024701 (2014).

[135] C. Townsend *et al.*, *Phase-space density in the magneto-optical trap*, Physical Review A **52**, 1423 (1995).

[136] R. Raj, D. Bloch, J. Snyder, G. Camy, and M. Ducloy, *High-frequency optically heterodyned saturation spectroscopy via resonant degenerate four-wave mixing*, Phys. Rev. Lett. **44**, 1251 (1980).

[137] M. Harris *et al.*, *Polarization spectroscopy in rubidium and cesium*, Physical Review A **73**, 062509 (2006).

[138] S. L. Kemp, I. G. Hughes, and S. L. Cornish, *An analytical model of off-resonant Faraday rotation in hot alkali metal vapours*, Journal of Physics B: Atomic, Molecular and Optical Physics **44**, 235004 (2011).

[139] A. Jayakumar, B. Plotkin-Swing, A. O. Jamison, and S. Gupta, *Dual-axis vapor cell for simultaneous laser frequency stabilization on disparate optical transitions*, Review of Scientific Instruments **86**, 073115 (2015).

[140] V. Ishchenko, S. Kochubei, N. Rubtsova, E. Khvorostov, and I. Yevseyev, *Polarization echo spectroscopy of ytterbium vapor in a magnetic field*, LASER PHYSICS-LAWRENCE- **12**, 1079 (2002).

[141] A. H. Hansen *et al.*, *Quantum degenerate mixture of ytterbium and lithium atoms*, Phys. Rev. A **84**, 011606 (2011).

[142] J. I. Kim, C. Y. Park, J. Y. Yeom, E. B. Kim, and T. H. Yoon, *Frequency-stabilized high-power violet laser diode with an ytterbium hollow-cathode lamp*, Optics letters **28**, 245 (2003).

[143] R. Maruyama *et al.*, *Investigation of sub-Doppler cooling in an ytterbium magneto-optical trap*, Physical Review A **68**, 011403 (2003).

[144] M. Köppinger, *Creation of ultracold RbCs molecules*, PhD thesis, Durham University, 2014.

[145] D. Boddy, *First observations of Rydberg blockade in a frozen gas of divalent atoms*, PhD thesis, Durham University, 2014.

[146] N. Nemitz, *Production and spectroscopy of ultracold YbRb* molecules*, PhD thesis, Heinrich-Heine-Universität Düsseldorf, 2008.

[147] F. Baumer, *Isotope dependent interactions in a mixture of ultracold atoms*, PhD thesis, Köln, Univ., Diss., 2010, 2010.

[148] Burr-Brown, *Photodiode monitoring with op-amps*, http://http://www.ti.com/lit/an/sboa035/sboa035.pdf, 1995.

[149] D. Das, S. Barthwal, A. Banerjee, and V. Natarajan, *Absolute frequency measurements in Yb with 0.08 ppb uncertainty: Isotope shifts and hyperfine structure in the 399- nm S 0 1 P 1 1 line*, Physical Review A **72**, 032506 (2005).

[150] M. Kitagawa *et al.*, *Two-color photoassociation spectroscopy of ytterbium atoms and the precise determinations of s-wave scattering lengths*, Phys. Rev. A **77**, 012719 (2008).

[151] K. Pandey, A. K. Singh, P. K. Kumar, M. Suryanarayana, and V. Natarajan, *Isotope shifts and hyperfine structure in the 555.8-nm S 1 0 P 3 1 line of Yb*, Physical Review A **80**, 022518 (2009).

[152] R. Zinkstok, E. Van Duijn, S. Witte, and W. Hogervorst, *Hyperfine structure and isotope shift of transitions in Yb I using UV and deep-UV cw laser light and the angular distribution of fluorescence radiation*, Journal of Physics B: Atomic, Molecular and Optical Physics **35**, 2693 (2002).

[153] P. Siddons, *Faraday rotation of pulsed and continuous-wave light in atomic vapour*, PhD thesis, Durham University, 2011.

[154] K. Ogiwara *et al.*, *Lamb-Dip Laser-Induced Fluorescence Spectroscopy for Measuring Magnetic Field in a Plasma*, Japanese Journal of Applied Physics **50**, 036101 (2011).

[155] S. Chu, L. Hollberg, J. E. Bjorkholm, A. Cable, and A. Ashkin, *Three-dimensional viscous confinement and cooling of atoms by resonance radiation pressure*, Phys. Rev. Lett. **55**, 48 (1985).

[156] E. Raab, M. Prentiss, A. Cable, S. Chu, and D. E. Pritchard, *Trapping of neutral sodium atoms with radiation pressure*, Phys. Rev. Lett. **59**, 2631 (1987).

[157] D. J. Wineland and W. M. Itano, *Laser cooling of atoms*, Physical Review A **20**, 1521 (1979).

[158] T. W. Hänsch and A. L. Schawlow, *Cooling of gases by laser radiation*, Optics Communications **13**, 68 (1975).

[159] C. J. Foot, *Atomic physics* (Oxford University Press, 2004).

[160] H. J. Metcalf and P. Van der Straten, *Laser cooling and trapping* (Springer Science & Business Media, 1999).

[161] J. Dalibard, *Le rôle des fluctuations dans la dynamique d'un atome couplé au champ électromagnétique*, PhD thesis, Université Pierre et Marie Curie-Paris VI, 1986.

[162] P. D. Lett *et al.*, *Optical molasses*, JOSA B **6**, 2084 (1989).

[163] J. Dalibard and C. Cohen-Tannoudji, *Laser cooling below the Doppler limit by polarization gradients: simple theoretical models*, JOSA B **6**, 2023 (1989).

[164] P. D. Lett *et al.*, *Observation of atoms laser cooled below the Doppler limit*, Physical Review Letters **61**, 169 (1988).

[165] D. S. Weiss, E. Riis, Y. Shevy, P. J. Ungar, and S. Chu, *Optical molasses and multilevel atoms: experiment*, JOSA B **6**, 2072 (1989).

[166] T. E. Barrett, S. W. Dapore-Schwartz, M. D. Ray, and G. P. Lafyatis, *Slowing atoms with σ-polarized light*, Physical review letters **67**, 3483 (1991).

[167] P. Molenaar, P. Van der Straten, H. Heideman, and H. Metcalf, *Diagnostic technique for Zeeman-compensated atomic beam slowing: Technique and results*, Physical Review A **55**, 605 (1997).

[168] U. Dammalapati, I. Norris, L. Maguire, M. Borkowski, and E. Riis, *A compact magneto-optical trap apparatus for calcium*, Measurement Science and Technology **20**, 095303 (2009).

[169] C. Dedman *et al.*, *Optimum design and construction of a Zeeman slower for use with a magneto-optic trap*, Rev. Sci. Instrum. **75**, 5136 (2004).

[170] S. Bell *et al.*, *A slow atom source using a collimated effusive oven and a single-layer variable pitch coil Zeeman slower*, Review of Scientific Instruments **81**, 013105 (2010).

[171] V. Bagnato, A. Aspect, and S. Zilio, *Study of laser deceleration of an atomic beam by monitoring the fluorescence along the deceleration path*, Optics Communications **72**, 76 (1989).

[172] R. Napolitano, S. Zilio, and V. Bagnato, *Adiabatic following conditions for the deceleration of atoms with the Zeeman tuning technique*, Optics communications **80**, 110 (1990).

[173] Y. B. Ovchinnikov, *A Zeeman slower based on magnetic dipoles*, Optics communications **276**, 261 (2007).

[174] S. Hopkins *et al.*, *A versatile dual-species Zeeman slower for caesium and ytterbium*, Review of Scientific Instruments **87**, 043109 (2016).

[175] A. Steane, M. Chowdhury, and C. Foot, *Radiation force in the magneto-optical trap*, JOSA B **9**, 2142 (1992).

[176] A. H. Hansen *et al.*, *Production of quantum-degenerate mixtures of ytterbium and lithium with controllable interspecies overlap*, Phys. Rev. A **87**, 013615 (2013).

[177] M. Scholl, *Probing an ytterbium Bose-Einstein condensate using an ultranarrow optical line: towards artificial gauge fields in optical lattices*, PhD thesis, Paris 6, 2014.

[178] F. Scazza, *Probing SU (N)-symmetric orbital interactions with ytterbium Fermi gases in optical lattices*, PhD thesis, lmu, 2015.

[179] A. D. Ludlow, *The strontium optical lattice clock: optical spectroscopy with sub-Hertz accuracy*, PhD thesis, University of Colorado, 2008.

[180] X. Xu, T. H. Loftus, J. L. Hall, A. Gallagher, and J. Ye, *Cooling and trapping of atomic strontium*, JOSA B **20**, 968 (2003).

[181] T. Chanelière, J.-L. Meunier, R. Kaiser, C. Miniatura, and D. Wilkowski, *Extra-heating mechanism in Doppler cooling experiments*, JOSA B **22**, 1819 (2005).

[182] S.-K. Choi, S. E. Park, J. Chen, and V. G. Minogin, *Three-dimensional analysis of the magneto-optical trap for (1+ 3)-level atoms*, Physical Review A **77**, 015405 (2008).

[183] R. Grimm, M. Weidemüller, and Y. B. Ovchinnikov, *Optical dipole traps for neutral atoms*, Adv. At., Mol., Opt. Phys. **42**, 95 (2000).

[184] M. Safronova, B. Arora, and C. W. Clark, *Frequency-dependent polarizabilities of alkali-metal atoms from ultraviolet through infrared spectral regions*, Phys. Rev. A **73**, 022505 (2006).

[185] M. M. H. Yu, *Towards interferometry with bright solitary waves in a ring*, PhD thesis, Durham University, 2016.

[186] G. D. Bruce, J. Mayoh, G. Smirne, L. Torralbo-Campo, and D. Cassettari, *A smooth, holographically generated ring trap for the investigation of superfluidity in ultracold atoms*, Physica Scripta **T143**, 014008 (2011).

[187] A. L. Gaunt and Z. Hadzibabic, *Robust digital holography for ultracold atom trapping*, arXiv preprint arXiv:1111.5941 (2011).

[188] G. Brooker, *Modern classical optics* (Oxford Univ. Press, 2003).

[189] Y.-J. Lin, A. Perry, R. Compton, I. Spielman, and J. Porto, *Rapid production of R 87 b Bose-Einstein condensates in a combined magnetic and optical potential*, Physical Review A **79**, 063631 (2009).

[190] A. E. Siegman, *Lasers* (University Science Books, 1986).

[191] J. Sansonetti, *Wavelengths, transition probabilities, and energy levels for the spectra of Cesium (Cs I-Cs LV)*, Journal of Physical and Chemical Reference Data **38**, 761 (2009).

[192] S. Tassy *et al.*, *Sympathetic cooling in a mixture of diamagnetic and paramagnetic atoms*, J. Phys. B: At., Mol. Opt. Phys. **43**, 205309 (2010).

[193] C.-L. Hung, X. Zhang, N. Gemelke, and C. Chin, *Runaway Evaporative Cooling to Bose-Einstein Condensation of Cesium Atoms in Optical Traps*, in *Laser Science*, p. LTuG4, Optical Society of America, 2008.

[194] C.-L. Hung, X. Zhang, N. Gemelke, and C. Chin, *Accelerating evaporative cooling of atoms into Bose-Einstein condensation in optical traps*, Phys. Rev. A **78**, 011604 (2008).

[195] J. Joykutty, V. Mathur, V. Venkataraman, and V. Natarajan, *Direct measurement of the oscillation frequency in an optical-tweezers trap by parametric excitation*, Physical review letters **95**, 193902 (2005).

[196] R. Jáuregui, *Nonperturbative and perturbative treatments of parametric heating in atom traps*, Physical Review A **64**, 053408 (2001).

[197] L. Landau and E. Lifshitz, *Mechanik Akademie-Verlag*, 1963.

[198] A. Szczepkowicz *et al.*, *Optimal geometry for efficient loading of an optical dipole trap*, Physical Review A **79**, 013408 (2009).

[199] S. Kuppens, K. Corwin, K. Miller, T. Chupp, and C. Wieman, *Loading an optical dipole trap*, Physical review A **62**, 013406 (2000).

[200] W. Ketterle, D. Durfee, and D. Stamper-Kurn, *Making, probing and understanding Bose-Einstein condensates*, arXiv preprint cond-mat/9904034 **5** (1999).

[201] Y.-J. Lin, A. Perry, R. Compton, I. Spielman, and J. Porto, *Rapid production of R 87 b Bose-Einstein condensates in a combined magnetic and optical potential*, Phys. Rev. A **79**, 063631 (2009).

[202] N. Lundblad, M. Schlosser, and J. Porto, *Experimental observation of magic-wavelength behavior of Rb 87 atoms in an optical lattice*, Physical Review A **81**, 031611 (2010).

[203] B. Karaçoban and L. Özdemir, *Electric Dipole Transitions for Neutral Ytterbium (Z = 70)*, Journal of the Korean Physical Society **58**, 417 (2011).

[204] C. J. Bowers *et al.*, *Experimental investigation of excited-state lifetimes in atomic ytterbium*, Phys. Rev. A **53**, 3103 (1996).

[205] S. Sugawa, R. Yamazaki, S. Taie, and Y. Takahashi, *Bose-Einstein condensate in gases of rare atomic species*, Phys. Rev. A **84**, 011610 (2011).

[206] A. Marchant, *Formation of bright solitary matter-waves*, PhD thesis, Durham University, 2012.

[207] H. F. Hess, *Evaporative cooling of magnetically trapped and compressed spin-polarized hydrogen*, Physical Review B **34**, 3476 (1986).

[208] C. S. Adams, H. J. Lee, N. Davidson, M. Kasevich, and S. Chu, *Evaporative cooling in a crossed dipole trap*, Physical review letters **74**, 3577 (1995).

[209] Y. Takasu *et al.*, *High-density trapping of cold ytterbium atoms by an optical dipole force*, Phys. Rev. Lett. **90**, 023003 (2003).

[210] J.-F. Clément *et al.*, *All-optical runaway evaporation to Bose-Einstein condensation*, Physical Review A **79**, 061406 (2009).

[211] R. Roy, A. Green, R. Bowler, and S. Gupta, *Rapid cooling to quantum degeneracy in dynamically shaped atom traps*, Physical Review A **93**, 043403 (2016).

[212] W. Ketterle and N. Van Druten, *Evaporative cooling of trapped atoms*, Adv. At., Mol., Opt. Phys. **37**, 181 (1996).

[213] S. Bose, *Planck's law and light quantum hypothesis*, Z. Phys **26**, 178 (1924).

[214] A. Einstein, *Quantentheorie des einatomigen idealen Gases* (Preussische Akademie der Wissenschaften, 1924).

[215] F. Dalfovo, S. Giorgini, L. P. Pitaevskii, and S. Stringari, *Theory of Bose-Einstein condensation in trapped gases*, Rev. Mod. Phys. **71**, 463 (1999).

[216] N. Bogolubov, *On the theory of superfluidity*, J. Phys **11**, 23 (1966).

[217] C. Pethick and H. Smith, *Bose-Einstein condensation in dilute gases* (Cambridge university press, 2002).

[218] J. Dalibard, *Collisional dynamics of ultra-cold atomic gases*, in *Proceedings of the International School of Physics-Enrico Fermi*, volume 321, p. 14, 1999.

[219] J. Weiner, V. S. Bagnato, S. Zilio, and P. S. Julienne, *Experiments and theory in cold and ultracold collisions*, Reviews of Modern Physics **71**, 1 (1999).

[220] T. Köhler, K. Góral, and P. S. Julienne, *Production of cold molecules via magnetically tunable Feshbach resonances*, Rev. Mod. Phys. **78**, 1311 (2006).

[221] H. Feshbach, *Unified theory of nuclear reactions*, Annals of Physics **5**, 357 (1958).

[222] S. Inouye *et al.*, *Observation of Feshbach resonances in a Bose–Einstein condensate*, Nature **392**, 151 (1998).

[223] M. Greiner, C. A. Regal, and D. S. Jin, *Emergence of a molecular Bose–Einstein condensate from a Fermi gas*, Nature **426**, 537 (2003).

[224] M. P. Köppinger *et al.*, *Production of optically trapped RbCs 87 Feshbach molecules*, Phys. Rev. A **89**, 033604 (2014).

[225] C. Bruni and A. Görlitz, *Observation of hyperfine interaction in photoassociation spectra of ultracold RbYb*, Physical Review A **94**, 022503 (2016).

[226] H. Thorsheim, J. Weiner, and P. S. Julienne, *Laser-induced photoassociation of ultracold sodium atoms*, Physical review letters **58**, 2420 (1987).

[227] J. Franck and E. Dymond, *Elementary processes of photochemical reactions*, Transactions of the Faraday Society **21**, 536 (1926).

[228] E. U. Condon, *Nuclear motions associated with electron transitions in diatomic molecules*, Physical Review **32**, 858 (1928).

[229] D. England, *Towards Ultrafast Photoassociation of Ultracold Atoms*, PhD thesis, Oxford University, 2011.

[230] T. Takekoshi, B. Patterson, and R. Knize, *Observation of cold ground-state cesium molecules produced in a magneto-optical trap*, Physical Review A **59**, R5 (1999).

[231] D. Comparat *et al.*, *Formation of cold Cs ground state molecules through photoassociation in the pure long-range state*, The European Physical Journal D-Atomic, Molecular, Optical and Plasma Physics **11**, 59 (2000).

[232] C. Gabbanini, A. Fioretti, A. Lucchesini, S. Gozzini, and M. Mazzoni, *Cold rubidium molecules formed in a magneto-optical trap*, Physical review letters **84**, 2814 (2000).

[233] A. Nikolov *et al.*, *Efficient production of ground-state potassium molecules at sub-mK temperatures by two-step photoassociation*, Physical review letters **84**, 246 (2000).

[234] F. K. Fatemi, K. M. Jones, P. D. Lett, and E. Tiesinga, *Ultracold ground-state molecule production in sodium*, Physical Review A **66**, 053401 (2002).

[235] A. J. Kerman, J. M. Sage, S. Sainis, T. Bergeman, and D. DeMille, *Production and state-selective detection of ultracold RbCs molecules*, Physical review letters **92**, 153001 (2004).

[236] C. Haimberger, J. Kleinert, M. Bhattacharya, and N. Bigelow, *Formation and detection of ultracold ground-state polar molecules*, Physical Review A **70**, 021402 (2004).

[237] D. Wang *et al.*, *Photoassociative production and trapping of ultracold KRb molecules*, Physical review letters **93**, 243005 (2004).

[238] M. Berninger *et al.*, *Feshbach resonances, weakly bound molecular states, and coupled-channel potentials for cesium at high magnetic fields*, Phys. Rev. A **87**, 032517 (2013).

[239] G. Delannoy *et al.*, *Understanding the production of dual Bose-Einstein condensation with sympathetic cooling*, Physical Review A **63**, 051602 (2001).

[240] A. Mosk *et al.*, *Mixture of ultracold lithium and cesium atoms in an optical dipole trap*, Applied Physics B **73**, 791 (2001).

[241] M. Anderlini *et al.*, *Sympathetic cooling and collisional properties of a Rb-Cs mixture*, Physical Review A **71**, 061401 (2005).

[242] F. Münchow, C. Bruni, M. Madalinski, and A. Görlitz, *Two-photon photoassociation spectroscopy of heteronuclear YbRb*, Phys. Chem. Chem. Phys. **13**, 18734 (2011).

[243] M. Borkowski *et al.*, *Scattering lengths in isotopologues of the RbYb system*, Phys. Rev. A **88**, 052708 (2013).

[244] S. H. Autler and C. H. Townes, *Stark effect in rapidly varying fields*, Physical Review **100**, 703 (1955).

[245] R. J. LeRoy and R. B. Bernstein, *Dissociation Energy and Long-Range Potential of Diatomic Molecules from Vibrational Spacings of Higher Levels*, The Journal of Chemical Physics **52**, 3869 (1970).

[246] P. Pillet *et al.*, *Photoassociation in a gas of cold alkali atoms: I. Perturbative quantum approach*, Journal of Physics B: Atomic, Molecular and Optical Physics **30**, 2801 (1997).

[247] M. Pichler, H. Chen, and W. C. Stwalley, *Photoassociation spectroscopy of ultracold Cs below the* $6P_{1/2}$ *limit*, The Journal of chemical physics **121**, 1796 (2004).

[248] W. Dowd *et al.*, *Magnetic field dependent interactions in an ultracold Li–Yb (*$^3P_2$*) mixture*, New Journal of Physics **17**, 055007 (2015).

[249] S. Kato, S. Sugawa, K. Shibata, R. Yamamoto, and Y. Takahashi, *Control of resonant interaction between electronic ground and excited states*, Physical review letters **110**, 173201 (2013).

[250] A. Klein, M. Bruderer, S. R. Clark, and D. Jaksch, *Dynamics, dephasing and clustering of impurity atoms in Bose–Einstein condensates*, New Journal of Physics **9**, 411 (2007).

[251] A. Griessner, A. Daley, S. Clark, D. Jaksch, and P. Zoller, *Dark-state cooling of atoms by superfluid immersion*, Physical review letters **97**, 220403 (2006).

[252] M. Bruderer, A. Klein, S. Clark, and D. Jaksch, *Transport of strong-coupling polarons in optical lattices*, New Journal of Physics **10**, 033015 (2008).

[253] Y. Castin, J. Dalibard, and C. Cohen-Tannoudji, *The limits of Sisyphus cooling*, in *Light induced kinetic effects on atoms, ions and Molecules. Proceeding of the LIKE Workshops, ETS Editrice, Pisa*, 1991.